Doctoral Dissertation
Doctoral Program in Ph.D. in Electrical, Electronics and Communications
Engineering (XXXIV Cycle)

Modelling and characterization of electronic conductivity in 3D printed PEGDA:PEDOT polymer composites
High frequency applications

By

Matteo Manachino
******

Supervisor(s):
Prof. L. Scaltrito
Prof. F. Pirri

Doctoral Examination Committee:
Prof.ssa Edvige Celasco, Referee, Università degli Studi di Genova
Dr. Angelo Angelini, Referee, Istituto Nazionale di Ricerca Metrologica

Politecnico di Torino
2021

Declaration

I hereby declare that, the contents and organization of this dissertation constitute my own original work and does not compromise in any way the rights of third parties, including those relating to the security of personal data.

....

Matteo Manachino

Turin, December 2021

I would like to dedicate this thesis to my loving parents
Anna and Maurizio

Acknowledgment

Abstract

Additive manufacturing is an emerging and promising technology in biomedical, automotive, avionic and electronic industries, allowing advantages in terms of cost, weight reduction and efficiency upscaling respect to traditional manufacturing. 3D printing technologies offer high degree of freedom to customize products and incorporate components such as passive circuitry elements and sensors. The availability of inexpensive, reliable, electrically conductive material is a necessary condition to fully develop the potential of 3D printing in industrial applications customizing products which incorporate electrical elements. In the electronic market to satisfy the increasing complexity of circuits layouts, while reducing the need of printed circuit board assemblies, the more efficient solution involves the incorporation of passive components in the layer-by-layer structure, which is printed during the additive manufacturing process. The idea is to print, directly through stereolithography, fundamental electronic components and sensors and furthermore to exploit the bi-material system to manufacture in the same printing process, conductive and isolating regions in up to overcome the idea of flatness in printed circuit boards (PCBs) allowing the development of a complete three-dimensional electronic. By in-process printing and the feasibility of a 3D bulk structure, vias and nets may be designed targeting non-planar electronics, by which a more compact layout geometry is obtained, enhancing the technology scaling by leading to a device miniaturization. In this way 3D printing of electronic devices in capable of enhancing the miniaturization of devices as outcome of its technology. The main focus of this Ph.D. research activity held in Materials and Micro Systems Laboratory of Politecnico di Torino (ChiLab) and in collaboration with Microla Optoelectronics S.r.l., is to model the electrical conduction mechanism in 3D printed composite material based on intrinsic conductive polymers. Several PEGDA:PEDOT resin compositions were prepared and tested with different concentration of the constituents, to evaluate through a design of experiment conductivity optimization as function of the resin formulation. The physics related to metal/polymer interface was tackled, to fabricate proper ohmic contact, while

reducing the contact resistivity. Performing DC characterizations, AC impedance and the broadband dielectric spectroscopies of multilayer 3D printed devices, a rigorous analysis methodology was established to correlate the estimated quantities to the process parameters, leading to a targeted optimization of the latter, regarding a specific application of the 3D printed device. In conclusion, both a sophisticated explanation of the electrical conduction mechanism in multilayer 3D printed PEGDA:PEDOT devices discussed through comprehensive mathematical models and a systematic methodology of impedancemetric analysis focused to the 3D printed device optimization, regarding its functionality, were accomplished. Finally, high-level experimental-numerical correlation between literature conductivity models and measures, for several 3D printed tested devices, was achieved leading to the proposition to exploit 3D printed PEGDA:PEDOT devices in different applications, such as 3D printed high frequency embedded antenna sensors or electronic traces in printed circuits for high speed signals ranging from the digital to radio-frequency domain.

This work is composed of a first section in which an introduction to intrinsic conductive polymers is described, with a direct focus on those used in a 3D printing process, while in the second the main 3D printing technologies are presented, with major focus on the Stereolithographic process. In the third section the principal models explaining the arise of conductivity in intrinsic conductive polymers are tackled, while the focus of the fourth section is on the charge transport mechanisms involved when an external electrical field is applied to the polymeric device. In the fifth chapter the measurements carried out to improve the electrical parameters of the final 3D printed device, are reported with final prototypal applications.

Contents

Modelling and characterization of electronic conductivity in 3D printed
PEGDA:PEDOT polymer composites - High frequency applications

3

List of Figures

Modelling and characterization of electronic conductivity in 3D printed
PEGDA:PEDOT polymer composites - High frequency applications

5

Modelling and characterization of electronic conductivity in 3D printed
PEGDA:PEDOT polymer composites - High frequency applications

7

List of Tables

Chapter 1

Introduction to Polymers

A polymer is defined as a material composed of long molecular chains, constituted by a repetition of covalent bonding of smaller molecules, which are referred as monomers[1].

Polymers are classified into two macro families, based on the composition: organic and inorganic polymers. The first are composed primarily of hydrogens and carbons combined with different sulfur, oxygen or nitrogen atoms and they are widely used as elastomers, plastics and films other than fibers, due to their high processability, strength and low density, despite their brittleness at low temperature and vitrification at high temperature properties[2]. The latter, instead, contain no organic element and they are exploited mainly as precursor to ceramics, whereas their structure is based on nitrogen, phosphorus, silicon and oxygen atoms.

According to their mechanical behavior, each polymeric material can be classified in two separate families: plastics or rubbers (Figure 1), which are distinguished in terms of Young's Module. Since plastics exhibit higher values of stiffness, they are more rigid compared to rubbers, whose flexibility is derived from a long-range elasticity[3]. Another classification is drawn up on the basis of the thermal behavior[4], in fact plastics can be classified in thermoplastics or thermosets. These terms describe the behavior of the material in terms of the variation of an applied temperature, causing different type of processability. Overheated thermoplastics pass to a viscoplastic state and flows as a result of crystallization or reaching the glass transition temperature. Thermoplastics are characterized by the reversibility

of this melting process and benefit of this enhancing their processability. On the other hand, thermosets, on heating, are subjected to irreversible internal chemical reactions, setting the material to a given shape.
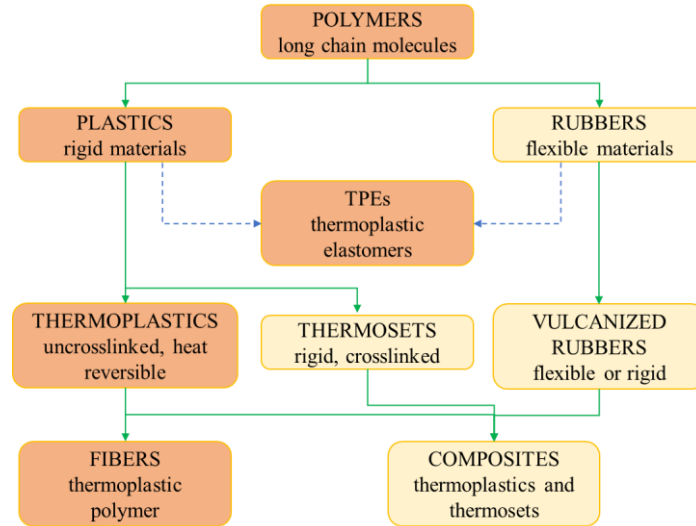
Figure 1: Classification of polymers by properties.

A polymer is primarily an insulator. It would be fairly impossible to consider that polymers or plastics might carry electricity. Their widespread use as an insulating material is the primary reason they are investigated and developed. Indeed, these materials are frequently used to encase copper wires and to construct the exterior shells of electrical gadgets, which protect humans from direct contact with electricity.

Property	Conducting Polymers	Metals	Insulators
Electrical conductivity [S/cm]	$10^{-11} - 10^3$	$10^{-4} - 10^6$	$10^{-20} - 10^{-12}$
Carriers	Electrons of conjungated double bonds	Valence electrons	−
Carriers density [cm^{-3}]			−
Impurities effect	Orders of magnitude	Weak	Strong
Magnetic behaviour	Paramagnetism	Ferro/Diamagnetism	Diamagnetism

Table 1: Physical properties of conducting polymers, metals and insulators.

Conjugated polymers are organic macromolecules having an alternating backbone chain of double and single bonds[5]. Their overlapping p-orbitals form a system of delocalized π-electrons, which exhibits a variety of intriguing and useful optical and

Modelling and characterization of electronic conductivity in 3D printed
PEGDA:PEDOT polymer composites - High frequency applications

3

electrical characteristics, because they are covalently linked and lack the valence band found in pure metals. It is well accepted that doping is an efficient approach for producing conducting polymers (Table 1). Due to the development of conduction bands, doping enables electrons to flow and as doping occurs, the loosely bound electrons in the conjugated system are able to hop along the polymer chain (Figure 2). When electrons move through polymer chains, an electric current is generated. Polyacetylene, Polypyrrole, Polyaniline, and Polythiopene are all examples of conjugated conducting polymers.
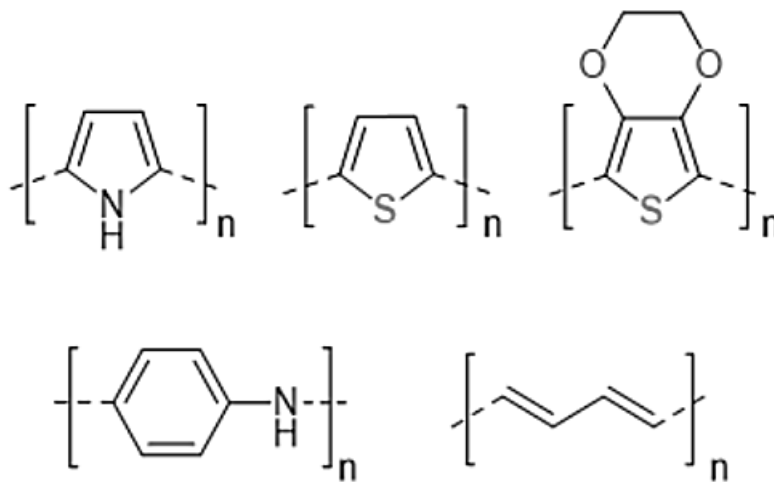
Figure 2: Basic structure of conjugated polymer

While polyacetylene is one of the most widely researched conducting polymers, it has several practical drawbacks, including its high instability in the presence of air. As a result, the creation of novel types of conducting polymers has garnered considerable attention. A notable exception is the family of Polyheterocycles composed of polymers such as the aforementioned Polypyrrole (PPy) or Polythiophene (PT), as well as Polyaniline (PANI) and Poly(3,4-ethylenedioxythiophene) (PEDOT). These materials exhibit excellent thermal stability, high conductivities and are facile to produce.

To understand why semiconducting polymers[6], such as conjugated polymers, exhibit intriguing conductivity characteristics, it is necessary to understand how polymers bind. The majority of organic molecules, in particular CH_4 molecules, that is the chemical formula of methane, are composed of covalent bonds (Figure 3a). In this molecule the valence shell, which is the outermost one of a carbon four

electrons are contained, while for hydrogen there is just one negative charge. To create a bond between the carbon and the hydrogen, the latter shares with carbon one electron, resulting in a covalent connection with two shared negative charges. The created ligand is referred to as sigma bond (σ-bond). Due to the fact that carbon has four electrons, the CH_4 molecule is constituted of four sigma bonds, differently angled due to electronic repulsion. Following considerations on the chemical structure of ethane, C_2H_6 (Figure 3b) assert it has a similar bonding structure to methane, each carbon is connected through three different σ-bonds to hydrogens and by another σ-bond to the other carbon and the structure is specular for the other carbon.
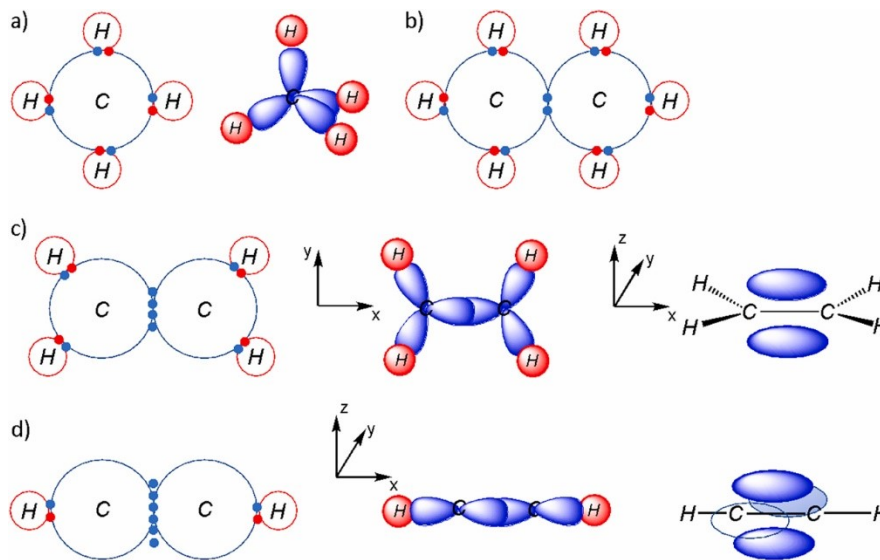
Figure 3: a) CH_4 covalent bond and σ-bond hybridized orbital; b) C_2H_6 covalent bond; c) C_2H_4 covalent bond, σ-bond in hybridized orbital, π-bond as hybridized orbitals; d) C_2H_2 covalent bond, σ-bond hybridized orbital.

When ethene or ethylene, C_2H_4, is introduced, the condition begins to improve (Figure 3c). The carbon, as the other one, will still make with hydrogen a σ-bond. In the end through the overlapping of two p_z orbitals a π-bond is formed (Figure 3c right). The electron-carrying link geometry, also called orbital,[7] starts to alter. Whereas inside the molecule's sheet is contained the σ orbital and it is sandwiched between two atoms, the π orbital extends up and down the molecule's sheet. In the molecule of acetylene, C_2H_2, the number of π orbitals increases (Figure 3d), because the connection between carbon and hydrogen is unique, resulting in three unpaired electrons for each carbon atom, which creates with the other carbon one σ and two

π hybrid orbitals, created through the orbital overlapping of a couple of p_z with another couple of p_y.

Considering the bonding properties of $[C_2H_4]_n$ (polyethylene) and $[C_2H_2]_n$ (polyacetylene), to whom referred as polymers. In polyethylene, the binding can be explained as a continuation of the process that occurs in ethane. Each carbon atom is bound to two atoms of carbon and hydrogen, so that only single bonds contribute to constitute the polymer distributing the electron density in the intermediate space of the atoms. Due to the fact that these localized electrons are unable to travel large distances, polyethylene is an electrically insulating substance. In comparison, polyacetylene's bonding is an extension of ethylene's. When the bonding between the carbon atoms is examined, it is noticeable that they all are σ orbitals, although π-bonds of hydrogens contribute to delocalize electron around the polymeric chain. When a sequence of π orbitals is uniformly spaced and near in proximity to one another, these orbitals might begin to interfere causing the electron to delocalize and this is the reason because the π-conjugation of the molecular structure increases the electron mobility enabling the polymer to conduct.

Another remarkable property of π-conjugated polymers is their vibrant coloration, meaning their capability to absorb and re-emit photons in the visible spectrum. To comprehend this characteristic, the bonding must be examined again, considering the orbital energy levels. In the molecule of H2, each atomic orbital generates a σ bond and additionally a hybridized orbital (i.e. anti-bonding orbital) is created, denoted by the symbol *, as presented in Figure 4a. The σ* bond has more energy respect to the σ one and since electronic states are occupied starting from the lower energy, the bonding state is occupied by the two electrons from each hydrogen. The bonding state (σ) is also referred to as the HOMO ("highest-occupied molecular orbital") in this situation, as it is the state at higher energy still containing electron charges. In comparison, the anti-bonding state (σ*) is referred to as the LUMO ("lowest-unoccupied molecular orbital"), as it is the state at lower energy devoid of electron charges[8].
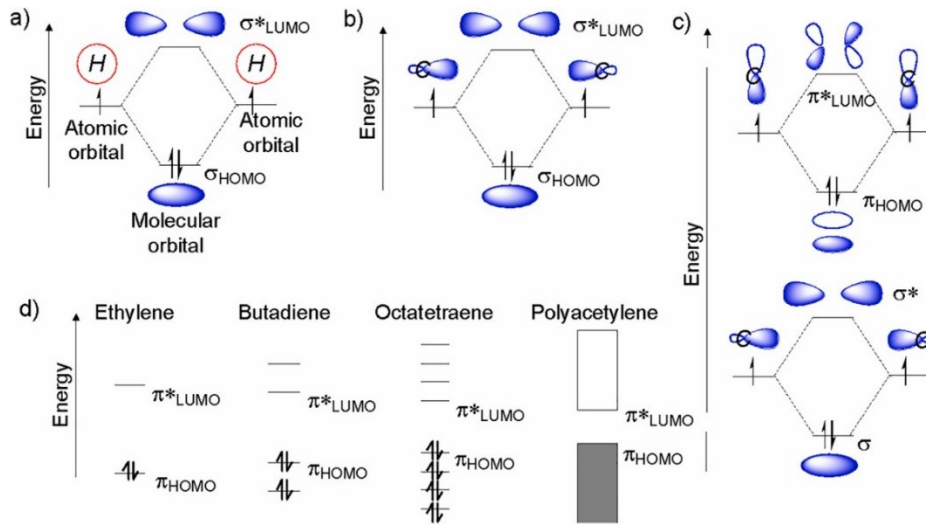
Figure 4: Hybridized orbital energy level diagrams for a) H_2; b) C_2H_6; c) C_2H_4; d) C_2H_4,
C_4H_6, C_8H_{10}, and $[C_2H_2]_n$ (i.e. polyacetylene).

Examining ethane once more, but focusing on the bond between the two carbon
atoms rather than the bond between the carbon and the hydrogen. Analogous to the
generation of σ bond and anti-bond for the H_2 molecule, the binding of the two
carbon atom is performed (Figure 4b). In the same way, C_2H_4 forms a σ state with
the anti-state. Additionally, π and π* orbital are created (Figure 4c). In ethane, the
σ state is the HOMO level, while the σ* is the LUMO, and in ethylene, the π bond
generates the HOMO level and the π* the LUMO. In a π-conjugated molecule the
increasing number of double bonds leads to the formation of C_4H_6, C_8H_{10} and
finally $[C_2H_2]_n$, causing the increase in the energy HOMO, while for the LUMO the
energy falls. Consequently, the conjugation length increases, so the HOMO-LUMO
energy gap shrinks (Figure 4d).

Investigating the optical absorption properties of organic polymers, the photon
interaction with a molecule is based on the photon energy, $E \approx \frac{1240 \, [eV \cdot \mu m]}{\lambda}$, where
'λ' is the wavelength of light radiation. if 'E' is greater than the energy difference
between the HOMO and the LUMO, an electron can transitate to the LUMO across
the energy gap (Figure 5a), by absorbing the photon energy. After a characteristic
time constant τ, defined by the inter-level energy difference, the electron may decay
to the HOMO state, causing a photon to be emitted if the transition respect Fermi's
golden rule. The wavelength of photon absorbed and emitted is proportional to the
difference in energies between the HOMO and the LUMO (i.e. energy gap).
Ethylene energy gap is such that the absorbed photon wavelength is included in the

range of 0.1-0.4 µm of UV light (Figure 5b), but this gap is narrow enough for extended π-conjugated molecules that visible photons (wavelength 0.4-0.8 µm) are interacts with the energy level by absorption or emission[9]. For this reason, π-conjugated orbitals enables not only the conduction of charges through the polymer, but even absorption and re-emission of photons in the visible light spectrum, that are critical characteristics for OLED and OSC based devices.
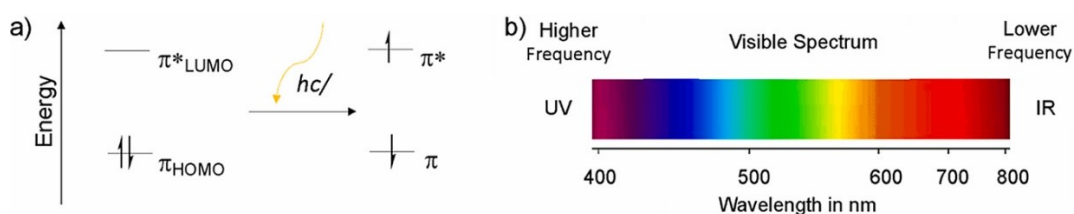
Figure 5: a) Photoexcitation transition energy levels diagrams of hybridized orbitals from HOMO to LUMO due to photon absorption; (b) Visible spectrum of light.

1.1 Conductive Conjugated Polymers

Conductive polymers are a category of organic polymers capable of conducting electricity[10]. These compounds might be metallic conductors or semiconductors. The primary benefit of conductive polymers is their processability, which is mostly achieved by dispersion. Conductive polymers are not typically thermoplastic, since they cannot be thermoformed, however, they are organic compounds, similar to insulating polymers. Although they exhibit excellent electrical conductivity, they lack the mechanical characteristics of other commercially available polymers. The electrical characteristics of the material may be fine-tuned implementing organic synthesis processes and sophisticated dispersion techniques.

The major class of conductive polymers and copolymers are those with a linear such as Polyindole, Polyaniline, Polyacetylene and Polypyrrole. Poly(p-phenylene vinylene) (PPV)[11] is a semiconducting polymer, which exhibits electroluminescent properties together with its soluble. Poly(3-alkylthiophenes) are archetypal material for transistors and solar cells nowadays. A prior classification (Table 2) of organic conductive polymers is due

to the constituent, specifically based on the content of the main chain, which constitutes the backbone structure.

Content of the main chain	No heteroatom	Heteroatoms present	
		Nitrogen-containing	Sulfur-containing
Aromatic cycles	Poly(fluorene)s polyphenylenes polypyrenes polyazulenes polynaphthalenes	The N is in the aromatic cycle: poly(pyrrole)s (PPY) polycarbazoles polyindoles polyazepines The N is outside the aromatic cycle: polyanilines (PANI)	The S is in the aromatic cycle: poly(thiophene)s (PT) poly(3,4-ethylenedioxythiophene) (PEDOT) The S is outside the aromatic cycle: poly(p-phenylene sulfide) (PPS)
Double bonds	Poly(acetylene)s (PAC)		
Aromatic cycles and double bonds	Poly(p-phenylene vinylene) (PPV)		

Table 2: Classification of organic conductive polymers based on composition.

Multiple mechanisms contribute to the conductivity of these polymers. For example, electrons in the valence band are bonded in covalent bonds which are sp^3 hybridized in conventional polymers such as Polyethylenes. Electrons involved in the σ bond have a limited mobility, so they do not provide a significant contribution to the material electrical conductivity. However, the situation is entirely different with conjugated materials. Conducting polymers feature adjacent sp^2 hybridized carbon centers, as their backbones in which each center has one valence electron in a p_z orbital, orthogonal to the other three σ-bonds. All of the p_z orbitals combine to form a molecule-wide collection of delocalized orbitals. When the material is "doped" by oxidation, which eliminates some of these delocalized electrons, the electrons in these delocalized orbitals acquire a high mobility. Thus, the conjugated p-orbitals create a one-dimensional electronic band, and when the band is partially depleted, the electrons inside it become mobile, so that with a tight binding model, the band structures of conductive polymers may be easily predicted. These same materials can theoretically be doped by reduction, which adds electrons to an otherwise empty band, although, the majority of organic conductors are oxidatively doped to produce p-type materials. The redox doping of organic conductors is comparable to the doping of silicon semiconductors, in which a tiny proportion of silicon atoms are replaced by electron-rich, for example, phosphorus, or electron-poor, for example, boron, atoms to form n-type and p-type semiconductors, respectively.

While "doping" conductive polymers is generally accomplished by oxidizing or reducing the substance, conductive organic polymers coupled with a protic solvent may also be "self-doped"[12].

Conjugated polymers that are not doped are semiconductors or insulators. The energy gap in such compounds may be more than 2 eV, which is too large for thermally triggered conduction. As a result, undoped conjugated polymers such as Polythiophenes and Polyacetylenes have a very poor electrical conductivity of around 10^{-10} to 10^{-8} S/cm. Electrical conductivity rises many orders of magnitude even at a relatively modest doping level (1%), reaching values of about 10^{-1} S/cm. Subsequent doping saturates conductivity at values between 10^2 and 10^4 S/cm for various polymers. The highest conductivity values recorded to far are for stretch orientated polyacetylene, with verified values of around $8 \cdot 10^4$ S/cm. Although polyacetylene π-electrons are delocalized along the chain, pure polyacetylene is not a metal. Polyacetylene is composed of alternating single and double bonds with lengths of 1.44 Å and 1.36 Å and its conductivity rises as a result of the bond modification. Conductivity enhancements without doping are also accomplishable using a field effect transistor (organic FET or OFET) and irradiation. Additionally, certain materials show negative differential resistance and voltage-controlled "switching," similar to inorganic amorphous semiconductors.

Despite extensive study, the connection between morphology, chain structure, and conductivity is not completely defined, nowadays, while it is generally thought that increased conductivity results may be achieved from a higher degree of crystallinity[13] and better chain alignment, this has not been demonstrated for polyaniline and was only recently proven for PEDOT, which is mainly amorphous.

Conductive polymers have been used in commercial displays and batteries to demonstrate their potential as antistatic materials. They may also be useful in printed electronic circuits, actuators, supercapacitors, organic light-emitting diodes, chemical and bio-sensors, as well as in flexible capacitive touch sensors, electromagnetic shielding, and possibly as a replacement for the popular transparent conductor indium tin oxide in organic solar cells, as hole acceptor layer[14].

1.1.1 Extrinsically conductive polymers

Extrinsically conducting polymers are capable of acquiring conductivity due to the presence of externally added components[15]. They are classified into three categories:

I.   Conductive element-filled polymers: the polymer behaves as a binder,
     binding the conducting components together to form a solid entity. The
     percolation threshold is the lowest concentration of the conductive filler that
     must be supplied to get the polymer to conduct (Figure 6).
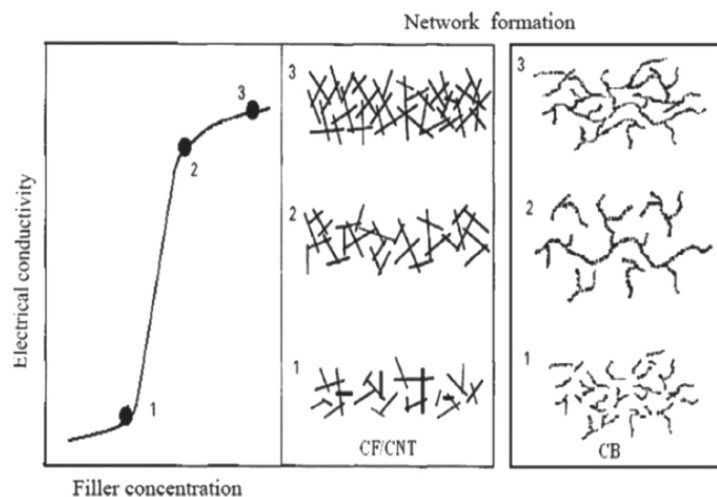
Figure 6: Conductivity of composites increase with different networks and increase of
filler for carbon fibre (CF), carbon nanotube (CNT) and carbon black (CB); [1] before
percolation, [2] percolation, [3] above percolation.

Several important properties of these polymers include the following:

    a.   High bulk conductivity.
    b.   Less expensive.
    c.   Quite lightweight.
    d.   Mechanically robust and durable.
    e.   Processable into a variety of shapes, forms, and sizes.

II. Blended conducting polymers: These polymers are created by physically or
     chemically combining an isolating polymer with a conducting polymer.
     These polymers are more processable and have improved physical, chemical,
     and mechanical characteristics.
III. Coordination or inorganic conducting polymers : These polymers include
     charge transfer complexes and are formed when metal atoms are combined
     with polydentate ligands.

Extrinsically conducting polymers include those composed of a matrix of
poly(ethene) with a proportion of conducting carbon black (as powdered graphite).

The material conducts when the carbon black particles are near enough to touch one another, and it is an insulator if the particles are not in touch. This implies that the degree of electrical conduction is temperature dependent. At elevated temperatures, the poly(ethene) matrix swells and pushes the carbon black particles apart, reducing conductivity. At lower temperatures, poly(ethene) shrinks, bringing the carbon black particles closer together and improving the material conductivity. Due to the conductivity temperature dependency, this material is frequently used in self-regulating heater cables and re-settable circuit protection devices[16].

1.1.2 Intrinsically conductive polymers

The simplest intrinsically conducting polymer is poly(ethyne), also known as poly(acetylene) (Figure 7). It is composed of a hydrocarbon chain with an alternating pattern of single and double bonds; this is referred to as a conjugated system[17]. The p-orbitals that constitute the double bonds might overlap, resulting in a delocalized π-system (similar to the one in benzene). The delocalised system conducts electrons, allowing the polymer to conduct. Indeed, chemicals additives (i.e. iodine) must be used to increase conductivity, guaranteeing that the polymer exists as delocalised single and double bonds, rather than as localised. Suitably doped poly(ethyne) can show conductivity equivalent to copper, when stretched to align the chains in the same direction. While poly(ethyne) presents difficulties in daily applications because to its susceptibility to attack by oxygen from the air, other more durable polymers with conjugated systems also exhibit conductivity.
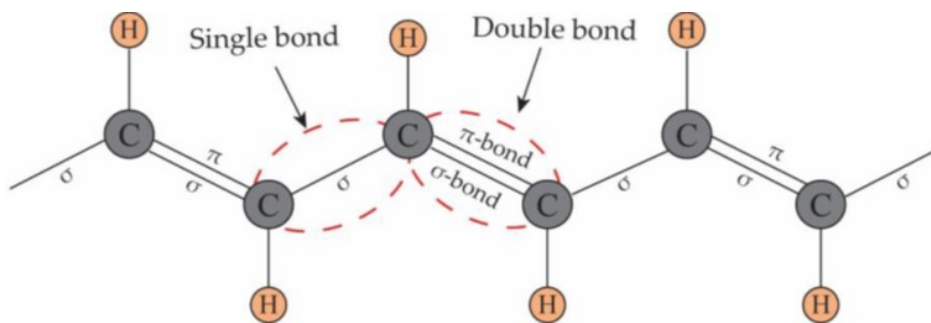
Figure 7: The backbone of polyacetylene is composed of conjugated double bonds.

Intrinsically conductive polymers have a strong backbone composed of many conjugated systems that contribute to their conductivity. They may be classified into two types[18]:

i.   Conducting polymers with a backbone containing conjugated π-electrons: These polymers are primarily composed of a conjugated π-electron backbone that carries the charge. The electrical field excites the conjugated π-electrons in the polymer, which may subsequently be transferred through the solid polymer. Additionally, the overlapping of conjugated π-electrons orbitals, throughout the whole backbone, results in the development of valence and conduction bands spanning through the entire polymer molecule. Conjugated π-electrons improve the conductivity of polymers.

ii. Doped conducting polymers: Conducting polymers are those that have been doped by exposing them to a charged transfer agent in either gas or solution phase. Doping is a technique that increases the conductivity of polymers by oxidizing or reducing the polymer backbone to create a negative or positive charge.

Doping may be classified into two types:

a)   p-Doping : This is carried out through the oxidation process. The conducting polymer is treated with a Lewis acid.

b)   n-Doping : This is carried out by a reduction procedure. The conducting polymer is treated with a Lewis base.

Intrinsically conductive polymers have a number of advantages.

i.   Conductivity.
ii.   Capacity for charge storage.
iii. Proclivity for ion exchange.
iv.   Absorption of visible light, resulting in a photoluminescence process.
v.   X-ray transparency.

The disadvantages of inherently conducting polymers include the following:

i.   Lower conductivities than metals.
ii.   Not suited to be processed.
iii. Mechanical weakness.
iv.   Decreased stability at elevated temperatures.
v.   Degradation of conductivity during storage.

1.2 Photo-activated conductivity in polymers

Different types of polymers can be sintered using a specific wavelength laser radiation, which initiates a chemical reaction that results in polymerization, a chemical reaction that polymerizes the chains. This process is known as photopolymerization. Polymerization is a generic term that refers to any reaction between monomers that results in the production of one or more polymeric chains and, thus, the term photopolymerization refers to the synthesis of polymers by a reaction between the chains, begun by the absorption of light radiation from the polymerizing system. The radiation employed supplies just the initial energy required to initiate the reaction and does not interfere with the process propagation or termination stages.

Photoinitiators can be used to induce both radical and ionic polymerizations. They are organic or inorganic substances that are thermally stable and capable of absorbing substantial amounts of light with an absorption peak wavelength in the ultraviolet or in the visible range. The photoinitiator function is to convert the incident light energy into chemical energy in the form of reactants intermediates, radical or excited state[19]. The photoinitiator must have a high absorbance at the wavelength of the incident radiation in order to undergo rapid photolysis and generate the initiating species, resulting in a high quantum efficiency (a measure of the efficiency by which light or other energy is converted or exploited)[20].

In the industrial sector, photoinitiators are commonly activated by UV radiation, with wavelengths ranging from 300 to 400 nm. Controlling UV-sensitive reagents is straightforward and does not require any particular precautions, beyond storing them in areas protected from light sources and away from heat sources. The polymerization process can be carried out at either room temperature or at lower temperatures. Additionally, formulations can be employed without the need of solvents.

UV radiation is required solely for the process's commencement (i.e. photoinitiation); reactions such as propagation, chain transfer, and termination do not require UV radiation. The latter are thermal reactions that are unaffected by light radiation. The following diagram (Figure 8) illustrates the macromolecule polymerization system:

Radical reactions

$$R\text{-}X \longrightarrow R^\bullet + X^\bullet \qquad\qquad \text{Activation}$$

$$R^\bullet + M \longrightarrow P_1^\bullet \qquad\qquad\qquad \text{Initiazion}$$

$$P_1^\bullet + M \longrightarrow P_{n+1}^\bullet \qquad\qquad\quad \text{Propagation}$$

$$P_n^\bullet + P_m^\bullet \longrightarrow P_{n+m} \qquad\qquad \text{Termination by recombination}$$

$$P_n^\bullet + P_m^\bullet \longrightarrow P_n + P_m \qquad \text{Termination by disproportion}$$

Secondary radical reactions

$$P\text{-}X \longleftrightarrow P^\bullet + X^\bullet \qquad\qquad \text{Dissociation-Recombination}$$

$$P\text{-}X + A \longleftrightarrow P^\bullet + AX^\bullet \qquad\quad \text{Atomic transfer}$$

$$P\text{-}X + P^{I\bullet} \longleftrightarrow P^\bullet + X\text{-}P^{I} \qquad \text{Chain transfer}$$
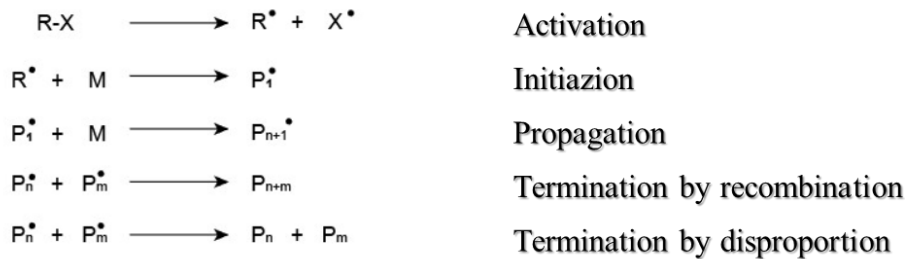
Figure 8: The photoinitiator reaction is depicted schematically following UV radiation absorption on the R-X photoinitiator. The generation of reactive species such as $R^\bullet$ and $X^\bullet$ radicals can initiate additional processes on M monomers, resulting in polymerization and cross-linking of the polymer chains P via propagation and chain transfer. Finally, the reaction can be terminated by the interaction of two $P^\bullet$ radical chains. Additionally, secondary radical reactions occur.

Photopolymerization is applied in different polymerization processes, such as radical, cationic and anionic, sol-gel and controlled polycondensation. Considering the synthesis of macromolecules through radical process, as it is typical of acrylate polymers, the radical process[21] occurs as a result of the generation of a free radical. The latter is able to interact with the monomers or with the already formed chains in the formulation, going to bind to the same monomer (or chain) forming a macroradical, which, in turn, will proceed to bind with another monomer (or chain), causing the molecular weight of the macromolecule to increase. The propagation of the reaction is triggered by the interaction of the initiator with the light radiation, which will react by transforming into a radical.

The creation of the first radicals is followed by the propagation stage, when the linear elongation of polymer chains is due to the radical addition of monomers.

This phase is continued until the chains are sufficiently long to form branches as a result of interaction between the chains or chain transfers (macroradical polymer chains react with a second monomer, where the RH monomer will donate its own hydrogen to the chain turning into an R- radical and the polymer chain will end its propagation). Polymerization can terminate due to three different causes: recombination, disproportion and chain occlusion. Recombination occurs when two radical polymer chains join to form a single polymer macro chain, increasing its molecular weight. Disproportion occurs when the two radical chains do not join but react, through a hydrogen transfer from one chain to the second, thus forming two distinct polymer chains. Occlusion occurs when a free radical is used as a terminator of the chain, going to extinguish the radical propagation. Radicals formation will be one of the principal reasons of polarons and bipolarons formation in 3D printed conductive polymers, as it will be discussed in Chapter 3.

Two types of compounds are used as photoinitiators for polymerization, differing in their mode of generating reactive free radicals. After absorption of a photon from incoming radiation, Type I initiators undergo fast bond cleavage. Type II initiators form excited states (i.e. triplet states) which are capable of exist for a certain period of time, so that they can generate a second reaction, such as the hydrogen transfer, leading to the creation of a radical[22].

Typically, photoinitiators of Type I contain aromatic carbonyl groups, which act as chromophores. The formation of radicals occurs due to the absorption of light radiation by the chromophores, which donates sufficient energy for the breaking of the C-C bond adjacent to the aromatic group. The bond splitting appears to be more advantageous than the singlet or triplet excited states, implying that the production of a pair of radicals is preferable to the development of an excited state of the molecule.

Similar to Type I initiators, Type II initiators include aromatic carbonyls aromatic carbonyl chromophores, but require co-initiators to reach the radical excited state. After photon absorption, the triplet excited state is more probable than the C-C bond cleavage, because the triplet energy is less than the energy necessary to break the bond. The triplet species, on the other hand, can react with a suitable co-initiator (i.e. alcohol or an amine), extracting a hydrogen to a lower energy state and so producing a radical on the co-initiator. Through correct mixing, both Type I and Type II initiators may be easily integrated into polymeric solutions.

1.2.1 Photopolymerization

Photopolymerization is a subfield of photochemistry concerned with the absorption of light by matter, namely molecules. In this discipline, light is seen as a reagent capable of excite molecules and allow them to pass the activation energy thresholds required for chemical processes to occur. Photoresists are often placed on surfaces and are engineered to change their characteristics when exposed to light. These modifications polymerize the liquid oligomers into insoluble cross-linked network or breakdown the solid polymers into liquid products.

Negative resist polymers are those that create networks as a result of photopolymerization. Positive resists, on the other hand, are those that degrade during photopolymerization. Positive and negative resists have a variety of applications, including the design and manufacture of microfabricated devices. Photolithography developed as a result of the ability to design the resist using a concentrated light source (Figure 9).
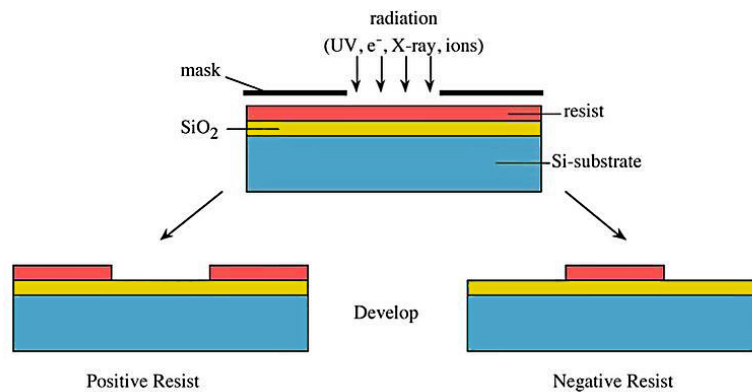
Figure 9: Positive and negative photoresist comparison.

A photopolymer, known as a photo-resin, is a kind of polymer that reacts chemically when exposed to ultraviolet or visible light. When oligomers or monomers are exposed to light, they crosslink, creating a thermoset network polymer and this process is also referred to as 'curing'. To be exact, light does not immediately activate the majority of monomers or oligomers; a photoinitiator is needed in this scenario. Light absorbed by a photoinitiator produces free radicals, which initiate cross-linking events between a mixture of functionalized oligomers and monomers, resulting in the formation of the cured film.

Modelling the photopolymerization process of an acrylic SL (i.e. Stereolithography) resin is extremely complicated, considering the presence of an great number of chemical and physical variables, critical in this sort of process. Several models are presented in the literature that allow the estimation of certain parameters such as the reaction speed of the process, which is a function of the concentrations of photoinitiators [I] and monomers [M].

The rate of polymerization[23] of a generic polymer chain is determined by the rate of monomer consumption, as shown in Eq. 1:

$$\text{Eq. 1:} \quad R_p = \frac{k_p}{k_t^{1/2}}[M]\left(\frac{R_i}{2}\right)$$

Where R_i is the reaction velocity of the initiators, whose concentration is denoted by [I], k_p and k_t are the coefficients of the velocities of propagation and termination stages, respectively and [M] is the concentration of monomers. In the case of a photopolymerization reaction, the rate of the photopolymerization process is given by Eq. 2:

$$\text{Eq. 2:} \quad R_p = \frac{k_p}{k_t^{1/2}}[M]\{\varphi \cdot I_0(1 - e^{G[I]b})\}^{1/2}$$

Where φ is the quantum efficiency of the initial stage, I_0 is the intensity of the incident light, G is the extinction coefficient, b is the desired thickness of the polymerized resin layer. These equations are true in case of a steady state condition.

The polymerization rate is related to both the monomer and the square root of the initiator concentration (Eq. 3). The average molecular weight of the polymer may be calculated as the ratio of the propagation and initiation rates. According to Eq. 4, the polymer weight indicates the average kinetics of chain length creation, v_0:

$$\text{Eq. 3:} \quad R_p = -\frac{\partial [M]}{\partial t} \sim [M]\{k[I]\}^{\frac{1}{2}} \rightarrow \text{Eq. 4:} \quad v_0 = -\frac{R_p}{R_i} \sim \frac{[M]}{[I]^{1/2}}$$

Eq. 3 and Eq. 4 are significant for the stereolithographic process and balancing the concentrations of photoinitiators [I] respect that of monomers [M], the greater the polymerization rate R_p, the more quickly the components are produced. Due to the fact that SL resins are made up of monomers or oligomers, their concentration is

considered to be constant. As a result, the only way to regulate both the rate of polymerization and the chain formation kinetics is by controlling the photoinitiator concentration.

1.3 PEDOT:PSS

PEDOT:PSS (Figure 10) is a polymer mixture composed of two different polymers. PEDOT is a conjugated polymer composed of poly(3,4-ethylenedioxythiophene), which is a hole carrier. The second component is polystyrene sulfonate, which contains deprotonated sulfonyl groups that are negatively charged.
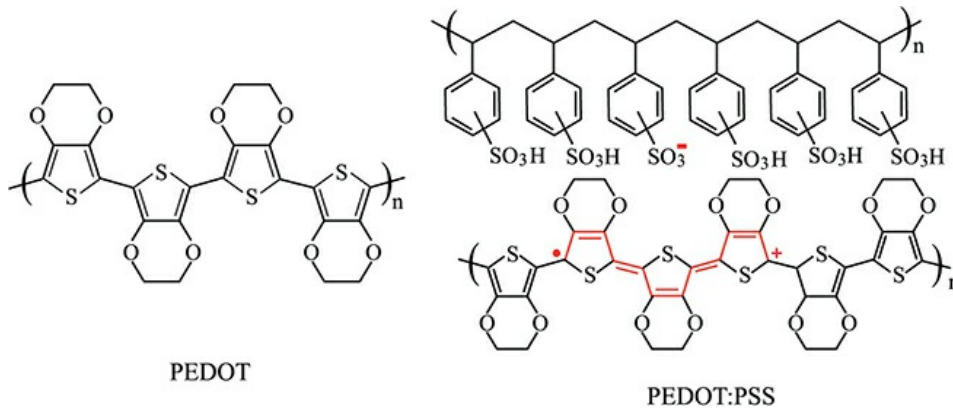
Figure 10: Chemical structures of poly(3,4-ethylenedioxythiophene) (PEDOT) and poly(3,4-ethylenedioxythiophene):polystyrene sulfonate (PEDOT:PSS).

The conducting PEDOT:PSS grains are encased in an insulating PSSH-rich layer[24][25][26] with a thickness of about 37 Å[24]. While percolation networks improve the DC current conductivity, structural and morphological inhomogeneities are obstacles for charge transfer and result in capacitive effects. The electronic band gap of neutral PEDOT is about $1.5 - 1.7$ eV, as determined by the beginning of the $\pi \rightarrow \pi^*$ absorption spectrum, with λ_{max} at 610 nm matching to its deep blue colour[27][28]. Even if PEDOT is not water-soluble, it may be coupled with a water-soluble polyelectrolyte, poly(styrene sulfonic acid) (PSS), that operates as a charge-balancing dopant during the polymerization process to produce PEDOT:PSS. This compound is a dispersion with outstanding film-forming characteristics, a high conductivity (about 10 S·cm^{-1}), a high transmittance of visible light, and great stability.

PEDOT:PSS thin films may be heated in air at 100 °C for over 1000 hours without significantly changing their conductivity[28] in the range of $1-10$ S·cm^{-1}. In Figure 10, which depicts PEDOT and the most often used PEDOT:PSS mix, the PEDOT chain is visible beneath the PSS chain, with one positive charge and one unpaired electron creating a polaron. The PEDOT chain positive charge is balanced by the PSS chain negative charge in the SO group. Only holes contribute to the electrical conductivity of PEDOT:PSS. Electrons injected into the system will instantly recombine at oxidized PEDOT sites. Electrochemical studies indicate that the oxidation level per monomer is on the order of one charge per three EDOT units, which suggests a hole density of around $\rho = 3 \cdot 10^{20}$ cm^{-3} for PEDOT:PSS films. Conductivity values on the order of 1000 S·cm^{-1} are seen in highly conductive sheets, meaning a hole mobility of $\mu_p = 20$ cm^2·V^{-1}·s^{-1}.

1.3.1 Electronic Structure

Starting the examination of the electrical structure of PEDOT:PSS by focusing on the PEDOT component, which is composed of the conjugated polymer backbone that confers the conducting characteristics. At the beginning, a very simple look at a short chain of EDOT units is taken.

Considering a chain of 12 EDOT units, a quantum chemical calculation of the DFT-B3LYP (i.e. Density functional theory − Becke[29], 3-parameter[30], Lee–Yang–Parr[31]) functional[32] to evaluate the level of the HOMO (highest occupied molecular orbital) and LUMO (lowest unoccupied molecular orbital) was performed to get an initial understanding of their shape and localization, as well as the energies of the associated levels and the energy gap. The HOMO results are displayed in Figure 11, while the LUMO results are shown in Figure 12.
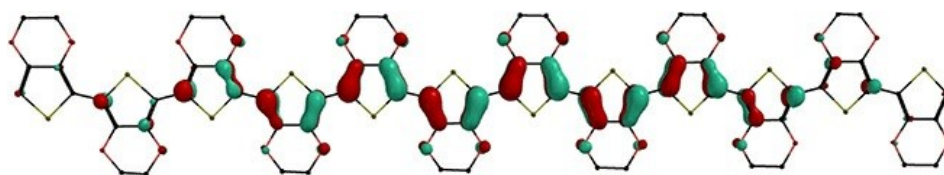
Figure 11: HOMO of a chain of 12 EDOT units quantum chemical calculation result. The HOMO energy level is −3.67 eV.
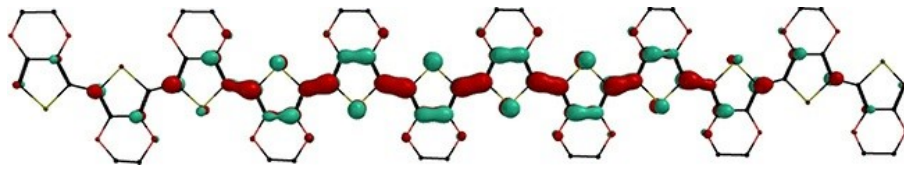
Figure 12: LUMO of a chain of 12 EDOT units. The energy value of LUMO energy level is
−1.62 eV. The HOMO–LUMO gap is 2.05 eV.

Both the HOMO and LUMO orbitals are confined along the conjugated thiophene backbone and the estimated values for the HOMO and LUMO energy levels are 3.67 eV and 1.62 eV, respectively, resulting in a 2.05 eV HOMO–LUMO gap. A B3LYP calculation of oligomers with lengths up to 8 units projected a band gap of around 2.2 eV at infinite length[33], recalling that the experimental electronic band gap has been calculated to be in the region of 1.5–1.7 eV from the beginning of the $\pi \rightarrow \pi*$ absorption spectra.

The calculations above carefully investigated the electronic structure transformation of a single isolated thiophene monomer, the basic unit of the polymer system, progressing through the band structures of the isolated PEDOT chain and the pristine crystal, and finally proposing a model for the band structure of the PEDOT:PSS mixture. The final band structure computations employed optimized crystal structures based on partial experimental data and included BLYP[34] exchange-correlation functionals within the GGA (i.e. Generalized Gradient Approximation). These specifics of the computations[24] lead to results summarized in Figure 13 by the band structures.
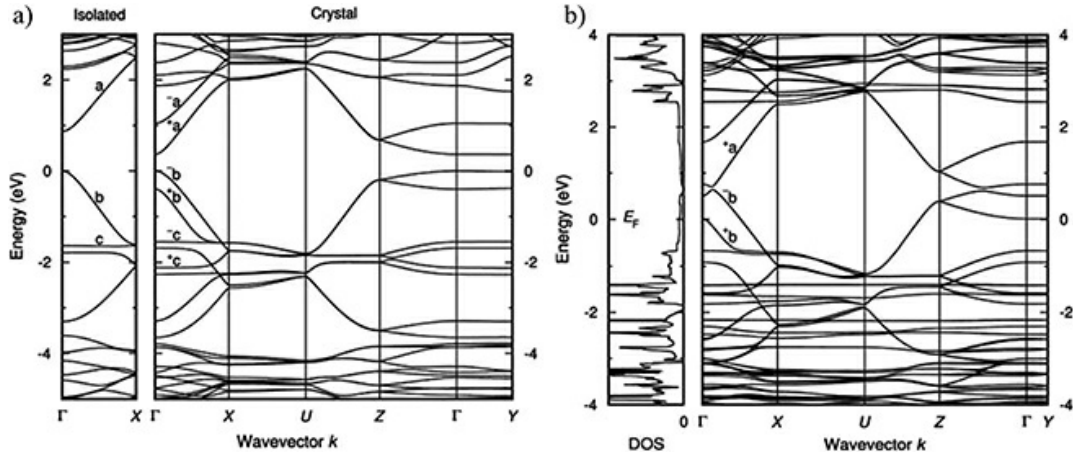
Figure 13: (a) Isolated chain and pristine PEDOT crystal band structures. Crystallographic coordinates of the Brillouin zone symmetry points in the of the orthorhombic lattice: X=(0.5,0,0), Y = (0, 0.5, 0), Z=(0, 0, 0.5) , U = (0.5, 0, 0.5). There is a shift of the energy levels, so the valence band edge is set to 0. (b) Band structure and Density of States (DOS) of PEDOT:Tos crystal, proposed as a model for PEDOT:PSS. Fermi level E_F is the 0 value.

Considering the band structure of the isolated chain and the pristine PEDOT crystal as a starting point, the isolated chain was modelled as a one-dimensional crystal with two monomer units per unit cell, the length of which was determined by geometry optimization of different cell lengths. The band structure of the PEDOT crystal is based on a predicted orthorhombic unit cell comprising two chains of two EDOT monomers each, with a = 7.935 Å, b = 10.52 Å, and c = 7.6 Å, where 'a' was optimized and 'b' and 'c' were determined experimentally. This orthorhombic structure was compared to the band structure of PEDOT:Tos (tosylate-doped PEDOT), which was exploited as a model for PEDOT:PSS (b). However, precise molecular structure studies demonstrate that the PEDOT crystal is more accurately described by a monoclinic unit cell. The monoclinic unit cell lattice parameters were estimated to be a = 12.978 Å, b = 7.935 Å, c = 7.6 Å, and β = 125.85°. The backbone of the chain in orthorhombic cell is oriented along the a-axis, whereas for the monoclinic it is orientated along the b-axis. A notable characteristic of the isolated chain is that the valence band, which has a global bandwidth of 3.30 eV, is composed of four subbands, the most dispersive of which is shown in Figure 13(a). E_g = 0.87 eV is the computed energy gap. When scaled by 200 percent, as is suggested for DFT values, this value is close to the value calculated from the optical absorption start, which is around 1.8 eV. The entire valence bandwidth of the pure

crystal, defined by the top eight subbands, is W = 3.65 eV, while the energy gap is E_g = 0.37 eV.

The effective masses, m*, of electrons and holes may be derived from the curvature of the energy bands E(k) using the equation $\frac{1}{m^*} = \frac{1}{\hbar^2} \frac{d^2 E(k)}{dk^2}$, and are often represented in terms of the free electron mass (m^*/m_0), where m_0 = 9.1·10^{-31} kg is the mass of an electron. For holes in the isolated chain m^*/m_0 = 0.093, while for holes in the pure crystal m^*/m_0 = 0.13 along the a-axis and 4.8 along the c-axis. For electrons in an isolated chain m^*/m_0 = 0.099, while in the pure crystal m^*/m_0 = 0.078 along the a-axis and 1.6 along the c-axis. The density of states and complete topography of the energy bands in crystalline PEDOT:Tos are depicted in Figure 13(b), as proved by photoelectron spectroscopy (UPS) data, accurately reproduces the bulk phase of PEDOT:PSS.

According to the estimated band structure[35], PEDOT:Tos is a metal, but only in the PEDOT layers. It is an insulator in the direction perpendicular to the PEDOT layers, as evidenced by the fact that the bands are flat at the Fermi level in the Brillouin zone (i.e. along the b-axis). The metallic composition and strong anisotropy of the conductivity are consistent with optical reflectance and spectroscopic ellipsometry measurements.

A complete model for the geometric and electrical structures of pure PEDOT and doped PEDOT:PSS was developed utilizing DFT quantum chemistry techniques in conjunction with crystallographic data and UPS. The most pertinent findings are as follows:

❖   PEDOT has an aromatic-like shape and a backbone composed of planar chains. The donor-type ethylenedioxy substitution decreases the charge carriers' band gap and intrachain effective mass. The estimated crystal structure of pristine PEDOT is a lamellar monoclinic with the lattice parameters as follows: a = 12.978 Å, b = 7.935 Å, c = 7.6 Å, and β = 125.85°. For the valence and conduction bands, the interchain electron transfer integrals are t_{VB} = 99 meV and t_{CB} = 170 meV, respectively.

❖   The relationship between PEDOT and PSS appears to be adequately represented by a two-phase model in which PEDOT:Tos represents the bulk of the PEDOT:PSS grains, whereas the surface is represented by a dimer of p-styrene sulfonic acid (DSSH).

❖ PEDOT:Tos contains four chains of two EDOT units and two tosylate ions in an orthorhombic unit cell (a = 7.9 Å, b = 28.0 Å, and c = 6.8 Å). PEDOT:Tos is a real metal within the PEDOT stacks, but an insulator in the perpendicular direction due to the Tos ions introduced between the PEDOT layers. However, by shrinking the unit cell along the c-axis, Tos doping enhances the interchain bandwidth.

❖ According to the Drude-Smith model, the effective mass m* of the charge carriers in PEDOT:PSS is $m^* = 0.815 \, m_0$.

The geometric and electronic structure of PEDOT:PSS were investigated, as well as the effect of the degree of doping on structural and optical characteristics. Three forms corresponding to increasing degrees of doping were explored, namely PEDOT:PSSH, $PEDOT^{+0.5}$:PSS/PSS, and $PEDOT^+$:PSS[36]. The energy band structure of PEDOT:PSS was computed, and the crystal structure with the most stable geometry optimization was discovered to be created by alternating PEDOT and PSS layers. The characteristics of the pristine PEDOT unit cell were determined to be as follows: a = 7.7 Å, b = 11.8 Å and c = 6.9 Å.

When these results are compared to prior estimates for pure PEDOT, it is noticeable that the lattice parameters along the backbone axis, which is 'a', are comparable. The stacking axis, which is 'c', is larger than the estimated value, but the interstack distance, along the b-axis, is slightly smaller. These calculations demonstrated that doping converts the neutral PEDOT chain to a quinoid structure, results in the loss of electrons from the PEDOT-conjugated system, and has a significant effect on the electronic structure. The predicted band gap for the undoped structure is 0.7 eV, much less than the observed band gap of 1.5 eV. A significant finding of this work is that some of the bands are partially filled in the doped forms, with the occupied states of the partially filled bands mostly concentrated in the PSS and the unoccupied states primarily in the PEDOT. This explains why PEDOT:PSS exhibits metallic-like behaviour at polymer–metal contacts and is employed as a hole transport layer in organic solar cells[37].

1.3.2 Methods for enhancing electrical conductivity

Conductivity of pristine PEDOT:PSS films is dependent on a great number of parameters, most notably the technique of production, and can range up to around

10 S·cm^{-1}. It can be enhanced in a variety of ways, the most frequent being the addition of organic solvents to the PEDOT:PSS water suspension or the treatment of the PEDOT:PSS films with those solvents in conjunction with thermal treatment.

The most successful methods for increasing the conductivity of PEDOT:PSS are described and discussed in further detail as follow:

➢ Treatments with heat and light: conductivity of PEDOT:PSS thin films may be increased through heat treatment at temperatures ranging from 100 °C to 250 °C in both air and an inert environment (e.g. N$_2$)[38] and UV irradiation, which also enhances the work function and band bending[39][40].

➢ Treatments with organic solvents: numerous polar and high boiling point organic solvents are employed to increase the conductivity of PEDOT:PSS, either by adding the solvent to the aqueous solution of PEDOT:PSS or by treating the PEDOT:PSS films. Solvent addition is referred to as secondary doping[41]. The most often utilized solvents include ethylene glycol (EG)[42], dimethyl sulfoxide (DMSO)[43], which was exploited in this work, N-dimethyl formamide (DMF)[44], glycerol, and sorbitol[39]. The Conductivity values for solvent-treated PEDOT:PSS vary between 0.61 and 677 S·cm^{-1} [46].

➢ Treatments with acid: the post-processing of PEDOT:PSS films with organic and inorganic acids, such as sulfuric acid, hydrochloric acid, oxalic acid, acetic acid, propionic acid, butyric acid, and sulphurous acid, at temperatures ranging from 120 °C to 160 °C, increases the conductivity by a factor of 3 orders of magnitude or more[47]. It was found that treatment[48] with extremely concentrated H$_2$SO$_4$, which was exploited in this work, increased the conductivity of PEDOT:PSS to up to 4380 S·cm^{-1}, because H$_2$SO$_4$ was capable of autoprotolysis ($2H_2SO_4 \leftrightarrow H_3SO_4^+ + HSO_4^-$) and that the two ions resulting, stabilize the segregated PEDOT$^+$ and PSS$^-$ ions.

The mechanism by which PEDOT:PSS conducts better is when treated with organic solvents[43], due to the presence of two or more polar groups which interact with the dipoles or charges of the PEDOT chains and convert the structure from benzoid to quinoid, resulting in the twisted polymer chains becoming more linear. This conformational shift would improve interchain contact, resulting in an increase in charge mobility. Additionally, STM (i.e. Scanning Tunnelling Microscopy) and AFM (i.e. Atomic Force Microscopy) investigations indicate that the addition of a solvent (e.g. sorbitol) results in the rearrangement of PEDOT-rich grains into

elongated forms[49], as well as phase segregation between PEDOT and PSS, resulting in the partial removal of PSS from PEDOT:PSS[46].

1.3.2 Applications

PEDOT:PSS is one of the most widely used conducting polymer today for a wide range of applications. This is because a variety of formulations are commercially available that address specific applications and properties such as conductivity with a range of four or more orders of magnitude, transparency, electrochromism, solution processability, flexible film forming ability, high work function, good chemical stability, and biocompatibility.

The most popular applications range from antistatic coatings on glass or polymer to organic electronic devices such as light emitting diode displays, biocompatible electrodes for cell stimulation, organic electrochemical transistors, hole collector layers for organic solar cells, electrolytic capacitors, electrochromic devices, and textile fibers. Others[50] discuss the applications of PEDOT and PEDOT:PSS in energy conversion and storage devices such as organic solar cells (OSCs), dye-sensitized solar cells, fuel cells, supercapacitors, thermoelectric devices, and flexible devices.

PEDOT:PSS is developing as a potential smart biomaterial for tissue engineering, biosensors, bioimplants, and bioengineering applications, including neural electrodes, nerve grafts, heart muscle patches, and organic bioelectronic devices and systems[51].

PEDOT:PSS electrochemical transistors are particularly well suited for applications in bioelectronics, such as biological and medical devices, as well as sensors of various types both printed and large area electronics, due to their biocompatibility and low-cost technological manufacturing.

Chapter 2

Photopolymerization and 3D Printing

Generally Additive Manufacturing (AM) refers also to 3D Printing, which is a term that indicates methods that are used to build a three-dimensional item by progressively forming layers of material under the control of a computer program. 3D printing techniques enable the creation of objects with almost any form or geometry. They are usually created using data from a computer model extracted from a three-dimensional or other CAD data sources, like Stereo Lithography interface (STL) file. The 3D source file containing the CAD geometry is split into several levels, called slices, with each one producing a set of machine commands. Both 3D printing and additive manufacturing are based on the concept of successive material addition or joining across a three-dimensional object. Slicing is the process of splitting or cutting a 3D model into multiple horizontal levels. Following the slicing operation, a new file format called G-code is produced. This is the most commonly used numerical code programming language in computer-aided manufacturing for automating the control of machine tools such as 3D printers and CNCs machines[52].

Originally, the 3D printing process was related to a technique in which an inkjet printer nozzle deposited layer by layer a binding agent onto a bed of powder material. It is essentially an additive technique instead of subtractive. Additive manufacturing (AM) is a wider and more comprehensive term rather than 3D Printing and it is often linked with industrial applications, such as prototype manufacturing. Additionally, AM is used for end-use applications such as mass manufacturing of components.

Considering that ASTM F42/ISO TC 261 specifies seven distinct additive manufacturing methods, it is necessary to identify the most suitable usage of the term 3D printing. One significant distinction is the comparison between the

industrial respect to the consumer application. Additionally, while comparing 3D printing to additive manufacturing, it is necessary to examine the utilitarian and ornamental character of the produced item. In conclusion, the primary distinction among additive manufacturing and 3D printing is that the latter entails the production of things via the accumulation of material layers, whereas in contrast, additive manufacturing can be defined as the process to create components via the addition of material, which may or not be layered.

During the early stages of 3D printing, the market was more concerned with consumer purpose than with industrial value. Rather than a single monolayer of ink, 3D print heads deposited several layers of construction material, which is usually supplied in the form of a thermoplastic filament. After each layer was completed, the print bed was gradually lowered to create space for the deposition of the following layer. Advancements in 3D printing allowed the transition from the fabrication of novelty objects to the production of fast prototypes. Today, additive manufacturing techniques are being exploited to mass manufacture end-use items.

3D printing of metals was not possible until laser melting and sintering methods were invented. Direct Metal Laser Sintering (DMLS) is a comprehensive term which includes sintering by melting by Selective Laser Melting (SLM) and Selective Laser Sintering (SLS).

ISO/ASTM52900-15 classifies additive manufacturing methods into seven distinct categories: direct energy deposition, , vat photopolymerization, binder jetting, sheet lamination, powder bed fusion, material jetting and material extrusion.

Capabilities of 3D Printing span many sectors such as plastics, metals, plastics food and biological materials. 3D Printing employs a wide variety of materials and each of them is meticulously tailored and engineered to the end-technical product specifications and it is typically compatible with a limited range of additive manufacturing methods.

One of the additive manufacturing techniques is Metal Powder Bed Fusion (PBF, Figure 14). This technology allows the precise fabrication of a wide variety of components, with complex geometry, by fusing layer by layer metallic powder grains, heated by a power source that can be a ytterbium fiber laser or electron beams to produce useful 3D solid components. Manufacturers gain from significant design flexibility, considering that PBF grants a wide range of technologies and materials. Among the many Powder Bed Fusion techniques are the following[53]:

- **SLS (Selective Laser Sintering):** It is a technique that layer by layer sinters powders through lasers to produce a structure that is solid. The finished part is subsequently cleaned using brushes and compressed air to remove the excess powder. Polyamides and also Alumide, which is a mix of polyamide and powder of aluminium, but in the SLS process even rubbers are exploited. Nylons are robust, flexible and durable which makes them ideal for spring, brackets and clip features. The vulnerability of thin components to shrinkage and warping should be addressed by designers during   the   conceptual   phase   of   the   work.

- **SLM (Selective Laser Melting):** It is a process during which the metal powder melts completely, so only metals, such as aluminium and no alloys, can be exploited to produce lightweight, robust replacements and prototypes. Direct Metal Laser Sintering (DMLS) joins the powder grains of metal alloys by sintering them, especially those containing titanium, instead. SLM and DMLS need an additional support structure to be produced in the same process of the part in order to counterbalance residual stresses and to prevent deformation from occurring. Replacement parts and prototypes, as well as the jewellery and dentistry sectors benefit from this technology.

- **EBM (Electron Beam Melting):** Through the employment of a high-energy electron beam, the EBM 3D printing technique achieves fusion and generates less residual stress, resulting in less deformation, consuming less energy and producing layers more quickly than SLS. This technique is particularly advantageous in industrial sectors where the cost per part is high, such as in defence/aerospace, medicine and motorsports.

- **MJF (Multi Jet Fusion):** It is distinct from the others in the use of an inkjet matrix to detail chemicals, subsequently fused into a solid layer and heated by the same matrix. There is no laser involved and the detailing chemicals are sprayed around contours to increase part resolution.

None of the previous indicated Metal Additive Manufacturing technique was exploited in this work. Regarding polymeric 3D Printing as SLA and FDM or FFF were extensively used to print test samples and test setup and they will be described further ahead.
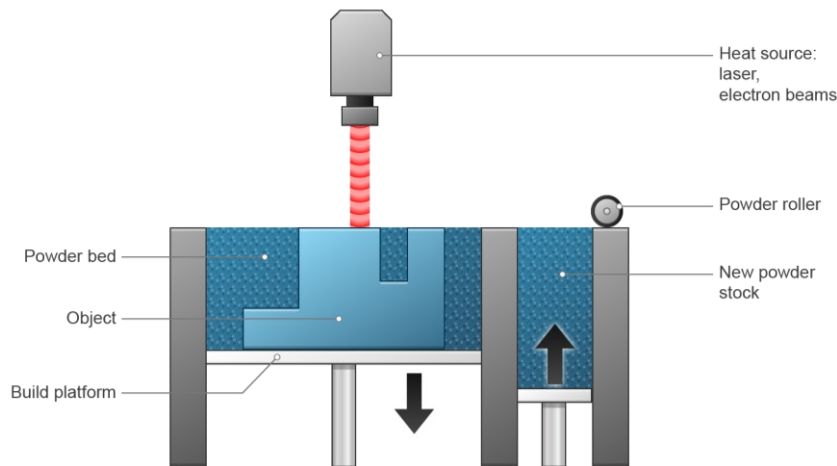
Figure 14: Powder Bed Fusion additive Manufacturing

Direct Energy Deposition (DED) 3D printing produces components by melting metal powders or wires directly and depositing them layer by layer on the workpiece. The majority of DED machines are in the industrial sector and they are closed to ensure inside a regulated environment. Thus, a typical DED system consists of one or more multi-axis arms on which a nozzle is mounted. This allows the deposition of the molten metal powder on the surface of the component, where heat dissipation let it solidify. This technique shares some similarity with 3D printing by material extrusion, however in DED, the nozzle may be mounted on a five axes roto-translational system, whereas on typical FFF machines it is just translational.

The concept "Direct Energy Deposition" (Figure 15) may refer to a variety of distinct technologies. They are differentiated by the manner the material is fused, with each being adapted to a unique and particular function. One of the most often used technologies is LDW (Laser Deposition Welding). It is an additive manufacturing technique which exploits metal deposition through a powder nozzle, that is up to ten times quicker than PBF technology. Additionally, modern machines have been incorporated into a 5-axis milling machine. This novel hybrid method combines the versatility of laser metal deposition with the accuracy of cutting, enabling additive production with the finishing typical of the milling process. These factors allow to manufacture very precise metal components.

Metals such as stainless steel, titanium, copper, aluminium, copper nickel alloys, and many other alloys may be 3D printed using the DED additive manufacturing

method. Each particular technique of DED has its specific set of restrictions and compatibility requirements.
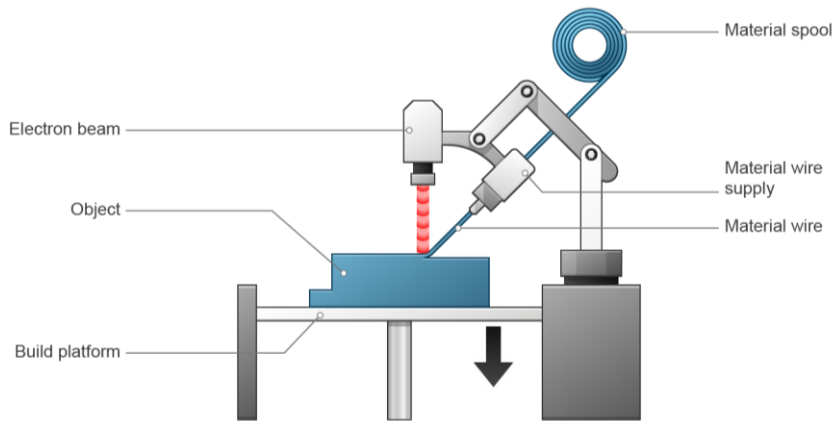
Figure 15: Direct Energy Deposition Additive Manufacturing

Plastics in the form of powder or filament, should melt to create the item layer by layer printed. Each material will need various 3D printing settings throughout the construction process and will provide components different characteristics.

Extrusion of materials is a 3D printing technique which exploits materials in the form of continuous filament of a thermoplastic substance. In a 3D printer the filament is fed from a coil via a moving heated extruder head. The molten material is forced out of the nozzle and deposited at first onto a heated 3D printing substrate for increased adherence. Once the first layer is complete, the computer controlled extruder and platform are separated, allowing for direct deposit of the second layer onto the developing workpiece. Each layer is placed on top of the preceding one, until the manufacturing of the item is complete.

Fused Filament Fabrication (FFF, Figure 16) is a term that refers to the technique of material extrusion, however this method has limits in terms of dimension precision and is very anisotropic. This process can be used employing a wide variety of materials, the most common of which are thermoplastics such as Nylon (PolyAmides), TPU (Thermoplastic PolyUrethane), HIPS (High-Impact Polystyrene), PLA (PolyLactic Acid) and ABS (Acrylonitrile Butadiene Styrene. This 3D printing method may be used to extrude paste-like materials such as ceramics, concrete, and chocolate.
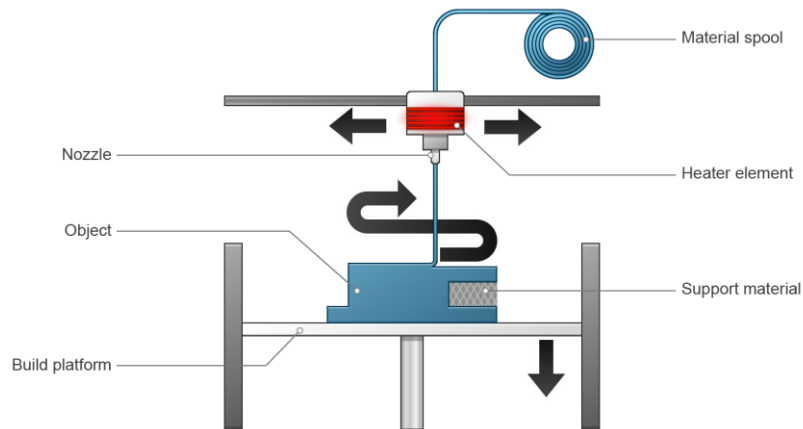
Figure 16: Fused Filament Fabrication 3D Printing

Photopolymerization is a 3D printing technique which includes many distinct processes that all follow the same fundamental strategy: a liquid photopolymer, housed in a tank, is selectively cured by a heat or light source and consequently a 3D physical item is produced layer by layer.

Besides the traditional method, which is based on lasers, there are many kinds of curing equipments. Due of the low cost and high resolution, digital light processing projectors have become a popular method of photopolymerizing materials. One of the benefits of these two methods over lasers is their capacity to cure a whole layer of resin simultaneously, while the laser must gradually advance enlightening the entire surface by depicting the slice geometry.

The following are the most widely used vat photopolymerization 3D printing technologies:

➢ **SLA (StereoLithogrAphy):** SL is an optical manufacturing process during while a concentrated beam of ultraviolet light or a laser is directed onto the surface of a vat filled with a liquid photopolymer (i.e. photosensitive resin). Through the cross-linking or degradation of a polymer, the beam or laser creates each solid layer of the desired 3D part (Figure 17).

➢ **DLP (Digital Light Processing):** A digital projector screen is used to flash a single picture of each layer over the whole platform throughout this 3D printing process. Due to the fact that the projector is a digital screen,

each layer picture is comprised of square pixels, resulting in a layer made up of tiny rectangular bricks called voxels. For certain components, DLP may achieve quicker print speeds since each whole layer is exposed simultaneously rather than pulled out with a laser.

Furthermore, two distinct methods are competing inside the photopolymerization 3D printing process, and both of them construct the component at the interface between the last layer and the resin tank surface. The top-down method entails situating the heat source underneath the tank, so that after gradually raising the 3D printing platform into the air, the final component is produced upside down. The bottom-up method, on the other hand, involves putting the heat source above the vat and as a result, the 3D printing platform is gradually immersed in the vat.

Photopolymerization has been effectively used to medical modeling, enabling the production of realistic three-dimensional representations of anatomical areas using data from computer scans. Due to the great resolution of this method, it is also suitable for prototyping and large manufacturing. Vat polymerization techniques excel at creating finely detailed components with a smooth surface finish.

Photopolymer resins are available in a variety of hues and possess a variety of physical characteristics, each suited to a particular use. Flexible polyurethane resins, minimal residue resins, translucent resins and tough resins are also available.
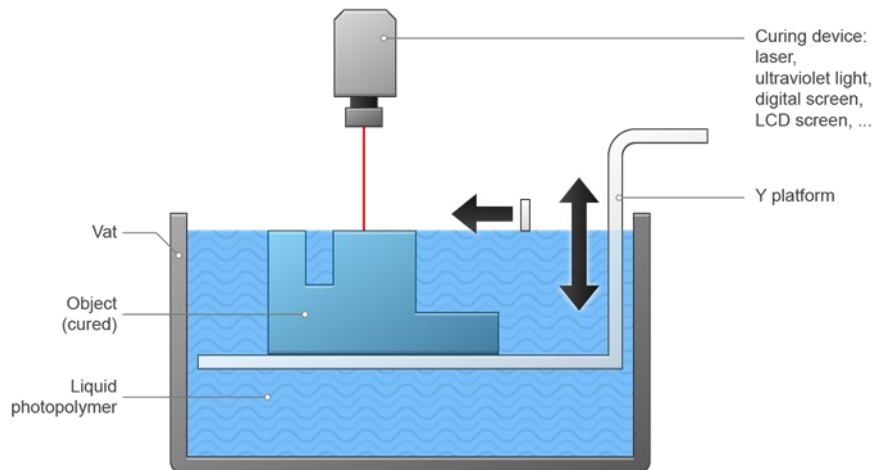
Figure 17: Stereolithography 3D Printing

Comparing 3D Printing and traditional manufacturing techniques, as shown in Figure 18, the processing of a component may be performed by using subtractive manufacturing as CNC, additive manufacturing (3D printing) or formative manufacturing (injection moulding) and each of these has its own set of benefits and drawbacks.
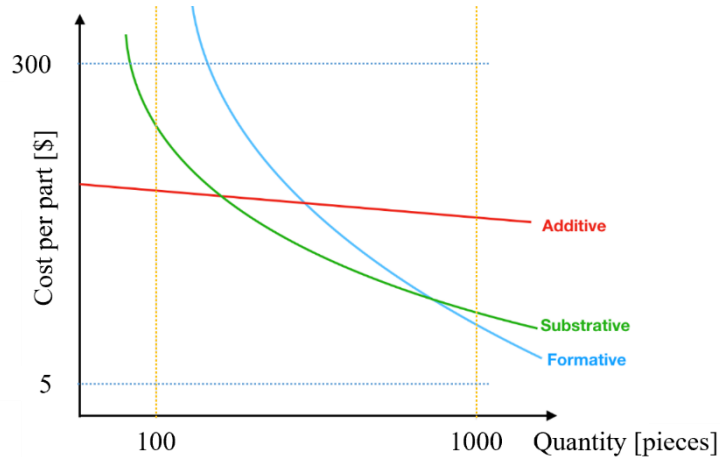
Figure 18: Cost per part vs quantity comparative diagram

Cost:

- Additive technology offers a cost advantage when it comes to prototyping or creating customized components.
- Subtractive technique is usually more cost effective in component production of more than 100 pieces.
- Formative manufacturing is advantageous in mass production.

Geometry:

➢ Additive technology enables the creation of complex geometries such as cavities, flow channels, cavities, etc.), whereas subtractive technology imposes geometric constraints and formative production process offers more geometric freedom.

Material:

❖ Additive manufacturing has material needs and each component has its own set of effects.

> ❖   Subtractive manufacturing processes virtually any solid, including metal, plastic.
> ❖   Formative manufacturing processes mostly plastic materials.

Quality:

> ✓   Subtractive technologies are often comparable to formative technologies in terms of quality and they are superior than additive technologies in terms of surface finishing, for instance.

Size:

> o   The smaller the component, the better for additive technology.
> o   The dimensions of subtractive and formative manufacturing may be considerably larger respect to additive manufacturing.

As 3D printing became more accessible to disciplines such as science, technology, and manufacturing, manufacturers began to see its promise fulfilled in a variety of novel ways. By embedding conductors into 3D printed products, different 3D printing methods have already been widely exploited for electronic devices such as active electronic materials, and devices with mass customisation and electrodes[54].

The manufacturing process for 3D printed electrodes, through FDM technique, is a low-cost and time-efficient method for mass producing electrode materials. In contrast to conventional electrodes made of metal, the shape of 3D electrode and surface may readily be modified to fit a specific application and the printing process is completely automated and very precise[55]. Moreover, active electronic devices or components are capable of amplifying and regulating electric current flow or generating electricity.

Batteries, diodes, LEDs, transistors, rectifiers and operational amplifiers are all examples of active electronic components. Due to the complexity of their functions, these components often need more complicated manufacturing procedures than passive components[56] and the 3D printing technology enables the processing of products in addition to their electronics. Multi-material printing technology may enable Industry Revolution 4.0 to embrace the efficiency of electronic systems, allowing for the creation of more creative designs in a single procedure[57]. The

Modelling and characterization of electronic conductivity in 3D printed
PEGDA:PEDOT polymer composites - High frequency applications

35

creation of a green electronic device with cheap manufacturing costs, high safety, high dependability and fast production is critical to address environmental pollution in contemporary civilization[55].

2.1 3D Printing of conductive polymers

The origins of printed electronics[58][59] can be traced back to organic electronics. The latter is concerned with organic molecules (carbon-based) that have been appropriately doped with elements that confer electrical conductivity. The appeal of these polymeric materials is due to their ease of processing in the form of inks. Thus, the goal of printed electronics is to eliminate the need for sophisticated and costly silicon processing technologies when integrating circuits into an existing device. This is not to say that printed electronics can completely replace conventional silicon microelectronics, but rather that they offer a viable, cost-effective, and rapid alternative when precision and high performance are not needed.

Electrically, materials are categorized according to their capacity to let or deny the passage of electronic charges. This propensity to charge flow is defined conductivity (σ) of the material and its reciprocal is the resistivity (ρ), as given in Eq. 5 and allows to quantify the opposition of the material per units of length to a charge. The greater the value, the easier it is to transfer the charge. This quantity varies of several order of magnitude for materials and allow to classify them into three macro categories: conductor, semiconductor or insulator.

$$\text{Eq. 5:} \quad \sigma = \rho^{-1} = \frac{l}{R \cdot A}$$

The length of the sample is defined as l; A denotes the area of the cross section of the material; the resistance measured in Ohms is the term R. Conductivity is measured in S/cm units and ranges of this quantity used to categorize a material are shown in Figure 19.
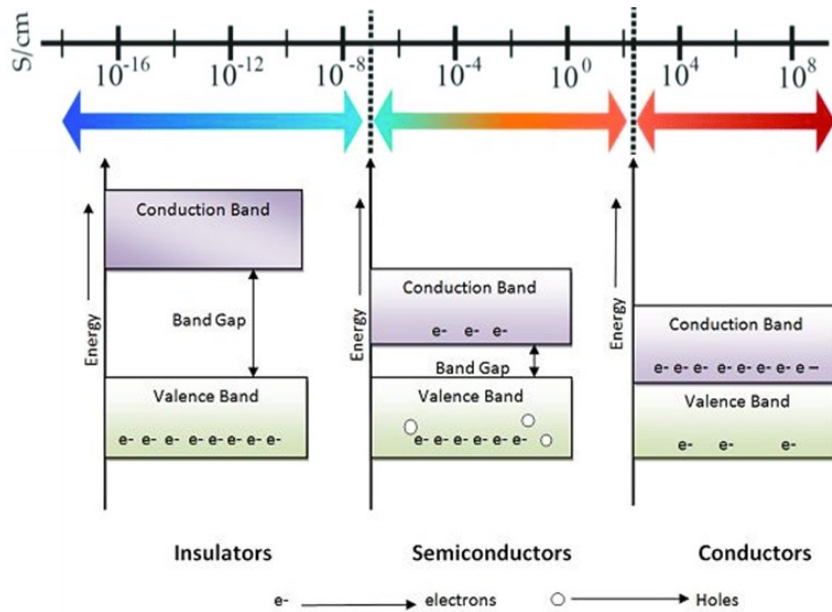
Figure 19: Conductivity-based categorization of materials

There are two families of materials used in printed electronics: inorganic and organic. Inorganic materials are a wide category that includes silicon, transparent oxides, metal particles, graphene and carbon nanotubes. Numerous efforts have been made to incorporate these elements effectively into inks based on solvents or water, resulting in conductive, semiconductive, or insulating mixes. Considering that solutions of ink must be stabilized to avoid the aggregation of particles, inks that are inorganic generally need a to be annealed at high temperature after being deposited to perform optimally. A treatment at a high temperature is incompatible with polymeric devices[58].

In terms of organic materials, inks based on polymers are examined. These inks may consist of intrinsically conductive polymers (polypyrrole, polyacetylene or PEDOT-poly(3,4-ethylenedioxythiophene)) or by combining insulant polymers with inorganic compounds (e.g. metal nanoparticles) or intrinsic conductive polymers. Organic inks are often used to create semiconductive circuits[59].

When the ink is prepared for printing, the proper technique should be selected based on the requested printing accuracy and on the ink material. The primary circuit printing technologies may be defined as the following: indirect, direct and inkjet printing[59].

Inkjet technology is almost identical to traditional printing, except it uses an ink that exhibit conductive properties. Liquid inks may be ejected from printing heads in two ways: through the generation of a pressure variation using a piezoelectric actuator or producing a propelling bubble, heating the ink. Typically, piezoelectric heads are employed for printing electronics with inks contain metal particles, P3HT (semiconductor), PMMA (insulant) or PEDOT (conductor)[59]. Inks present difficulties in production due to adhesion and specific viscosity values and they are prone to clogging printer heads. Inkjet printing resolution is about 0.02 mm and may be increased as in aerosol jet printing technique by converting ink to an aerosol and then conveying it to a nozzle[60].

Unlike inkjet printing, that successively digitizes a design to replicate it via the movement of the head of a printer, printing technique that are indirect and direct begin with reproduction from the master piece. Between direct and indirect printing, the primary distinction is the existence of an intermediary part. Direct methods place the layer to be printed directly on the master, whereas indirect methods require an extra layer onto which the design is placed from the master. Metallic meshes are used in conjunction with high viscosity pastes that often include metal particles, carbon, or polymers. Incorporating conductive elements into pastes may have a negative effect on their electrical conductivity. On the other hand, the employment of stamps enables the use of low viscosity inks, which may result in an increase of the printing resolution, even inferior to 0.01 mm[61].

The printing process consists of three different steps: pre-printing preparation, printing itself, and post-curing.

2.1.1 Pre-printing stage

Because the inks employed are liquid, it is critical to examine the interaction between liquid and substrate in order to get correct results. Indeed, it is well knowledge that when on a surface that is hydrophilic a water-based solution is deposited, it exhibits a proclivity for spreading and expanding in the effort to recover enough surface to minimize its surface stress, whereas if an interface, exhibiting hydrophobic or hydrophilic properties, exists among two materials, then the spilled ink remains stationary and a large contact angle is generated between the two surfaces. As a consequence, a smart approach for achieving satisfactory

printing results is to adjust the surface energy according to the ink type. Oxygen plasma, UV irradiation and corona treatments are examples of common techniques for varying the surface energy. The latter is used to prepare the surface of the polymer, increasing the surface tension and its porosity, by applying through top and bottom surface electrodes, an electric field whose effects increases the surface adhesion of the polymer.

2.1.2 Post curing stage

A post-curing process is often needed to ensure that a printed circuit performs optimally. Allowing a deposited design to dry is not always sufficient to assume it ready to use. UV curing, sintering or thermal annealing are the most often used post-curing processes[59].

In the presence of metal particles, sintering is used. The latter are often protected by a coating to avoid these from accumulating the nozzle of the printer. As a result, thermal annealing is needed to remove the polymeric coating, in order to contact the conductive particles. The process of sintering is usually carried out inside an oven or using a laser emitting infrared light, which by heating just the sintered design, greatly minimizes substrate damage.

Finally, although annealing is a thermal process similar to sintering, the goal is different: while sintering is used to connect conductive particles, annealing is used to alleviate internal tensions and substantially enhance circuit performance by changing the material shape. Solvent vapor annealing at ambient temperature was developed to prevent the usage of high damaging temperatures[62].

Post processing is the removal of unpolymerized resin and cleaning of the constructed item at the conclusion of an SL process. After rinsing the formed item in a suitable solvent (e.g. ethanol), supports are carefully removed. This procedure requires further UV irradiation to complete the polymerization process. It is critical to remove supports, if present, prior to UV final irradiation when the resin is not yet mechanically stable, even if adjacent paths of the UV laser can cause the intermediate region to over-polymerize, causing the material to exhibit different characteristic respect to the ideal cured material. As shown schematically in Figure 20, the overlapping of these over-cured region strands traps some liquid resin within the item.
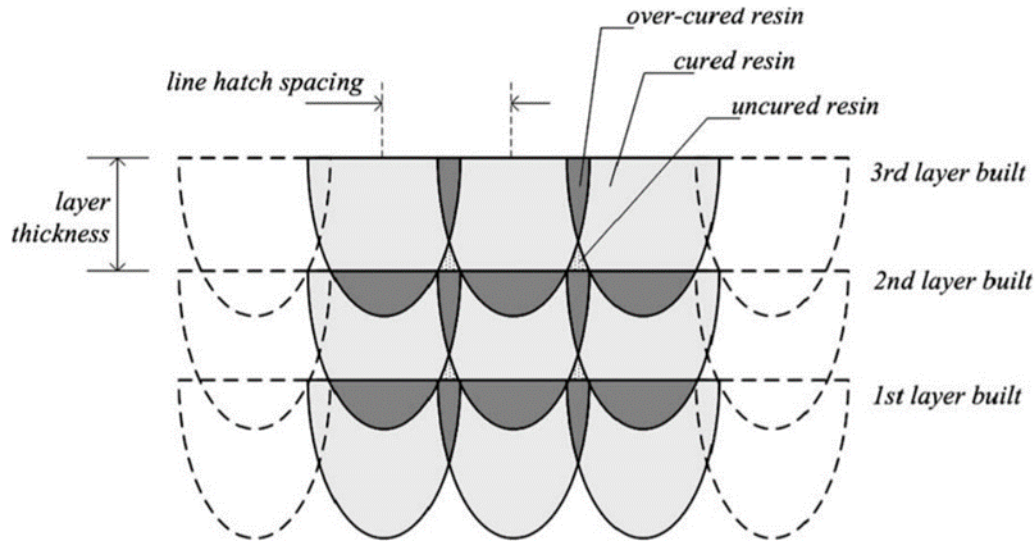
Figure 20: UV exposure regions in a 3D Printing process

It is thus critical to complete the polymerization process with a last phase of UV irradiation. Analyses of the material density, glass transition temperature and mechanical resistance may be used to determine whether the polymerization process is complete. Additionally, infrared spectroscopy or differential scanning calorimetry may be performed.

2.2 Shrinkage

Shrinkage is a frequent issue in the manufacturing of items exploiting UV curing. Shrinkage occurs because a portion of the free volume between the polymer chains prior to cross-linking is reduced once the polymer is cross-linked; in fact, prior to cross-linking, the chains are defined by a distance dictated by Van der Waals forces, whereas after cross-linking, which results in the formation of covalent bonds, the chains are defined by a distance dictated by covalent bonds. This method results in a shrinkage of up to 10 % of the total free volume[61].

Residual stress inside the component is created as a result of shrinking, which may manifest as deformation (e.g. bending or twisting) or fracture (e.g. cracks). The

magnitude of the impact is dependent on the chemical composition of the formulation, crosslinking and curing properties and the post-curing procedure[63].

Initially, shrinkage may occur during the printing process: each layer is subjected to internal stress during polymerization when exposed to the printer light source. These stresses have an effect not just on the single layer, but even on the interaction of succeeding layers, resulting in the portion curling. As shown in Figure 21, the distortion may be quantified using the curl factor '*cf*' defined in Eq. 6.

$$\text{Eq. 6:} \quad cf = \frac{vertical\ maximum\ displacement\ (h)}{horizontal\ projection\ length\ (L)}$$
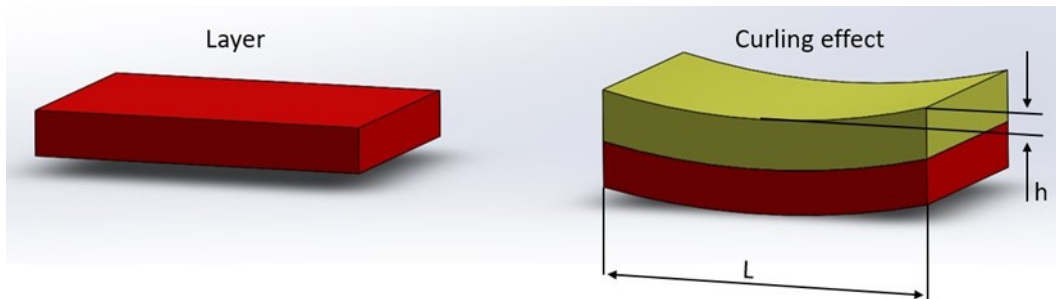
Figure 21: Explanation of the curling effect in 3D Printing

The removal of supports is acknowledged as another cause of shrinking. Indeed, during this step, the object internal stresses are released, and a new equilibrium is often established, resulting in the curling of the component. Finally, curl distortion is possible during the post-curing process. Indeed, as previously stated, post-curing is the process by which the unpolymerized resin trapped inside the polymerized matrix of the item is fully cured. Thus, the remaining liquid resin solidifies, creating tensions that are difficult for the surrounding solid structure to disperse, resulting in shrinkage. In terms of chemical composition, different functional groups at the ends of oligomers used to facilitate cross-linking, may result in a variety of polymerization types (condensation, radical or step addition etc.). Depending on the type, the shrinking effect will be more or less apparent[64].

With regards to polymerization and crosslinking characteristics, there are a variety of methods for limiting shrinkage, primarily based on polymerization times and speeds, such that the lattice can be relaxed during formation, depending on the hatch spacing (i.e. the distance between adjacent laser tracks), the polymerization depth and the laser power and speed[62].

Modelling and characterization of electronic conductivity in 3D printed
PEGDA:PEDOT polymer composites - High frequency applications

41

The laser power is proportional to the component degree of polymerization, which increases when the laser power rises. This is because when a high-power laser is used, the resin is exposed to UV light at a higher intensity, which results in increased cross-linking. Indeed, as the intensity of the radiation increases, the initiation speed increases, thus extending the first cross-linking.

On the other hand, the depth of polymerization is inversely proportional to the degree of polymerization, because using a shallow depth results in fewer overlaps between consecutive layers, which results in a reduction in the quantity of resin cured, thus reducing shrinkage. Similarly, hatch spacing produces the same effects, in the way that increasing hatch spacing results in a larger quantity of uncured resin owing to reduced contact between previously cured components and lowering the degree of polymerization. In the photopolymerization process, scanning speed has an effect on the degree of polymerization. When the scanning speed is increased, the exposure energy per unit area is decreased, lowering the degree of polymerization.

Finally, as previous stated, the post-curing process creates a significant condition of internal stress development as a result of shrinking. The aim of post-curing procedures is to completely polymerize the partially cross-linked resin remaining inside the structure and to enhance its mechanical characteristics. However, the presence of shrinkage leads in significant deformation inside the component, which in certain instances may result in fracture or the development of internal cracks.

To minimize the effect of post-curing shrinkage, it is possible to optimize the process by taking appropriate precautions; in particular, during the initial stages of post-curing, it is necessary to alternate UV exposure and non-radiation condition to allow for gradual relaxation of the generated internal tensions. Additionally, sufficient thermal exchange inside the chamber is recommended to prevent the component overheating and subsequent stress states caused by uncontrolled cooling. Through this procedure, interior fractures may be avoided, resulting in a reduction in the component mechanical characteristics.

2.3 3D Printing of PEGDA:PEDOT Composites

In SL 3D Printing the conductive resin formulation is determined on the base of its final printability and conductive properties. Thus, it is mandatory to establish a

compromise among the previous characteristics. The bulk material used in the composition is PEGDA (Poly(ethylene glycol) diacrylate), while the agent capable of crosslinking is Irgacure. This resin is filled with precipitated particles of a highly conductive and biocompatibility polymer: PEDOT. Compression and resistivity experiments were subsequently performed to evaluate the mechanical and electrical characteristics of the novel formulation of the resin. Despite the fact that the mixture of PEGDA with PEDOT:PSS has been used to produce conductive and biocompatible samples in the literature, the majority of researches uses moulding of replica or exposure via photomask and they are targeted at the fabrication of wet moisturizers used in bioengineering[65][66]. On the contrary, this formulation is unique in that it employs a composite resin in a conventional 3D printer (SL) to produce a stiff and dry part. The purpose of this formulation is to develop a photocurable SL resin composed of PEGDA as stiff matrix and conductive filler PEDOT:PSS. Intermediate experiments were performed to determine the surfactant mixing ratio, filler (PEDOT) and optimal photoinitiator (PI).

2.3.1 PEGDA

PEGDA (Poly(ethylene-glycol)-diacrylate) is a hydrogel widely used especially in the biomedical and pharmaceutical industries. It consists of a polymer chain (Figure 22) of PEG (poly(ethylene-glycol)) with variable length and terminating acrylate groups on both sides, which allow cross-linking during 3D printing.
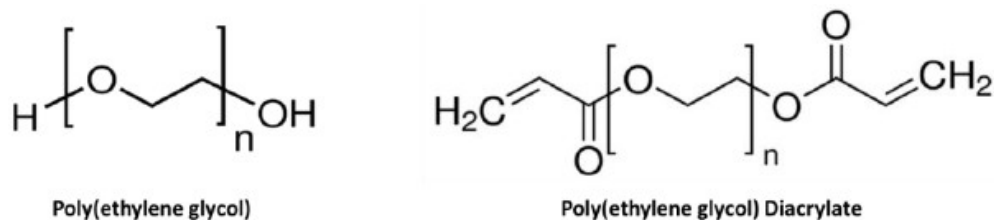
Figure 22: Left, chemical structure of poly(ethylene-glycol) (PEG); right, chemical structure of PEGDA. The n is an integer indicating the repeat number of the monomeric unit of the polymer.

This polymer has been widely exploited in recent years for the creation of matrices and scaffolds, thanks to its peculiar characteristics: in fact, PEGDA is biocompatible and presents low cytotoxicity without generation of an immune response[67].

Moreover, it is transparent to the visible light, therefore it allows an easy distinction of the dispersion of PEDOT within the matrix with optical microscopy[68].

Modelling and characterization of electronic conductivity in 3D printed
PEGDA:PEDOT polymer composites - High frequency applications

43

The chemical and structural properties can be easily modified, as well as the mechanical properties, which depend on the amount of photoinitiator used, on molecular weight and on the swelling, defined as the process through which the volume of a solid increases in response to the absorption of a liquid or gas. The absorption of liquids alters the mechanical characteristics of the swollen material and may result in a variety of deformations. The molecular weight (Mn) of the chains can vary in the range Mn $250 \div 100000$[69]: higher molecular weights imply higher viscosity, due to the greater length of the chains, but also a lower cross-linking, since, with the same weight, there are fewer acrylate terminal groups than in PEGDA with a lower molecular weight. In addition, with higher molecular weights, the elasticity of the polymer increases, since there are longer chains that resist more to the applied stress than shorter chains, since they are characterized by a lower strain, being more cross-linked and with a shorter length[70].

Through the modification of these parameters, it is possible to obtain a resin that may have different properties of tensile strength, stability over time, or solubility with PEDOT.

PEGDA is widely used in the biomedical field as a matrix for making different components, because it benefits of the properties of low cytotoxicity and the possibility of obtaining hydrogels with different water contents.

As mentioned above, PEGDA chains consist of acrylate end groups, which allow the creation of the crosslinks between the oligomers during polymerization process. Crosslinking can occur in the traditional method through gel forming or through UV activation of a photoinitiator. In the following considerations, the second method is considered.

2.3.2 Photoinitiator and Photo-crosslinking

Oligomers are macro-monomers with intermediary molecular weight that have a longer chain structure composed of a few monomer units. By mixing to raw resins as reactive diluents they are primarily used to decrease the viscosity of the oligomer and regulate the characteristics of the cured preparation.

Monomers or oligomers that polymerize to produce strongly cross-linked polymer structures and photoinitiators (PIs) that generate reactive starting species following

UV exposure are required for photopolymerization[71][72]. Thus, typical raw resins for SL include PIs (5 wt.%), monomers (25 wt.%), and oligomers (70 wt.%).

The majority of monomers and oligomers do not produce reactive species that are capable of initiating photopolymerization. As a result, organic PIs with low molecular weight are employed in resins to produce reactive species capable of reacting with functional groups of monomers and oligomers. Once the functional group is broken down, each reactive carbon double bond may be replaced by another carbon atom from another monomer molecule. When strong covalent connections between neighbouring molecules take the place of weak van der Waals interactions, the liquid resin changes into a solid structure with distinct bulk characteristics[73].

After absorption of incoming UV radiation, free radical photoinitiators develop free radical, which quickly attack the double bonds of particular monomers, such as acrylates[71]. In contrast to free radical PIs, when exposed to light, cationic PIs generate acids. The resulting acids easily react with a bond in certain monomers, such as epoxides, thus initiating photopolymerization[74].

Photoinitiator PI Irgacure 819 is capable of producing radical species, when exposed to UV light and it is mainly employed to prepare polymeric formulations containing acrylate groups in the monomers, such as poly(methyl methacrylate) (PMMA), polyacrylamide (PA), or PEGDA. These radicals will be transferred to the monomers, dissolving the double bond in the vinyl group of the acrylate terminal and enabling for the creation of links amongst the various PEGDA monomers. After crosslinking, any leftover monomers and radicals from the process may be removed. Once the photopolymerization process is complete, PEGDA transforms into a thermosetting polymer that chemically degrades upon heating[75].

The PEGDA matrix was tested with various concentrations of Irgacure photoinitiator to find out the optimal concentrations to enhance the final electrical and mechanical characteristics of the final composite material. To the liquid PEGDA resin, various concentrations of PI Irgacure were added to produce matrixes different in term of composition ratios. Numerous PI mixing ratios have been utilized in the literature to rapidly enhance the matrix mechanical characteristics. It is possible to create hard[76] or soft[77] components at low or high concentrations.

Modelling and characterization of electronic conductivity in 3D printed PEGDA:PEDOT polymer composites - High frequency applications

45

2.3.3 Resin filler

PEDOT:PSS, commercially called Clevios PH 1000 and produced by Heraeus, is the conductive polymer employed to perform as a filler agent in order to create a new preparation of the resin for stereolithography 3D printing of conductive polymers. When treated in an H_2SO_4 solution, it has been shown that it is possible to decrease the electrostatic potential between the PSS, which exhibit negative charge and PEDOT, exhibiting positive charge, resulting in the removal of certain PSS groups and the conformational modification of the PEDOT chains from random to linear[78], resulting in an increase in conductivity. PEDOT:PSS is mixed in a solution of H_2SO_4 for several hours to produce a precipitate of PEDOT which is in an ethanol suspension and through centrifugation precipitate of PEDOT is obtained. After discarding the supernatant, through magnetic stirring, PEDOT particles are introduced to the photocurable resin. Initially the optimal the mass ratio of PEGDA to PEDOT was researched testing several ratios in order to find out optimal composition of the resin that allowed to maximize the electrical conductivity parameter.

2.3.4 Surfactant

PEDOT:PSS and PEGDA are not miscible and they compose a binary system of separate components[79], owing to the fact that they have been synthesized employing distinct solvents: precipitated PEDOT:PSS forms a solid-like phase, while PEGDA dissolves in water. Polar solvents were exploited for PEDOT:PSS, as previously described in the literature. To further improve the resin performances, different surfactants were evaluated in detail at the same concentration, such as Dimethylsulfoxide (DMSO)[80], Dimethylformamide (DMF)[81] and TritonX-100 (Tx)[82]. The optimal surfactant was found by comparing the rheological properties of different liquid resins having equal amount of PEDOT respect to PEGDA. Surfactant has the role to act as a tensio-active agent lowering the surface tension between the two phases of the system in order to improve their miscibility.

2.3.5 3D Printing process of resin composites

In this thesis work a modified SL 3D printer was employed to adjust the print setting parameters calibrating the printing process to photopolymerize a PEGDA:PEDOT resin. The stereolithographic printing machine, produced by Microla Optoelectronics S.r.l., can photopolymerize resins, using a laser at the wavelength of 405 nm placed on a galvanometric scanner, on a maximum area of 17×20 cm^2. To determine the optimal resin mixture, both temporal stability and viscosity of the blend were studied within the printer. The SL 3D printer was configured with the following parameters: 100 μm layer thickness, 50 μm hatch spacing, 1000 mm/s velocity of scan and 15 W·mm^2 laser power density. Two components with a square and planar geometry were produced for each parameter combination stretching a homogeneous resin layer on a glass surface. After carefully removing using isopropyl alcohol the resin that remained uncured, all the specimens were examined using a digital microscope to determine the amount of the surface geometry that actually polymerized.

Manufactured components will undergo morphological, mechanical and electrical tests to fully characterize the material in order to quantify the main engineering quantities such as tolerances of the printed geometry, stress-strain curve in mechanics, current-voltage curve in electronics.

2.3.6 3D Printed PEGDA:PEDOT Morphology

As shown in the field emission scanning electron microscopy (i.e. FESEM) characterization of Figure 23A, the treated PEDOT:PSS exhibits columnar formations, which are fairly ascribed to the reorganization of PEDOT:PSS converted to nanofibrils after being treated with H$_2$SO$_4$[48] . Protons produced by acid combines with PSS ions and convert them to PSSH, thus decreases the coulombic interaction between PEDOT components[83]. In this way, hydrogen sulphate ions act as counter ions to PSS$^-$, resulting in phase separation between PEDOT and PSS units and reorganization of the polyelectrolyte chains into linearly oriented structures.
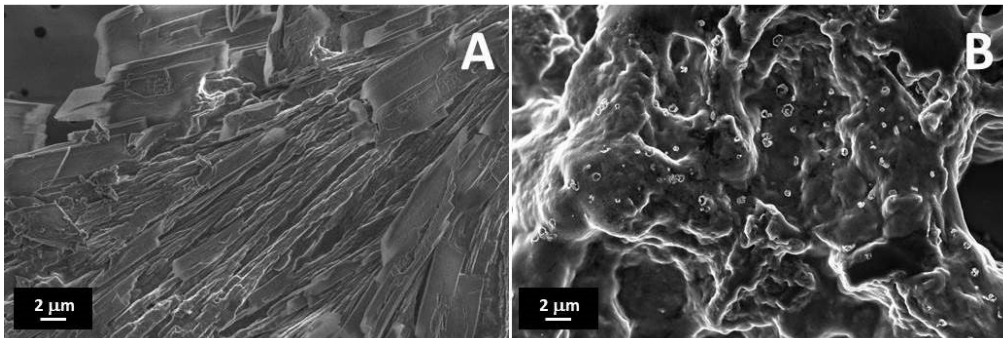
Figure 23: A) FESEM pictures of a treated PEDOT:PSS structure; B) 3D printed
PEGDA:PEDOT double helical structure with a 45 wt.% filler inclusion[84].

Concentrated H_2SO_4 undergoes autoprotolysis[84], in which two H_2SO_4 molecules produce two ions, $2H_2SO_4 \leftrightarrow H_3SO_4^+ + HSO_4^-$. As a result, when PEDOT:PSS is treated with highly concentrated H_2SO_4, the two ions stabilize the positively charged PEDOT and negatively charged PSS in their segregated forms. Then, through the development of a crystalline nanofibril structure, the strong $\pi-\pi$ stacking nature of PEDOT and the stiffness of its backbone generate dense PEDOT networks with substantial modifications in both the crystallographic and morphological features[85]. In this procedure, water is used to wash away the H_2SO_4 and the excess of uncoupled PSS, while some of the PSS gets restructured with PEDOT and serves as a counterion.

The surface morphology of the printed item with increased filler loading (Figure 23B) supports the development of a composite resin with a homogeneous globular shape and no appreciable phase separation between the PEGDA and treated PEDOT:PSS components. This implies that even with large filler loadings, effective mixing of the two components may be achieved at the microscale while retaining a high conversion yield of the photocurable PEGDA polymer.

2.3.7 3D Printed PEGDA:PEDOT Metallization process

Multiple metallization techniques have been studied in order to determinate which method provides the best contact in term of minimization of the electrical contact resistance and enhancing of mechanical adhesion force. Cu electroplating, metal sputtering and deposition of silver paste have been compared as metallization processes to determine the most suited to exploit as contacting technique.

Copper electroplating was performed by immersing samples in an acid aqueous electrolyte solution, composed of $CuSO_4$ dissolved salt and H_2SO_4. The anode was

a copper plate, and the cathode was the conductive printed sample attached to a collector in the experimental setup. The collector is critical in the electrodeposition process. To achieve a homogeneous deposition, it is essential to have good adhesion and a solid electrical connection between the sample to be metal plated and the collector surface. Copper tape was exploited as collector, which has been tuned to be conductive from both the adhesive and the conductive side.

Prior to cathodic fixation, each sample was covered with an insulating sheet in order to selectively electrodeposit copper at the parallelepiped extremities of the polymer sample. The mask was evaluated for its ability to deposit a surface area of 80 mm^2. The anode and cathode were attached to a U-shaped PMMA support to verify that the distance between the anode and the cathode was the same in each deposition test and that the two were parallel (Figure 24). A power source applied a voltage between the anode and cathode and simultaneously, an ionic current flowed through the electrolyte solution, causing copper positive ions to migrate and deposit on the negative cathode, which was the 3D printed PEGDA:PEDOT sample. Although, when exposed to water, the PEGDA insulating matrix swells, it was essential to determine if immersion in the aqueous electrolyte would result in irreversible damage to the conductor samples.

In Gold sputtering a similar masking was used, so in this method, each sample was wrapped in an insulating tape, leaving just the extremities exposed to Au deposition. The chamber was then filled with samples and the pressure adjusted to 10^{-4} mbar and 30 mA current for 180 seconds were used for the deposition procedure.

Finally, for silver metallization, conductive silver paste was manually applied at the sample extremities, covering both the top and three sides of the samples and resulting in a covered surface area comparable to that of the unmasked electrodeposited and sputtered samples.
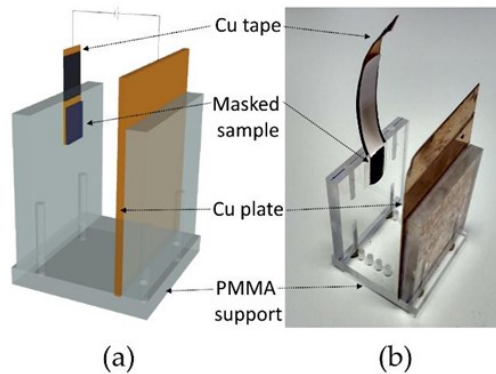
Figure 24: Setup for Electrodeposition: a) CAD model; b) built setup.

In the end, FESEM and EDX (i.e. energy dispersive X-ray spectroscopy) were employed to characterize the electrodeposited copper atomic composition and shape, which exhibited a dependency on the setup.

A FESEM analysis of the porous electrodeposited Cu layer showed the presence of typical copper grains on samples deposited using optimal setting parameters, as shown in Figure 25a, whereas copper traces were not detected in EDX measures at 8−9 keV in the masked areas (Figure 25b).
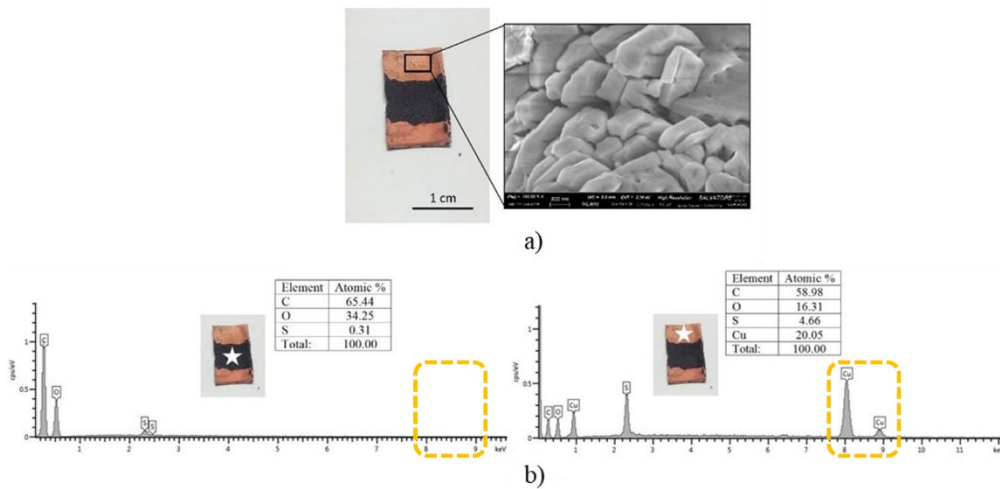
Figure 25: a) FESEM characterization for Cu electrodeposited samples showing copper grains; b) Atomic composition of the polymer (left) and metal-electroplated (right) surface.

Unlike Cu electroplating, neither Au sputtering nor Ag spreading required adjustment for this application. Thus, electrical characterisation was conducted after deposition and an almost equal mean conductivity was determined for Au sputtered and Ag plated components[86].

Chapter 3

Conduction Mechanisms

The movement of electrons and holes within polymers is critical for designing polymer electronics and optoelectronics devices. The fundamentals of charge transport inside polymer devices must be examined, as well as the major charge transport processes. The effect of doping on charge transport and the behaviour of traps will be discussed.

It is critical to remember that polymer crystallinity will never approach the grade of a perfect crystal, except in a few relatively artificial and essentially irrelevant environments. Charge transfer is significantly less affected by grain boundaries in a typical metallic conductor than it is in polymers and is similarly unaffected in an inorganic semiconductor, but also the morphology of polymeric materials is critical for charge transfer. By definition, conjugated polymers are stiff; the double bond imparts a degree of stiffness to the molecule that saturated polymers lack. Because stiffness facilitates packing, many conjugated polymers are semi-crystalline, which has implications for charge transfer.

To measure charge transport in polymeric materials, a very straightforward scenario is examined in which a material is injected with either holes or electrons at the anode, without loss at any desired density, which is regulated by the bias voltage. In real-world circumstances, complicated factors exist; materials may be combined, and the device may be pumped with both holes and electrons. Nonetheless, such complexities must be removed in order to comprehend transport operations.

3.1 Order, disorder and crystallinity

Crystallography is a major subfield of condensed matter physics concerned with the study of crystalline formations. Each crystalline structure may be simplified to a single unit cell, which when repeated over space forms the crystal and the unit cell

Modelling and characterization of electronic conductivity in 3D printed
PEGDA:PEDOT polymer composites - High frequency applications

51

is arranged in a lattice called a Bravais lattice. The simplest kind of lattice is cubic, in which all atoms or molecules are arranged along the cube edges. A body-centred cubic lattice is a variant of the Bravais lattice on a cubic structure in which another atom or molecule occupies the central position of the basic cubic structure. It is not essential for all crystalline formations to be cubic; the lengths of the sides need not be identical, nor do the angles between them have to be 90°. There are seven distinct types of crystalline structures, each of which has fourteen Bravais lattices, and three of these crystalline forms are shown in Figure 26.
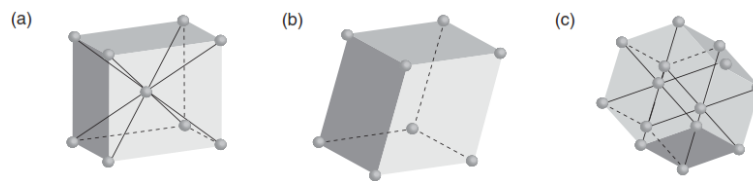
Figure 26: Examples of crystal systems include the following: (a) An orthorhombic crystal (b) A monoclinic crystal (c) A hexagonal. In (a), an orthorhombic. This is one of the four Bravais lattices that exist for the orthorhombic system. The structures of the other types of Bravais lattices are slightly different: It is referred to as a simple orthorhombic lattice in the absence of the molecule or atom at the body centre. A base-cantered atom or molecule is one that is centred on two opposing faces, whereas the fourth lattice is made up of an atom or molecule that is cantered on all six faces.

Polymers are arranged in all these crystalline structures. The presence of dopants in a conjugated polymer must affect its crystalline structure because dopant ions, which are necessary for overall charge neutrality, are often larger than the crystal lattice, frequently requiring the crystal shape to alter to accommodate the dopant impurity, consequently doping a polymer frequently alters the crystalline structure. When doping is used in small amounts, the overall effect is often the insertion of defects into the lattice.

3.1.1 Block copolymers

Phase separation of polymer mixtures results in micron-scale structures with a degree of order. Regrettably, the phase separation process makes it difficult to produce structures with high degree of order. Complete ordering is required in the case of spinodal decomposition (spontaneous thermodynamic phase separation) since it demands that the whole material be at a constant temperature and simultaneously 'senses' the start of phase separation. Block copolymers provide a

solution to both of these issues. It is now feasible to create block copolymers with manometer-sized features that are perfectly homogeneous across several microns.
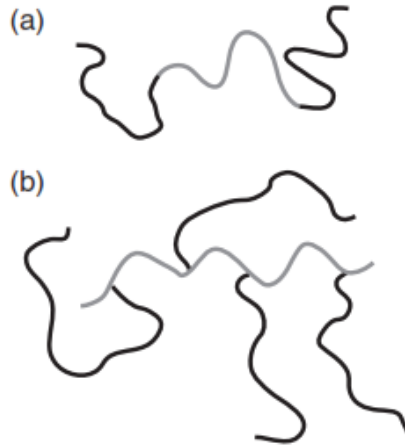
Figure 27: (a) Block copolymer is made up of two or more polymers that are covalently linked together to produce a longer linear chain. This picture shows a schematic representation of an ABA triblock copolymer. If the three blocks are constructed of different homo polymers, an ABC triblock copolymer is formed; if two polymers are used, a diblock copolymer is formed. (b) A graft copolymer, often referred to as a comb polymer. Linear chains stretch from a chain backbone in this case.

Copolymers are classified as block copolymers, alternating copolymers, random copolymers, and graft copolymers. Figure 27 illustrates two of these instances. Generally, block copolymers are miscible. While it is feasible to synthesize block copolymers of miscible blocks, it is difficult to see why this would be done since a random copolymer of the same components is often considerably quicker to synthesize and normally results in identical material characteristics. Immiscible block copolymers are prevented from generating bigger spinodal breakdown structures by the covalent bonds connecting the blocks. Nonetheless, block copolymers may be used to create a variety of shapes, as seen in Figure 28. Like polymer blends, block copolymers have a phase diagram. The shift from a two-phase to a one-phase state is referred to as the order–disorder transition, and the two-phase state is referred to as microphase separation. Phase separation occurs at the nanoscale, not at the microscale length. The three primary morphologies of block copolymers are spherical, cylindrical, and lamellar. To summarize, the physics requires minimizing the input of interfacial energy and stretching the polymer chains[87].

Modelling and characterization of electronic conductivity in 3D printed
PEGDA:PEDOT polymer composites - High frequency applications

53

There is some trade-off between these many elements and the use of self-consistent mean-field theory enables a complete prediction of the potential structures. The structure is governed by two critical parameters: the interaction parameter between the two components and the chain length ratio. If the individual blocks are strongly asymmetric, the morphology will be spherical; in block copolymers, a spherical shape enables the smaller block to have a lower surface area while the larger block forms a matrix (Figure 28).
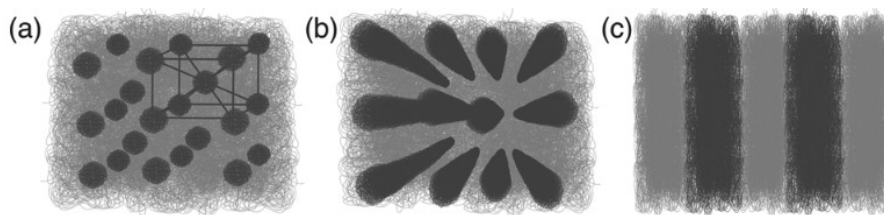
Figure 28: Block copolymers can have a wide range of different structures based on the block length ratio and, to a lesser degree, on factors such as temperature. When a single block is exceedingly small, it will result in a spherical morphology, with spheres arranged in a body-centred cubic structure (a). When the blocks are comparable in length, a lamellar structure is formed (c). Between these two is the cylindrical morphology (b).

3.1.2 Charge transport and grade of order

In comparison to a semiconductor solid, such as silicon, a conjugated polymeric structure is far less regular. Polymers are made up of individual molecules with variable chain lengths, flaws, and chain ends; they can also be amorphous or partly crystalline. Additional distinctions emerge as a result of aging. Finally, the polymer chains can be oriented in any of the three spatial directions (x, y, or z), resulting in a range of electrical characteristics. As a result, disorder has a significant influence on the electrical characteristics of conjugated polymers. In general, disorder results in the localisation of charges. Order, on the other hand, is not a necessary requirement for charge transport, because even in a highly ordered system, macroscopic charge transport is impossible unless the charges may hop or diffuse between chains[88]. Certain polyacetylene samples exhibited high crystallinity percentages of up to 80% to 90%. As a result of this enhanced crystallinity, the sample conductivity is also significantly boosted, supporting the overall pattern that disorder results in charge localisation. PEDOT has a finite crystallographic order. In the instance of PEDOT:Tosylate films, evidence for a paracrystalline structure is

discovered, in which the order decays over large distances. In the case of PEDOT:PSS films, no crystalline structure was seen by x-ray examination, but the presence of a lower degree of order that is not detectable by x-ray analysis but has a significant influence on charge transport has been demonstrated.

The various forms of doping discussed above can be used to add new charge carriers into conjugated polymers. These charge carriers must be mobile in order to participate in charge transport. Anderson presented a model for charge transfer in randomly disordered systems in 1958. These systems are also referred to be homogeneously disordered if their disorder length scale is equal to or less than the electronic correlation length. Anderson proposed that at low impurity concentrations, charge transfer occurs not by free charge carriers distributed across the medium, but rather via quantum mechanical jumps between specific local sites. He then described the circumstances under which charge carriers' wave functions become confined and no charge transfer is possible. A Fermi glass is another term for a system having completely confined states at the Fermi level. Mott suggested that when a system is sufficiently disordered, a metal–insulator transition, dubbed the Anderson transition, must occur. Heterogeneously disordered systems are those in which the disorder length scale is greater than the electronic correlation length[89].

Heterogeneous disorder has been proposed for several kinds of polyacetylene, and it is also applicable for PEDOT:PSS. It has been demonstrated that homogeneous or heterogeneous disorder alone is insufficient to characterize the unique carrier behaviour of conjugated polymers. Nonetheless, these models can provide a starting point for understanding charge transport in intrinsically conductive polymers, and the computed data fits the actual results well[89].

Conducting polymer materials have in common a disordered structure. Since the length of polymeric chains is variable, due to a non-uniform defect distribution, also the delocalization length of electrons along the chain (i.e. 'conjugation length') is variable, leading to more or less well-stacked polymer chains where a weak interaction between π-π electrons exists in the type of Van der Waals forces.

As indicated in Figure 29, the overall materials consist of amorphous domains and crystalline domains with a size range of ~10 nm. Charge transfer is faster along chains, moderate across chains and between lamellar planes is slower in such disordered materials (Figure 30)[90]. Additionally, the chains can be positioned arbitrarily along the x, y, or z axes. It is self-evident that in the scenario shown in

Figure 29a, rather than Figure 29c, transport characteristics would be optimal. It is well accepted that an increase in charge mobility is related to the relative stacking of the chains and to the amount of order. To improve the transport characteristics of conducting polymers, the upgrade in intra- and inter-chain charge transport and the increase in charge mobility must be accomplished[91].
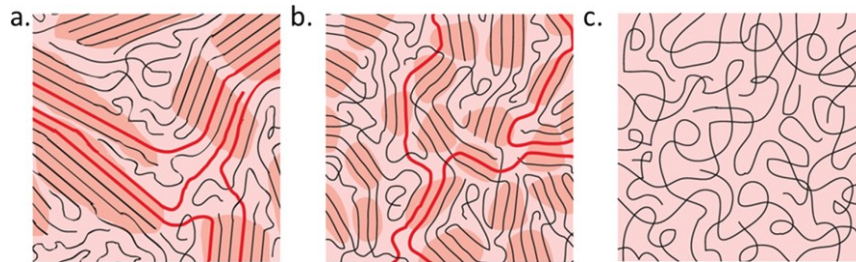
Figure 29: representation of polymer chain structure of with varying degrees of order. (a) Highly organized aggregates; (b) disordered aggregates; (c) totally disordered aggregates. Without reduction in the conjugation length ordered areas (dark orange) and long chains (red) can link together[90].
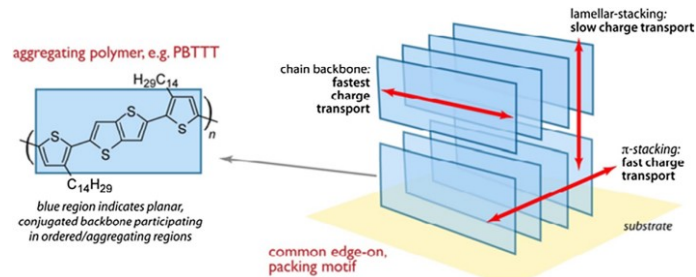
Figure 30: Schematic representation of charge transport along the chain backbone, the π-π stacking, and the lamellar stacking is fast, moderate, and slow, respectively.

3.2 Band structure in conjugated polymers

Polymers have a more complex band gap than inorganic semiconductors. Polymers are rarely pure, complicating much of the physics description and resulting in a lack of a complete understanding of the polymer semiconducting characteristics. To characterize charge transport processes, it is necessary to understand the genesis of the band gap in these conjugated systems, beginning with the behaviour of molecular orbitals. The chemistry of polymer electronics is based on the concept of linear combination of atomic orbitals.

3.2.1 Primitive cell

In a one-dimensional crystal with a lattice parameter of 'a' and one atom per primitive cell (Figure 31), the linear combination is constructed using just one 's' type orbital of each atom. A real system would consist of a single electron and a linear chain of hydrogen ions, H^+.
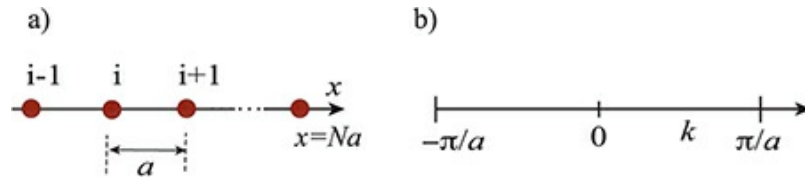
Figure 31: (a) A linear chain of N atoms separated by distance 'a' (i.e. lattice parameter). (b) The first Brillouin zone. The limits of the Brillouin zone are planes that passing through points and are perpendicular to the chain.

The computation is conducted on the assumption that there is only one electron in the crystal and that the wave functions represent all of the electron possible states. It is acceptable to fill the states of the bands with two electrons in each state, until the crystal total number of electrons. The mean field potential includes all interactions. All overlap integrals are ignored and only the transfer integrals between first neighbours are evaluated.

$$\text{Eq. 7:} \quad E(k) = \sum_{j}^{N} e^{ik \cdot (R_j - R_i)} H_{ij}$$

where R_i and R_j denote the orbital 'j' to orbital 'i' distance vectors. It is worth noting that the band energy function in Eq. 7, E(k) is solely dependent on the distances ($R_j - R_i$) and the nature of the orbitals. In the limit of an infinite crystal, the set of all discrete values of k becomes dense, permitting identification of the set of eigenvalues E_k. The matrix elements H_{ij} are the Coulomb integrals (if i = j) and the transfer integrals (if i ≠ j), considering $H_{ij} = \langle \phi_i | H | \phi_j \rangle$. If V(r) matched the precise atomic potential and ϕ_i the exact atomic orbital, this term equals the atomic energy ϵ_0.

Considering the following in the first neighbours approximation:

$$H_{ii} = \epsilon_0 \ (Coulomb \ integral)$$

$$H_{i,i+1} = V \ (Transfer \ integral)$$

The Coulomb integral represents the energy of the electron within the orbital, whereas the transfer integral represents the energy necessary to move the electron from one orbital to one of its initial neighbours, i+1 or i–1. Integrals between distant neighbours are omitted: $H_{i,j'>|i\pm1|} = 0$. Eq. 8 is produced by making the appropriate substitutions:

$$Eq. 8: \ E(k) = e^{ika}V + \epsilon_0 + e^{-ika}V = \epsilon_0 + 2V cos(ka)$$

with

$$k = \frac{2\pi}{Na}m; \quad m = -\frac{N}{2}, ..., 0, ..., \frac{N}{2}$$

This is seen in Figure 32a. The free electron band is depicted in Figure 32b for comparison. This comparison may aid in determining the magnitudes of the transfer integrals and their dependency on the distance between the atoms.
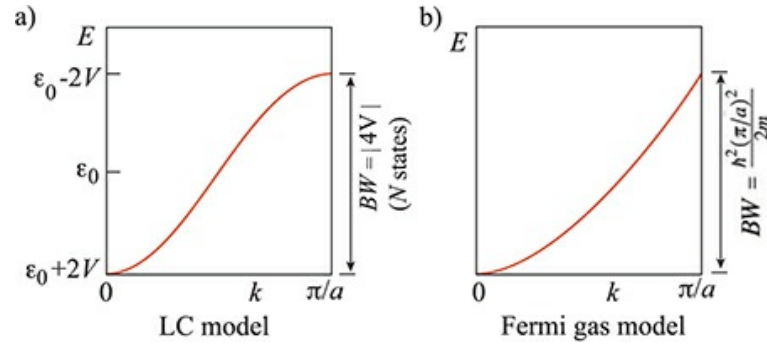
Figure 32: (a) Energy bands for a one-dimensional crystal (linear chain of atoms), calculated using the linear combination (LC) approximation; BW denotes the band width. (b) The free electron (Fermi gas) model's associated energy band. It is worth noting that V < 0 is true if s type orbitals are used as the foundation for the LC. If each atom has just one electron, $E_F = \epsilon_0$.

As noted previously, this band structure is reminiscent of a linear chain of hydrogen atoms, each with its own electron. There will then be N electrons in the energy band to occupy the N states. Due to the fact that each state can be occupied by two electrons (with antiparallel spins), the band will be half full at absolute zero (T = 0

K), and this chain will correspond to the electrical structure of a one-dimensional metal.

In the case of a two-atom primitive cell and therefore two orbitals per cell, as seen in Figure 33, two different transfer integrals, V_1 and V_2, must be considered. Due to the fact that the primitive cell has doubled in size, $b = 2a$, the new Brillouin zone has been half, with the new borders being $\pm\frac{\pi}{2a}$, and two energy bands will exist separated by an energy gap.
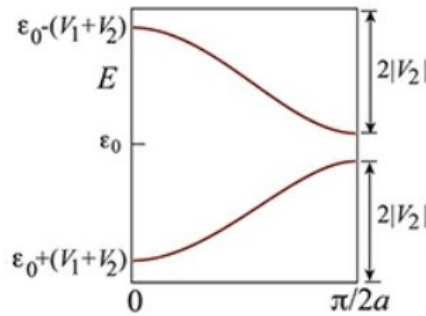
Figure 33: Band structure resembling a two-atom primitive cell.

3.2.1 Energy band gap

The de Broglie relation states that the total energy of the electron, unaffected by any periodic potential, is

$$\text{Eq. 9:} \quad E = \frac{\hbar^2 k^2}{2m_e}$$

Electrons can be regarded free in this case, with a parabolic potential as a function of k, and they are treated similarly to free electrons in metals.

The periodic potential of a conjugated polymer system is denoted by the Su–Schrieffer–Heeger model, as shown in Figure 34. Electron energies inside the band gap (E_g) are banned, whereas electrons with energy above the gaps are permitted to conduct. The idea is similar to that of the Kronig–Penney model, which was the first to explain electron energy bands in crystals, although there are notable differences. Brillouin zones, for example, can be linked to the reciprocal lattice in the band theory of inorganic semiconductors. Conjugated polymers, on the other

hand, whose conductivity may be considered one-dimensional, cannot be characterized in this way. The Su–Schrieffer–Heeger model is straightforward in comparison to other models, and predicts an electron energy as given by Eq. 10:

$$\text{Eq. 10:} \quad E = E_F \pm \sqrt{E_0^2 \cos^2(ka) + \left(E_g/2\right)^2 \sin^2(ka)}$$

where $2E_0$ is the band width and E_F is the Fermi level situated in the band gap centre. Indeed, the existence of a band gap in a polymer such as polyacetylene seems intuitive, considering π electrons to be delocalized and therefore free to travel about the polyacetylene backbone.

However, polyacetylene (C_2H_2) has an alternating pattern of single and double bonds. This, it turns out, requires less energy than delocalizing the electrons. Due to the alternation of single and double bonds, there are distinct bond lengths for C–C and C=C. The energy required to reverse the C–C and C=C bonding is approximately 1.5 eV for polyacetylene. Unsaturated polymers, such as polyacetylene, include carbon–carbon (C=C) double bonds; conjugated polymers (i.e. those with alternating single and double bonds –C=C–C=...) are invariably unsaturated, but not all unsaturated polymers are conjugated.
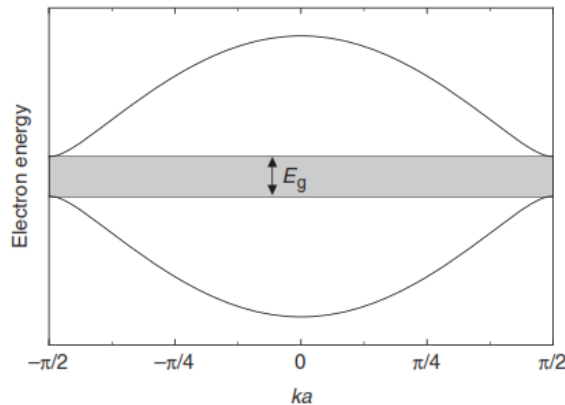
Figure 34: Su–Schrieffer–Heeger theory (strict binding approximation) indicates that polyacetylene has a periodic potential. The band gap, $E_g = E_L - E_H$, is defined as the difference between the energy limitations of the HOMO and LUMO bands. The Fermi level (E_F) is located in the band gap centre.

When these double bonds are situated throughout the chain backbone, they often impart a degree of stiffness to such polymers that is not present in polymers composed entirely of C–C single bonds, such as polystyrene. By solving the

Schrödinger equation for a periodic function, it was proven how bands may form in semiconductors and how mobile electrons can exist and be accessible for conduction using the free electron model. Conduction occurs in metals because of electrons, which are incorporated into the bonds. Even when doped, the linkages of a polymer remain unaltered. The polymer backbone is unaffected by the electronic behaviour, which could not be the case if electronic transitions were caused by bonds. Finally, the extended system along the chain backbones (i.e. conjugation) is responsible for electronic transitions in polymers, providing the critical distinction between organic and inorganic semiconductors electronic behaviour.

3.2.2 Su–Schrieffer–Heeger theory

The formation of the band gap in polyacetylene has been eloquently described using a fairly simple hypothesis that incorporates the energy costs of transporting an electron by hopping between monomers. Additionally, the total energy contains components for the potential energy of stretching or compressing the bonds (i.e., adjacent monomers are considered as springs) and the associated kinetic energy. When the chain is believed to be completely dimerized, the question of how a band gap is generated becomes considerably more tractable. This means that we consider two CH units in order to deal with two distinct bond lengths, assuming they are constant throughout the chain. By comparison, the undimerized chain would have a single equilibrium bond length and no bond alternation.

According to Su–Schrieffer–Heeger theory, electrons interact with the lattice via electron–phonon coupling. This implies that electrons are unable to travel independently of the chain backbone. This model makes a critical assumption: electrons do not interact with one another. The energy of the chain is defined as the sum of the energies of each of the N CH groups:

$$\text{Eq. 11:} \quad H = -\sum_n (t_0 + (-1)^n 2\alpha u)\left(c_{n+1}^\dagger c_n + c_n^\dagger c_{n+1}\right) 2NKu^2$$

where the formalism of the original paper has been reported[92]: 'u' is the perturbation to the bond spacing in the unperturbed system, so that the difference in bond length between the (longer) single and (shorter) double bond is 2u; 'K' is an effective spring constant representing the behaviour of σ bonds ($2NKu^2$ is an elastic energy due to bond distortion); 't' is an energy associated with moving

electrons from one monomer to its neighbour; 'α' is an electron–phonon coupling parameter, and accounts for the perturbation due to different bond lengths; and c_n and $c^{\dagger}_{n+1}$ are fermion (i.e. here π or $2p_z$ electrons) annihilation and creation operators, which allow for electron movement from monomer to monomer. As such $t_0 (c^{\dagger}_{n+1}c_n + c^{\dagger}_n c_{n+1})$ represents the transfer of an electron between one π orbital to another, which consequently means the transfer of an electron between different sites, because different π orbitals are on different carbon atoms. Strictly 'H' is a Hamiltonian, because it is an operator (or the sum of operators).

The creation and annihilation operators, which take into account the fact that when an electron arrives to a CH unit, it is lost (annihilated) from its neighbours. These operators simplify the Schrödinger equation and Eq. 11 is essentially the time-independent Schrödinger equation for π electrons in dimerized polyacetylene.

While moving electrons across sites is an expression of their kinetic energy, a Hamiltonian requires a component for potential energy. Along with the elastic energy resulting from bond distortion, there is a term resulting from the alternating double and single bonds with varying bond lengths. Because the π bonds are not situated on an aromatic ring with equal bond lengths on each side of the carbon atom, the system energy is altered and this disturbance caused by nearest-neighbour hybridization has an associated energy provided by Eq. 12:

$$\text{Eq. 12:} \quad \Delta_n = -\alpha (u_{n+1} - u_n) = -2 (-1)^n u = (-1)^n \Delta$$

where $\Delta = -2u$, and $2u = u_{n+1} - u_n$; u_n is the deviation from the bond length in the linear (undimerized) chain and may take positive or negative values depending on whether the bond to which refers is single ($u_n > 0$) or double ($u_n < 0$).

Because the chain is kept together by constant bonds, they are not related with the creation and annihilation operators and they are affected by bond distortions contributing a potential energy of $K(u_{n+1} - u_n)^2/2$, which is equal to $2NKu^2$ for the entire chain.

3.2.3 Density of states in Polyacetylene

The density of states, denoted by $g(E)$, in Eq. 13, is the number of electronic states at a given energy level, denoted by dN/dE. However, using the periodic boundary conditions and considering the polymer chain to be a circle with radius 'r', In this calculation, the total number of states is N = 2πr/a, where '2a' denotes the dimer's size or length. Thus, the density of states becomes as seen in Figure 35.

$$\text{Eq. 13:} \quad g(E) = \frac{dN}{dE} = r\frac{dk}{dE} = \frac{Na}{2\pi dE/dk} = \frac{NE_k}{2\pi}\left\{\left[\left(\frac{E_g}{2}\right)^2 - E_k^2\right][E_k^2 - E_0^2]\right\}^{-\frac{1}{2}}$$

where $\Delta_k = \frac{E_g}{2}\cos(ka)$ and $E_k = E_0\cos(ka)$.
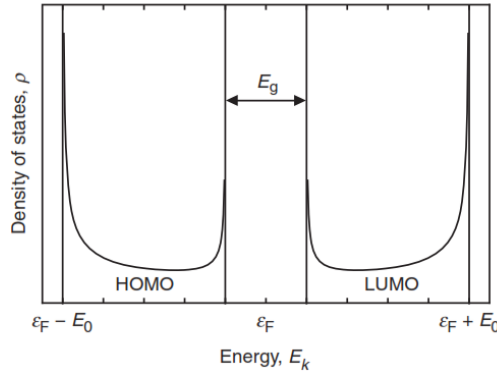
Figure 35: The one-electron density of states predicted by the Su–Schrieffer–Heeger theory for a dimerized chain.

Notably, only states satisfying $|E_0| > |E_k| > |E_g/2|$ are those an electron can be contained within. This density of states is a one-electron kind which contains all free electrons and fill the energy levels from the lowest to the highest. The assumption of examining one electron is due to the fact that there are no free or virtually free electrons, since an electron is linked with a monomer. It can be demonstrated that the numbers used to calculate the density of states (Eq. 13) are equivalent to those in the Hamiltonian formulation (Eq. 11) when $8\alpha u = E_g$ and $2t_0 = E_0$.

3.3 Quasiparticles in conductive polymers

Field effect measurements, the thermo-magnetic dependence of the electrical conductivity and of the Seebeck coefficient from 300 K to 4 K are the primary methods for determining transport mechanisms[93], although in this work only measures @RT were performed and a bibliographic and theoretical dissertation is treated in this section. The thermo-magnetic behaviour of conductivity has been mostly employed in literature because it is more accessible to distinguish the various contribution to the material conductivity[94]. Eq. 14 gives the electrical conductivity of a substance.

$$\text{Eq. 14: } \sigma = n|e|\mu$$

With n denoting the charge carriers' density, e denoting the electronic charge, and μ denoting the charge carriers' mobility.

The origins of conjugated polymers high conductivity will be discussed in terms of quasiparticles, which are critical for describing band formation and charge transport processes. The mobile charges referred as polarons, bipolarons and solitons hop between different sites, if no charge is present nearby the counter-ion, which is a fixed charge and at the acceptor site, since high coupling potential between them.

3.3.1 Peierls transitions

In highly anisotropic solids, such as organic conductors and semiconductors, both in molecular materials and conjugated polymers, electron–electron interactions mediated by phonons (lattice vibrations) cause structural instabilities and metal–insulator and spin transitions. The Peierls transition[95] is one of the most significant of these processes that affect organic semiconductors[96].

In quasi-one-dimensional materials, the ion–ion, electron–electron, and electron–phonon interactions can be different depending on the crystallographic orientation. This group includes the majority of organic conductors and semiconductors, as well as tiny molecule solids and polymers. The anisotropy of these materials can reach extreme levels. There are numerous instabilities in a purely one-dimensional solid that make these systems extremely rich in terms of their physics:

- If electron–phonon interactions are significant, the ground state is unstable in the presence of charge density waves (CDW) with wave vector q = k_F, resulting in what is known as the Peierls instability.
- If magnetic interactions exist, spin density waves (SDW) can form without causing lattice distortion or with lattice distortion causing a spin-Peierls instability.
- Thermal fluctuations at $T \gg 0$ K disrupt long range order in the presence of short-range interactions.
- A low grade of disorder may result in electron localization and the formation of a metal–insulator transition.

At low temperatures, the elastic energy required to modify the lattice is less than the gain in electronic energy in quasi-1D metals. As a result, the CDW state is the ground state. Under these conditions, it is typical to observe the opening of a gap in the energy band at $k = k_F$, as illustrated in Figure 36, as well as the Peierls transition.
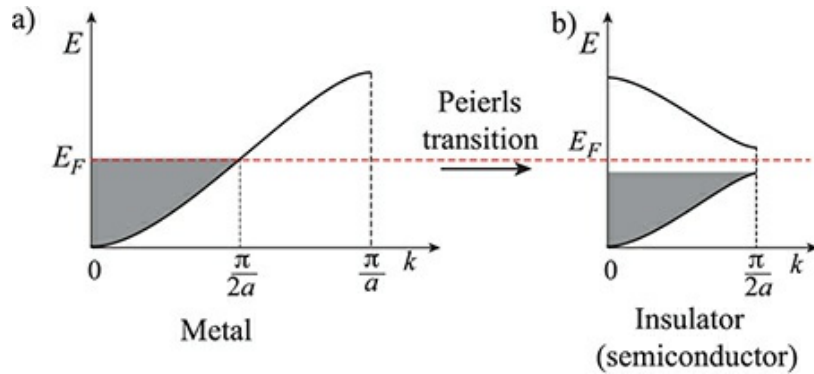
Figure 36: Transition of Peierls When the electronic energy of a 1D metal is reduced more than the elastic (phonon) energy, the band creates a gap at $k = k_F$. When $k_F = \pi/2a$, the gap is opened, the lattice dimerizes.

The Peierls instability and subsequent transition are observed in a wide variety of organic conductors, most notably those with charge transfer. At elevated temperatures, these materials may be metals with crystal structures that favor π-π interactions along stacks of evenly spaced molecules or ions. When the conduction band is half filled, a charge density wave of wavelength '2a' develops and the stacks may dimerize and as a result, a gap at the Fermi wave vector, k_F, will open, but in general, if the degree of band filling is 1/n, $k_F = \pi/na$, the charge density wave will have the wavelength equal to 'na'.

3.3.2 Solitons

Topological defects are characteristic of semiconducting polymers and play a critical role in charge transport characteristics[92]. Solitons (also referred as kink solitons or bond-alternation defects) are topological defects that correspond to non-bonding $2p_z$ orbitals populated by a single electron. These neutral solitons are important for charge transfer and hence conductivity, because they divide two segments of $(CH)_x$ with the same energy and travel along the chain (Figure 37).
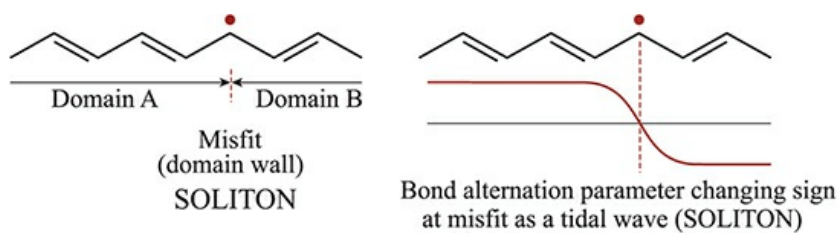
Figure 37: A neutral soliton that separates two $(CH)_x$ segments with opposite double bond alternation directions.

Solitons arise in polyacetylene because the two domains A and B with opposing orientations of double bond alternation are degenerate and the energy cost of forming the soliton is less than the energy cost of band excitation.

The soliton is a term that refers to non-bonding levels in the gap between the π^* (conduction) and π (valence) bands. The neutral soliton has a spin of 1/2, while solitons with charges $\pm e$ have a spin equal to 0. As seen in Figure 38, doping allows for the creation of solitons with positive or negative charge, zero spin, as well as neutral solitons with spin 1/2 and even fractional charges. Solitons are delocalized over a large number of CH units and can freely travel along a chain without altering its form. The effective mass has been calculated to be approximately six times that of the unbound electron[97].
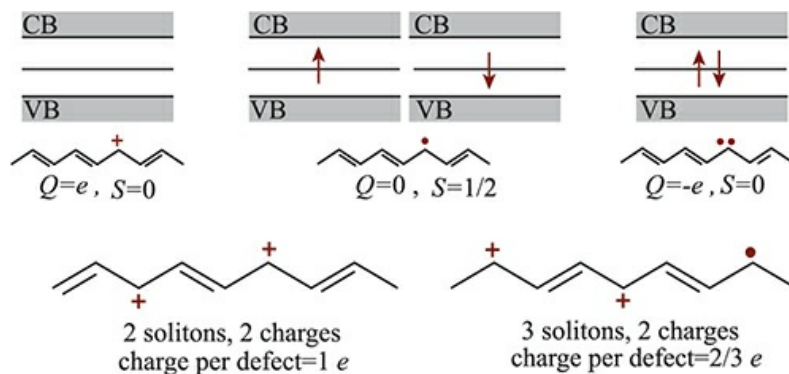
Figure 38: A schematic illustration of the formation of a soliton, illustrating different
charge and spin combinations.

The polymer is not flawless and may have kinks or other defects that allow charge
carriers to pass across the band gap. In terms of the chain chemistry, this is the point
at which two single bonds are linked, thereby breaking the conjugation. When this
occurs, a bi-radical is formed. A double bond is broken, resulting in the formation
of two unpaired electrons, implying that a CH group is connected to both of its
neighbors through single bonds.

Solitons are radicals that can move by swapping single and double bonds. The
interchange of single and double bonds does not necessitate the provision of band
gap energy for each monomer along the chain. The two radicals formed are a pair
of soliton–antisoliton radicals that can travel apart along the chain, as seen in Figure
39. This process has no energy barrier, as electrons are believed to be delocalized.
It is useful to understand soliton and antisoliton since they are capable of
annihilation. To conserve total spin, a neutral soliton has spin 1/2 and an anti-soliton
-1/2. Solitons are also formed in chains because of defects. Due to the fact that
solitons are self-moving, they do not need to be connected with an antisoliton. The
soliton has a spin due to its connection with an electron. Solitons can travel along
the chain backbone, indicating that they are delocalized to some extent.
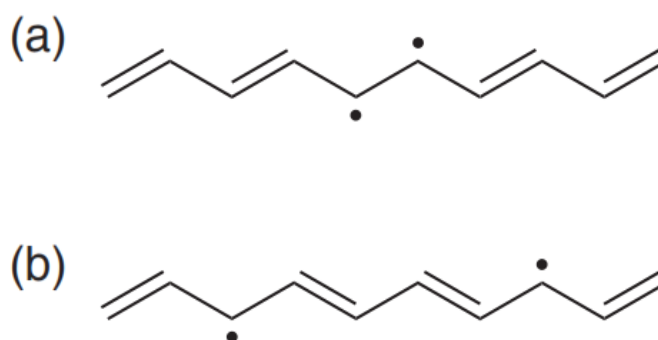
Figure 39: A soliton and antisoliton produced concurrently (e.g. thermally) may
travel in opposite directions down the chain as in (a) (b).

This is what it means when solitons are described as delocalized, since the soliton
effect may span between three and five monomers. Solitons have an associated
energy and they are located above the HOMO level but below the LUMO level.
The soliton is positioned approximately halfway up the band gap, which reflects the
fact that the bond lengths on each side of the soliton's center are equal. The energy

level associated with the soliton can only be partly filled, as the soliton is limited by Fermi–Dirac statistics owing to its spin.

Polymers with ring structures along their backbones or those that are not degenerate conjugated polymers (PEDOT), in which the exchange of single and double bonds throughout the polymer chain results in the same structure, are not sensitive to this degeneracy and hence do not form solitons.

3.3.3 Polarons and Bipolarons

When an electron is added or extracted from a conjugated polymer chain, the electron–lattice coupling causes a deformation of the lattice associated with the charge. This topological flaw will result in the formation of a quasiparticle known as a polaron. When two electrons or two holes interact via the Coulomb or electron–phonon–electron interaction, they can create two separate polarons or they can associate to form a bound state termed a bipolaron. Figure 40 illustrates polarons and bipolarons in Poly(ThienyleneVinylene) (PTV).
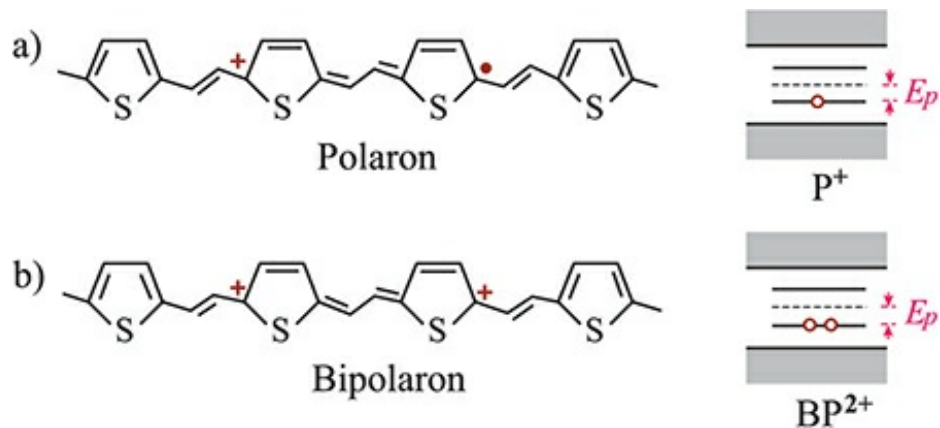
Figure 40: (a) The generation of a polaron P^+ in a section of PTV by removing one electron and creating a positive charge and an unpaired electron that will dissociate due to lattice relaxation. (b) The removal of a second electron results in the formation of a bipolaron BP^{2+} with two positive charges. Only the holes in the gap are displayed since the bonding level is occupied in the normal state without topological flaws[98].

The localized electronic states in a polaron or bipolaron are symmetrically located at energies $\pm E_p$ relative to the gap center, as seen in Figure 40 energy level diagram. E_p value is dependent on the defect shape.

Polarons, in contrast to solitons, are charged, although they, like solitons, exhibit lattice distortions. A polaron is a neutral soliton coupled to another neutral soliton, and they often occur on chains with non-degenerate ground states. Others significant distinctions between polarons and solitons is that polarons are not linked with unpaired electrons, despite their band gap location and that polarons, then, have a spin of 1/2. When the spins of two distinct polarons combine to form a bipolaron, a more complex event happens. Because the charges are identical, they cannot cancel, resulting in the formation of a longer quinoid structure with the charges at either extremity. As a result, a bipolaron has twice the electrical charge and can be positive or negative. Although bipolarons have been discovered spectroscopically, they remain a novelty due to their high energy state. They are more prone to develop in the presence of faults or at high charge densities.

Between the HOMO and LUMO levels there are the polaron and bipolaron levels. There are two tiers of this kind (Figure 41). In the case of the negative polaron, the upper of these two levels has one charge, whereas the lower level is half-filled in the case of the positive polaron. Each of these has a 1/2 spin. When it comes to bipolarons, the negative bipolaron has all of its levels filled, while the positive bipolaron has none, resulting in zero spin.
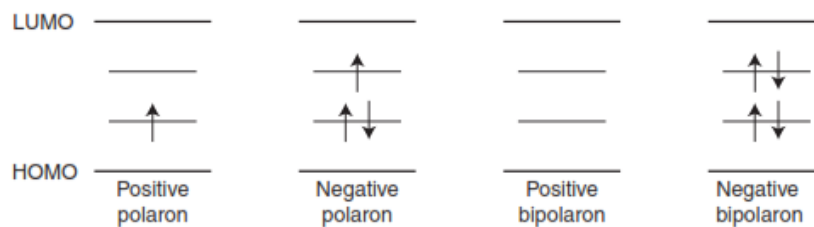
Figure 41: Polarons and bipolarons are generated at energy levels close to the band gap. Both the hole and electron polarons have a spin of 1/2, while bipolarons have no spin. Bipolarons have double the electrical charge of polarons.

3.3.3.1 Large and small polarons

A charge is screened in a polarizable media. The process is described by dielectric theory as the induction of polarization around the charge carrier. When a charge carrier moves across a medium, the induced polarization might follow it. The carrier and the induced polarization are regarded to be a single entity, a polaron (Figure 42). A polaron's physical characteristics are distinct from those of a band-carrier. A

polaron's binding (or self-) energy E_0, effective mass m*, and distinctive response to external electric and magnetic fields (e.g. optical absorption coefficient and dc mobility) are all characteristics.
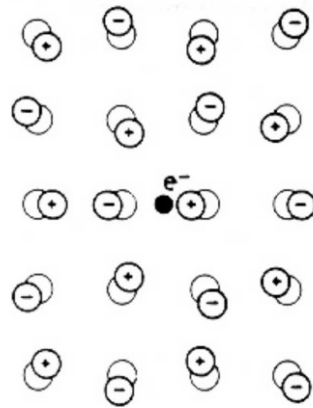
Figure 42: Artistic representation of a polaron. In a ionic crystal or polar semiconductor, a conduction electron repels negative ions and attracts positive ions. A self-induced potential is generated, which works in reverse on the electron, altering its physical characteristics.

When the spatial extension of a polaron exceeds the lattice parameter of a solid, the latter might be considered a polarizable continuum. This is a large (Fröhlich)[99] polaron. When an electron or hole self-induced polarization approaches the order of the lattice parameter, a small (Holstein)[100] polaron can form[101]. Small polarons, in contrast to large polarons, are regulated by short-range interactions.

3.3.3.2 Polarons classification

When a molecule acquires or loses an electron, its charge causes a disturbance in the lattice's potential energy, deforming the orbitals in order to minimize the system energy.

Polaron refers to the excited and electrically charged state formed by the electric charge and deformation produced in the molecular lattice. The size and energy of the polaron are dependent on the kind and degree of the lattice deformation produced. The molecular lattice deforms in three stages, as depicted in Figure 43, considering a molecule A that loses an electron as an example:

1. Electron Polaron[102]: The electron clouds are first polarized due to the electric field created by the positive charge of molecule A. Two contributions affect the electronic polaron: the free carrier and the deformation of electronic clouds. The polarization of the electron clouds occurs in 0.1 - 1 fs.
2. Molecular Polaron[103]: To stabilize the molecule A, the covalent bonds charges are redistributed. The bond distance and angle vary in response to the charged molecule. 1 - 10 fs is the relaxation time.
3. Lattice Polaron[104]: When the charge of molecule A interacts with the charges of nearby molecules, a lattice deformation occurs. This phenomenon occurs in 100 - 1000 fs.
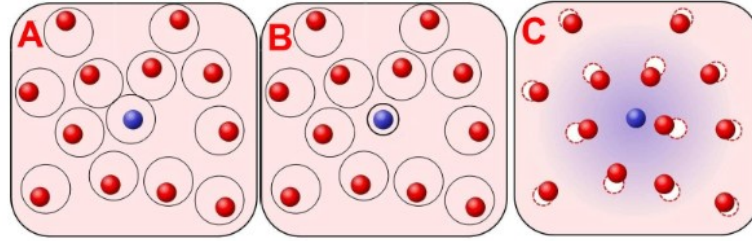
Figure 43: a) Electron Polaron b) Molecular Polaron c) Lattice Polaron

3.3.3.3 Polaron radius, coupling constant and mobility

A) The radius of a polaron

When a longitudinal optical (LO) phonon field with frequency ω_{LO} interacts with an electron and the quadratic mean square deviation of the electron velocity is denoted by Δv, the electron can move a distance if the electron-phonon interaction is weak, which is Eq. 15:

$$\text{Eq. 15:} \quad \Delta x \approx \frac{\Delta v}{\omega_{LO}}$$

over the time interval ω_{LO}^{-1}, which is typical of the lattice period, because it is the distance within which the electron may be localized using the phonon field as measurement instrument. Eq. 16a and Eq. 16b follow from the uncertainty relations:

$$\Delta p \Delta x = \frac{m}{\omega_{LO}} (\Delta v)^2 \approx \hbar$$

$$\text{Eq. 16a:} \quad \Delta v \sim \sqrt{\frac{\hbar \omega_{LO}}{m}}$$

$$\text{Eq. 16b:} \quad \Delta x \sim \sqrt{\frac{\hbar}{m \omega_{LO}}}$$

At weak coupling, Δx denotes the polaron radius r_p. To be consistent with the definition of a large polaron, the radius of the polaron r_p must be much greater than the lattice parameter 'a'. $r_p \approx 10\ nm$ for semiconductors II-VI and II-V.

B) The coupling constant

When a strong electron-phonon interaction occurs in a polar crystal, the electron of mass 'm' becomes localized and may be approximated by a static charge distribution inside a sphere of radius 'l_1'[105]. If the medium has an average dielectric constant of ε_m, the potential energy of an evenly charged sphere of radius l_1 in a vacuum is expressed in Eq. 17[106].

$$\text{Eq. 17:} \quad U_{vac} = \frac{3}{5}\frac{e^2}{l_1}$$

The potential energy of an evenly charged sphere in a material with a high frequency dielectric constant ε_∞ is

$$U_1 = \frac{3}{5}\frac{e^2}{\varepsilon_\infty l_1}$$

This is the potential energy of the charge e distributed evenly across the radius l_1 sphere in a material with the dielectric constant ε_∞. The potential energy of a uniformly charged sphere in a medium with an inertial polarization field caused by LO phonons is

$$U_2 = \frac{3}{5}\frac{e^2}{\varepsilon_0 l_1}$$

where ε_0 is the static dielectric constant. The polaron effect is thus associated with the change in the potential energy of the charged sphere interaction with the inertial polarization field. This difference is equal to the potential energy U_2 of the uniformly charged sphere in the presence of the inertial polarization field minus the

potential energy U_2 of the charge e evenly distributed across the sphere in a medium devoid of inertial polarization:

$$U_{pol} = U_2 - U_1 = -\frac{3}{5}\frac{e^2}{\varepsilon_m l_1}$$

with

$$\frac{1}{\varepsilon_m} = \frac{1}{\varepsilon_\infty} - \frac{1}{\varepsilon_0}$$

The distribution of electrons in a sphere may be non-uniform, which may have an effect on the numerical coefficient. The potential energy, in Eq. 18, may be calculated as follows using this correction:

$$\text{Eq. 18:} \quad U_{pol} \sim -\frac{e^2}{\varepsilon_m l_1}$$

Due to the electron confinement in space, its De Broglie wavelength must be of order l_1, and its kinetic energy must be of order $4\pi^2\hbar^2/2ml_1^2$. Minimizing total energy in relation to l_1 results in

$$\frac{\partial}{\partial l_1}\left(-\frac{e^2}{l_1\varepsilon_m} + \frac{4\pi^2\hbar^2}{2ml_1^2}\right) = 0 \Rightarrow \frac{1}{l_1} = \frac{e^2}{4\pi^2\hbar^2\varepsilon_m}$$

where the binding energy is calculated in Eq. 19:

$$\text{Eq. 19:} \quad U_1 = -\frac{e^4 m}{8\pi^2\hbar^2\varepsilon_m^2}$$

For weak coupling, the electron kinetic energy may be ignored. Given the radius of the polaron, $r_p = \sqrt{2\hbar/m\omega_{LO}}$, the binding energy is expressed in Eq. 20.

$$\text{Eq. 20:} \quad U_2 = -\frac{e^2}{r_p\varepsilon_m} = -\frac{e^2}{\varepsilon_m}\sqrt{\frac{m\omega_{LO}}{2\hbar}}$$

It is noticeable that

$$\frac{U_1}{\hbar\omega_{LO}} = -\frac{1}{4\pi^2}\left(\frac{U_2}{\hbar\omega_{LO}}\right)^2$$

According to field theory standards, the self-energy at weak coupling is denoted by

$$U_2 = -\alpha\hbar\omega_{LO}$$

As a result, the Fröhlich polaron coupling constant is determined in Eq. 21:

$$\text{Eq. 21:} \quad \alpha = \frac{e^2}{\hbar c}\sqrt{\frac{mc}{2\hbar\omega_{LO}}}\frac{1}{\varepsilon_m}$$

For the average dielectric constant, it is shown that

$$\frac{1}{\varepsilon_m} = \frac{1}{\varepsilon_\infty} - \frac{1}{\varepsilon_0}$$

where ε_∞ and ε_0 are the polar crystal electronic and static dielectric constants, respectively. The difference $1/\varepsilon_\infty - 1/\varepsilon_0$ occurs because ionic vibrations occur in the infrared spectrum and electrons in the shells may adiabatically follow the conduction electron.

C) The mobility of a polaron

The essential concept in evaluating a basic derivation of the mobility behaviour, particularly its temperature dependency, is that the mobility changes as the number of phonons in the lattice with which the polaron interacts, changes with temperature. The phonon density is given by

$$n = \frac{1}{e^{\frac{\hbar\omega_{LO}}{kT}} - 1}$$

For large polarons, the mobility is proportional to the inverse of the number of phonons:

$$\mu \approx \frac{1}{n} = e^{\frac{\hbar\omega_{LO}}{kT}} - 1$$

and for low temperatures $kT \ll \hbar\omega_{LO}$

$$\mu \approx e^{\frac{\hbar\omega_{LO}}{kT}}$$

The mobility of continuum polarons diminishes exponentially with increasing temperature. The LO phonon frequency determines the slope of the straight line in $\log(\mu)$ versus $1/T$. Systematic research, particularly by Fröhlich and Kadanoff, reveals

$$\mu = \frac{e}{2m\omega_{LO}} e^{\frac{\hbar\omega_{LO}}{kT}}$$

Under the influence of optical phonons, the small polaron will hop from ion to ion. The more phonons there are, the greater the mobility. Small polaron behaves in the opposite manner to the large polaron. It is expected:

$$\mu \approx n = \frac{1}{e^{\frac{\hbar\omega_{LO}}{kT}} - 1}$$

For low temperatures $kT \ll \hbar\omega_{LO}$:

$$\mu \approx e^{-\frac{\hbar\omega_{LO}}{kT}}$$

thermal energy is used to trigger the mobility of tiny polarons. A thorough examination of the small polaron hypothesis demonstrates that the mobility, for low temperatures, can be expressed as in Eq. 22:

$$\text{Eq. 22:} \quad \mu \approx e^{-5\frac{\hbar\omega_{LO}}{kT}}$$

3.4 Solitons and polarons bands

Conjugated polymers are semiconductors or insulators in their pure state due to the gap between the π and π^* bands. Doping produces solitons or polarons/bipolarons. When dopants are added in sufficient concentrations, soliton bands, as in polyacetylene and polaron/bipolaron bands, as in non-degenerate conjugated polymers, can develop, resulting in high conductivities, as for PEDOT:PSS. Only polyaniline exhibits a true metallic state, with conductivity values of 300 S/cm and $(\frac{d\rho}{dT} > 0)$ down to 5 K[107].

The doping level is defined as the ratio of counter-ions to monomers in a chain. Doping a semiconducting polymer enables electrons to occupy bands near to the LUMO and holes to occupy bands slightly above the HOMO. If the charge carrier is positive, the resultant charge is referred to as a radical cation; if the charge carrier is negative, the resulting charge is referred to as a radical anion; in both circumstances, they are referred to as polarons. Doping does affect the chemistry of the polymer chain, since the dopant charges the polymer. As a result, the electrical energy levels are twisted and rearranged to minimize the cost of adding an electron

or hole to the chain. This can be accomplished by altering the type of the polymeric bonds. This is accomplished in polyacetylene simply by doping. In some polymers, bond distortion can result in the creation of a novel geometry, such as the quinoid shape. This has the effect that the vacuum level of semiconducting polymers does not accurately represent the total energy required to remove an electron. Without the electron, the polymer can relax into a new structure with a different bond arrangement, recouping part of the energy cost of removing the electron[108].

A double bond is eliminated as a result of p-type doping in polyacetylene, but the insertion of a soliton stabilizes this. If the doping level is high enough, two of these solitons can combine in the same chain.

Despite their importance for conduction in polyacetylene, solitons have a considerably smaller role in charge transfer in other conjugated polymers, where polarons and bipolarons predominate.
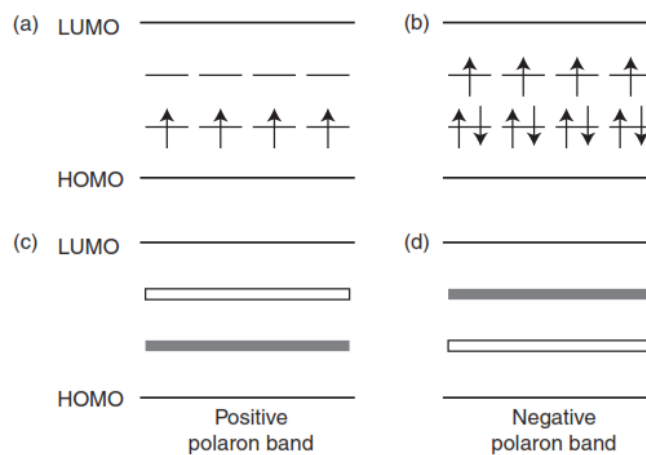
Figure 44: When several polarons are present in adjacent molecules (a and b), they interact and the energy levels become less well defined, allowing for the formation of bands inside the band gap (c and d)[109].

Certain semiconducting polymers, particularly those highly doped with metals to exhibit n-type behavior, lack such distinct energy levels, with bands spreading out where single polaron levels develop. These are seen in Figure 44.

3.5 Introduction to charge transport mechanism

The conductivity, σ, of a typical semiconductor is attributable to the contributions of the electron density, n, and the hole density, p, being expressed in Eq. 23 as

$$\text{Eq. 23:} \quad \sigma = ne\mu_e + pe\mu_p$$

where e is the elementary charge, μ_e is the electron mobility, $\mu_e = \frac{e\tau_e}{m_c^*}$, and μ_p, the hole mobility, $\mu_p = \frac{e\tau_p}{m_v^*}$, m_c^* and m_v^* being the effective masses of electrons in the conduction band and holes in the valence band, respectively, and τ is the mean scattering time. Due to the band gap, the conductivity is proportional to $\exp(-\frac{E_g}{2k_bT})$. While mobility diminishes with increasing temperature, the exponential factor remains dominating, and the conductivity may be expressed as in Eq. 24:

$$\text{Eq. 24:} \quad \sigma = \sigma_0 \exp(-\frac{E_g}{2k_bT})$$

In general, two types of restricting regimes may be considered: the band and the hopping regimes. In the band regime, charge carriers' wave functions are delocalized and the charge transport is coherent. The hopping regime is characterized by localized wave functions of the charge carriers and the transport consists of incoherent jumps.

An alternative description of charge transport in conjugated polymers that is easier to understand is intrachain transfer, which is the starting point for comprehend the characteristics of polyacetylene, for instance. Certain polymers, may exhibit a strong interchain charge transfer mechanism which is referred to as hopping. Interchain hopping is promoted in semi-crystalline materials due to the availability of closely packed neighbouring chains. Grain limits and contaminants, on the other hand, exist and oppose to the movement of charges, which may traverse grain boundaries. These phenomena illustrate the difficulties inherent in comprehending the intricacy of such morphology-dependent charge transfer.

While increasingly excellent electron transporting polymers are being found in polymeric semiconductors, materials that transport holes, such as PEDOT, have a higher mobility and stability. The reasons for the superior quality of hole carrying materials over electron transporting materials are phenomenological in nature and not well understood. Electron traps, such as the presence of oxygen, are one way to reduce electron mobility.

One theory for why electron transport is less common than hole transport is that holes and electrons have asymmetric characteristics; mobile electrons are

Modelling and characterization of electronic conductivity in 3D printed
PEGDA:PEDOT polymer composites - High frequency applications

77

associated with the LUMO, whereas holes are linked with the HOMO. There is no obvious reason why these characteristics could not result in symmetry and comparable charge transfer. The LUMO, with which the electron polaron is linked, has been hypothesized to be more localized than the HOMO. As a result, electron transport is inefficient in comparison to hole transport. Localization distinguishes inorganic materials from biological materials, which include delocalized charge carriers and hence exhibit greater wave-like motion. The more localized the charges, the greater the contribution of hopping to the transport characteristics and the less is the mobility.

3.5.1 Introduction to coherent and incoherent charge transport

The Variable Range Hopping (VRH) hypothesis introduced by Mott, provided a first theory on the transport processes in severely disordered semiconductors[110]. According to this concept, charge transfer is determined by the difference in energies and the localization distance between two different sites[111]. Thus, hopping between two localized states happens in conducting polymers when the chain thermal vibration alters the energy of these states. The hopping model successfully described the behaviour of early developed conducting polymers with a high degree of disorder, but it is not completely satisfactory because it does not account for the relatively high conductivity (> 10 S·cm^{-1}) or some metallic properties of conducting polymers such as highly doped polyacetylene, polyaniline, or PEDOT[112].

Considering charge transport in PEDOT:TOS, when it is treated with an acid, a ionic liquid or an organic solvent exhibits conductivities more than 1500 S·cm^{-1}, allowing them to be easily characterized as having a metallic behaviour[113][114] between 77 K and 370 K, with an increase in the electrical conductivity as temperature decrease[115]. PEDOT:PSS treated with DEG demonstrated a shift from semiconducting to metallic behaviour with just a small temperature dependency, whereas untreated PEDOT:PSS demonstrated normal semiconducting behaviour with a weak temperature dependence.

The substantial differences in transport characteristics across PEDOT samples have been attributed to the grade of order and to the predominant charge carriers[115]. Scattered charges form a discontinuous band in extremely disordered materials and

because of this the Fermi energy is located between the valence band and the bipolaron band if charges are not polarons or in the centre of the polaron band if the charges are polarons. As a result, a Fermi glass is produced (Figure 46). Fermi glass is a substance in which charge carriers are confined at the Fermi energy exhibiting no long range interaction in the wave functions. In such systems the predominant mechanism of charge transport is hopping, in accordance with the Mott's VRH model (Figure 45).
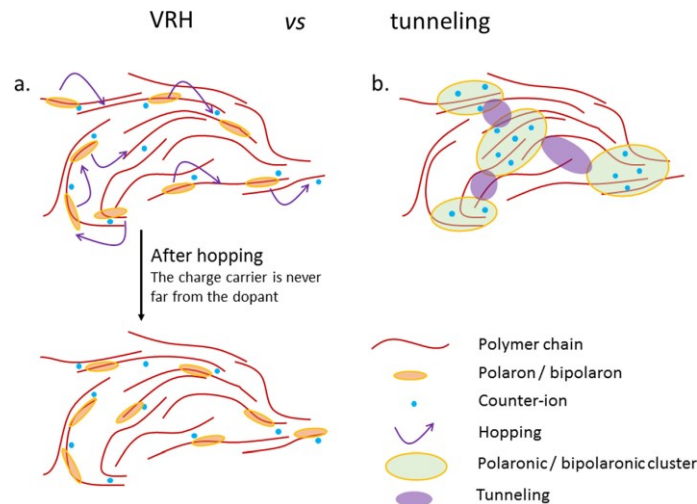
Figure 45: Comparison between (a) VRH model (b) Quantum tunnelling model. The charge carriers' wavefunctions localization due to the disorder is defined as Anderson localization. In (a) a severe delocalized occurs, while in (b) a less disorder system promotes a local delocalization in charges leading to the formation of polaronic/bipolaronic clusters with high charge density.

Polymer chains get increasingly layered and charges become more delocalized as order increases. When wavefunctions of multiple chains overlap in polaron predominant polymers, a band of polarons is formed with the Fermi level located in the middle of it (Figure 46). As a result, the polymer exhibits metallic properties as in polyaniline[116].

PEDOT contains bipolaron rather than polaron charge carriers, as demonstrated by Electron Paramagnetic Resonance (EPR)[115]. Interchain transport is also favoured in highly ordered PEDOT films groups, although the bipolaronic and valence bands somewhat overlap, resulting in the Fermi level being contained inside the interface. A material where the predominant charge transport is determined by the amount of order and the ratio of polarons respect to bipolarons and where hopping and band transport coexist and is referred as a semi-metal [117]. A transition from three-

dimensional VRH to anisotropic unidimensional VRH or quasi-metallic transport may occur with intermediate amount of order. In this situation the chain alignment is sufficiently good to allow a local delocalization of charges, but the Fermi energy level is not contained in a full band as occur in PEDOT:PSS treated with solvents, which has been observed to undergo similar transitions[118]. This transition from an insulator to a semi-metal has been observed in PEDOT, considering its shape and electronic structure, by simulating its density of states.
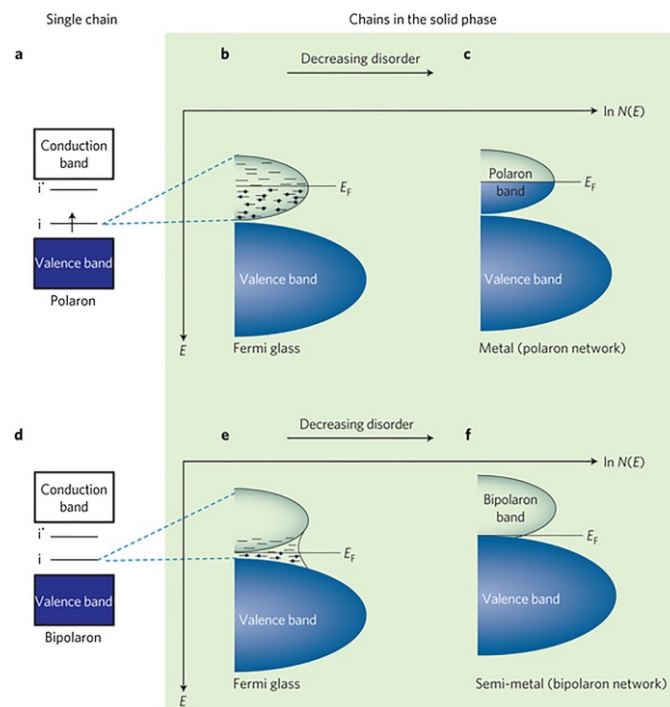
Figure 46: Electronic structure in PEDOT mater. a–c, polarons are the predominant charges: (a) one polaron in the chain and the Fermi level is surrounded by localized states, (b) a disordered material (c) ordered metallic material in which the Fermi level is contained inside the delocalized polaron band, whereas in the former. d–f, bipolarons are the predominant charges: (d) one polaron in the chain, (e) a disordered bipolaronic polymeric material (f) ordered semi-metallic polymer in which between the valence band and the empty bipolaronic band the Fermi energy level is located.

3.5.2 Generation and recombination of charges

The connection between the electron and hole in the exciton, which is an excited state of a strong coupled electron-hole pair, is strong in organic semiconductors.

The excited molecule can interact with nearby molecules, transferring energy to them. Thus, the exciton can travel from one molecule to another without charge transfer, simply by energy transmission. Exciton energy may be transferred in two ways: via dipole-dipole resonance or via resonance exchange.

Dipole-Dipole Resonance: Resonance energy transmission occurs through the interaction of two molecules and does not need the emission of light[119]. The donor molecule decays completely, transferring all the exceeding energy to the acceptor molecule. This transfer happens as a result of the long-range dipole-dipole interaction and requires that the acceptor molecule absorption spectrum overlaps with the donor molecule emission spectrum. For distances less than 10 nm, this process is quite efficient.

Resonance Exchange: When the donor and acceptor molecules are in close proximity, their excited and ground state orbitals partially overlap[120]. An electron may travel from the excited state of the donor molecule to the excited state of the acceptor molecule; at the same time, an electron from the acceptor molecule ground state may move to the donor molecule ground state. This technique is quite efficient for distances of less than 1-2 nm.

3.6 Intramolecular and Intermolecular charge transport

The transfer of charges in conjugated polymers at the nano and micro scale is based on two phenomena:

- Intramolecular: Transport of the charges into the molecule.
- Intermolecular: Transport of the charges between distinct molecules.

Considering at first the intramolecular charge transport, the electron structure of a molecule can be thought structured as a small lattice in which the electron is free to move within the molecular orbital[121]; in a 'molecular lattice', the electron can only move in one direction and without colliding with anything else due to the anisotropy and small size of the molecule[122]. Thus, the molecule may be thought of as a one-dimensional potential well with distinct energy levels; in the absence of external stress, the electron can remain within the potential walls, while retaining its energy

and momentum and avoiding collision. The Landauer Model describes the charge transfer in a one-dimensional system such as a molecule[123]: quantum resistance in a one-dimensional lattice linked between two metallic electrodes to which a voltage is supplied is theoretically constant and independent of conductor length.

Intermolecular transport is a mechanism that enables charges to travel across molecules due to the overlapping orbitals[124]. In an organic semiconductor, the situation is entirely different from in a conventional semiconductor, in fact typical characteristics of the former are the following:

- Large lattice: Typically, the organic molecules, polymers, and groups of molecules that comprise the lattice are large.
- Weak bond: Van Der Waals bonds between molecules interact in a short-range manner.
- Polaron: Charge transport is often based on polarons, and the charge is confined within a single molecule; the polaron deforms the 'molecular lattice' and therefore the energy required to move the polaron is linked to both the elastic lattice deformation and the carrier electrostatic energy.
- Small mobility: Organic semiconductors have extremely low mobility.

Carriers are confined in distinct energy levels as in the VHR model, although they can travel across them. These levels are separated by a potential barrier, and the carrier can jump between them by three mechanisms, as shown in Figure 47:

- Tunnel effect: The likelihood of tunnelling decreases exponentially with the breadth of the barrier, so the acceptor energy state cannot be located at a large distance from the donor energy state.
- Temperature: Phonons provide the energy required to compensate for the variation in energy levels.
- External electric field: The electric field bends the lattice energy band, allowing carriers to readily transition to the next energy level.
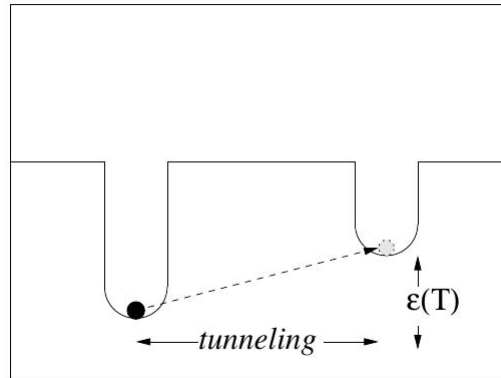
Figure 47: Phono-assisted Tunnelling mechanism: through quantum mechanical tunnelling and with sufficient thermal energy, an electron can travel to another energy state.

3.7 Effective conductivity models in polymer composites

Figure 48 is a flowchart illustrating the many classifications of analytical-mathematical models[125], which may be classified into three categories:

(1) (ROM) Empirical mixing rule models like general mixing rule and the Lichtenecker models.
(2) Percolation theory models such as McLachlan's power-law model, Kirkpatrick's and Zallen's, Mamunya's shell structure, Malliaris' and Turner's models.
(3) Mathematical models such as the Maxwell model.

Modelling and characterization of electronic conductivity in 3D printed
PEGDA:PEDOT polymer composites - High frequency applications

83
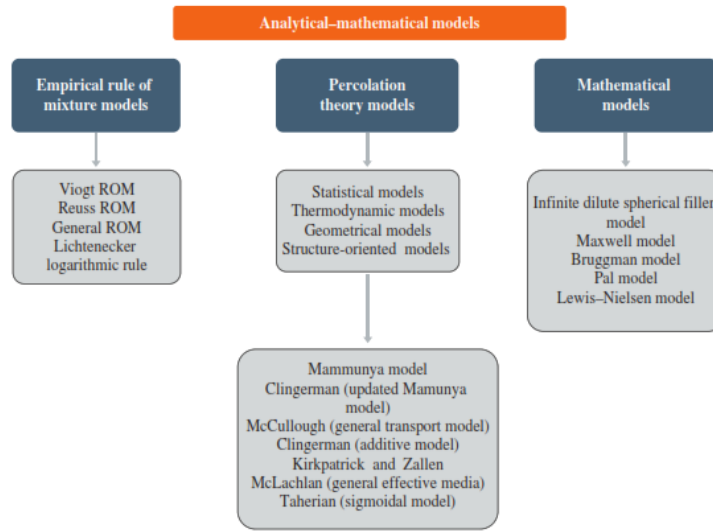
Figure 48: Analytical-mathematical models classification in polymer-based
composite materials based on the electrical conductivity.

3.7.1 Empirical mixing rule model

As implied by the name, in composite materials the electrical conductivity may be
expressed using Eq. 25 as mixing rule:

$$\text{Eq. 25:} \quad P_{composite} = \phi \cdot P_{filler} + (1 - \phi) \cdot P_{matrix}$$

P is an intrinsic property of the polymer (e.g. conductivity) which follows the
mixing rule and ϕ is the volume percentage of the filler in the composite[125].

3.7.2 General mixing rule model

The general rule of mixing is described below in Eq. 26[125]:

$$\text{Eq. 26:} \quad \sigma^n = \phi \cdot \sigma_d^n + (1 - \phi) \cdot \sigma_m^n$$

where the electrical conductivities of the matrix, the dispersed phase and the
composite are respectively σ_m, σ_d and σ.

3.7.3 Lichtenecker model

This model, expressed in Eq. 27 is a logarithmic representation of the mixing rule[125]:

$$\text{Eq. 27:} \quad \log(\sigma) = \phi \cdot \log(\sigma_d) + (1 - \phi) \cdot \log(\sigma_m)$$

where the electrical conductivity of the matrix is σ_m, σ_d is the conductivity of the dispersed phase and σ that related to the composite. This semi-empirical model is valid for homogenised mixtures of different conductivities.

3.7.4 Mathematical models − Maxwell model

Maxwell[126] used the effective medium technique to create an equation (Eq. 28) to model the final conductivity in particle composites: σ_d is the conductivity of filler spheres and σ_m of the matrix.

$$\text{Eq. 28:} \quad \left(\frac{\sigma - \sigma_m}{\sigma + 2\sigma_m} \right) = \phi \left(\frac{\sigma_d - \sigma_m}{\sigma_d + 2\sigma_m} \right)$$

Using this equation, it is possible to evaluate the total conductivity of particle composites materials, σ, as in Eq. 29:

$$\text{Eq. 29:} \quad \sigma_r = \frac{\sigma}{\sigma_m} = \left(\frac{1 + 2\phi \left(\frac{\lambda - 1}{\lambda + 2} \right)}{1 - \phi \left(\frac{\lambda - 1}{\lambda + 2} \right)} \right) \quad ; \quad \lambda = \frac{\sigma_d}{\sigma_m}$$

3.7.5 Percolative model – Percolation threshold

The correlation between the filler volume fraction with the composite conductivity follows the mixing rules, implying that by adding the filler, the composite conductivity rises linearly. However, this relationship is approximately linear in a specific region although it exhibits a sigmoidal shape globally[127].

Considering an electrically insulating matrix, if the conductive filler volume fraction steadily increases, consequentially the mean separation distance between conductive particles would be high for extremely low filler loadings, whereas when

Modelling and characterization of electronic conductivity in 3D printed
PEGDA:PEDOT polymer composites - High frequency applications

85

a sufficient amount of filler is added, the filler particles form a conductive channel through the entire material because they get closer. The filler volume fraction reaches the 'percolation threshold', the first conductive path through the polymer bulk is formed. Beyond this critical filler concentration value, the composite conductivity varies by many orders of magnitude with a minor variation in the filler content, since a new route is generated with a small increase in the amount of the filler value[128]. A further increment with high filler loading leads to the formation of a 3D network of conductive paths, till saturation when the high conductivity will be less sensitive to small volume fraction variations; thus, increasing the filler value does not result in an increase in new paths, but also in paths connecting together via branches, which has little effect on the electrical conductivity of the composite (Figure 49). It should be highlighted that the conductivity exponential rise occurs when the increment in the filler volume fraction results in the development of a new channel that does not link the existing paths. Conductivity changes less with filler volume fraction below and above the percolation threshold, but rapidly rises near the threshold[129][130].
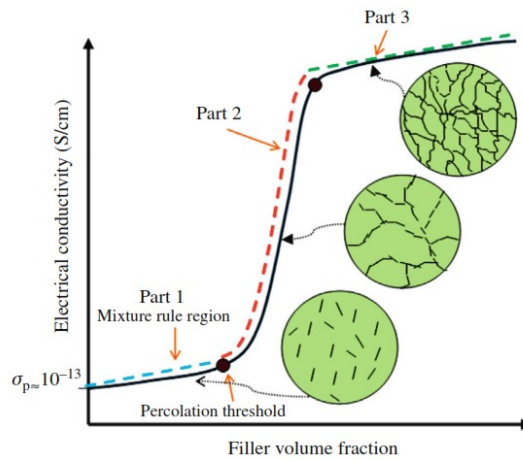
Figure 49: Electrical conductivity of polymer/carbon composites as a function of filler volume percent for the development of conductive networks through the carbon filled composite[131].

3.7.6 Percolative model – Tunnelling effect

Two conductive inclusions may produce an electrical contact through either mechanical contact or electronic tunnelling processes. The arise of the composite

conductivity in the percolation mechanism is based on two types of concurrent processes: quantum tunnelling and the formation of conductive networks. The former is responsible for the arise of the nanoscale conductivity and the latter for the microscale[132]. According to quantum mechanics, electrons in an insulated matrix can jump short distances (i.e. less than 10 nm) between neighbouring fillers and the tunnelling conductivity has been demonstrated in several investigations below the percolation threshold, where there is no contact between the fillers, to be the major factor determining the exponential rise of the conductivity in insulating polymers loaded with conductive inclusions. The second mechanism is dominant at filler loadings over the percolation threshold, where there is contact between the fillers[133].

3.7.7 Classification of Percolative models

There are several elements that affect the percolation concentration, the most significant of which are the filler interactions with the matrix, shape and distribution. According to these parameters and percolation, several types of analytical models have been proposed[134]:

(1) Statistical models such as the McLachlan model and the power-law model.
(2) Thermodynamic models such as the Kirkpatrick's and Zallen's model and the Mamunya's shell structure model.
(3) Geometric models such as the Malliaris' and Turner's model.

3.7.7.1 McLachlan model

A generalized mixing rule was presented by McCullough[125] to evaluate the electrical transport characteristics of composite materials. This rule incorporates a structural variable taking into account the concentration of inclusions. McLachlan's general effective media (GEM) model[135] is expressed in Eq. 30:

$$\text{Eq. 30:} \quad \frac{f\left(\sigma_l^{\frac{1}{t}} - \sigma^{\frac{1}{t}}\right)}{\left(\sigma_l^{\frac{1}{t}} + \{f_c(1-f)\}\sigma^{\frac{1}{t}}\right)} + \frac{(1-f)\left(\sigma_h^{\frac{1}{t}} - \sigma^{\frac{1}{t}}\right)}{\left(\sigma_h^{\frac{1}{t}} + \{f_c(1-f_c)\}\sigma^{\frac{1}{t}}\right)} = 0$$

where f denotes the conductive filler volume fraction, f_c denotes the percolation threshold, σ_l denotes the insulating matrix conductivity, σ_h denotes the conductive filler conductivity, σ the composite conductivity and t denotes a phenomenological exponent.

3.7.7.2 Power law model

The power law model is used to calculate the conductivity of nanoscale percolative composites. It is based on classical percolation theory. While some experimental validations of this law revealed the goodness of this formula, others demonstrated that the approximation is not valid, since not all the phenomenological parameters that are considered to affect the composite are taken into account. Additionally, in the power law equation the electrical conductivity prior to the percolation threshold is neglected and consequentially the distinction between the two conductivity processes[136].

On the upper percolation threshold, for filler volume content in the $\varphi > \varphi_c$ area, where t is a crucial exponent equal to 1.6-1.9[137], it may be expressed[125] as in Eq. 31:

$$\text{Eq. 31:} \quad \sigma = (\varphi - \varphi_c)^t$$

For conductive composites including dispersed fillers, the power law equation does not match the experimental data. This is because this equation does not account for the system structural characteristics, such as particle shape or polymer-filler interaction[138].

3.7.7.3 Kirkpatrick's and Zallen's model

This model (Eq. 32) is a comparable to the power law mode:

$$\text{Eq. 32:} \quad \sigma = \sigma_0 (V - V_c)^s$$

where σ is the conductivity of the mixture, σ_0 is the conductivity of the filler particles, V is the volume fraction of the filler, $V_c = p_c^{site} v$ is the volume percolation

concentration, s is a quantity indicating the strength of the conductivity increase above V_r, and V is the filling factor of the unit cell of a particular point arrangement. According to the literature[139], the values of V_r and s should be invariant in terms of the lattice's dimensions. This approach is applicable to a broad variety of metal/polymer combinations[140], inorganic mixes[136] and intrinsically conductive polymer (ICP) mixtures[141].

3.7.7.4 Mamunya's shell structure model

Thermodynamic models are based on the interfacial interaction between the matrix and the filler, in which the formation of the percolative network is a phase separation process[142] led by surface energies.

Mamunya[143] presented a thermodynamic model aimed to characterize electric conductivity of the shell structure in a polymer matrix with distributed fillers. The composite consists of polymer particles with a diameter D and conductive filler particles with a diameter d, so that $D \gg d$. The percolation threshold value φ_c was shown to be dependent on the spatial distribution (segregated or random), the aspect ratio and the shape of the particles. A linear correlation between the packing factor and the percolation threshold is observed because of the lack of filler-polymer interactions: $\varphi_c = X_c F$.

$$\text{Eq. 33: } \varphi_{cs} = X_c F_s = \frac{X_c F}{K_s} = \left[1 - \left(-\frac{nd}{d} \right)^3 \right]$$

$$K_s = \frac{\varphi_{loc}}{\varphi} = \frac{F}{F_s}$$

φ_{loc} represents the true filler content at the localization site, and n represents the filler layer number. Packing factor F_s and the related φ_{cs} percolation threshold values are used to describe systems in which the filler is metallic and it has the shape of shell structure and the spatial distribution is segregated, as reported in Eq. 33. Considering a random spatial distribution of the filler, previous values are lower. The presented model[144] takes into account both the polymer surface energy and the aspect ratio of the filler, as in Eq. 34[145]:

Eq. 34:
$$\begin{cases} Log(\sigma) = Log(\sigma_h) + \dfrac{\phi}{\phi_c}\left(Log(\sigma_{\phi_c}) - Log(\sigma_h)\right) & \text{for } \phi < \phi_c \\[3mm] Log(\sigma) = Log(\sigma_{\phi_c}) + \left(Log(\sigma_{Max}) - Log(\sigma_{\phi_c})\right)\left[\dfrac{\phi - \phi_c}{F - \phi_c}\right]^k & \text{for } \phi \geq \phi_c \end{cases}$$

where the interfacial tension is γ_{pf}, the percolation threshold is ϕ_c, the filler volume fraction is ϕ, F is the maximum packing fraction and σ_{Max} denotes the conductivity at $\phi = F$.

$$k = \frac{R\phi_c}{(\phi - \phi_n)^n}$$

$$R = D + G\gamma_{pf}$$

R and n are additional parameters, whereas D and G are constants. The Mamunya model exhibits a high degree of agreement between predicted and experimental values for carbon black in a variety of polymers. This does not apply to other forms of fillers. n is around 0.75. According to further sources[146], the surface energy between the filler and the polymer may be calculated, in Eq. 35, as follows:

$$\text{Eq. 35: } \gamma_{pf} = \gamma_p + \gamma_f - 2(\gamma_f \cdot \gamma_f)^{\frac{1}{2}}$$

The thermodynamic Nielsen's model employed for metallic particles in the case of $\phi \geq \phi_c$, was partially derived by Mamunya, which has been reported in Eq. 36[147]:

$$\text{Eq. 36: } Log(\sigma) = Log(\sigma_c) + \left(Log(\sigma_F) - Log(\sigma_c)\right)\left[\frac{\phi - \phi_c}{F - \phi_c}\right]^k$$

$$k = \frac{K\phi_c}{(\phi - \phi_c)^{\frac{3}{4}}}$$

$$K = 0.28 - 0.036\gamma_{pf}$$

3.7.7.5 Geometrical percolation model

These percolative models are concerned with the phenomena of percolation in premixed dry sintered mixture of insulating and conductive powder particles. All

these models are based on the deformation of insulating particles during the sintering process towards a more cubic-like shape. The insulating powder particles are deformed into more or less regular cubic particles, resulting in a surface packaging of these conductive powder particles.

Chapter 4

Charge Transport Mechanism

Prigodin and Efetov predicted the existence of four distinct conductivity modes for a random network of linked one-dimensional metallic wires. At first, the material exhibits a range-hopping conductivity. The following form of transit is hopping between nearby states, followed by correlation areas. Finally, it is possible to achieve band transport[148]. The variable range hopping behaviour is represented by Mott's temperature model. Localized and extended states coexist in heavily doped conjugated polymers. There is a critical energy E_c that divides localized and extended states. The electrical behaviour that results, is dependent on the Fermi level E_F location, relative to the mobility edge E_c. PEDOT:PSS may be thought of as a disordered conjugated polymer that is heterogeneously disordered[149]. The high degree of disorder present in PEDOT:PSS distinguishes it from other conductive polymers such as polyacetylene or polypyrrole.

4.1 Band and Hopping charge transport

Conjugated polymers with high conductivities have been compared to disordered metals on the verge of a metal–insulator transition. Typically, DC conductivity is thermally activated, lowering as the temperature decreases, or at least to a point below room temperature.

If the Fermi level is contained inside the extended states, the conductivity is positive as T approaches zero, as charge transfer does not need thermal activation. Although the number of mobile charge carriers is relatively small, they nonetheless dominate the material electrical behaviour. Additionally, as defined in Eq. 37, the slope of the decreased activation energy, $W(T)$, over the temperature may be used to identify whether a conjugated polymer is semiconducting or metallic:

$$\text{Eq. 37:} \quad W(T) = \frac{\Delta E(T)}{kT} = \frac{d\ln(\sigma)}{d\ln(T)}$$

If the Fermi level is in the area of extended states, the slope of the plot of W against T is positive, σ_{dc} is finite as T approaches zero, and the material is in the metallic regime[44]. If the disorder is sufficiently high to place the Fermi level in the area of localized states, the carriers exhibit hopping behaviour, σ approaches zero at low temperatures, and the material is in an insulating or semiconducting state. In this situation, the slope of the plot of W versus T is negative. At T = 0 K, the motion of electrons or holes in a perfect crystal may be characterized in terms of band theory[150], and mobility is proportional to the bandwidth, which is linked to the transfer integrals t. The transfer integra is small in organic materials, with bandwidths ranging from 50–500 meV. Mobility is temperature dependent as follows in Eq. 38:

$$\text{Eq. 38:} \quad \mu \propto T^{-n} \ ; \ 0 < n < 3$$

The reason for this is mostly due to electron–phonon and electron–electron interactions, as well as impurities. When the mobility follows empirical Eq. 38, the band model is widely recognized as adoptable. Generally, band transport can be considered when the mobility reaches $\sim 5 \ cm^2 V^{-1} s^{-1}$. The band model was used to describe carrier mobilities in a naphthalene crystal throughout the temperature range 4–300 K[151]. At normal temperature, the mobilities of small molecule organic semiconductors are on the order of $1 \ cm^2 V^{-1} s^{-1}$, indicating that the band model is insufficient[152]. Indeed, one of the primary limiting characteristics of organic semiconductors is their low carrier mobilities, which typically vary between $\mu \cong 10^{-10} - 10 \ cm^2 V^{-1} s^{-1}$. These values are hundreds of orders of magnitude less than those observed in inorganic semiconductors, which range between $\mu \cong 10^2 - 10^4 \ cm^2 V^{-1} s^{-1}$. This discrepancy is explained by the fact that charge carrier transport is a hopping mechanism in disordered organic semiconductors. The transport characteristics of a large number of small molecule organic semiconductors are attributable to the mobility of electron or hole polarons.

Numerous phenomena have been proposed that contribute to the complexity of charge transport mechanisms in polymers[153]. However, these issues may be resolved by treating band transport as a mechanism for intrachain motion alone and hopping as a mechanism for both intrachain and interchain motion.

Modelling and characterization of electronic conductivity in 3D printed
PEGDA:PEDOT polymer composites - High frequency applications

93

4.1.1 Coherent charge transport

When the concept of conjugation is addressed, band transport is the mechanism that should be expected. Due to the effect of the applied field on the charge wave functions, polarons move along the chain in the direction defined by the field. Band transport can only generate a limited contribution to conduction in polymeric materials. Even if a pure polymeric crystal could be synthesized, band transfer would be limited. As a first approximation, there is no need to assume that the chain is parallel to the applied field; a polaron on a chain that is parallel to the applied field cannot contribute to band transport without jumping onto another chain, consequentially for this reason polaron transport will be interrupted in a flawless crystal by phonons. As these lattice vibrations increase with temperature, the resistivity of the material also increases. Given that polarons may be dispersed by phonons, the mobility of carriers is temperature dependent, and empirically, the carrier mobility scales as in Eq. 38. Indeed, the Einstein relation may be used to demonstrate that a polaron mobility is anticipated to be inversely proportional to its temperature, as expressed in Eq. 39:

$$\text{Eq. 39:} \quad \mu = \frac{De}{k_B T}$$

given that, the charge carriers diffusion coefficient D does not exhibit a complex temperature dependency. The diffusion coefficient is defined as $D = v\lambda_m$, where λ_m denotes the mean free path and v denotes the drift velocity. The issue is with λ_m, which is temperature dependent; at higher temperatures, more phonon modes with shorter wavelength lattice vibrations are generated, reducing the polaron mean free path prior to scattering. At temperatures above the Debye temperature, the quantity of phonons in a non-metallic crystal rises linearly with temperature, resulting in an inversely proportional diffusion coefficient and a mobility scaled by $\mu \propto T^{-2}$. It must be noted that the mobility[154] is predicted to be slightly more temperature dependent than T^{-1}, i.e. $v > 1$.

Rather than real polymeric materials, this temperature behaviour of band transport is more effectively studied on small organic compounds that can form flawless crystals. The existence of traps significantly complicates the temperature dependence of carrier mobility in polymeric systems. Even in small-molecule organic crystals, the dispute over the real contribution of band transport to conduction is still open, owing to reports of very small carrier mean free pathways

in these crystals that are lower than predicted even when phonon scattering is taken into account.

The presence of traps in a material does not exclude the possibility of a band transport mechanism, since the mobility may be altered to accommodate this. In this case, the charges are considered to move in response to an applied electric field. When they become trapped, they require a specific amount of thermal energy to escape, which should follow an Arrhenius-type rate behaviour[155]. Thus, the modified mobility is given by Eq. 40:

$$\text{Eq. 40:}\quad \mu = \mu_0 \exp\left(\frac{-\Delta\varepsilon_t}{k_B T}\right)$$

Where $-\Delta\varepsilon_t$ denotes the depth of the trap, which typically indicates that the trap energy is somewhere within the band gap, and μ_0 denotes a constant that depends on the degeneracy of the trap states (i.e., how many states exist with a trap energy $\Delta\varepsilon_t$ less than the LUMO for an electron or greater than the HOMO for a hole). Clearly, only polarons trapped at energies close to or less than $k_B T$ from the LUMO (or HOMO, depending on the charge carrier type) have a reasonable chance of being released rapidly enough to contribute to charge transport. Multiple trapping and release band transport is the name given to this modified band transport process. There is no assurance that the polaron will not end up on a different chain after being freed from a trap and this multiple trapping and release model makes no distinction between the two. Indeed, because the temperature dependency of the behaviour is analogous to hopping, this model neglects the difference between the two processes.

4.1.2 Incoherent charge transport

Transport in doped semiconductors happens not as a consequence of free carriers, but as a result of charge transfer between impurity states at sufficiently low temperatures. When the concentration of impurities is large, the impurity states significantly overlap. In this situation, the electron wave functions of all the impurities are shared; this is referred to as delocalization. Then, it is frequently stated that an impurity band forms and conduction occurs inside this "band." At low concentrations, the impurity states overlap very slightly, the electron wave functions are intensely localized, and conduction occurs through electron hopping between occupied and empty localized donor states.

Modelling and characterization of electronic conductivity in 3D printed
PEGDA:PEDOT polymer composites - High frequency applications

95

Figure 50 illustrates four temperature ranges, each of which is defined by a distinct conduction type. The ranges A and D are critical when comparing electron transport across the conduction band at elevated temperatures to hopping transit at low temperatures. B and C will be explored in later in this thesis. As seen in Figure 51, the conduction of range A is characterized by the thermal activation of electrons into the conduction band. The semiconductor approaches region D, where hopping conduction begins, as the temperature decreases. There is insufficient thermal energy in the hopping temperature range to raise the electrons to the conduction band. However, as seen in Figure 52, thermal energy can enable electron transport via small energy jumps on the empty impurity levels inside the band gap.
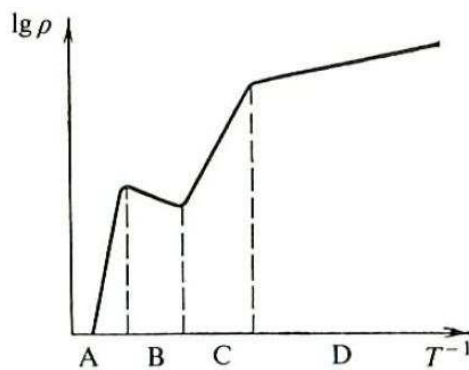
Figure 50: The logarithm of resistivity as a function of inverse temperature may be split into four areas A - Range of intrinsic conduction. B - The impurity conduction saturation range. C - Freeze out range; contaminants capture the free carriers. D - Range of hopping[156]
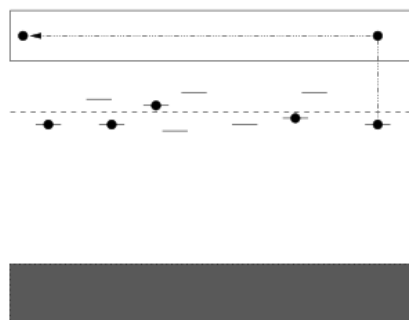
Figure 51: High temperature conduction mechanism: thermal energy lifts electrons into the conduction band.
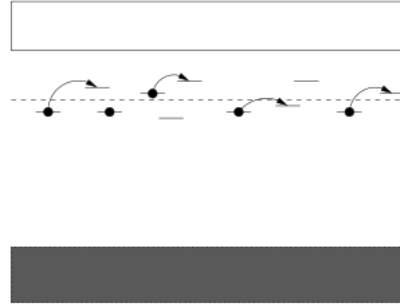
Figure 52: Low temperature conduction mechanism: electrons hop between impurity
energy levels using a significantly less amount of thermal energy.

The D region can be further subdivided into two sections: the electron transport in
the leftmost section of the hopping range D in Figure 50 is mostly due to closest
neighbour hops on impurity energy levels in the semiconductor band gap[111].
Thermal energy, frequently represented as ε, is used to trigger the leaps since it is
constant down to a certain temperature limit. It is feasible to demonstrate that when
the temperature is reduced farther to the rightmost half of area D, the activation
energy $\varepsilon(T)$ becomes temperature dependent and the average electron jumping
length R increases[156]. Generally, this effect is referred to as Variable Range
Hopping.

4.1.3 Charge and Polaron hopping transport

When the transfer integral t is small in comparison to the other energies, as is the
case when disordered processes are involved, the band model cannot accurately
represent the transport characteristics. Transport becomes disorganized, and charge
carriers jump from site to site, as previously stated.

Conductivity in a large number of disordered semiconductors below the metal–
insulator transition with localized states inside the band gap is due to a hopping
process in which charge carriers tunnel between the localized states at various
locations aided by electron–phonon interactions. Mott's generalized law for variable
range hopping[157] describes this process as follows in Eq. 41:

$$\text{Eq. 41:} \quad \sigma(T) = \sigma_0 \exp\left(-\left(\frac{T}{T_0}\right)^\gamma\right)$$

σ_0 depends on the temperature but that dependence is usually constant compared to the temperature dependence of the exponential term. T_0 is given by $T_0 \sim \beta/[k_B N(E_F) L_{Loc}^3]$ where β is a numerical factor in the range 16–22, and $N(E_F)$ is the density of localized states at the Fermi level and L_{Loc} is the localization length. The exponent γ depends on the dimensionality, D, of the transport process and is given by $\gamma = 1/(1 + D)$. It is $\gamma = 1/4$ for hopping in three dimensions and $\gamma = 1/2$ for 1D hopping and in disordered conducting polymers when the conductivity is governed by charge-limited tunnelling between metallic grains, as well as for 3D hopping when electron–electron interactions are taken into account [6]. At high temperatures, the hopping is to the nearest neighbours and the conductivity will follow the simple activated form with $\gamma = 1$ as in crystalline semiconductors.

To understand the reason of the temperature dependence in Mott's law, it must be considered that the addition or removal of an electron causes a local deformation of the lattice or molecule associated with the electron or hole in conjugated polymers with a non-degenerate ground state and in small molecule materials. The energy difference between a molecule pre- and post-distortion states is referred to as the polaron binding energy, E_{pol}. The activation energy required for charge transfer is half that required for polaron binding[158]. If the phonon energy is negligible in comparison to the thermal energy $k_B T$, the hopping rate is given by Eq. 42:

$$\text{Eq. 42:} \quad k_{ET} = \frac{t^2}{\hbar} \left(\frac{\pi}{2E_{pol} k_B T} \right)^{\frac{1}{2}} \exp \left(-\frac{E_{pol}}{2k_B T} \right)$$

where t is the transfer integral and E_{pol} is half of the lattice reorganization energy. The mobility can now be derived taking into account that it is related to the diffusion constant D, through the Einstein equation $\mu = eD/k_B T$, and D depends on the hopping rate, k_{ET}, as $D = \frac{1}{2n} k_{ET} a^2$ in which n is the dimensionality of the system and a is the distance between sites. For a three-dimensional system, $n = 3$, the mobility is expressed in Eq. 43:

$$\text{Eq. 43:} \quad \mu = \frac{eat^2}{6\hbar(k_B T)^{\frac{3}{2}}} \left(\frac{\pi}{2E_{pol}} \right)^{\frac{1}{2}} \exp \left(-\frac{E_{pol}}{2k_B T} \right) = \mu_0 \exp \left(-\frac{E_{pol}}{2k_B T} \right)$$

This approximation is reasonable only at intermediate temperatures, when the exponential factor is dominant, that is, if $\frac{E_{pol}}{2k_B T} \gg 1$. At high temperatures, the pre-

exponential factor containing $T^{-\frac{3}{2}}$ may be dominant. For a typical value of $E_{pol} =$ 100 meV, the $T^{-\frac{3}{2}}$ is dominant above 600 K. At low temperatures, and when the electron–phonon interaction is small, the mobility may be better described by the energy band model, where $\mu \propto T^{-n}$ It is therefore possible to have a temperature dependent mobility, which goes as T^{-n} at low temperatures, passes through an intermediate temperature range where it is controlled by thermally activated hopping, $\mu \propto T^{-E/k_B T}$, and goes as $T^{-\frac{3}{2}}$ at high temperatures.

4.1.4 Miller-Abrahams hopping model

Hopping is a thermally activated quantum-mechanical tunnelling phenomenon in which charge carriers hop between monomers rather than traveling coherently (Figure 53). While it is unavoidable that band transport plays a role in charge transfer in both polymeric semiconductors and their small molecule organic equivalents, it is apparent that hopping processes contribute far more to carrier mobility. For conjugated polymers, a combination of the two is more plausible, as a pure hopping mechanism is likewise improbable. It should be emphasized that intrachain transport can also involve hopping, even for conjugated polymers. A kink or flaw in a conjugated polymer allows charge to flow from one end of the chain to the other without traveling the entire length of the chain (Figure 53a)[159]. Similarly, many non-conjugated materials have excellent semiconducting properties, with charge transfer occurring only via hopping. PVK, or Poly(Vinyl Carbazole), is arguably the simplest example of a polymer in which only hopping transport occurs (Figure 53c)[160]. Transport in such a polymer can occur between neighbouring chains or along the same chain, either by hopping from one portion to the next as seen in Figure 53a, or it can occur along the chain, simulating coherent band transport.

Naturally, in PVK the carrier cannot travel coherently since the chain is not conjugated, but the hole may travel between the aromatic rings without engaging the chain backbone.
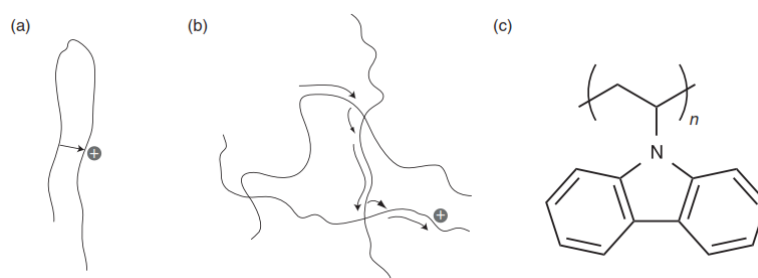
Figure 53: One distinction between hopping and coherent (band) transmission is that the charge carrier does not have to go between monomers. This does not prohibit intrachain transfer through a hopping mechanism, which may occur in the presence of chain defects (a). A combination of coherent transport and hopping is conceivable in conjugated polymers, with the charge carrier hopping from one chain to the next (b). Certain polymers, such as PVK (c), can only move through hopping due to their lack of a conjugated backbone.

Hopping transport does not provide as high mobilities, respect to pure band transport. One reason for the reduced mobility is the requirement for activation energy during the hopping process. In the case of PVK, delocalization happens both on and between the two aromatic rings, for this reason a hole must have sufficient energy to leave one and travel to another carbazole unit. As a result, hopping transport becomes more efficient as temperature increases, whereas band transport loses mobility due to phonon dispersion. The easiest approach to associate an electronic motion with phonons is to realize that phonons add energy to the system altering the charge carrier energy levels. If a hole on a carbazole unit localized in its HOMO level, is considered, when a phonon enters, it raises the energy of the hole, allowing it to lower its energy by relocating to a neighbouring carbazole.

The probability of hopping occurring is dependent on the energy difference between the two locations, as well as their distance from one another. Miller and Abrahams provided a simple theoretical model for this hopping process for transport in doped inorganic semiconductors, but there is no fundamental reason why this model cannot be extended to organic materials as well[161]. To apply the Miller–Abrahams model to polymeric systems, each monomer must be considered basically isolated from its neighbour, even if they share a chain. This must be true for polycarbazoles, as the monomers are linked via an unconjugated backbone. The Miller–Abrahams phonon-assisted hopping rate is provided by Eq. 44:

$$\text{Eq. 44:} \quad \gamma_{ij} = \gamma_0 P(E_i)\big(1 - P(E_j)\big) \exp\left(-\frac{E_j - E_i}{k_B T}\right) \exp\left(-\frac{2r_{ij}}{a}\right)$$

where r_{ij} is the inter-site separation distance between a donor pair, E_i and E_j are the donor and acceptor respective energy levels, a is the spatial extension of the states involved in the hopping transport, referred to as the localization radius, γ_0 is a constant, and P represents the Fermi–Dirac probability distribution. The hopping rate is predicted to decrease exponentially as the energy of the acceptor state and the distance between them increase.

Figure 54 depicts a schematic representation of the hopping transport in PEDOT. Holes in the polaron/bipolaron band are promoted to the valence band by phonon energy and move across the polymer film via phonon-assisted state hopping, which might be associated with the same chain or with distinct chains.
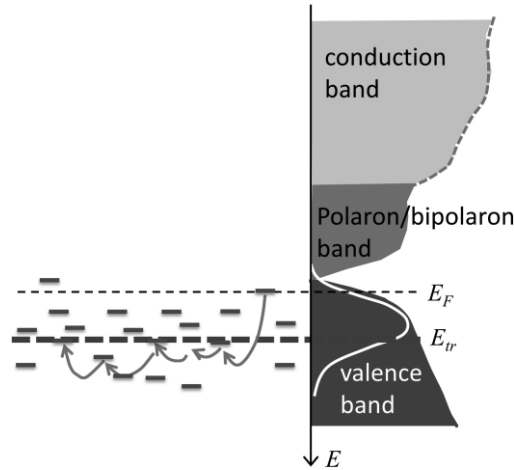
Figure 54: Hopping transport in PEDOT is illustrated using a schematic design. The left panel depicts a charge carrier bouncing between valence band locations with varying energies. The right panel illustrates the band structure of a PEDOT film that has been doped. E$_{tr}$ is the transport energy at which charge carriers are most effectively transported.

The exponent including $E_j - E_i$ is a straightforward Boltzmann factor, but the exponential containing r_{ij} is a measure of the degree of overlap between the electronic wave functions[162]. If the donor has a higher energy level than the acceptor, i.e. if $E_i < E_j$, this exponential is replaced by unity, resulting in Eq. 45:

$$\text{Eq. 45:} \quad \gamma_{ij} = \gamma_0 P(E_i)\big(1 - P(E_j)\big) \exp\left(-\frac{2r_{ij}}{a}\right)$$

The Fermi–Dirac probability distributions denote the chance that a charge carrier exists in the donor site and is accessible to hop to the acceptor, as well as the probability that an acceptor state exists to receive that charge carrier. The Miller-Abrahams model is significant because it establishes a connection between distance, energy and hopping rate. However, this model is difficult to apply to actual systems due to the disorder characteristic of non-crystalline materials, which makes it difficult to link r_{ij} to a crystalline lattice location. Similarly, defining the energy states E_i and E_j is challenging since they are affected by phonons. To account for the dispersion of energies and distances, Bässler added a gaussian density of states in the energy levels (as well as a degree of position disorder) that is likewise gaussian[163]. The gaussian density of states may therefore be calculated as follows in Eq. 46:

$$\text{Eq. 46:} \quad g(E) = \frac{N}{\left(2\pi\sigma_g\right)^2} \exp\left(-\frac{E^2}{2\sigma_g^2}\right)$$

where N is the total number of states and σ_g denotes the width of the Gaussian density of states. In the free electron model of metals, all electrons are accessible for conduction, and their energies are assigned based on the availability of states at a particular electronic wave vector, starting with the lowest available wave vector. The distinctions between this hopping mechanism and the coherent transport mechanism must be carefully considered in this situation.

The wavelengths of charge carriers are largely governed by structural flaws and the availability of sites for them to hop. Due to disorder in the surrounding medium, the charge carrier's wave function is effectively confined inside a restricted lattice. The number of accessible states rises in a manner similar to that of crystals, starting with a finite number of low-energy states, which increases as shorter wavelengths are reached, owing to rising degeneracy. However, at the shortest wavelengths, which are equivalent to the distance between monomers, disorder persists, preventing a fast cut-off in the density of states distribution. Similarly, because perfect crystals are not considered, a distribution of nearest neighbour distances will exist, implying that some carriers would experience different maximum wave vectors than others.

These two effects, HOMO spread and positional disorder, are referred to as diagonal and off-diagonal disorder, respectively, and are defined by gaussian deviations from the mean HOMO by σ_g or position by Σ. As a result, the final density of states is different from the preceding $g(E)$.

Bässler suggested the carrier mobility provided by Eq. 47, to represent the effect of these many parameters[164], where E is the electric field and μ_0 is a constant:

$$\text{Eq. 47:} \quad \mu(E,T) = \mu_0 \exp\left[-\frac{2}{3}\left(\frac{\sigma_g}{k_B T}\right)^2\right] \exp\left\{\left[\left(\frac{\sigma_g}{k_B T}\right)^2 - \Sigma^2\right]\sqrt{E}\right\}$$

Additionally, the LUMO is affected by this disorder in energy levels in the same way as the HOMO, as seen in Eq. 47. For low fields, the second exponential can be omitted and the temperature dependency is governed by the first component, resulting in linear logarithmic graphs of mobility as a function of the square of the inverse temperature.

One implication of Eq. 47 is that the mobility can decrease as the field increases if Σ^2 is sufficiently big, i.e. $\Sigma > \sigma_g/k_B T$. Since for the most systems with disorder, the effect of growing disorder diminishes, Σ^2 is often limited to 2.25, as any further abnormality is not viewed as producing further reductions in mobility. Nonetheless, the model is not complete and does not account for the effect of polarons on their surroundings or for actual evidence that mobility increases with increasing carrier density.

4.1.5 Hopping conduction in the random resistor network model

Miller and Abrahams defined the hopping rate as a function of phonon-assisted tunnelling and proposed the random resistor network model to characterize macroscopic hopping transport. Percolation theory can be used to address the random resistor network problem. Mott extended the Miller and Abrahams hopping rate and shown that a universal rule for the hopping conductivity may be derived by making a few assumptions. Efros and Shklovskii included Coulomb interactions into Mott's theory, altering his initial conclusions.

Modelling and characterization of electronic conductivity in 3D printed PEGDA:PEDOT polymer composites - High frequency applications

103
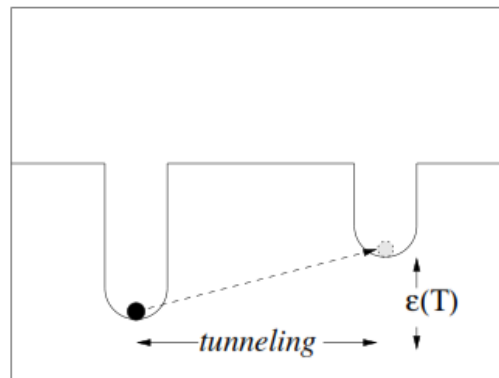
Figure 55: With the assistance of quantum mechanical tunnelling and thermal energy, an electron can travel to another impurity. The VHR model describes an electron's travel as a percolative path: the electron jumps between close energy levels to reduce the tunnel distance, but if the nearest state's energy is too high, the electron chooses to make the "longest leap" to a lower energy state.

Miller−Abrahams' concept is based on the following hypothesis: a lightly n-doped semiconductor with a low dopant concentration in the temperature range D shown in Figure 50, is considered. Due to the differences in the local electric field generated by ionized donors and acceptors, the compensation generates charged particles with distributed site energies. Due to the low dopant concentrations, there is small overlap between the wave functions of adjacent impurity sites. Anderson localization of the electron wave functions is facilitated by the impurity energy disorder and low dopant concentration.

When a donor electron is near to another ionized donor, it can tunnel into this location. The transmission of energy is accompanied by the emission or absorption of a phonon. The purpose of absorption or emission is to save energy. This is referred to as phonon aided tunnelling. This type of transfer is seen in Figure 55. The hopping conduction is the product of several such transitions in succession. Prior to that, the Miller-Abrahams hopping rate is specified[161]. In the absence of an electric field, charge transport is detailed and so there is no net current. When a weak electric field exists, more transitions will occur against the field to locations with lower field energy than would occur in the other direction, resulting in a net current proportional to the electric field. A rough estimate of the current yields a value for the resistance R_{ij} of a particular donor pair. When a large number of

occupied and unoccupied donors are combined, the system resembles a network of random resistances.

In the random resistor network model resistances are generated by approximating them using a self-consistent field. This approximation is not trivial, yet it is consistent with a large number of experimental results: donor occupation number n_i varies over time. This results in changes in the donor potentials, which varies $E_j - E_i$ as well. As a result, γ_{ij} fluctuates in time and can be estimated using time averages of the occupancy numbers $\langle P(E_i) \rangle = f_i^0$ and the single particle energies $\langle E_i \rangle = E_{m,i}^0$. Averages are perturbed by this weak electric field.

$$f_i = f_i^0 + \delta f_i \qquad E_{m,i} = E_{m,i}^0 + \delta E_i$$

These variations can be interpreted as a contribution to a local electrochemical potential drop $U_i - U_j$ between the two donors. Considering $\Gamma_{ij} = \langle \gamma_{ij} P(E_i)\big(1 - P(E_i)\big) \rangle$, the electronic current can be expressed as in Eq. 48[156]:

$$\text{Eq. 48:} \quad I_{ij} = -e\big(\Gamma_{ij} - \Gamma_{ji}\big) = \frac{1}{R_{ij}}\big(U_i - U_j\big)$$

with

$$R_{ij} = R_{ij}^0 \cdot \exp\big(\xi_{ij}\big)$$

$$R_{ij}^0 = \frac{k_B T}{e^2 \gamma_{ij}^0} \quad ; \quad \xi_{ij} = \frac{2r_{ij}}{a} + \frac{E_{ij}}{k_B T}$$

$$E_{ij} = \frac{1}{2}\Big[\big|E_{m,i} - E_{m,j}\big| + |E_{m,i} - \mu| + |E_{m,j} - \mu|\Big]$$

In a large sample, there will be several pairings with a broad range of resistances that produce a network of random resistances similar to the one seen in Figure 56. The phonon aided hopping rate and resistor network model concepts and findings resulted in a technique for calculating the effective conductivity of such materials. The two most investigated approaches were averaging the local conductance and the 'voids and chains' method, although both were wrong. The former method falls short by covering just the very low resistances that occur rarely. This enables the

conductivity of small conducting islands within a large insulating sea to be calculated.
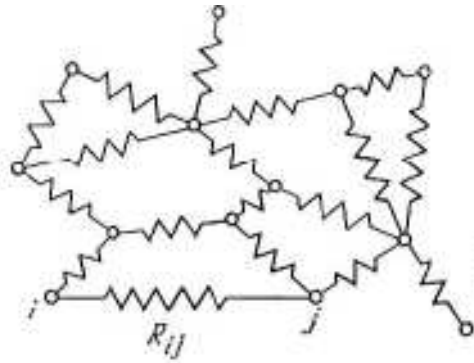
Figure 56: As a model for hopping conductivity, the Miller-Abrahams random resistor network is used[156].

The latter strategy was proposed due to the existence of a succession of separate chains of resistance. These chains might break as a result of huge voids, resulting in very high distances between impurity sites, with such high resistance, that no current can flow. The current favours voids of a particular radius in this model, as they will dominate the resistances. Additionally, the occurrence of such voids is rather unusual. This technique enables the conductivity of dielectric islands in a conducting sea to be calculated. The final conclusion about these two approaches is that they are used to determine the effective conductivity limits. The wrong assumption of both the approaches is that they overemphasize the importance of uncommon resistances[156]. Following that, a novel method of percolation was suggested, which proved to be critical in resolving the conductivity problem in a random resistor network.

4.1.6 Mott's hopping conduction in a percolative system

As seen in Figure 57, Mott's theory is based on the assumption of a constant density of states at the Fermi level, $g(\epsilon) = g(\mu)$. This means that Coulomb interactions between particles are ignored.
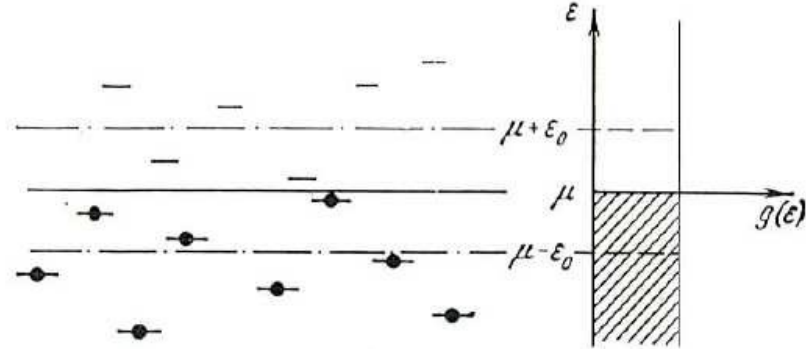
Figure 57: Constant density of states in a narrow energy interval of $2\varepsilon_0$ cantered on the Fermi level. The system is in its initial condition and no Coulomb interactions are considered.

The generic derivation of conductivity $\sigma(T)$ and average jumping length $r_m(T)$ in d dimensions will be described and it will be demonstrated that when the temperature lowers, the available thermal activation energy $\varepsilon_0(T)$ reduces as well. This indicates that only electrons in close proximity to the Fermi level μ are permitted to hop. The energy cost of an electron jump from an occupied to an empty impurity state is equal to $\varepsilon_0(T)$. Empty energy states which are $\varepsilon_0(T)$ or closer to μ are quite rare and they are separated by a bigger spatial distance. The lower the temperature, the fewer energy-affordable sites exist and their spatial dispersion is greater[165]. As a result, as the temperature decreases, the jump lengths rise.

Derivation of $\sigma(T)$

Considering a narrow energy interval with a width of $2\varepsilon_0$ centred around the Fermi level, as seen in Figure 57, when the factor of two is omitted, the electronic density of localized states per unit energy interval at the Fermi level, $g(\mu)$, remains constant, as expressed in Eq. 49:

$$\text{Eq. 49: } \quad N(\varepsilon_0) \approx g(\mu)\varepsilon_0$$

Conductivity due to hopping on impurity levels, within the energy interval may be determined by assuming that all pairs, within this interval, have an average energy difference of $\varepsilon_{ij} = \varepsilon_0$ and an average jumping length of $r_{ij} = r_m$. The hopping resistivity is then calculated in Eq. 50 as follows[166]:

$$\text{Eq. 50: } \quad \rho = \rho_0 \exp\left(\frac{2r_m}{a} + \frac{\varepsilon_0}{k_B T}\right)$$

The two variables in the brackets of Eq. 50 compete to determine whether the overlap of the wave functions or the thermal activation energy dominates the resistivity. The minimal resistivity exponent may be determined by expressing both components in brackets in terms of ε_0, differentiating them with regard to ε_0 and equating the total to zero. This relates to a scenario in which thermal activation and tunnelling between the sites both contribute equally to the resistivity. Additionally, we determine the $\varepsilon_0(T)$ of this minimum and reintroduce it into Eq. 50. Given $\varepsilon_0(T)$ expressed as in Eq. 51:

$$\text{Eq. 51:} \quad \varepsilon_0(T) \approx \left(\frac{(k_B T)^d}{a^d g(\mu)}\right)^{\frac{1}{1+d}}$$

A general expression for the temperature-dependent hopping conductivity is derived from this in Eq. 52, demonstrating that the activation energy is temperature-dependent and decreases with decreasing temperature:

$$\text{Eq. 52:} \quad \sigma(T) = \sigma_0 \exp\left(-\left(\frac{T_0}{T}\right)^{\frac{1}{1+d}}\right) \quad ; \quad T_0 = \frac{\beta}{k_B g(\mu) a^d} \quad ; \quad \sigma_0 = \frac{3e^2 \nu_{ph} g(\mu)}{8\pi a k_B T}$$

β is a numerical coefficient that contains all of the exponent missing prefactors in addition to the unknown prefactor of the density of states $g(\mu)$, T_0 is the Mott's characteristic temperature, which indicates the degree of disorder, and ν_{ph} denotes the phonon frequency ($\sim 30\ THz$). In three dimensions, $p = 1/4$. As a result, Mott's law for hopping conductivity is sometimes abbreviated as the $T^{-\frac{1}{4}}$ law. It is now self-evident that the average hopping distance increases as the temperature decreases, as stated in Eq. 53:

$$\text{Eq. 53:} \quad r_m(T) \approx a \left(\frac{T_0}{T}\right)^{\frac{1}{1+d}}$$

Finally, in comparison to conventional semiconductor theory, mobility may be described in a three-dimensional system as expressed in Eq. 54:

$$\text{Eq. 54:} \quad \mu \cong \frac{e\nu_{ph} a^2 g(\mu)}{k_B T} \exp\left(-\left(\frac{T_0}{T}\right)^{\frac{1}{4}}\right)$$

Assumptions in Mott's Law

Mott's law is based on the Miller and Abrahams hopping rate derivation, in addition to few approximations[167]. The first and most critical assumption is that the density of states around the Fermi level is constant, implying that there are no interactions between the particles. Experiments and theoretical studies demonstrate that at sufficiently low temperatures, a depletion in the density of states around the Fermi level occurs. This phenomenon is referred to as the Coulomb gap. The spacing between charged particles is generated by Coulomb interactions and has a significant effect on conductivity. The assumption that all pairings have an equal energy difference $\varepsilon_{ij} = \varepsilon_0$ and that all hops have an average distance r_m, which is not entirely accurate in terms of particles interactions.

In many materials, such as amorphous semiconductors, structural flaws are the primary source of disorder, smearing out the Coulomb gap. The experimental results in these materials are best characterized by Mott's law. Smearing of the gap can also occur as a result of elevated temperature. This proves that systems with a low degree of structural disorder are better characterized by Mott's law. Other enhanced models are applicable to high-quality materials with a minimal degree of structural disorder.

4.1.7 Coulomb gap and Efros-Shklovskii Law

By incorporating Coulomb interactions between charged particles inside the system, Mott's Variable Range hopping theory was extended and modified. When powerful interactions are considered, a scenario other than that anticipated by Mott's law emerges. The Coulomb gap occurs when the ground state electronic density of states disappears at the Fermi level. At the Fermi level and zero temperature, the density of states will be zero. As the temperature rises, the gap widens owing to temperature fluctuations. The Coulomb gap has a significant effect on the conductivity behaviour. The hopping transport looks to be more complicated than it would be in a comparable system without interactions. Each hop modifies the charge configuration and the energy of single particle in the system[168].

The Coulomb Gap[169] (CG) develops in the density of states as a result of the significant Coulomb Interaction (CI) between electron energy levels around the Fermi level (Figure 58). Assuming the system is in its ground state, all electron

energy levels below the Fermi level μ are occupied, whereas all states above the Fermi level μ are vacant, as seen in Figure 59 . Since the ground state has the lowest energy, every electron transfer from $\varepsilon_i < \mu$ to $\varepsilon_i > \mu$ must result in a positive energy change. Eq. 55a illustrates the energy shift caused by a single electron jump. This is the amount of energy necessary to move one electron from site i to j. Eq. 55b is the equation for the energy of a single particle. The energy of a single particle ε_i is dependent on the site potential U_i and the Coulomb interactions between all of the system surrounding sites.

$$\text{Eq. 55a:} \quad \Delta E_{i \to j} = \varepsilon_j - \varepsilon_i - \frac{e^2}{k_B r_{ij}} > 0$$

$$\text{Eq. 55b:} \quad \varepsilon_i = U_i + \sum_{j \neq i} \frac{e^2}{k_B r_{ij}}$$
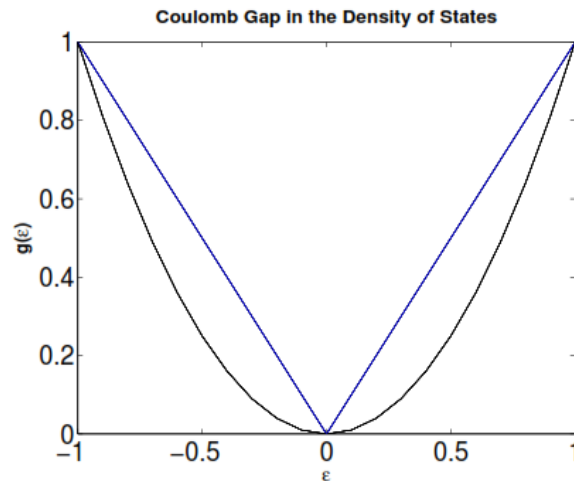
Figure 58: The Coulomb Gap is a discontinuity in the density of states. The linear graph depicts the gap creation in two dimensions. The parabolic graph depicts the 3D gap.
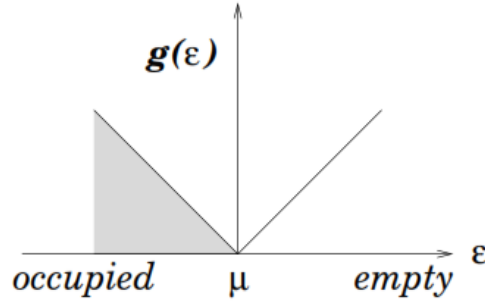
Figure 59: In two dimensions, the Coulomb gap exists in the density of states. The states below the Fermi level μ are populated in the ground state, whereas the states above are vacant.

The energy of $-\varepsilon_i$ is required to remove the electron from location i. To transfer the electron to the site j, the work $\varepsilon_j - \dfrac{e^2}{k_B r_{ij}}$ must be provided. The equation $\dfrac{e^2}{k_B r_{ij}}$ is included to account for the interaction between the now-empty donor on site i and the electron on site j. In other words, by removing $\dfrac{e^2}{k_B r_{ij}}$, the electron is prevented from interacting with itself on its former location i.

Considering again a small energy interval ε_0 cantered around μ, any two non-empty and empty sites with energies within this interval must be separated by a distance $r_{ij} > \dfrac{e^2}{k_B \varepsilon_0}$. The closer ε_i and ε_j energies are to μ, the greater the spatial gap between these states must be. According to Eq. 55a, the total number of donors within a volume of radius r_{ij} cannot exceed one. The concentration of donors in d dimensions with energies $|\varepsilon - \mu| < \varepsilon_0$ is therefore given by Eq. 56:

$$\text{Eq. 56:} \quad n(\varepsilon_0) = \frac{1}{r(\varepsilon_0)_{ij}^d} = \left(\frac{k_B \varepsilon_0}{e^2}\right)^d$$

From this it follows that the density of states may be expressed as in Eq. 57:

$$\text{Eq. 57:} \quad g(\varepsilon_0) = \left|\frac{\partial n(\varepsilon_0)}{\partial \varepsilon_0}\right| = d\left(\frac{k_B}{e^2}\right)^d \varepsilon_0^{d-1}$$

$g(\varepsilon_0)$ cannot be constant in 2 and 3 dimensions as the energy approaches μ. In three dimensions the gap is parabolic $g(\varepsilon) \sim |\varepsilon - \mu|^2$, so a general density of states affected by Coulomb interactions can be denoted as:

$$g(\varepsilon) \sim |\varepsilon - \mu|^n$$

It is now feasible to employ the result of the diminishing density of states to derive conductivity in the same manner. A generic expression is given for the relationship between p and the shape of the density of states $g(\varepsilon)$ and the spatial dimension d. When Coulomb interactions are considered, the final result is sometimes referred to as the Efros-Shklovskii $T^{-\frac{1}{2}}$ law, which calculates the hopping conductivity. At first the resistivity expression (Eq. 58) is considered to focus on the exponent.

$$\text{Eq. 58:} \quad \rho = \rho_0 \, exp\left(\frac{2r_m}{a} + \frac{\varepsilon_0}{k_B T}\right) \sim exp\left(\frac{T_0}{T}\right)^p, \qquad 0 < p < 1$$

Because the behaviour of the exponent p, which is of primary significance, constants and prefactors are omitted throughout the derivation. Finally, a generic equation for resistivity is obtained in Eq. 59, stating that:

$$\text{Eq. 59:} \quad \rho(T) = \rho_0 exp\left(\frac{T_0}{T}\right)^p, \quad p = \frac{n+1}{n+d+1}$$

In 2 dimensions with $d = 2$ and $n = 1$ or for 3 dimensions with $d = 3$ and $n = 2$, so $p = 1/2$. Hence the resistivity is given by Eq. 60[168]:

$$\text{Eq. 60:} \quad \rho_{CI}(T) = \rho_0 exp\left(\frac{T_0}{T}\right)^{\frac{1}{2}}$$

4.1.8 Conductivity and morphology

The material electrical mobility has a dependence upon temperature (i.e. higher temperature implies more mobility) and energy (i.e. energy increase implies more available states), but it is independent of the electric field; these considerations are true for small values of the electric field, but for high values, the VHR model approximations are incorrect[170]. Without making any assumptions, the relationship between mobility and electric field is as stated in Eq. 61:

$$\text{Eq. 61:} \quad \mu \sim \exp\left(\beta\sqrt{E}\right)$$

Additionally, mobility is dependent upon:

- Morphology: The morphology of an organic polymer has an effect on the overlapping of molecular orbitals and hence on the charge transport through the material.
- Molecular Orientation: In an inorganic semiconductor, the unit is the atom.

The molecules are the fundamental components of organic semiconductors; they typically have an at structure with one side being longer than the others.

Three axes are possible to be defined:

- Conjugation axis: it contains the double bonds.
- Substituents axis: it is orthogonal to the axis of conjugation.
- Bonds axis: it is orthogonal to the molecular plane and it corresponds to the direction of the unhybridized P_z orbitals.

Conductivity and molecular morphology follow the following qualitative relationships:

- The conductivity of a single polymer is greatest along the conjugation axis because carriers travel inside molecular orbitals with an higher mobility. However, conductivity between molecules oriented along the conjugation axis is limited due to insufficient orbital overlap.
- The conductivity between molecules oriented along the $\pi - \pi$ axis is superior to the former case due to greater overlap of the molecular orbitals; hopping transport restricts the mobility of molecules.
- The conductivity along the substituent axis is dependent on the presence of substituent groups.

4.2 AC incoherent charge transport

In the frequency domain two different models are discussed:

The Drude-Smith model is a phenomenological extension of the Drude formula that includes an extra component that suppresses conductivity at low frequencies, simulating the behaviour found in weakly confined systems where long-range carrier transport is inhibited.

Using his path-integral formalism, Feynman constructed a better all-coupling tiny polaron hopping transport theory[171]. He began by examining polarons self-energy E_0 and effective mass m^*. Feynman had the notion to express the polaron issue in quantum mechanics Lagrangian formalism and subsequently to remove the field oscillators[172]. Applying the variational principle to path integrals therefore yields an upper bound on the polaron self-energy, which is correct for both weak and strong coupling, discovering even a smooth interpolation for the ground state between weak and strong coupling[173].

4.2.1 Feynman's all-coupling theory

Feynman demonstrated that the ground-state energy and effective mass of the polaron can be calculated with high precision using a variational principle obeying by path integrals, thereby determining the polaron impedance and more broadly, its response to weak, spatially uniform, time-varying electric fields. This is a more complex problem that involves the rate at which a drifting electron loses momentum due to phonon interactions, either through phonon emission or collisions with pre-existing phonons. In practice, at temperatures below the crystal melting point, the density of optical phonons is relatively low due to the considerable energy required to activate them. Losses can occur solely in the idealized model due to collisions with optical phonons, which can be analysed using the collision cross section and subsequently the Boltzmann equation or equivalently the formulas for transport cross section to obtain the mobility[172].

Feynman obtained $X(v)$ as the final expression for the polaron impedance[172]:

$$\text{Eq. } 62: \quad X(v) = \int_0^\infty [1 - \exp(ivu)]\, Im[S(u)]\, du$$

$$S(u) = \int \frac{d^3K}{(2\pi)^3} |C_K|^2 \frac{2K^2}{3} \exp\left(\frac{-K^2 D(u)}{2}\right) [\exp(i\omega_K u) + 2P(\beta\omega_K)\cos(i\omega_K u)]$$

$$D(u) = \frac{w^2}{v^2}\left[\frac{v^2 - w^2}{w^2 v}\left[1 + e^{ivu} + 4P(\beta v)\sin^2\left(\frac{vu}{2}\right)\right] - iu + \frac{u^2}{\beta}\right]$$

In this expression, K, ω_K and C_K are respectively the momentum the frequency and the coupling coefficient with the electron of the phonon, ν is the frequency, $\beta = 1/k_B T$ and P is the momentum of the electron.

4.2.2 Drude-Smith model

Within the Drude model approximation, the plasma frequency was specified as $\omega_p^2 = \frac{ne^2}{\varepsilon_0 m}$. Conducting polymers typically exhibit electron densities between $2 \div 4 \cdot 10^{21}$ electrons/cm^3, resulting in plasma frequencies that are considerably below the visible light spectrum.

The Drude–Smith model incorporates a 'localization parameter' as parameter c, which represents the degree of backscattering and describes the complex conductivity in a single-scattering approximation[174].

In Eq. 63, the Drude-Smith formula is given in the form that is most frequently used in the literature[175] to express the AC behaviour of the conductivity of the medium.

$$\text{Eq. 63:}\quad \sigma(\omega) = \frac{Ne^2}{m^*}\frac{\tau_{DS}}{1 - i\omega\tau_{DS}}\left[1 + \frac{c}{1 - i\omega\tau_{DS}}\right]$$

where e denotes the elementary charge, N denotes the charge carrier density, m^* denotes the carrier effective mass, τ_{DS} denotes the Drude-Smith scattering time (which may differ from the Drude scattering time for a particular material), and c denotes a constant occasionally referred to as the 'localization parameter'. This definition of c occurs because the bracketed term separates Eq. 63 from the original Drude model formula (whose effect on conductivity is regulated by the c parameter). c can be any value between 0 and -1, with $c = 0$ recovering the Drude model and $c = -1$ completely suppressing the DC conductivity. The suppression of low-frequency conductivity at $c = -1$ is generally attributed to 'carrier backscattering', which has been described as both backwards-biased carrier scattering and a memory effect, in which carriers retain some information about their previous state before scattering, for example, because phase coherence is destroyed only after a certain number of scattering events greater than one[176].

Despite its benefits, the Drude-Smith model has two major criticisms: (i) no formal explanation for the assumption that backscattering endures for just one scattering event has been offered; (ii) the fit parameters meanings are unclear beyond phenomenological representations dependent on many physical factors.

By considering isotropic scattering, the Drude model can be easily obtained via the impulse response approach: for every carrier that interacts with a phonon, a lattice impurity, or another electron, resulting in a new forward velocity, another carrier collides with a phonon, resulting in a new backward velocity. As a result, the contribution of dispersed particles to the impulse response will be approximately null. Scattering reduces the number of charge particles since only unscattered particles contribute to the impulse response. Carrier scattering is not isotropic in the Drude-Smith model, and hence scattering cannot be considered as a simple population decay in the impulse-response formalism. Rather than that, the probability p that a carrier has experienced n scattering events between 0 and time t is represented using Poisson statistics; if $c_n = -1$, the nth collision of a particle will result in it scattering back in the direction it came from. As a result, the sign of the particle contribution to the average current changes. Taking the Fourier transform of Eq. 63 results in the following:

$$\text{Eq. 64:} \quad \sigma(\omega) = \frac{n^* e^2}{m} \frac{\tau}{1 - i\omega\tau_{DS}} \left[1 + \sum_{n=1}^{\infty} \frac{c_n}{(1 - i\omega\tau)^n} \right]$$

This is the Drude-Smith conductivity formula in its most generic version[175]. However, Eq. 64 does not represent the conductivity associated with the Drude-Smith model. Smith established a critical assumption in order to get the shortened Drude-Smith conductivity formula, namely that the backscattering bias occurs only during the initial scattering event, leading to $c_{n>1} = 0$ and c_1 renamed as c in this approximation. The shortened Drude-Smith conductivity formula is obtained by performing on Eq. 64 a Fourier transform on this impulse response to produce Eq. 63[175].

Carrier backscattering in the Drude-Smith model

Evaluating the effect of carrier backscattering on the conductivity of the model system described in the Drude-Smith model and approximations, recalling that $v_{th} = \sqrt{k_B T / m}$ is defined in this formalism as the root mean square speed in a single direction, and assuming a single charged particle is located in the centre of a

1D box of width L with a boundary reflection probability $R = 1$. The impulse response resembles a triangle wave with a period of roughly $2L/v_{th}$. By using $t_0 = L/v_{th}$ and assuming that $R = 1$ carrier reflecting barriers exist, a generic equation for the conductivity of the Drude-Smith model incorporating backscattering in the first degree of approximation is found as Eq. 65[175]:

$$\text{Eq. 65:} \quad \sigma_0(\omega) = \frac{n^* e^2}{m} \frac{\tau}{1 - i\omega\tau} \left[1 + \frac{\frac{2\tau}{t_0}}{1 - i\omega\tau} \left(\frac{e^{\frac{t_0}{\tau}} e^{i\omega t_0} - 1}{e^{\frac{t_0}{\tau}} e^{i\omega t_0} + 1} \right) \right]$$

4.2.3 Drude-Smith in THz spectroscopy in PEDOT:PSS

Because the PEDOT-rich particles in spin coated films are flat, anisotropy exists between the perpendicular and lateral directions relative to the substrate surface, both in terms of conductivity values and conduction processes. Atomic force microscopy studies indicate that transport orthogonal to the substrate is dominated by space charge effects, in contrast to parallel transport, which may be explained by a variable range hopping mechanism[177].

Nardes reported on the morphology of spin cast films using atomic force microscopy and scanning tunnelling microscopy, as well as the temperature dependence of the dc conductivity, in a thorough research on the anisotropic dc conductivity of thin films of PEDOT:PSS[25]. They discovered that $\sigma_{\|}(T)$ follows the VRH model in the direction parallel to the substrate. In the direction orthogonal the substrate, the conductivity exhibited a thermally activated Arrhenius type behaviour with $\gamma = 1$, where T_0 is the activation energy, $E_a \approx 1/N(E_F)L_{Loc}^3 k_B$ in which L_{Loc} is the average nearest-neighbour distance, according to $T_0 = E_a/k_B$.

AC conductance in the Terahertz (THz) frequency region is critical for conducting polymers, most notably PEDOT:PSS[178]. The carrier density n, and mobility, μ of DMSO-doped PEDOT:PSS films[179] were measured using terahertz time-domain spectroscopy and fitting the dielectric permittivity to the Drude–Smith model. The charge carrier density n, the mobility, μ, and the DC conductivity, σ_{DC}, may all be calculated from this data using the following equations Eq. 66, Eq. 67 and Eq. 68:

$$\text{Eq. 66:} \quad n = \frac{\varepsilon_0 \omega_p^2 m^*}{e^2}$$

$$\text{Eq. 67:} \quad \mu = \frac{(1 + c_1)e}{\omega_\tau m^*}$$

$$\text{Eq. 68:} \quad \sigma_{DC} = (1 + c_1)\frac{\varepsilon_0 \omega_p^2}{\omega_\tau}$$

where ε_0 is the permittivity of the vacuum, ω_p is the frequency of the plasma, m^* is the effective mass of the charge carriers, and $\omega_\tau = 1/\tau$ is the damping rate. where c_1 is the degree of backscattering used to explain carrier localization in disordered metals; it can range between 0 and -1, being 0 for isotropic scattering and -1 for complete backscattering. In the Drude model, the plasma frequency is given by Eq. 69:

$$\text{Eq. 69:} \quad \omega_p = \sqrt{\frac{ne^2}{\varepsilon_0 m^*}}$$

4.3 Space charge limited transport, traps and charge electrode injection

The charge transport of carriers in a semiconducting polymer has been explained in terms of coherent transport or hopping of electrons or holes down the chain or from one chain to another, all of which pertain to in-plane transport at different scale lengths. In order to evaluate orthogonal charge transfer, it is necessary to first analyse traps that will affect the movement of charges. The type and purity of a substance are not the sole variables affecting charge transfer. When electrodes are connected across a conducting material, a current flows between them. However, if the charge density inside the medium is low, the current has a straightforward dependency on the applied electric field. In this scenario, the charges existing in the medium do not interact with one another, and so may be regarded as isolated charges subjected to the influence of an electric field, E. Thus, the voltage between the electrodes may be thought of as a parallel plate capacitor, with a capacitance equal to $C = Q_e/V$, where Q_e is the charge on the electrodes and the electric field

is $E = V/d$, where d is the plate spacing. Because the capacitance of a parallel plate capacitor with plate area A equals $C = \varepsilon_r \varepsilon_0 A/d$, the simplest way to minimize the presence of charge carriers in the medium is to simply treat it as a constant ε_r dielectric medium.

If there are significant numbers of charge carriers in the medium, the charge carriers are not ignorable if their total charge Q is equivalent to Q_e. Under these conditions, the applied electric field is screened by neighbouring charges, reducing its effect. Due to the fact that these adjacent charges are closer to a particular charge than the charges on the plates, the electrostatic force and therefore the field exerted on the test charge by the neighbours is larger than the field exerted by the plates.

Thus, the current drawn between the electrodes is restricted by these space charges. This phenomenon is called Space Charge Limited Current (SCLC)[180], and it is a critical idea in practical devices such as light-emitting diodes. The SCLC density, which is a charge flux, may be calculated in Eq. 70 as follows:

$$\text{Eq. 70:} \quad j = \frac{9\varepsilon_r \varepsilon_0 \mu V^2}{8d^3}$$

where μ is the free charge mobility. This equation holds true when electrostatic effects (i.e., the applied electric field) dominate the movement of the charges rather than simple thermal diffusion. The significance of this finding, which is frequently referred to as Child's law or Mott–Gurney law, is that it is independent of the injection barriers at the active layer interface, but rather of the bulk characteristics of the medium (i.e. ε_r, μ), the applied voltage V, and the layer thickness, d. Indeed, this SCLC regime enables the determination of μ for specific materials, as mobility is defined as the gradient of a plot of j as a function of V^2.

Assuming that a given charge takes time τ to move between two electrodes. The electric charge would be Q_e, which indicates that $j = Q_e/A\tau$. Supposing that charges move a distance d in time τ, the current density may be approximated as follows in Eq. 71:

$$\text{Eq. 71:} \quad j = \frac{Q_e \mu E}{Ad} = \frac{\varepsilon_r \varepsilon_0 \mu V^2}{d^3}$$

4.3.1 Mott-Gurney space charge limited transport model

Since between electrodes there will not be any scattering event, because of the vacuum absence, the Child-Langmuir space charge equation appears to have no applicability to insulator or semiconducting materials. As a result, Mott-Gurney presented for polymer diodes a new space charge–limited current equation that is analogous to the Child-Langmuir equation assuming that[181]: in the active layer there are no injection traps, carrier diffusion is minimal and at the injecting electrode, there is no electric field. In general, the latter two assumptions hold true for the majority of polymeric semiconducting materials. However, under the former, the space charge–limited current model is extended to include a trapped space charge–limited current model.

Considering the diode active layer, sandwiched between two electrodes, supplied with an external voltage, an electric field (E) is created within. The mobility of a free carrier (μ) may be defined as $v = \mu E$, due to the fact that such an electric field causes charge carriers to travel with drift velocity (v) parallel to it. By solving all of the preceding equations for a one-dimensional direction with $V(0) = V$ and $V(L) = 0$ as boundary conditions, the pure space charge–limited current is found as reported in Eq. 72:

$$\text{Eq.}\,72:\ j = \frac{9}{8}\varepsilon_r\varepsilon_0\mu\frac{V^2}{d^3}$$

The dual logarithmic graph of $j(V)$ of the preceding Eq. 72, produces a straight line with slope 2, when between electrodes the current density is due to the polymer trap-free space charge–limited mechanism, as seen in Figure 60.
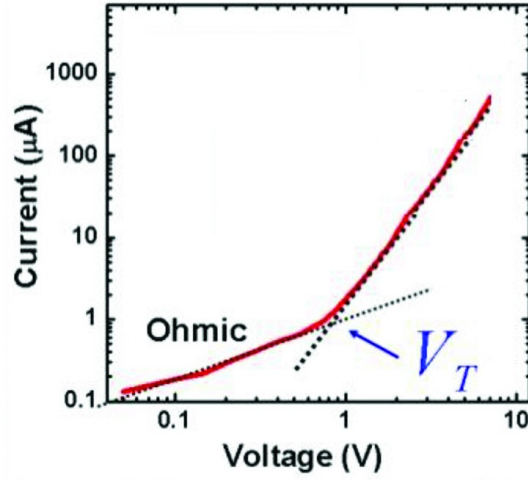
Figure 60: It is shown in a polymer diode the ideal I(V) which can be distinguished
into two regions, by the slope value: ohmic (J α V) and space charge (J α V²) separated by
the threshold voltage V_T.

4.3.2 Trap space charge limited transport model

The SCLC density is calculated ignoring the presence of traps, which function as
charge storage areas. Traps help to lower j, the SCLC density, by assisting in the
screening of any electric field passing through the material. While charge carriers
trapped in flaws or at the interface between two different species do not travel from
electrode to electrode, they do affect their surroundings, adding to the space
charge[182]. Thus μ, in Child's law (Eq. 72), may be substituted by an effective
mobility, μ_{eff} provided by Eq. 73:

$$\text{Eq. 73: } \mu_{eff} = \frac{n_m - n_{trap}}{n_m} \mu$$

where n_{trap} is the density of trapped charge and n_m is the charge density in the
material.

Not only traps reduce the mobility of space charge–limited current, but they also
begin the thermo–electric deterioration of polymer electronic devices. Traps are
typically classed as shallow or deep traps. Shallow traps have a depth of $\sim k_B T$,
which indicates that the charge will escape by thermal motion. If traps for electrons
are located closely to the LUMO (conduction band) inside the energy bandgap, they

Modelling and characterization of electronic conductivity in 3D printed PEGDA:PEDOT polymer composites - High frequency applications

121

are classed as shallow traps and the same is for holes, as in Figure 61. On the other hand, as seen in Figure 61, deep traps exist far away, from the conduction and valence bands, in the middle of the bandgap.
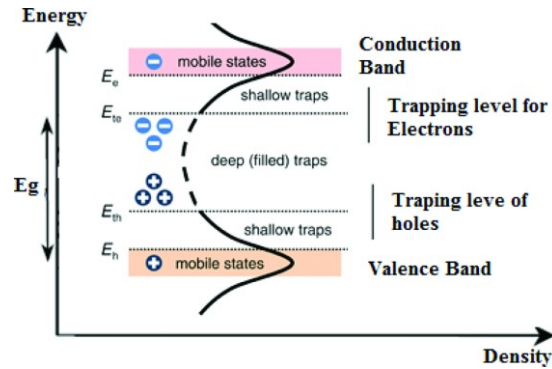
Figure 61: deep and shallow traps in polymer semiconductors are represented symbolically.

Trap space charge–limited current model does not take into account the energy depth of traps. The dynamic behaviour of the traps may be determined only if the model is evaluated using single traps in frequency domain analysis. By changing the energy of the single trap, it is feasible to distinguish between deep or shallow traps for both electrons and holes in the polymers, provided this is sandwiched between appropriately chosen electrodes[183].

When transport is largely based on hopping, it is difficult to distinguish between hopping and trap motion, as both have a thermal activation energy barrier. Charges can evade deep traps if the applied field is sufficiently large. After all, the electric field has an effect on the energy landscape, and by exerting an electrostatic force on the trapped charge E_q, it can increase its energy over the trap depth, allowing it to escape. Clearly, the larger E, the more mobile charges there are, which increases μ_{eff}.

While traps are inherently unexpected, known quantities of contaminants may be loaded into a material to influence how it behaves. If charge carriers are confined in isolated impurities, then the controlled addition of sufficient impurity should allow charges to flow across impurities. PVK (Figure 53c) is an example of a polymer with a high ionization potential that relies heavily on hopping transport. Due to the high ionization potential, it requires a great deal of energy to remove an electron, which is essentially the situation for a polymer that exhibits hole transport.

Of course, huge energies are not necessary for hole travel, because as a hole bounces from one site to the next, the energy cost of arriving at a new location is offset by the energy earned by leaving a previous site. This is not energy that must be purchased at one point and repaid later; while activation energy exists in hopping transport, the overlap of the wave functions enables the charges to travel from one site to another. If this hole falls into a trap with a lower ionization energy, it will decrease its total energy for the same reason (Figure 62).
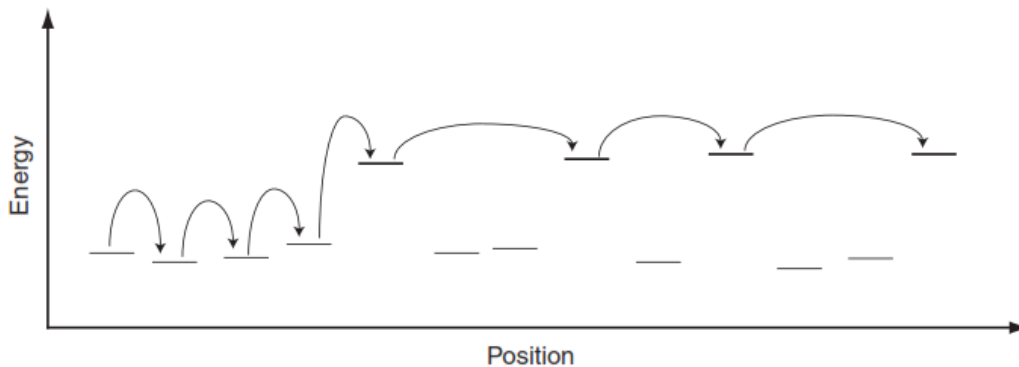
Figure 62: A schematic illustration of holes jumping between locations. These holes can be trapped if an impurity is present. However, if there are several such traps, a great degree of mobility is restored, as the holes bounce from trap to trap. Traps are denoted by bolded energy levels. Because energy in this diagram refers to electron energy, holes jumping in energy to a trap does not result in an increase in the system energy, because when the hole leaves for a trap with a lower ionization potential, the site it left behind recovers its electron, resulting in a net energy reduction for the system due to the difference in ionization potentials. The locations do not have identical energies, but rather a distribution of energies.

Generally, an intermediate zone between ohmic and space charge–limited behaviour is also seen, which in literature is referred to as the trapped space charge region, as illustrated in Figure 63. Charge carriers trapping and detrapping mechanism govern transport, spatial and energetic distributions of charges in the polymer. Traps are impurities or structural flaws that create localized states between the polymer HOMO and LUMO energy bandgaps. These localized states capture free carriers and prevent them from participating in the charge transport process, therefore degrading the polymer electrical characteristics and hence the device performance[184]. The polymer exhibits trap free space charge limited current behaviour when the applied voltage exceeds the mean trap energy, as seen in Figure 63.
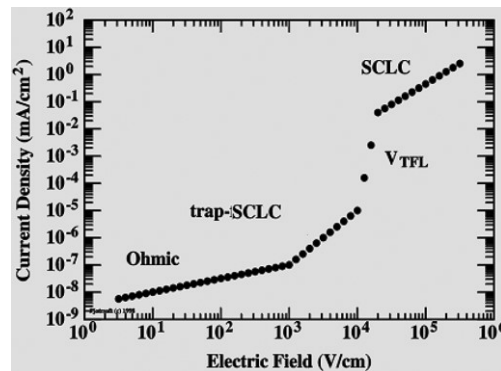
Figure 63: Space charge–limited current characteristics in polymer semiconductor. Regions: (1) ohmic (J α μV), (2) trap-SCLC (J α μVn), (3) VTFL (J α μN$_t$d^2) and (4) SCLC region (J α μV^2) [185].

The trapped space charge–limited current is dependent on the trap state distribution and generally, conducting polymers exhibit the following electronic trap density distributions:

1.   The density of a single energy level trap.
2.   The density of traps is distributed exponentially.
3.   The density of traps follows a Gaussian distribution.

4.3.3 Phonon-assisted tunnelling model

Phonon-assisted tunnelling is a quantum mechanical phenomenon in which electrons tunnel through an energetic barrier using the energy of lattice phonons. The presence of phonons results in a clear temperature dependency of the tunnelling process. Keldysh was the first to assess the theory of electron tunnelling from the valence band to the conduction band in the effective mass approximation[186]. A similar hypothesis was established for charge carriers tunnelling from their local trap states to the conduction band with the assistance of phonons[187].

Thermally activated electrical current in a semiconductor or dielectric occurs as a result of the production of free charge carriers via the phonon-assisted tunnelling process from the electronic trap levels at the electrode-semiconductor interface. In the DC situation, due to the mechanism of resonant tunnelling, the traps at the Fermi level of metal are continuously filled from the electrode. Assuming that all released

electrons are transported via the Schottky barrier depletion zone, the current is proportional to the tunnelling rate W, as in Eq. 74:

$$Eq.\,74:\;\; I = eN_S WS$$

where W denotes the tunneling rate, N_S denotes the surface density of localized electrons at the interface, and S denotes the barrier electrode area. Without a barrier, bulk limited current was seen to be caused by tunneling electrons hopping from trap to trap via the conduction band, but in the VRH model, the current is caused by carriers moving from trap to trap in the absence of a conduction band. If trapped electrons dominate, the current flowing through the device can be represented as follows[188] in Eq. 75:

$$Eq.\,75:\;\; I = \frac{1}{2} AeN_V W$$

where A is the effective generation volume and N_V is the trap density.

4.4 Charge injection through electrodes and energy barrier
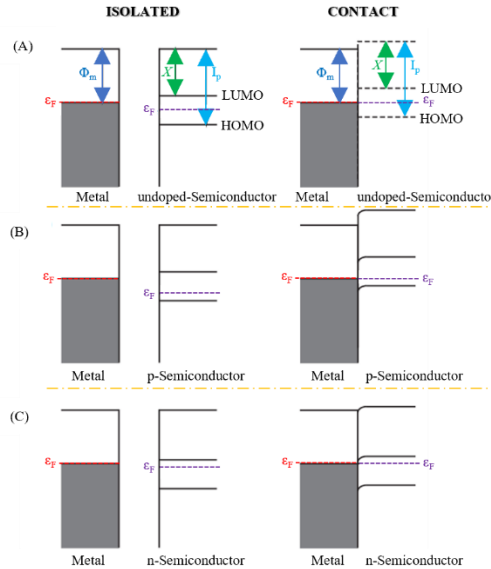
Figure 64: The metal-semiconductor junction is schematized for three types of semiconductors: (A) metal and undoped semiconductor (pristine polymer), (B) metal and p-doped semiconductor polymer, and (C) metal and n-type semiconductor.

The left-side of Figure 64 depict the energy levels of the separated materials, whereas the right-hand images depict the materials following contact. It is assumed in each scenario that there are sufficient charge carriers to equalize the Fermi levels. X denotes the semiconductor electron affinity, I_P denotes the semiconductor ionization potential, ϕ_m denotes the metal work function, and ϵ_F denotes the semiconductor or metal Fermi level. The pure polymer exhibits no band bending because it contains no mobile charge carriers. When p- and n-type materials are used, holes and electrons can flow from the semiconductor to the metal and vice versa. In the case depicted in (C), the metal Fermi level is higher than one of the semiconductor, implying that the net electron flow will be from the metal to the semiconductor, but charge flow can occur in either direction for the p-type semiconductor. In both (B) and (C), mobile charges within the semiconductor react to the potential difference created by Fermi level equalization by generating a depletion zone at the interface. Band bending happens at this point.

When two metals come into contact, their Fermi levels become equal. By flowing into the other metal, free electrons in the metal with the higher Fermi level can reduce the system total energy. This procedure continues until the two Fermi levels are equal, or, equivalently, until the chemical potential across the border is continuous and equal. Metal connections are still used in polymer devices, with the exception of a few instances when synthetic metals such as PEDOT are used. Electrons from the metal cannot escape into the LUMO in the absence of an applied field, as they are usually higher energy states[189].

Charge flow across the metal–semiconductor interface occurs as a result of sufficiently mobile charge carriers crossing the contact to equalize the two Fermi levels, given an acceptable amount of doping. Although the Fermi levels can be equalized, the band gap, which is a property of the polymeric electronic structure, must remain constant in magnitude. While the Fermi level is a property of any material, it is a reflection of the number of mobile carriers present in that material and thus can be altered by adding or subtracting charge carriers. To account for the shift in Fermi level in an n-type semiconductor, the HOMO and LUMO levels are both dropped by the same amount, but in a p-type semiconductor, they are both increased. Even at equilibrium, the equalization of the Fermi levels is linked with a potential difference across the border. This potential difference is accompanied by an electric field, which acts as a repellent for further charges attempting to cross the interface.

The magnitude of the electric field is ϵ_b/l_d, where l_d is the distance this field
covers, which is usually a few nm and ϵ_b is the energy height of the barrier, as
defined by Eq. 76:

$$\text{Eq. 76:} \quad \epsilon_b = I_p - \phi_m$$

for a p-type device, where ϕ_m denotes the metal work function. If the work function
is sufficiently large $\left(\phi_m < I_p\right)$, no barrier exists and carriers are not required to
tunnel through the boundary. This situation allows for more efficient carrier
injection in a device. The injection barrier of a n-type semiconductor is given by
Eq. 77:

$$\text{Eq. 77:} \quad \epsilon_b = \phi_m - X$$

This barrier that prevents additional charge injection is referred to as a 'depletion
layer'. This band bending phenomena happens not only at metal–semiconductor
contacts, but also at the interface of two different semiconductors (i.e.
heterojunctions). While these effects are particularly significant for inorganic
semiconductors, they will be significant only for highly doped organic
semiconductors[190].

4.4.1 Charge transport across the barrier

When an electric field is applied across a polymeric semiconductor, the bands are
affected; the HOMO and LUMO do not remain constant in energy but fluctuate as
a function of distance from the electrodes. A reverse bias creates a potential barrier
across the device by compelling electrons to increase their energy in order to move
over to the anode and holes to the cathode. Under these conditions, carrier injection
will be impossible. However, a forward bias enables charge transfer over the active
layer. If the bias is sufficiently enough, holes or electrons or both can tunnel through
the barrier and be injected into the semiconducting polymer. The greater the field
strength across the device, the shorter the tunnelling distance for charge injection
becomes.

Charges injected at one end must be permitted to exit at the other in order for the
device to function as part of a circuit. If current cannot easily flow through the
device, the voltage required to operate must be rather high, which is not desired.

Electrodes are consequently critical in a well-designed device, as their selection is critical for effective charge injection. To minimize rectifying current-voltage behaviour, ideal Ohmic contacts with no charge injection barrier at the electrode-active layer interface should be designed[191].

Under a positive bias, the size of a device barrier regulates the injection of holes and electrons into the device. The injection over this barrier may be classified into regimes of low and high electric fields. The Schottky equation (Eq. 78) is adequate to describe the emission at low fields:

$$\text{Eq. 78:} \quad j_S = AT^2 \exp\left(\frac{-(\Delta W - W_S(E))}{k_B T}\right)$$

Where $A = 1.20 \cdot 10^6 \, Am^{-2}K^{-2}$, and T^2 term is a function of the density of states scaling with the square root of the carrier energy, which holds true exclusively in the free electron model. The exponential component dominates this temperature dependency, making it difficult to verify the T^2 term experimentally. W denotes the injection or Schottky energy barrier, which is decreased by an amount denoted by $W_S(E)$, defined in Eq. 79:

$$\text{Eq. 79:} \quad W_S(E) = e\sqrt{\frac{eE}{4\pi\varepsilon_r\varepsilon_0}}$$

Eq. 78 is different from the Richardson–Dushman equation for thermionic emission by the term $W_S(E)$, which is recovered when $W_S(E) = 0$. For larger fields, there is a tunneling current density given by Eq. 80[192]:

$$\text{Eq. 80:} \quad j_{FN} = \frac{BV^2}{d^2\Delta V} \exp\left(-\kappa\frac{d\Delta V^{\frac{3}{2}}}{V}\right)$$

where B and κ are constants, and V is the bias voltage across the device of thickness d. Eq. 80 is referred to be the Fowler–Nordheim equation because it represents a tunnelling current differently than the Schottky equation (Eq. 78) does. By enabling charges to tunnel through the barrier, the electric field distorts the HOMO and LUMO. This is the more frequent injection mode in devices, and while it is useful for describing behaviour, experimental verification is not always effective owing to the injection current being compensated by a reverse current[193].

4.5 SCLC model with Pool-Frenkel Effect

The electronic current density in a polymer sample may be described as due to the trap-free space charge–limited mechanism when it flows through a length (L) exhibiting a square voltage dependence ($J \alpha V^2$) and inversely to the cubic length ($J \alpha L^{-3}$). To account for the trap distribution width, the space charge–limited current model is upgraded to become the trapped space charge–limited current model. Traps are dispersed energetically and spatially throughout the energy bandgap, capturing free carriers and posing an energy barrier to their release. Both the space charge–limited current and trap space charge–limited current models require a constant trapping energy barrier in the device. Indeed, a stronger field reduces the trapping energy barrier height, increasing the emission rate and therefore the current density, as predicted by the trap space charge–limited current model depicted in Figure 65a.

The Poole-Frenkel effect is defined as the decrease in detrapping emission rate or in trapping energy barrier at high electric fields[194], as seen in the schematic energy band diagram (Figure 65b). The total current density (J) flowing through the polymer as a result of Poole-Frenkel emission is denoted by the formula in Eq. 81, where $q\phi_T$ is the trapping energy barrier:

$$\text{Eq. 81:} \quad J = q\mu N_c \exp\left[\frac{-q\left(\varphi_T - \sqrt{\frac{qE}{\pi\varepsilon_r\varepsilon_0}}\right)}{k_B T}\right]$$

Murgatroyd solved the issue of the reduction in the barrier height of traps by integrating the Poole-Frenkel effect into the space charge–limited current model and driving an approximation equation[195], which is Eq. 82.

$$\text{Eq. 82:} \quad J = \frac{9}{8}\varepsilon_r\varepsilon_0\mu_h \exp\left(0.98\gamma\sqrt{E}\right)\frac{V^2}{L^3}$$

The Poole–Frenkel effect is theoretically related to the Schottky effect, which is the decrease in the energy barrier between metals and insulators caused by electrostatic interaction with an electric field at a metal–insulator contact. However, conductivity due to the Poole–Frenkel effect is observed in the presence of bulk-

limited conduction, which happens when the limiting conduction mechanism occurs in the bulk of a material, whereas the Schottky current is observed in the presence of contact-limited conduction, which occurs when the limiting conduction mechanism arises at the metal–insulator interface.
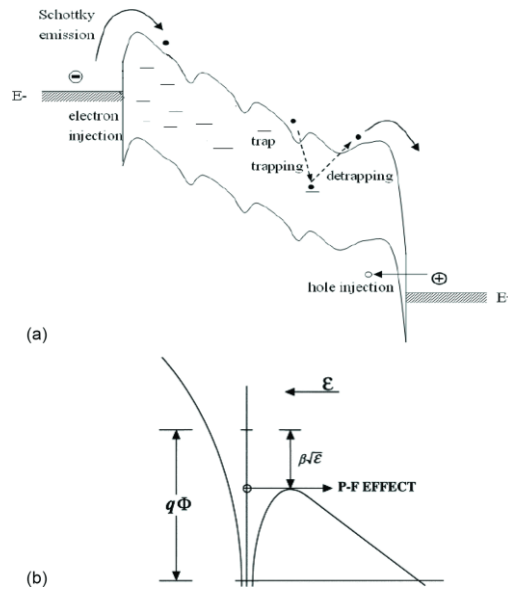
Figure 65: a) Reduction in the trapping energy barrier due to the increment of electric fields b) Pool-Frenkel effect.

Because the Murgatroyd equation is straightforward and convenient, but it is an approximation, Barbe calculated the impact of trap barrier height decrease on the space charge–limited current model analytically and obtained the equation reported as Eq. 83[196].

$$\text{Eq. 83:} \quad \frac{Jx}{\mu\varepsilon\theta} = \frac{2(k_BT)^4}{\beta^4}\left[\exp\left(\frac{\beta\sqrt{E}}{k_BT}\right)\left\{\left(\frac{\beta\sqrt{E}}{k_BT}\right)^3 - 3\left(\frac{\beta\sqrt{E}}{k_BT}\right)^2 + 6\frac{\beta\sqrt{E}}{k_BT} - 6\right\} + 6\right]$$

Barbe's law is used to calculate the current density (J) as a function of the defined electric field at point x. Both Murgatroyd and Barbe modifications are claimed to be relevant to the electrical response of a variety of polymer devices[197]. Due to the fact that the same charge transport mechanism is shared by both semiconducting and insulating polymers, Eq. 83 is reasonably applicable for both types of polymers.

Frenkel, Murgatroyd, and Barbe's basic effort was to alter the space charge–limited current to allow for a reduction in trap barrier height for only one-dimensional trap

distribution. These models do not perform well for the three-dimensional trap distribution. In this domain, it is reasonable to accept the Hartke adjustment for accommodating three-dimensional reduction of the trapping energy barrier in the space charge–limited current model[198].

Chapter 5

Experimental Validation

The electrical, optical and morphological properties of PEGDA:PEDOT polymer composites have been studied and tested through a wide range of methods in order to characterize the behaviour of 3D printed devices, while optimizing both their printability and conductivity. Furthermore, these measurements allowed a deep insight in the investigation on the electrical conduction mechanism in 3D printed intrinsic conductive polymer composites, in comparison with other materials and 3D printing technologies. Starting from the study of the interface between the printed and external devices, through rigorous impedance spectroscopies, a proper experimental characterization methodology has been designed to properly optimize the printing process parameters with the medium conductivity, leading to the production of numerous applications.

5.1 Materials and Methods

Several technologies and different materials have been extensively compared by literature to comprehend the state of art in 3D printing electronics, as reported in Table **3**. Evidence of the bibliographic research found Stereolithography as the primary method to 3D print PEGDA/PEDOT composites, where PEGDA matrix, the long-chain, hydrophilic, crosslinking and electrically insulating monomer confers printability to the medium while PEDOT, the conjugated polymer filler, its conductivity. DC characterizations were performed in a 2-probe setup with the Keithley 6430 Source Measure Unit.

Printing technique	Filler	Conductivity [S/cm]	Matrix	Ref.
Direct Laser Printing	Ag NPs	$6 \cdot 10^{-6}$	PEGDA	[199]
Stereolithography	Ag NPs	$8 \cdot 10^{-11}$	Acrylic monomers	[200]
Direct Laser Writing	SWCNT	$1 \cdot 10^{-6}$	PU	[201]
Direct Laser Printing	MWCNT	$27 \cdot 10^{-5}$	Acrylic monomers	[202]
Direct Laser Printing	MWCNT	$8 \cdot 10^{-6}$	PEDGA/PEGMEMA	[203]
Two Photon Polymerization	PEDOT	$4 \cdot 10^{-2}$	PEGDA	[204]
Stereolithography	PEDOT	$5 \cdot 10^{-2}$	PEGDA	[205]

Table 3: Comparison of the state of art of different materials and 3D printing technologies.

Referring to PEDOT:PSS (Clevios™ PH1000, Heraeus) as the primary stable polymeric resin, before printing, it is separated in its constituents by dilution in a solution of H_2SO_4, to obtain the PEDOT precipitate. Comparing PEDOT:PSS, as an amorphous p-type polymeric semiconductor, to electronic grade intrinsic Silicon, as described in Table **4**, it is noticeable that even if carrier mobility is lower than the latter, the first exhibits very high density of states, leading the high conductivity of the polymer.

Property	PEDOT:PSS	Intrinsic Silicon
Electron affinity [eV]	3.6	4.05
Band gap [eV]	1.57	1.12
Effective conduction band density [cm^{-3}]	$2 \cdot 10^{21}$	$2.8 \cdot 10^{19}$
Effective valence band density [cm^{-3}]	$2 \cdot 10^{21}$	$1.04 \cdot 10^{19}$
Electron mobility [cm^{2}V^{-1}s^{-1}]	1	1350
Hole mobility [cm^{2}V^{-1}s^{-1}]	40	450
Midgap density of states [cm^{-3}eV^{-1}]	$2.7 \cdot 10^{19}$	$1 \cdot 10^{12}$

Table 4: Comparison of the material properties of PEDOT:PSS and intrinsic Silicon[206].

It must be evidenced that the parameters reported in Table **4** are not standard for PEDOT:PSS, since they strongly depend on a very large set of variables to produce the polymer mixture and on the polymerization process, in fact as reported in Figure **66** the band gap energy value (i.e. E_g) and the Fermi level (i.e. E_f) may slightly vary and in the same way the HOMO and LUMO energy positions.
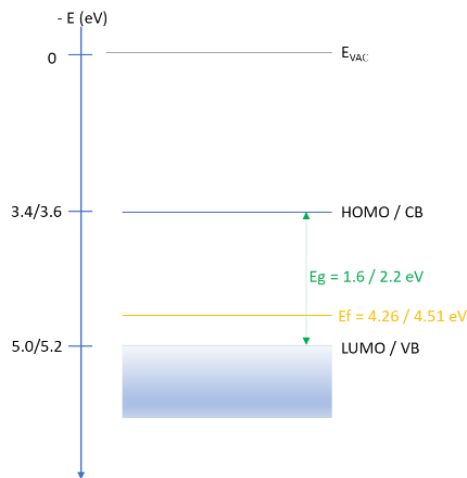
Figure 66: Energy level representation in PEDOT material.

This variability is due to the absence of a long range order in the polymeric chains arrangement respect to electronic grade intrinsic Silicon, which exhibits high order of the crystal lattice. Nevertheless, in Figure **67** the results of a FESEM morphological characterization are reported for 500X and 4000X magnifications at 5 kV and 30 μm of aperture with no tilting. It can be observed that as the percentage of PEDOT decreases, the structural order increases, due to the presence of a greater amount of PEGDA matrix, which forms a crystalline lattice. The white streaks are cracks within the PEGDA, due both to the cutting of the sample and to the relaxation effect, or shrinkage, which is obtained after photo cross-linking. It is also evident, especially in images 4, 5 and 6, the presence of the laser path.
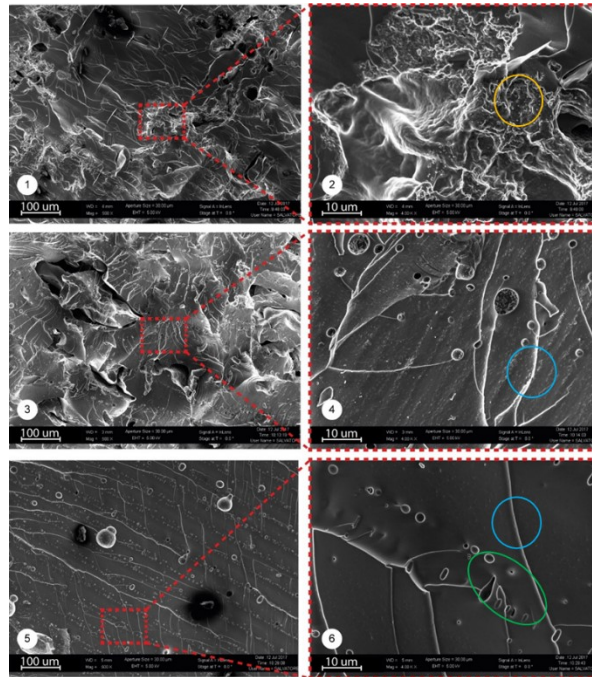
Figure 67: FESEM Supra 40 images: (1-2) PEGDA-PEDOT [1:1] ; (3-4) PEGDA-
PEDOT [5:1] ; (5-6) PEGDA-PEDOT [10:1] ; 2) Orange circle: PEDOT segregated in
the PEGDA matrix; 4-6) Blue circle: cracks ascribed to the shrinkage; 6) Green circle:
laser scanning direction.

In order to optimize the conductivity along with the printability of the polymer
composite different quantities of the Photoinitiator PI Irgacure 819 were added to
liquid PEGDA 575, while PEDOT precipitate was obtained by dilution in a solution
of H_2SO_4 solution for 12 h. The final addition of different DMSO (i.e.
Dimethylsulfoxide) concentration allowed to determine the optimal mass fraction
between the resin constituents, as reported in Figure 68.

Modelling and characterization of electronic conductivity in 3D printed
PEGDA:PEDOT polymer composites - High frequency applications

135
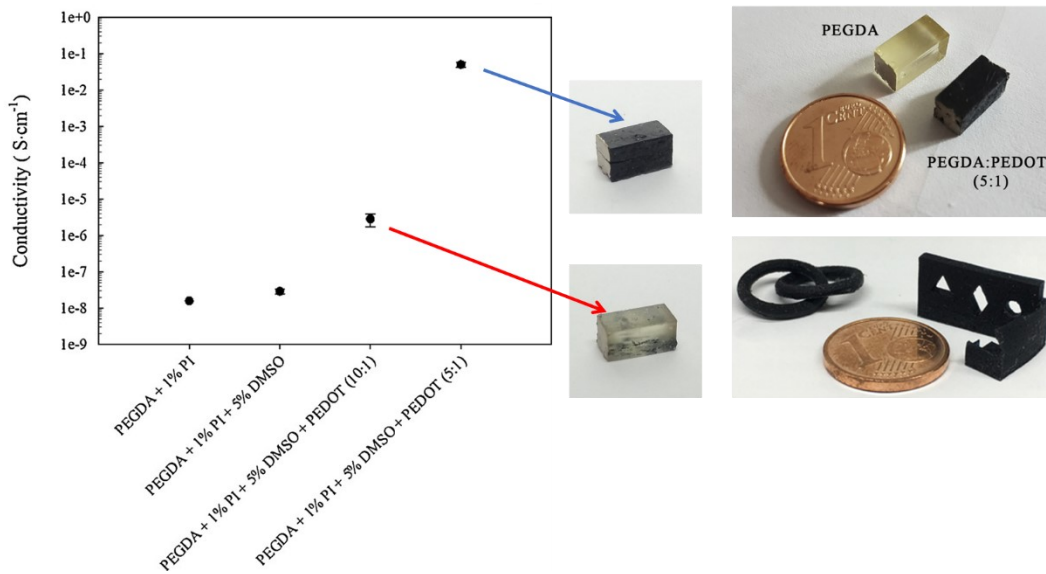
Figure 68: Conductivity plot of different constituent wt.%[205]; Final 3D printed devices.

A Design of Experiment (DOE) was mandatory to effectively discover the optimal relative mass fraction, in addition with the variation of the PEDOT content, which affects nonlinearly the conductivity of the final 3D printed device (Figure 69).
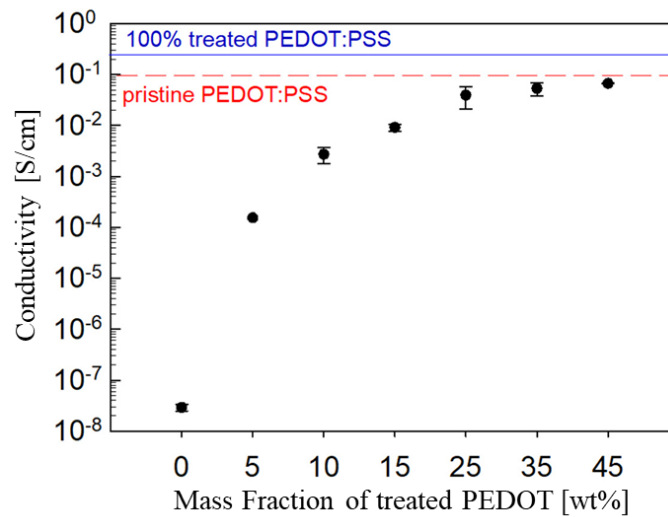
Figure 69: Conductivity of the PEGDA:PEDOT samples at different treated PEDOT:PSS contents[207].

It was demonstrated that a filler content of treated PEDOT, $[M]_{PEDOT} \gtrsim 25$ wt% was sufficient to guarantee a conductivity $\sigma \gtrsim 0.05$ S/cm, above the percolation threshold[208].

5.1.1 Bipolaronic transitions in Raman Spectroscopy

The Fourier Transform Raman spectroscopy (i.e. FT-Raman), reported in Figure 70A, may be used to investigate changes occurring at the molecular level in order to get insight into the material vibrational modes, in fact the Raman band associated with $C_\alpha = C_\beta$ symmetrical stretching at 1400–1500 cm^{-1} is exploited to differentiate between benzenoid and quinonoid forms and to deduce secondary doping information[209]. The convolution of peaks $C_\alpha - C_\beta$ (1440 cm^{-1}) and $C_\alpha = C_\beta$ (1460 cm^{-1}) symmetric stretching modes are related to benzoid (i.e. aromatic) and to the quinoid chain structure found in Polythiophenes with a π-conjugated backbone structure (i.e. PEDOT).

It is well established that Polythiophenes such as PEDOT show defects originating a semi-metallic bipolaron network[210]. PEDOT that has been highly oxidized has up to one charge carrier per three monomer units (Figure 70B-C)[211], although according to quantum chemistry calculations, a bipolaron in PEDOT extends over six or more monomer units[115], as reported in Figure 70D.
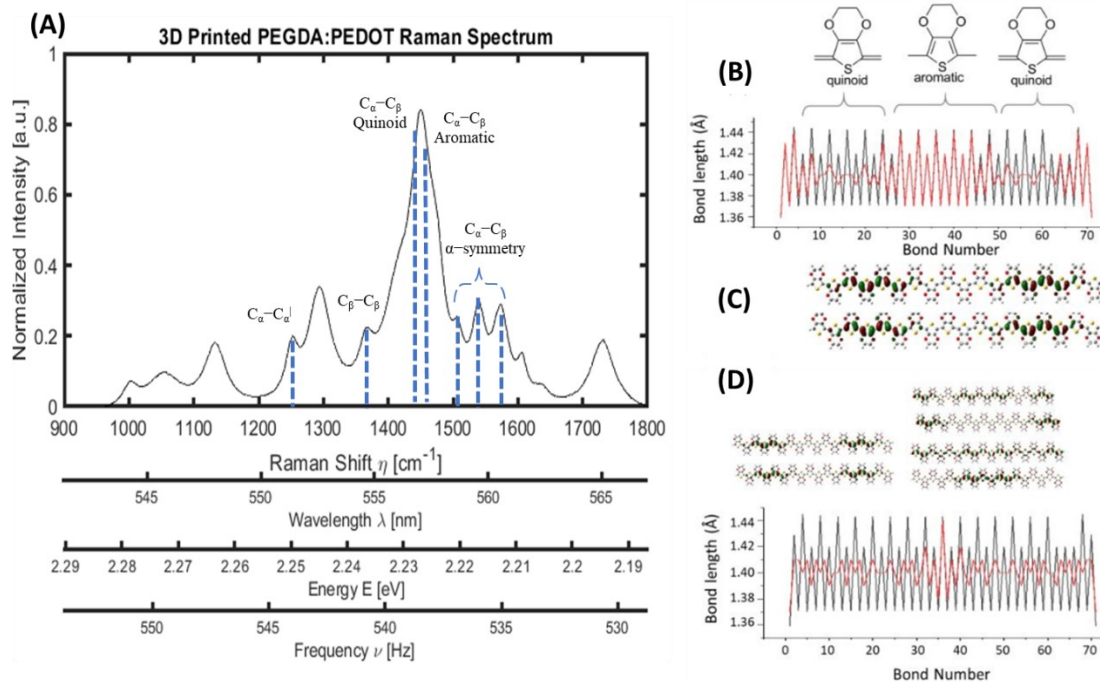
Figure 70: (A) FT-Raman convolutional spectrum of 3D printed
PEGDA:PEDOT[207]; (B) DFT calculations of the bond length alternation between
aromatic (i.e. quinoid) and benzoid arrangements; (C) DFT calculations of the electron
density distribution in a PEDOT chain of 18 units for a bipolaron of total charge Q = +2e
and total spin number S = 1; (D) DFT calculations of the bond length alternation and
electron density distribution for the bipolaronic states of total charge Q = +6e and total
spin number S = 1[212].

There are two extreme geometric structures possible: one that is entirely benzenoid
and another that is fully quinonoid, with the latter structure usually having greater
energy and hence being less favourable than the benzenoid structure. The benzenoid
structure may be preferable for coil conformations in the low conductivity regime,
while the quinonoid structure may be preferable for linear or extended coil
structures in the high conductivity regime[213].

Clear evidence of the bond alternation structure between benzoid and quinoid
arrangements is found in the FT-Raman (Figure 70A), which demonstrates the
existence of a semi-metallic bipolaronic network in 3D printed PEGDA:PEDOT
polymer composites.

5.2 Metal-PEDOT Interface: Contact behaviour

In order to address, in this section, the issue of interfacing 3D printed PEGDA:PEDOT devices with metal contacts, PEDOT can be regarded as a p-type semiconductor at a first approximation.

The band structure of electrically isolated metal and p-type semiconductor, the ohmic contact between metal and semiconductor and the rectifying or Schottky contact are pictured in Figure 71. Regarding to the metal work function as ϕ_M and to the p-type semiconductor as ϕ_S, in case of ohmic contact $\phi_M > \phi_S$ and at thermal equilibrium in the semiconductor, due to the adjustment of the Fermi level, an upward band bending phenomenon is generated, leaving at the interface a hole accumulation region[214]. This mechanism is modelled as a linearly behaving contact resistance, which allows charge carriers to flow. In case of rectifying or Schottky contact, $\phi_M < \phi_S$, the adjustment of the Fermi level gives rise to downward band bending in the p-type semiconductor, leading to the generation of a bult-in potential, called Schottky barrier ϕ_b. In the semiconductor, at the metal interface, negative acceptors are left, generating a diffusion potential barrier V_{d0}, inhibiting charge carriers injection towards the metal.
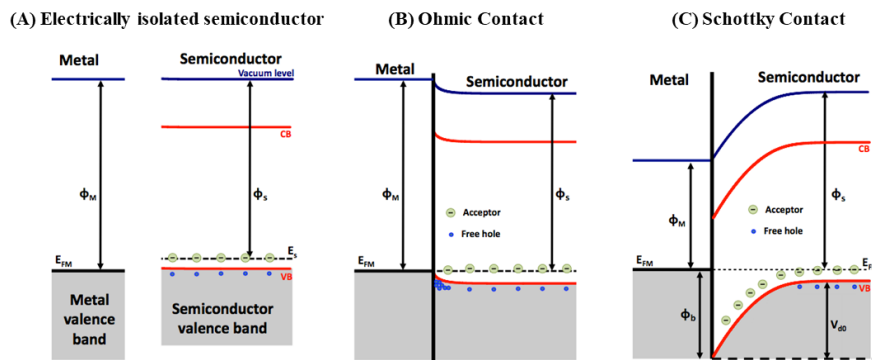
Figure 71: Band structure metal and p-type semiconductor at thermal equilibrium:
(A) Isolated metal and p-type semiconductor; (B) Ohmic junction; (C) Schottky junction.
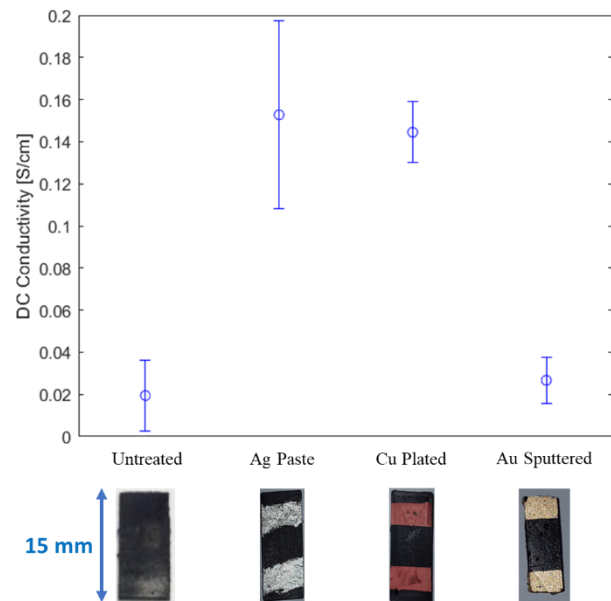
Figure 72: DC Conductivity of 3D printed PEGDA:PEDOT polymer samples
differently contacted: Untreated: Direct metal 2-probe conductivity measurement; Ag
Paste: Silver paste manually deposited on the sample; Cu Plated: Copper electroplating
on the sample; Au Sputtered: Gold sputtering on the sample.

Any of the 3D printed PEGDA:PEDOT (Figure 72), whose constituents were: PEGDA (1%wt. PI) + 45% PEDOT (15 min) + 5% DMSO, were tested in groups of three per contact method. Untreated sample has been contacted directly by the 2-probe measurement setup, while the Ag paste (RS Pro Silver paste) has been deposited manually by a tape mask on the same sample. Gold sputtering, which is a traditional process in microelectronics to deposit pads on the contact area, has been performed by placing the samples in a vacuum chamber at 10 mtorr, with a current of 30 mA for 180 seconds, producing 100 nm of deposited gold.

Finally, the copper electrodeposition has been performed prior to cathodic fixation, covering each sample with an insulating polyvinyl acetate sheet in order to selectively electrodeposit copper at the parallelepiped extremities, through the designed mask on a surface area of 0.8 cm^2. The anode and cathode have been mounted at a distance of 2.5 cm, to a U-shaped PMMA (i.e. polymethylmethacrylate) support to ensure the same anode to cathode distance and the parallelism between the two, throughout each deposition test. A DuPR10-1-3 (Dynatronix) power source provided a voltage between the anode and cathode, and at the same time, an ionic current flowed through the electrolyte solution, causing copper positive ions to migrate and deposit on the negative cathode, which was the

masked 3D printed device. Different settings have been investigated to determine the optimal electrodeposition parameters: a nominal current of 50 mA, corresponding to a current density of 62.5 mA·cm^{-2}, was determined to be the threshold value required for the setup to begin observing copper deposition on the sample.

Metal	Workfunction [eV]
Al	$4.06 - 4.26$
Pb	4.25
Ag	$4.26 - 4.74$
Zn	$3.63 - 4.9$
Ti	4.33
Sn	4.42
Cu	$4.53 - 5.10$
Ni	$5.04 - 5.35$
Au	$5.10 - 5.47$
Pt	$5.12 - 5.93$
Pd	$5.22 - 5.60$

Table 5: Metal work function table[215].

The motivation of the selection of metals and deposition processes is evident due to its feasibility on the sample device, although as it is evident in Figure 72, the 2-probe DC conductivity measurement is affected by a significant uncertainty, due to the capability of the process to produce a "good" electrical contact either by mechanical interference or by surface contact between the PEDOT and the metal. Untreated and gold sputtered sample exhibit a lower conductivity with a significant relative error, respectively 85% and 41%, which in case of Au sputtering meant that the process was not capable to produce a "good" electrical contact, even if this metal was chosen to produce an ohmic contact, since its high work function value (Table 5). Nonetheless, silver paste deposition produced an unstable contact, since the relatively high uncertainty (29%), although the increase of 1 order of magnitude in the DC conductivity leads to hypothesize that the paste deposition allowed a better spreading on the polymeric sample rough surface at a microscale level. Copper, as reported in Table 5, exhibit sufficiently high work function values, with a variability due to the crystal plane exposed as contact surface, described by the Miller's indices, to produce an ohmic contact. Finally copper electroplating allowed to obtain an increasing in the conductivity measurement, while producing an effective

contact surface higher than the previous processes, with a relative uncertainty equal to 10% of the measured value, demonstrating stable contacting properties.

Further two probe DC characterizations were performed in the range of ± 1 V, ± 10 V and ± 20 V, to evaluate in all the voltage ranges the linear behaviour of Current-Voltage characteristic (i.e. I-V). Measures were repeated three times for each sample and range and no evidence of rectifying behaviour was proved to be.

Considering that the Fermi level and consequently the work function of PEGDA:PEDOT can be estimated in the range of 4.2−4.5 eV (Figure **66**), it should be mandatory to employ a metal with a work function greater than previous values to produce an ohmic contact. Nonetheless, the formation of the bipolaronic network must be considered after the photopolymerization process. This network provides available charge states in the band gap of the polymer near the valence band, leading the Fermi level to higher values and consequently the work function of the polymer to reduce.

5.3 Impedance spectroscopy of DMSO-treated samples

Four terminal-pair, also referred to as four probe impedance spectroscopy[216] was the principal investigation technique employed to characterize the frequency dependence of the electrical conductivity in PEGDA:PEDOT devices. This method allows to extract from the impedance, the dielectric permittivity of the material and to isolate in a frequency range the unique contributions of charge carriers to the overall conductivity in the convolutional spectrum, as reported in Figure 73.
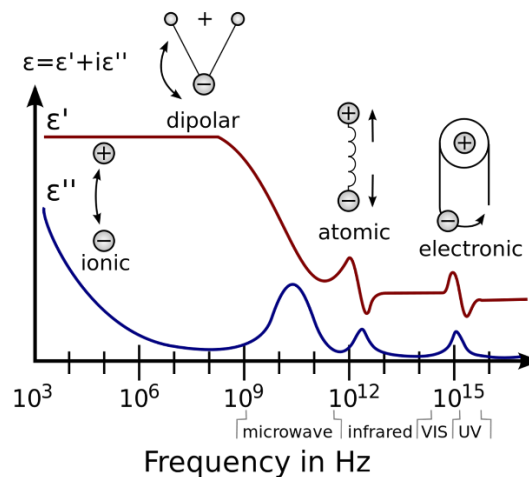
Figure 73: Response dielectric permittivity spectrum to an external excitation time-varying electric field from kHz to visible frequencies[217].

Modulus ($|Z|$) and phase shift (Θ) of impedance data were acquired and evaluated as complex impedance Z in Eq. 84, where the real part is defined by R, which is the Resistance and the imaginary part is defined by X, which is the Reactance. The Conductance (G) and Susceptance (B) are defined as the real and imaginary part of Admittance (Y), which is the inverse of the Impedance (Z).

$$\text{Eq. 84:} \quad Z = |Z|e^{j\phi} = R + jX = Z^{|} + jZ^{||} = [Y]^{-1} = [G + jB]^{-1} = \left[Y^{|} + jY^{||}\right]^{-1}$$

Considering the schematic four terminal-pair impedance setup, reported in Figure 74A, the four probes represented are the core of the coaxial cable connected to the Impedance Analyser (HP4192A) and their port function is defined as follows:

- HC: High Current terminal is the high side of the current generator.
- HP: High Potential terminal is the high side of the voltmeter.
- LP: Low Potential terminal is the low side of the voltmeter.
- LP: Low Current terminal is the low side of the current generator.

In Figure 74A it is represented one of the possible operating principles, which is defined by the application of an alternating (i.e. AC) sinusoidal current wave at the measuring frequency between the HC and LC terminals, while the measured voltage is the voltage drop between the HP and LP terminals. The imposed AC current is measured in the HC-LC branch to increase the measurement accuracy[218]. The shields (i.e. ground) of each coaxial cable are connected to the ground of their voltmeter or current generator, respectively. To perform a proper four probe impedance characterization, it must be satisfied at any frequency that the measured voltage "V_{HP}" is defined at the HP port and the measured current "I_{LC}" is defined at LC port, in order to setup the boundary conditions needed to define the four probe impedance of the DUT (i.e. Device Under Test), Z_{4P}, the condition of $I_{HP} \equiv V_{LP} \equiv I_{LP} \equiv 0$ must be met by ground connections, as previously stated (Figure 74B-C). In this setup configuration the definition of the four probe impedance as $Z_{4P} = \frac{V_{HP}}{I_{LC}}$ allows to the measured value to be independent from the stray parasitic elements and the contact contribution to the impedance, conferring to this method the capability of being suitable to measure impedance modulus values ranging from mΩ to MΩ.

Modelling and characterization of electronic conductivity in 3D printed
PEGDA:PEDOT polymer composites - High frequency applications

143
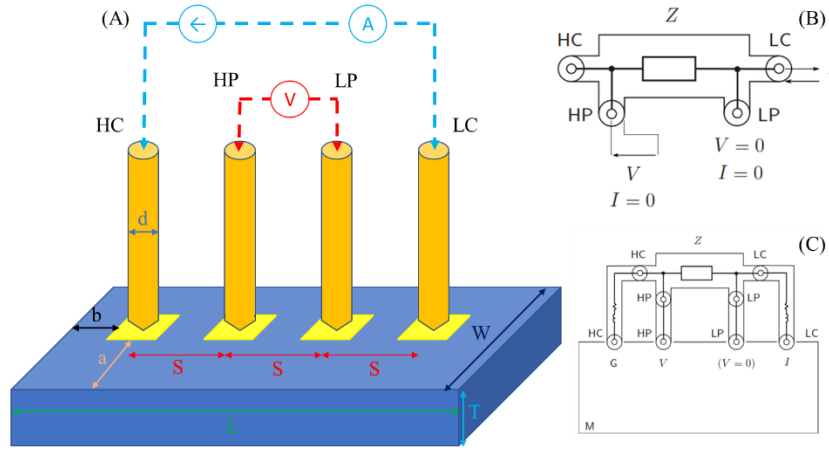
Figure 74: (A) Four probe impedance setup on the sample: "L", "W" and "T" are respectively the sample length, width and thickness, "S" is the interaxial distance of each terminal, "a" and "b" are the distances between the metal pad edge from the sample border and "d" is the probe diameter; (B) Schematic representation of four probe impedance setup; (C) Schematic representation of four probe impedance setup with shield and stray parasitic elements.

Regarding Figure 74A a classical linear disposition of the probe is represented. In this configuration from the measured four probe impedance[219], it is possible to calculate the resistivity (ρ) and conductivity (σ) of the material, since they are defined as a function of the experimental setup. Although it is necessary to take into account some correction parameters for this measurement, the material complex resistivity is defined as in Eq. 85[220]:

$$\text{Eq. 85:} \quad \rho = [\sigma]^{-1} = Z \cdot 2\pi S$$

Further considerations on the sample and setup physical dimensions are needed to distinguish between the meanings of the measured resistivity. In AC characterization the sample resistivity may be due to two main contributions: the sample either superficial or body resistivities, also referred to as "sheet" and "bulk" resistivities, respectively. Different dimensioning of the inter-probe spacing (S) respect to the sample thickness (T) allow to measure the single contributions to the overall resistivity in the case that $S \gg d$: if $S \gg T$, it is measured the sheet impedance, while if $S \ll T$, it is measured the bulk impedance[221]. To retrieve the value of the bulk resistivity, if only thin samples, compared to the S dimension are at disposal, it is necessary to apply geometrical correction factors to the measured value[222]. Furthermore, to prevent the measure to be affected by border effect it is necessary that $S \gg a$ and $S \gg b$.

A custom impedancemetry setup (Figure 75A) was built to perform four terminal-pair measurements. It consisted of an Impedance Analyser (HP4192A-LF), four 3D printed probe holders in ABS (Figure 75B) (i.e. thermoplastic polymer produced from the polymerization of styrene and acrylonitrile) with four magnetic cylindrical pivots at the base corners and four single axis micromanipulators. Each micromanipulator was fixed to the support and to a FR4 both side copper covered PCB, screwed to the axis, to create the electrical contact between the latter and the gold plated tungsten probe tip (Figure 75C). Each single axis was manipulated at the beginning of the measurement to align at the same hight, along the z-axis, the four probe tip at a contact angle of 45°.
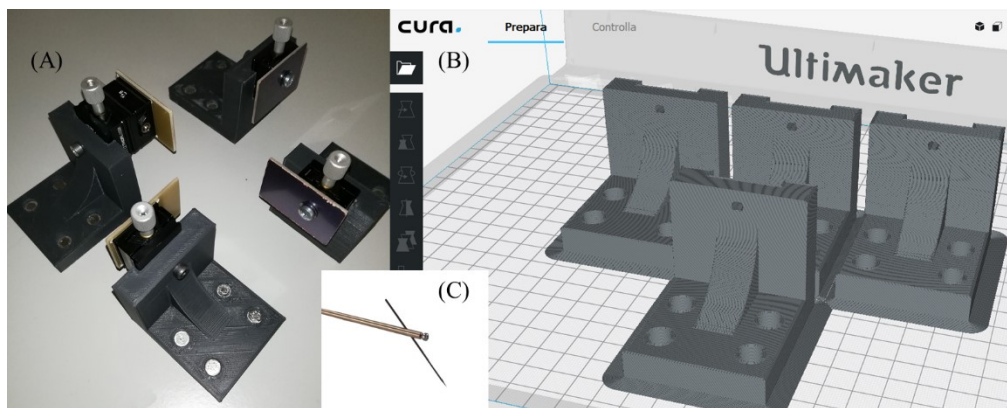
Figure 75: (A) 3D printed 4-probe measurement setup; (B) CAD assisted design of 3D printed probe holders; (C) Gold plated tungsten probe tip with point radius equal to 50.0 μm ("The Micromanipulator Company") and support holder screw.

The HP4192A-LF Impedance Analyser presented in the accuracy chart (Figure 76) the relative standard error (Std. Err.) on the performed impedance modulus and phase shift depending on the frequency and on the applied oscillation level, in accordance with the expected magnitude range of the measured impedancemetric values.

Modelling and characterization of electronic conductivity in 3D printed
PEGDA:PEDOT polymer composites - High frequency applications

145
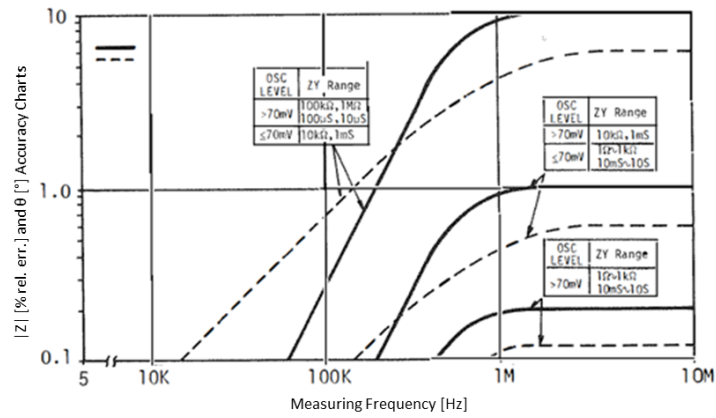
Figure 76: HP Model 4192A-LF Impedance Analyser – Impedance magnitude and phase shift accuracy chart[223].

The HP4192 Impedance Analyser was used to perform 4 terminal-pair impedance measurements in a non-shielded configuration, applying 100 mV sinusoidal waveform in a frequency range from 5 Hz to 1 MHz. Four metal pads to connect High/Low Potential and Current were fabricated depositing silver paste on the PEGDA:PEDOT sample (45 wt.% of PEDOT), which was made of three layers (i.e. ~150 μm/layer) 3D printed in the shape of a parallelepiped. Thickness (T) of the sample was equal to (0.05 ± 0.01) cm, the width (W) (0.5 ± 0.1) cm and the distance between the two extremal probes ($3S$) was approximately (1.7 ± 0.1) cm. The sheet impedance was measured and the bulk value was reported in Figure 77.
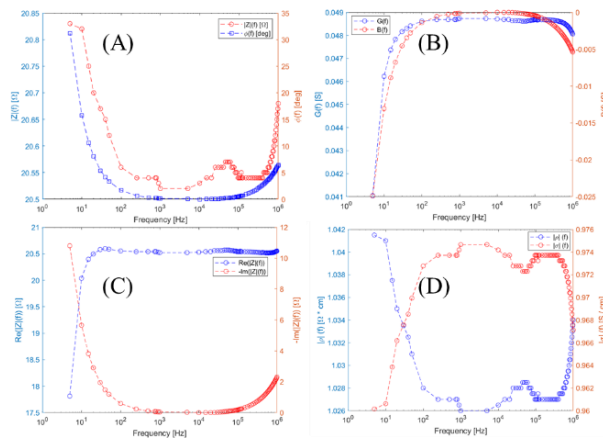
Figure 77: (A) modulus and phase of impedance measurement; (B) conductance and susceptance; (C) real and imaginary part of impedance measurement; (D) resistivity and conductivity modulus; Std. Err. < 1% of the measured values.

Eq. 86:
$$\begin{cases} Re[Z] = \dfrac{2}{\pi} \displaystyle\int_0^\infty \dfrac{\omega' * Im[Z(\omega')]}{\omega^2 - \omega'^2} d\omega' \\ Im[Z] = -\dfrac{2}{\pi} \displaystyle\int_0^\infty \dfrac{\omega' * Re[Z(\omega')]}{\omega^2 - \omega'^2} d\omega' \end{cases}$$

To check the validity of the measurements the Kramers-Kronig transformation was applied in a more sophisticated formulation[224] rather than the classical form expressed in Eq. 86, employing an automated μ-criterion[225] to get the optimal number of fitting RC circuits[226], avoiding ambiguous results. Fit results and measured values are compared in Figure 78A-B. According to the value of reduced chi-squared equal to 0.73, the goodness of these measures was accepted.
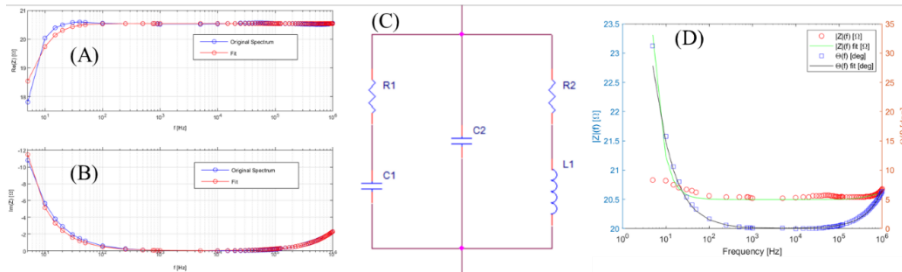
Figure 78: Linear Kramers-Kronig validity test fit[225] of the real (A) and imaginary (B) part of the impedance; (C) Impedance test fit circuit; (D) Impedance fit results.

Considering figure Figure 77A-B there is evidence of a small variation in impedance modulus, while the phase decreases at low frequency and starts to increase again at high frequency. These phenomena can be explained and modelled as the effect of two parallel circuits, capacitive and inductive, whose impedance is compensated in modulus. The circuit proposed in Figure 78C is tested to fit the experimental data, through numerical minimization of the chi-squared objective function defined as in Eq. 87:

Eq. 87: $\quad X^2 = \sum \left| \dfrac{Z_{fitted} - Z_{measured}}{|Z_{measured}|} \right|^2$

According to the purposed circuit these assumptions are done on each element: C2 is a parasitic capacitance of the experimental setup, R2 as the DC resistance and ESR (Equivalent Series Resistor) of the inductor L1, while R1 is the ESR of C1 capacitor. Besides, it is important to say that in the test frequency range the material behaves like an "embedded" gyrator circuit.

Eq. 88: $Z(f) = \dfrac{-C1\,L1\,R1\,s^2 - (L1 + C1\,R1\,R2)\,s - R2}{C1\,C2\,L1\,R1\,s^3 + (C2\,L1 - C1\,L1 + C1\,C2\,R1\,R2)\,s^2 + (C1\,R1 - C1\,R2 + C2\,R2)\,s + 1}$

When examining the limit condition of the circuit transfer function (Eq. 88), the two limits of the transfer function at zero and infinite (Eq. 90) of the complex frequency "s" are evaluated to define the R2 contribution to the impedance as the DC resistance, while the R1 as the AC resistance of the sample. The numerical minimization algorithm is started from the two probe DC resistance measured with a tester and the AC value obtained through impedancemetry and fitting values of the parasitic capacitance C2 are limited superimposing the condition of C2 much smaller than C1 and the best fit is obtained, values recalculated on the base of the approximated transfer function (Eq. 89) and graphed in Figure 78D.

Eq. 89: $\displaystyle \lim_{C2 \to 0} Z(f) = \dfrac{C1\,L1\,R1\,s^2 + (L1 + C1\,R1\,R2)\,s + R2}{C1\,L1\,s^2 + (R2 - R1)\,s - 1}$

Eq. 90: $\begin{cases} \displaystyle \lim_{\substack{C2 \to 0 \\ s \to 0}} Z(f) = R2 \;\; ; \; short\ circuit\ condition \\[2em] \displaystyle \lim_{\substack{C2 \to 0 \\ s \to \infty}} Z(f) = R1 \;\; ; \; open\ circuit\ condition \end{cases}$

According to the value of reduced chi-squared ($x^2 = 0.68$) best fit results are accepted, resulting in the following values, reported in Eq. 91:

Eq. 91: $\begin{cases} C2 = (967.2 \pm 53.4)\ [pF] \\ C1 = (2.81 \pm 0.9)\,[mF] \\ R1 = (20.9 \pm 0.4)\,[\Omega] \\ L1 = (166.0 \pm 1.5)\,[uH] \\ R2 = (990 \pm 65)\,[\Omega] \end{cases}$

Examining the RL circuit as the contribution to the DC resistance and the parallel RC circuit as the ac contribution to the impedance, the following hypothesis can be presented: the DC contribution may be explained as due to the contribution of electronic charge transfer along the chain of delocalized electrons, while the AC contribution can be modelled as an incoherent hopping of charges between different polymer chains, described by Mott's Variable Range Hopping and producing a capacitive effect. A further explanation of the inductive behaviour will be treated later in this chapter.

5.4 Impedance spectroscopy of not DMSO-treated samples

After the removal of DMSO treatment in the resin preparation process, the new samples were tested in a revised four probe impedance setup, reported in Figure 79A. This setup consisted of multiple 3D printed templates interchangeable to perform different dispositions of the four probes. Gold plated phosphor bronze probes were acquired by RS (RS PRO Test Pin 3A) with a contact area on the sample equal to 0.64 mm. Performing a pre-positioning operation, also referred to as Z-alignment, of the four probes in the template, equally distanced of 5 mm and screwing the grain to lock their position, the subsequent LCR Meter calibration or trimming procedure is performed.

This task requires to perform for the overall impedance spectrum (20 Hz – 10 MHz) the offset compensation for the condition of open (i.e. O/C) and short (i.e. S/C) circuit by tuning the instrument in the two conditions. The first is set up by connecting both the HC with the HP terminal and the LC with the LP terminal. The latter instead is set up by connecting together all the terminals. The calibration procedure is needed to eliminate the contributions of stray capacitance and series impedance from the measurement.

The revised setup (Figure 79B) is equipped with a translational Z-axis to perform a pressing operation of the probe contact area on the sample surface in order to guarantee a good mechanical contact by interference of the probe with the medium, as in Figure 79C.

Modelling and characterization of electronic conductivity in 3D printed PEGDA:PEDOT polymer composites - High frequency applications

149
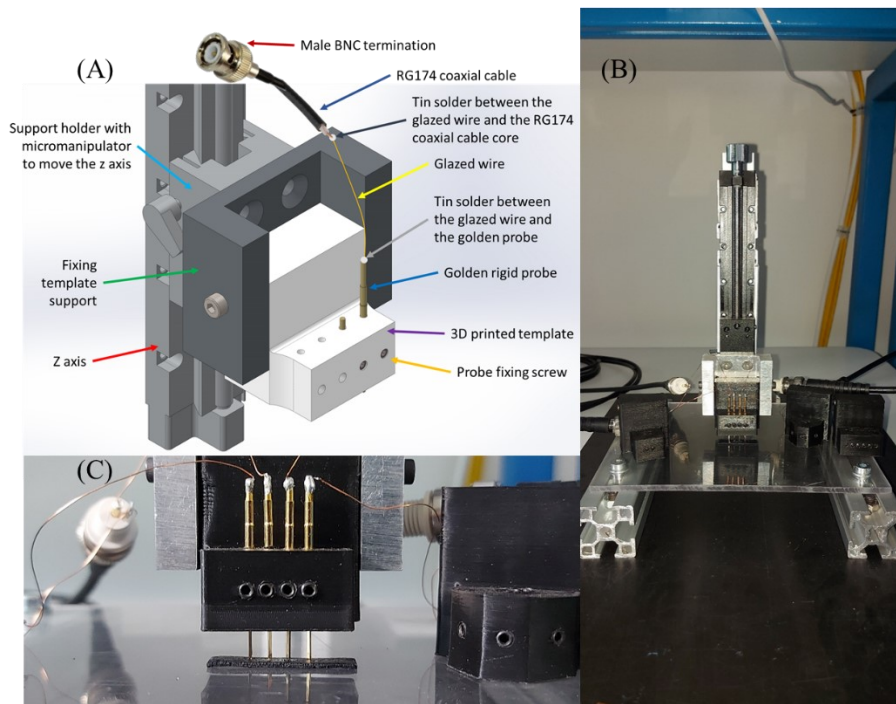
Figure 79: (A) Revised four terminal-pair impedance setup with aligned four probes; (B) Revised setup with interchangeable 3D printed template for non-aligned probe distribution and moving Z-axis; (C) Detail of the template with a test sample.

The GW-Instek LCR-8110G Precision LCR Meter presented in the accuracy chart (Figure 80) the relative standard error (Std. Err.) on the measured impedance modulus depending on the frequency.
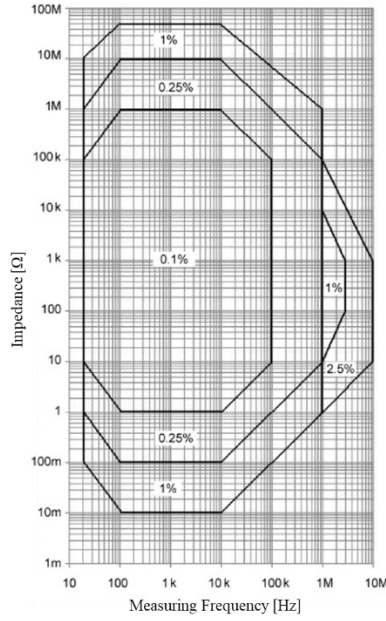
Figure 80: GW-Instek LCR-8110G Precision LCR Meter – Impedance magnitude
accuracy chart[227].

In order to evaluate the non-standardization of the process (i.e. repeatability), that
is the capability of the printing process to produce geometrically and electrically
identical samples in the same printing, five No-DMSO-treated PEGDA:PEDOT
samples (35 wt.% of PEDOT) were 3D printed in the shape of parallelepiped of
length (28.4 ± 0.1) mm, width (7.4 ± 0.1) mm and thickness (0.9 ± 0.1) mm,
corresponding to 18 layers (i.e. ~50 µm/layer), were produced and characterized
with impedance spectroscopy measurements, in the revised setup.

To extend this analysis the complex dielectric permittivity[228] ε and electric
modulus[229] M, in fact if SCL transport provides a high contribution to the
conductivity, relaxations peaks are not so well recognisable in permittivity graphs
as in imaginary electric modulus spectra[230]. Considering a shape factor $G_f = \frac{Contact\ surface}{Sample\ thickness}$ to evaluate corrections due to the experimental setup, the previous
quantities were derived as in Eq. 92:

$$\text{Eq. 92:} \quad \begin{cases} \varepsilon^{|} = -\dfrac{Z^{||}}{|Z|^2 \varepsilon_0 \omega G_f} \\ \varepsilon^{||} = \dfrac{Z^{|}}{|Z|^2 \varepsilon_0 \omega G_f} \end{cases} \text{and} \quad \begin{cases} M^{|} = -Z^{||}\varepsilon_0 \omega G_f \\ M^{||} = Z^{|}\varepsilon_0 \omega G_f \end{cases}$$

To further extend the data analysis, the AC conductivity is calculated (Eq. 93) in the formalism of the "Universal Power Law" of Jonscher[231]. The law states that the AC conductivity can be modelled as sum of a DC frequency-constant and temperature-dependant conductivity (i.e. σ_{DC}) with a frequency-dependant term (i.e. $A\omega^p$), which is due to a charge hopping transport contribution, defined by a hopping time constant (i.e. τ_p) and a hopping frequency (i.e. ω_p)[232].

$$\text{Eq. 93:} \quad \begin{cases} \sigma_{AC} = \sigma_{DC} + A\omega^p = \sigma_{DC}\left(1 + \left(\dfrac{\omega}{\omega_p}\right)^p\right) \\[2ex] \omega_p = \left(\dfrac{\sigma_{DC}}{A}\right)^{\frac{1}{p}} ; \tau_p = \dfrac{2\pi}{\omega_p} \end{cases}$$

Due to the conformation of the setup (Figure 79A) it is possible to characterize either the top or the bottom surface at the same time. The modulus impedance and the phase shift were measured to calculate firstly the top and bottom resistance and reactance, reported in Figure 81.
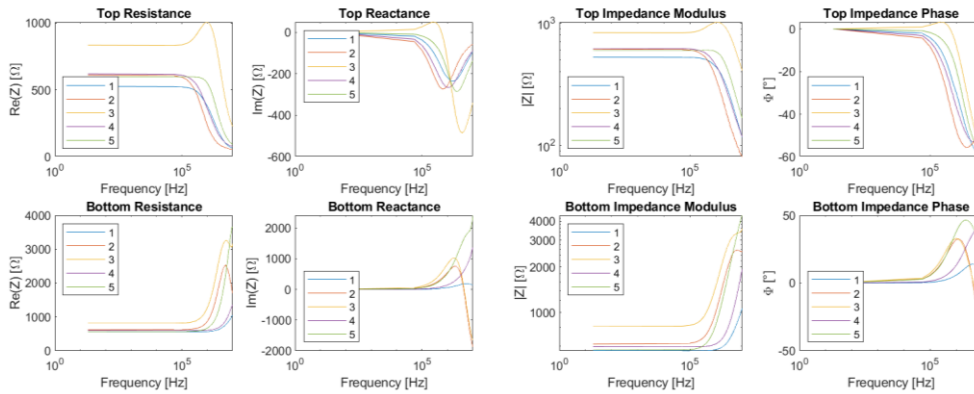
Figure 81: Impedance modulus, phase shift, reactance and resistance of top or bottom measures for five samples.

Despite the evidence, in Figure 81, of the inhomogeneity between different samples, common trends can be examined: in terms of the graphed physical quantities, top and bottom exhibit different behaviours: considering a RC circuit parallel to an RL circuit as in Figure 78C, but without capacitor C2, it is possible to state that the test circuit can model both the top and the bottom impedance transfer function, in fact considering for both the case studies common inductor and resistor values and varying only the quantity C1 the same experimental behaviour is obtained by applying for the capacitance value of the bottom a lower value than for

the top surface ($C1_{Bottom} \ll C1_{Top}$). This evaluation is explained by the following consideration: during the photopolymerization process the bottom layer is the adhesion layer, which is attached to the glass plate of the 3D printer, for this reason the face in direct contact with the glass does not have the oxygen contribution to the radicalization process, instead the top surface is the last layer to be photopolymerized receiving a much greater oxygen contribution to the process. Oxygens attribute an insulating behaviour to the surface of the sample and the more oxygen concentration on the surface the more C1 value is higher.
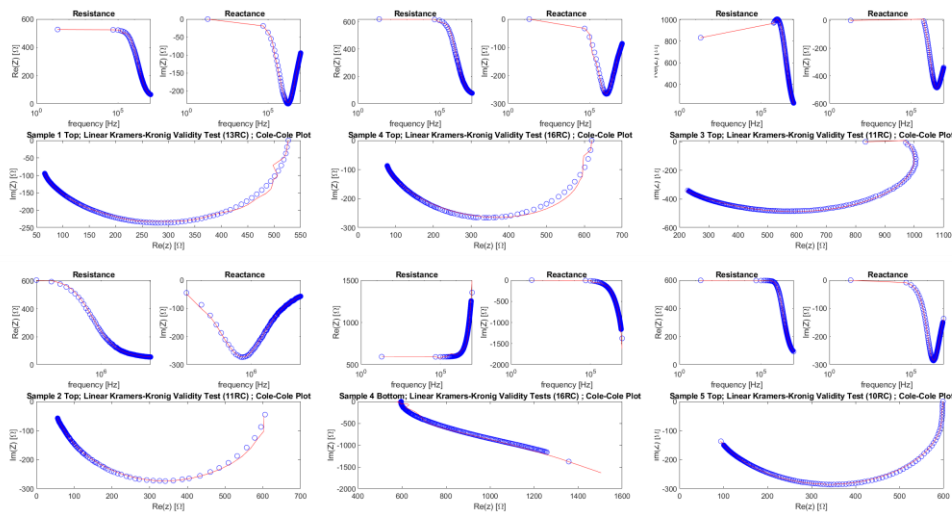
Figure 82: Resistance, reactance and Cole-Cole plot with Linear Kramers-Kronig validity test fit[225] of different sample surfaces with multiple RC compensation.

To proceed in the analysis the Linear KK validity test (Figure 82) was performed in order to validate the physical meaning of the measurements and to prevent data analysis of systematic error affected measures.

As expressed in Eq. 92 the real and imaginary part of the dielectric permittivity were calculated from impedance measurements, focusing on the imaginary dielectric permittivity ($\varepsilon^{||}$) as a function of the frequency (Figure 83) and even the electric modulus is reported for completeness. In conductive polymeric networks, a linear decrease in the imaginary component of the dielectric permittivity is observable as in RC networks[233].
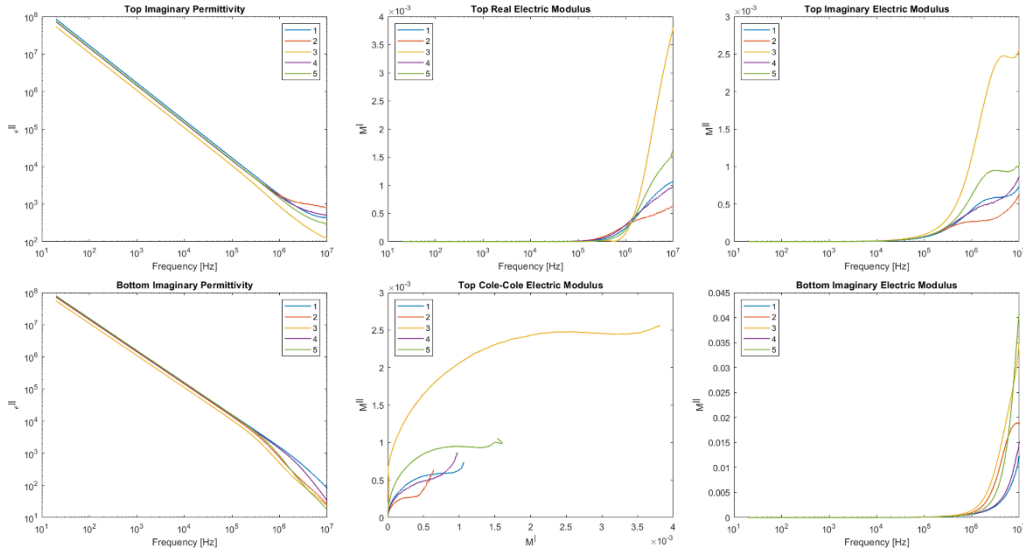
Figure 83: Top/Bottom imaginary part of the dielectric permittivity and electric modulus.

The final test circuit, purposed in Figure 84E, was fitted to the experimental data by the numerical minimization of the chi-squared function (i.e. objective function) in the space of the complex impedance. In order to establish a good fitting procedure, the objective function has been estimated as the chordal distance between the complex impedance measures and fitted values projected on the Riemann sphere[234], as expressed in Eq. 94, in fact this objective function was defined with the goal to reduce the discrepancy between the fitted impedance values and the measured, both for the real and the imaginary part, whereas defining the X^2 function only based on the modulus or phase shift led to the consequence of optimizing the agreement either the real or the imaginary part.

$$\text{Eq. 94: } X^2 = \sum_i \left\| \frac{2|Z_{fit,i} - Z_{measured,i}|}{\sqrt{|Z_{fit,i}|^2 + 1}\sqrt{|Z_{measured,i}|^2 + 1}} \right\|^2$$

Results of the test circuit purposed in Figure 84E, are reported in Figure 84A-D. it is evident, as discussed previously, that the top surface capacitance (C1) values are higher than bottom values, as believed due to the content of oxygen, while inductance (L1) values are higher in the bottom surface measurements.

In the resin preparation process the PSS content is removed from the PH1000 prepared, to obtain the PEDOT precipitate without the addiction of DMSO. This process variation may be justified in analytical terms by the inductance and capacitance values. Since the addiction of DMSO to remove the PSS causes a segregation of the residual PSS in the PEDOT rich material, this phenomenon produces electrically insulating islands in the conductive material, rising higher capacitive values as calculated previously in case of the DMSO-treated samples.
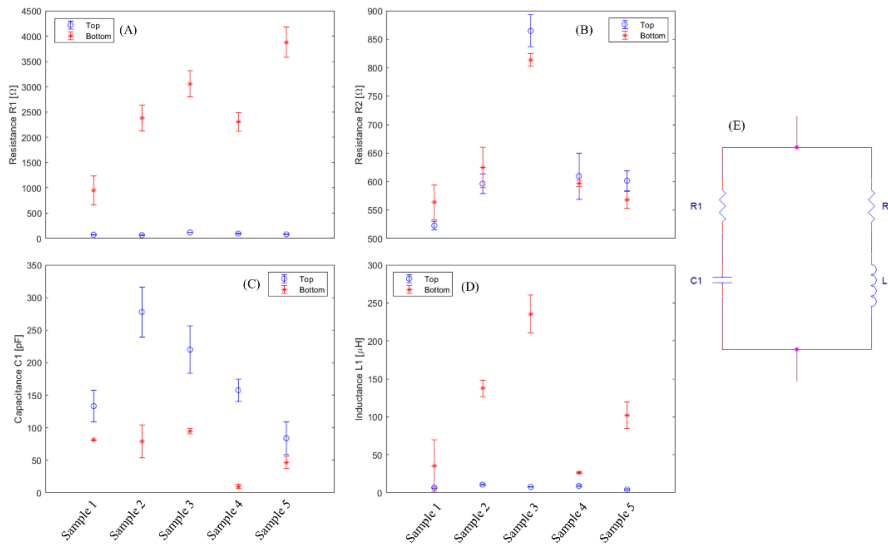
Figure 84: (A-D) Fitted values of the test circuit elements for all the samples and both surfaces; (E) Purposed test circuit.

Modelling and characterization of electronic conductivity in 3D printed PEGDA:PEDOT polymer composites - High frequency applications

155
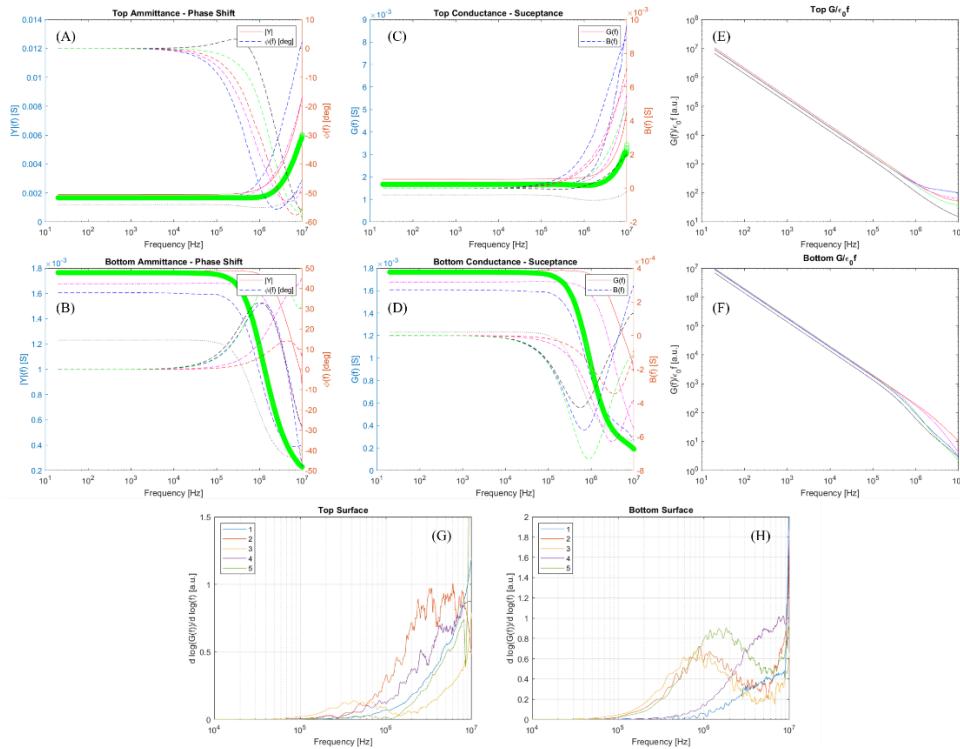
Figure 85: (A) Top surface Admittance |Y| and Phase shift Φ; (B) Bottom surface Admittance and Phase shift; (C-D) Top-Bottom surface Conductance G and Susceptance B; (E-F) Top-Bottom surface frequency-independent AC conductance (G/ε_0f); (G-H) Top-Bottom surface smoothed derivative of the frequency-independent AC conductance (d(log(G))/d(f)).

In order to evaluate the resonance frequency visible in the spectra the frequency-independent AC conductance is calculated as in Figure 85 for both top and bottom surfaces related to the previous five samples[235]. The derivative of the latter quantity is calculated and smoothed by Savitzky-Golay filter[236] to better fit the resonance frequency, through a chi-squared parabolic fit near the resonance peak and the following values were obtained for the bottom surface for samples from 1 to 5: (8.35 ± 0.32) MHz, (1.57 ± 0.21) MHz, (0.92 ± 0.08) MHz, (8.41 ± 0.31) MHz and (1.48 ± 0.12) MHz; for the top surface were calculated the frequencies of (4.07 ± 0.25) MHz and (9.46 ± 0.34) MHz for sample 2 and 4 since peaks are not visible in the other samples.

The presence in this frequency range of a unique relaxation peak, at very high frequency is in accordance with a unique conductor model, since only PEDOT constituent participate to the conduction[237], although it is mandatory to state that this analysis was performed on a limited frequency range and that the impedance

characteristic of this samples is unrecorded at higher frequencies (10 MHz-100 MHz). The conclusion on this analysis led to the classification of this resonance peaks as Debye peaks due to a thermal activated conduction mechanism with a characteristic frequency which follows an Arrhenius law[238] as $f_{max} = f_0 \exp\left(\frac{E_{activation}}{k_B T}\right)$. Finally, as reported in Figure 85, it is evident that the inductive contribution of the conduction mechanism on the bottom surface is far higher than the top surface[239]. The reason must be recorded in the oxygen inhibition of the photopolymerization process which increases the capacitive contribution on the to surface and decreases the inductive contribution on the bottom surface, since during the radical photopolymerization the benzoid and quinoid alternated chains are produced and from this bipolarons, the inhibition of this process decreases the probability of bipolaronic creation decreasing the inductive term. In case of inhibited photopolymerization (i.e. top surface) the density of bipolarons decreases and the contrary happens on the opposite surface (i.e. bottom) since no oxygen inhibition takes place[240]. As discussed in the previous chapter, bipolarons are characterized by a large effective mass which in case of in increased density, it is the reason of an increase in the inertial term. Describing in fact the system conduction mechanism as a classical harmonic oscillator (e.g. RLC oscillating circuit) the inductive contribution is related to the coefficient of the quadratic term in the 2nd-order linear differential equation ($L\frac{d^2 i}{dt^2} + R\frac{di}{dt} + \frac{1}{C}i = 0$, where "i" is the current and no external forcing is applied), generally connected with the effective mass matrix term in the mechanical harmonic oscillator ($[M]\frac{d^2 u}{dt^2} + [D]\frac{du}{dt} + [K]u = 0$, where "u" is the displacement and [M], [D], [K] are the inertia, viscous damping and stiffness matrices and no external forcing is applied).

5.4.1 Metal contact in two probe impedance spectroscopy

In order to estimate the effect of the metal contact in the impedance spectroscopy measures, a two probe measurement was performed using gold plated four terminal-pair Kelvin clips (GW Instek LCR-12). The setup was reduced to a two probe configuration using copper adhesive tape to short-circuit HC with HP terminals and LC with LP terminals. To determinate the contact area to evaluate the geometric correction facto G_f the length (L) of the clip was equal to (13.0 ± 0.1) mm and the width (W) (2.02 ± 0.01) mm.

For the two different metal contacts the measured and estimated physical quantities
were reported in Figure 86. The derived quantities were calculated on the base of
formula expressed in Eq. 92 and Eq. 93.
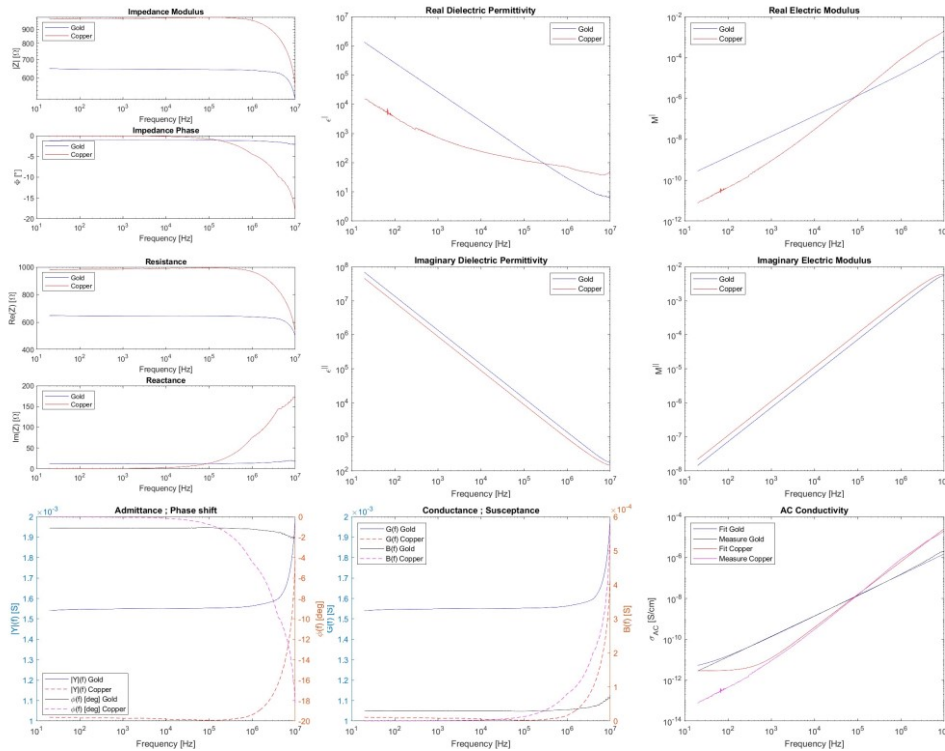
Figure 86: Comparison of the measured and estimated quantities with gold and
copper contact: Impedance modulus with phase shift, resistance, reactance admittance
with phase shift, conductance, susceptance, real and imaginary part of the dielectric
permittivity ε and electric modulus M; comparison of the AC conductivities σ_{AC} with
power-law fitted and measured values.

The Linear KK validity test was performed to check the presence of systematic
measurement errors and consequentially the data were fitted to an equivalent test
circuit (Figure 84E) where the inductive contribution was neglected and considered
as a short-circuit. Calculated capacitive and resistive parameters were for gold:
$R1 = (644 \pm 3) \, [\Omega]$, $C1 = (6.47 \pm 0.6) \, [pF]$ and $R2 = (5609 \pm 73) \, [\Omega]$ and
copper: $R1 = (983 \pm 7) \, [\Omega]$, $C1 = (13.9 \pm 0.3) \, [pF]$ and $R2 = (1481 \pm 34) \, [\Omega]$.

Since resonance peaks were not detectable in these measures, a detailed analysis
was performed on the AC conductivity behaviour of the two configurations. The
universal power law was fitted to the high frequency spectra to estimate the values
reported in Table 6.

Universal Power Law: $\sigma_{AC} = \sigma_{DC} + A\omega^p = \sigma_{DC}\left(1 + \left(\frac{\omega}{\omega_p}\right)^p\right)$		
Contact Metal	Gold	Copper
$\left(\sigma_{DC} \pm \sigma_{\sigma_{DC}}\right)\left[\frac{S}{cm}\right]$	$(2.8 \pm 0.3) \cdot 10^{-10}$	$(7.3 \pm 0.2) \cdot 10^{-12}$
$\left(A \pm \sigma_A\right)\left[\frac{S}{\sqrt[p]{Hz}}\right]$	$(1.8 \pm 0.01) \cdot 10^{-12}$	$(7.0 \pm 0.2) \cdot 10^{-16}$
$\left(p \pm \sigma_p\right)$	(1.01 ± 0.01)	(1.6 ± 0.01)
$\left(\omega_p \pm \sigma_{\omega_p}\right)[Hz]$	(144.6 ± 0.7)	(311 ± 5)
Regression Standard Error	0.001	0.002

Table 6: Comparison of the physical quantities calculated through the universal
power-law fitted measures.

Analysing and comparing the results obtained for gold and copper contact, charge
transport through the percolative network can be identified as the origin the DC
contribution (σ_{DC}) due to delocalized electrons moving in the $\pi - \pi$ stack. The
increment of σ_{DC} the in gold, respect to copper can be justified by the higher work
function of the first metal enabling the electron collector electrode to collect charges
more efficiently, by lowering the effective contact barrier potential.

The exponent "p" value is in general a temperature dependent term, in fact in case
$0 < p \lesssim 1$ it describes a thermally activated conduction mechanism due to a short
range hopping motion (i.e. translational hopping) conformal to a Debye behaviour.
In case of $p > 1$, a deviation from the Debye characteristic is present and the
hopping conduction mechanism is referred to a more localized hopping (i.e.
reorientational hopping), visible in the range of MHz frequencies[230].

The incoherent hopping of bipolarons between different polymer chains explains
the rise of σ_{AC}, in fact high resonance frequency peaks, referred to top and bottom
analysis, are associated with a high heterogeneous material structure linked to the

mean distance covered by bipolarons during the hopping process[228], in fact considering the hopping frequency value (ω_p), it is inversely proportional to the mean covered distance and to the inductive contribution. Following the previous argument, the increase in the hopping frequency is more related to a decrease in the mean path covered by bipolarons and also related to a density decrease of large bipolarons, carrying high charge values.

5.5   Broadband   spectroscopy   of   3D   printed PEGDA:PEDOT samples

Broadband spectroscopy characterizations were performed to analyse the behaviour of 3D printed PEGDA:PEDOT samples at very high frequencies in the GHz range. These measures were evaluated with the objective of producing a tree-dimensional 3D printed antenna, which could exploit the third dimension. In fact, in literature was found evidence of the use of PEDOT in the realisation of microstrip patch antennas tuned at 6 GHz[241] or at 5.8 GHz with a different geometric dimensioning[242]. PEDOT:PSS was employed even to produce an ethanol transducer based on transmission line circuit in the range of 0.5−2 GHz[243], whereas others reported that an optimized resin formulation allowed to obtain the electromagnetic transparency in the MHz range, lowering the plasma frequency, and realising a capacitive touch pressure transducer[244].

Broadband spectroscopy allowed to directly calculate the scattering parameters[245] of the designed sample (Figure 87A) in the cavity (Figure 87B), modelled as two port network, in the GHz range using a cylindrical coaxial cell (EpsiMu toolkit[246]), where the sample was contained as a dielectric spacer between a 3 mm and a 7 mm diameter conductors. Two conical components were connected to the cell, ensuring to fix the characteristic impedance at 50 Ohm, while cancelling mismatches and energy losses. An appropriately calibrated Rohde Schwarz ZVK Vector Network Analyzer, was connected to the cell. De-embedding[247] and the Nicolson-Ross-Weir transmission/reflection method[248] were exploited to calculate the complex dielectric permittivity of the sample.

Three samples with two different thicknesses and PEDOT concentrations were 3D printed (Figure 87C): 25 wt.% PEDOT with thickness 's' equal to 0.8 mm, 25 wt.%

PEDOT with thickness 's' equal to 1.1 mm, 15 wt.% PEDOT with thickness 's' equal to 0.8 mm and 15 wt.% PEDOT with thickness 's' equal to 1.1 mm.
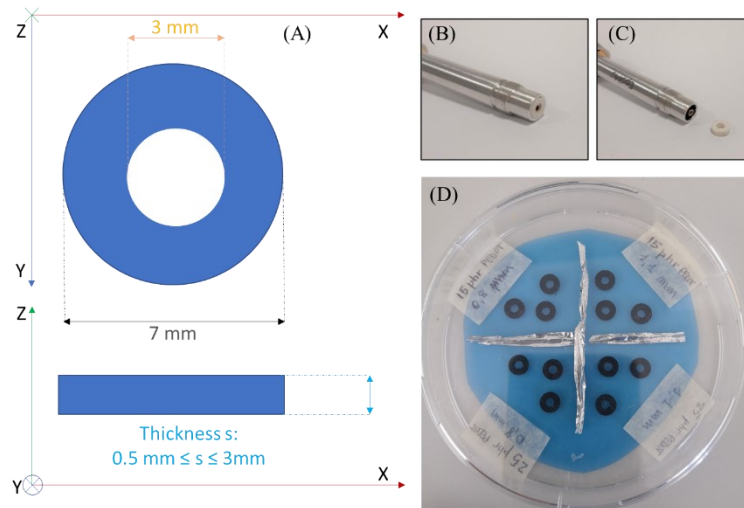
Figure 87: (A) Geometrical design of 3D printed PEGDA:PEDOT samples; (B) Cylindrical coaxial cell for broadband characterization; (C) 3D printed PEGDA:PEDOT test samples (i.e. DUT).

Each of the three samples (Figure 87D) per thickness and concentration were measured and the physical measured and derived quantities were statistically mediated over this population for each frequency in the measurement range of 0.1−16 GHz.

Scattering parameter, reported in Figure 88, were calculated in decibel as the $S_{ij} = 20\,log_{10}|s_{ij}|$, where s_{ij} is the coefficient of the forward or reverse fields at the input or output. S_{11} is defined as the "Input return loss", while S_{22} is the "Output return loss", S_{12} and S_{21} are respectively the "Reverse transmission gain" and the "Forward transmission gain".
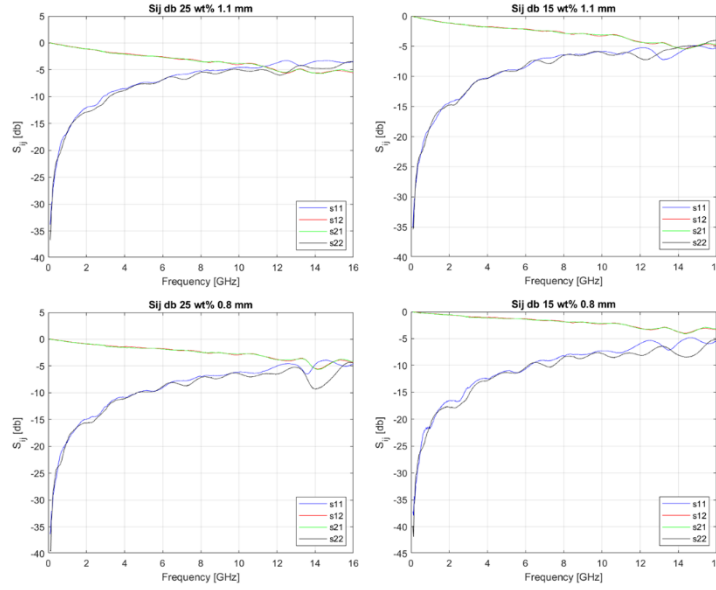
Figure 88: Measured scattering parameters (S_{ij}) of the four DUT.

It is evident in Figure 88 as due to the cylindrical symmetry of the system, since scattering matrix parameters were calculated from amplitude of the electric field, which is contained in the circular crown defined by the 3D printing plane, that $S_{21} = S_{12}$ because the network is symmetric and lossy.

$$
\text{Eq. 95:} \quad
\begin{cases}
\sigma = \varepsilon_0 \varepsilon^{||} \omega \left[\dfrac{S}{cm} \right] \\[2mm]
\tan(\delta) = \dfrac{1 + |S_{11}|}{1 - |S_{11}|} \\[2mm]
Input\ VSWR = \dfrac{\omega \varepsilon^{||} + \sigma}{\omega \varepsilon^{|}} \\[2mm]
IL = 20 \log_{10} \left(\dfrac{P_{out}}{P_{in}} \right) = 10 \log_{10} \left(\dfrac{1 - |S_{11}|^2}{|S_{21}|^2} \right) \\[2mm]
L_R = 10 \log_{10} (1 - |S_{11}|^2 - |S_{21}|^2) \\[2mm]
\hat{n} = \sqrt{\varepsilon^{|} + i\varepsilon^{||}} = n + ik = n - i \dfrac{\lambda \alpha}{4\pi}
\end{cases}
$$

Further physical quantities were calculated in order to evaluate a wide range of electromagnetic properties at high frequencies (Eq. 95): the conductivity σ, the delta tangent ($\tan(\delta)$) were the high frequency electrical characteristics related to the material, whereas the input standing wave ratio ($Input\ VSWR$), the insertion loss (IL) and the radiation loss (L_R) were calculated parameters related to the

device[249], or more specifically to its geometrical shape and finally the real (n) and imaginary (k) components of the complex refractive index ($\hat{n}$)[250], together with the material absorption coefficient (α), were estimated as function of the wavelength (λ). These parameters are reported in Figure 89 and Figure 90.
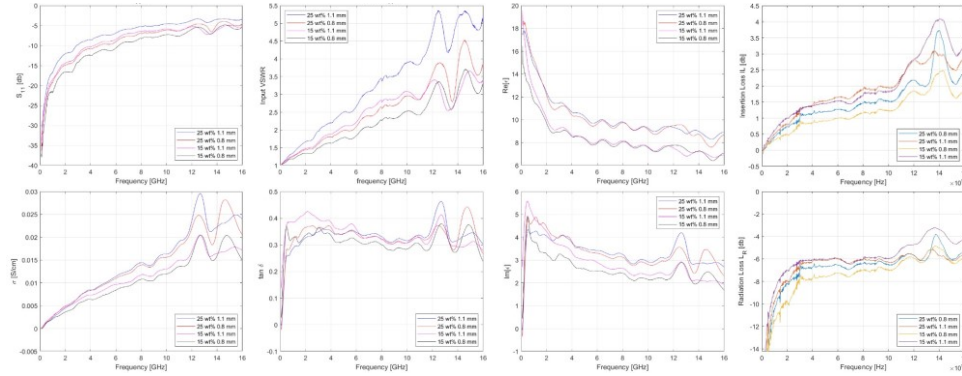
Figure 89: Measured S_{11} and calculated conductivity (σ), delta tangent
(***Input VSWR***), input standing wave ratio (σ), real and imaginary dielectric permittivity
(ε), insertion loss (***IL***) and radiation loss (L_R)[251].

It is observable in Figure 89, that increasing the PEDOT filler concentration increases the conductivity of almost the 50% causing no considerable increment in losses expresses by the delta tangent. Analysing the *Input VSWR* around 13 GHz, almost the 36% of the power delivered to the sample is reflected by the antenna device, which still can be considered acceptable for an antenna device, in fact L_R are marginally constant around -6 dB, while the *IL* exhibit a significant increase of lost power in the medium respect to the amount provided above 11 GHz.

Regarding the dielectric permittivity (Figure 90) it is observable a net increase in the real and imaginary components respect to the increase in the amount of filler content, which can be explained in a two media system as the geometrical mean of the dielectric permittivities. This increment is more significant in the real components, which is reflected in the refractive index, despite the k values, in fact even the absorption coefficient exhibits a unique behaviour.

Modelling and characterization of electronic conductivity in 3D printed
PEGDA:PEDOT polymer composites - High frequency applications

163
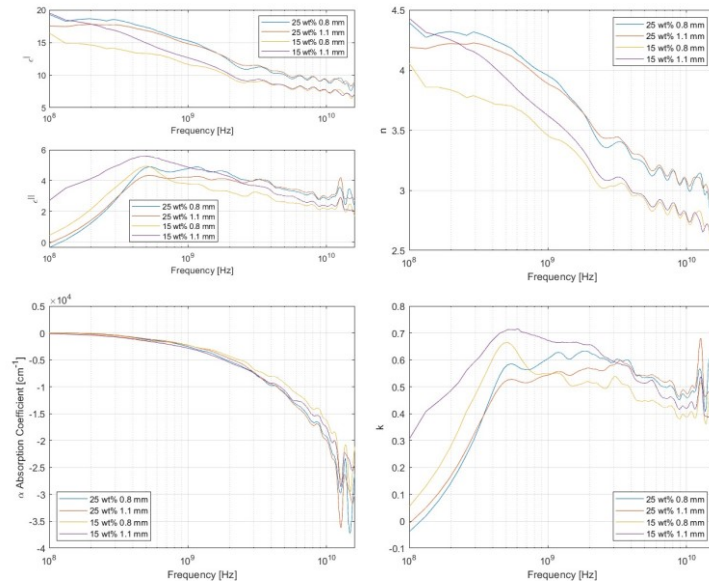
Figure 90: Log scale plot of the real ($\varepsilon^{|}$) and imaginary ($\varepsilon^{||}$) pert of the dielectric permittivity, real (n) and imaginary (k) pert of the refractive index and absorption coefficient (α).

In conclusion, especially in the conductivity measures in Figure 89, the presence of two resonance peaks was observed. The first around (12.6 ± 0.1) GHz and the latter around (14.7 ± 0.1) GHz for samples with thickness equal to 0.8 mm, moving to (15.5 ± 0.1) GHz, with a reduced intensity and increased broadening, for samples with thickness equal to 1.1 mm. The presence of these absorption peaks with increased Insertion loss, not corresponding to a significant increment in the Radiation loss, proves that these resonances are not radiative phenomena, probably related to the unsuccessful incoherent bipolaron hopping, due to inelastic scattering with the grain borders or inhomogeneities (Figure 67). As consequence, a possible exploitation of these peaks could be a high frequency antenna force or pressure transduces, capable of measuring, with very high accuracy, the force connected to the deformation though the frequency shift of the peaks.

5.6 3D printed PEGDA:PEDOT prototypes and applications

A wide range of 3D printed prototypes was designed targeted to different applications. Several objects were manufactured to test the printability property of the resin formulation, related to the printing process parameters (Figure 91A). Others, instead, were printed with the final purpose of optimizing the photopolymerized resin conductivity by balancing the relative mass fractions of PEGDA, PEDOT, Photoinitiator and Surfactant.
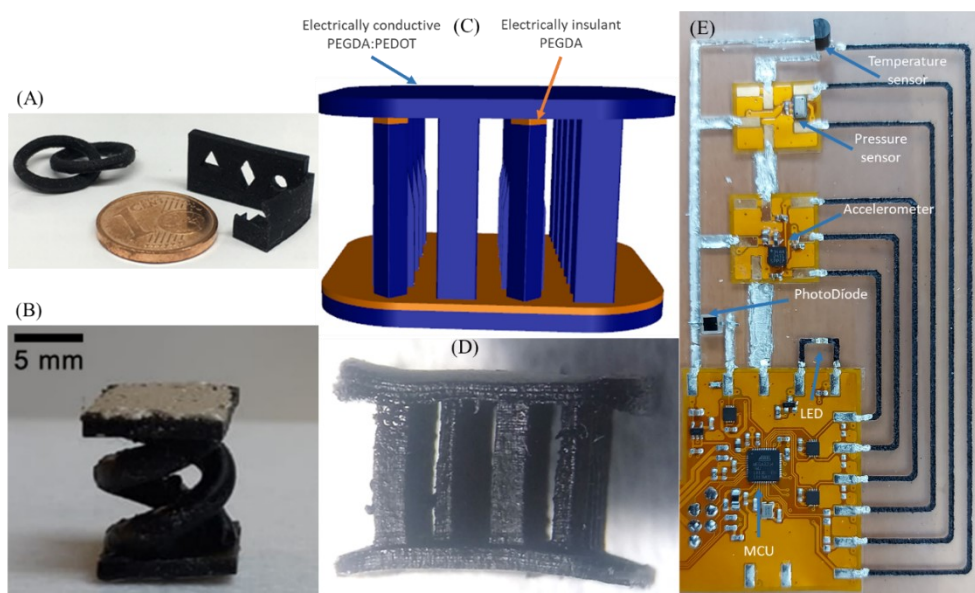
Figure 91: (A) General 3D printed objects; (B) Double helix ethanol gas transducer; (C) CAD design of the 3D printed PEGDA:PEDOT supercapacitor; (D) 3D printed supercapacitor prototype; (E) 3D printed high speed signal and analog traces connected to multiple flexible printed circuit boards.

With regard to applications such as sensors, a double helix device[207] was produced acting as an ethanol or acetone gas transducer. The capability to adsorb ethanol and acetone vapours of the stereolithographic 3D printed PEGDA:PEDOT device was tested under I/V characterization at fixed different exposure times. The device conductivity was measured in air at ambient temperature to be $\sigma \approx 55$ mS/cm and it was noted that under acetone exposure the conductivity decrease was more rapid respect to the ethanol exposure, in particular the steady value of conductivity was reached after 20 minutes of exposure time, with negligible variation between 1.4

Modelling and characterization of electronic conductivity in 3D printed PEGDA:PEDOT polymer composites - High frequency applications

165

mS/cm and 0.9 mS/cm at 60 and 120 minutes. The resistance of the double helix device increased of the 90% under vapour exposure (Figure 91B) leading to its possible exploitation as a VOC (i.e. volatile organic compound) adsorbent device.

In terms of embedded devices, a sub-millimetre supercapacitive device was designed (Figure 91C) and 3D printed in PEGDA:PEDOT (Figure 91D), with 45 filler wt.% and the measured weight-normalised gravimetric capacitance $C_S = 200$ mF/g, with energy density $J_E = 27.8$ µWh/g and power density $J_P = 4$ mW/g. The reported values were considered advantageous for energy storage and harvesting in low power Internet of Things (i.e. IoT) applications, with comparable or superior values respect to the literature reported for PEDOT based supercapacitors[252][253].

In the end, due to the fact that the photopolymerized resin exhibits an excellent impedance behaviour, which is maintained constant until the cut-off frequency in the MHz range, 3D printed PEGDA:PEDOT was employed to fabricate traces in an advanced prototypal printed circuit board. A microcontroller (i.e. MCU) based flexible printed circuit board was connected to other pheripherals and sensors, via 3D printed PEGDA:PEDOT traces, in the context of the regional funded project "SMART3D", as reported in Figure 91E. The MCU was capable of sampling the voltage signal of the temperature and pressure sensor (commercially available). The signal reading of the photodiode was also acquired, through silver paste traces, although the current driving of the LED was successfully performed via the PEGDA:PEDOT traces. In conclusion, the trace width and thickness were designed to exhibit a constant impedance until 2.5 MHz, in order to provide to the Accelerometer traces the impedance adaptation to 50 Ω, since the three traces carry high speed digital signals of the SPI peripherical from the MCU to the accelerometer and vice versa, at a fixed baud rate equal to 1 Mbps.

Chapter 6

Conclusions and perspectives

The primary topic of this dissertation was the modelling of the electronic conduction mechanism in 3D printed intrinsic conductive polymer composite materials. 3D printing technologies offer high degree of freedom to customize products and incorporate components, such as passive circuitry elements and sensors. The innovative idea of printing, directly through stereolithography, fundamental electronic components and sensors, allowing the manufacturing in the same printing process to overcome the flatness of traditional printed circuit boards and completely develop three-dimensional electronics, is the ultimate mission of the research.

The vision of this research activity was focused on an exhaustive investigation of the conduction phenomena in 3D printed PEGDA:PEDOT devices, since in literature a complete theory of the electrical conduction mechanism in intrinsic conductive polymers is missing. To accomplish this purpose, several PEGDA:PEDOT resin formulations were prepared and tested with different concentration of the constituents, varying also the photoinitiator and the surfactant mass fraction, with the final purpose of performing a design of experiment to optimize the conductivity of the photopolymerized material. After this accomplishment, the PEDOT filler concentration was parameterised to better understand the percolative nature of the DC conductivity, setting the percolation threshold, while minimizing the PEDOT concentration to increase the printability of 3D printed devices. Furthermore, to produce an ohmic contact with the polymeric device, the metal/polymer interface was analysed, while reducing the contact resistivity.

The extensive investigation on the conduction mechanism of 3D printed PEGDA:PEDOT polymer composite devices, performed from DC and impedancemetric measurements to broadband dielectric spectroscopy, led primarily to the explanation of the material conductivity as due to concurrent bipolaron

Modelling and characterization of electronic conductivity in 3D printed
PEGDA:PEDOT polymer composites - High frequency applications

167

incoherent hopping processes and percolative network electronic conduction and secondarily the development of an experimental and analytical rigorous methodology was accomplished and purposed. This procedure was targeted to the printing process calibration and optimization, with major focus on the final functionality of the 3D printed device and it was established on: the four coaxial terminal-pair impedance spectroscopy measures and their validation through the Linear Kramers-Kronig Transformation test, proceeding with the equivalent electrical circuit fit, based on the minimization of the Riemann chordal distance, in order to analyse the deconvolution of the different contributes to the complex impedance transfer function of the device. Regarding the material properties, the analysis of the AC conductivity, hopping and resonance frequencies and the frequency power exponent allowed the correlation of the estimated electrical circuit values with the latter, leading the calibration and optimization of the printing process parameters. Furthermore, broadband dielectric spectroscopy analysis was purposed to accomplish the fabrication of several devices with different final applications, such as: 3D printed high frequency embedded antenna sensors, signal traces for high speed signals ranging from the digital (i.e. $1-10$ MHz) to the RF (i.e. $1-16$ GHz) domains.

References

[1]   R. J. Young and P. A. Lovell, *Introduction to Polymers, Third Edition*. CRC Press, 2011.

[2]   S. Koltzenburg, M. Maskos, and O. Nuyken, *Polymer Chemistry*. Berlin Heidelberg: Springer-Verlag, 2017. doi: 10.1007/978-3-662-49279-6.

[3]   J. Bergström, "4 - Continuum Mechanics Foundations," in *Mechanics of Solid Polymers*, J. Bergström, Ed. William Andrew Publishing, 2015, pp. 131–207. doi: 10.1016/B978-0-323-31150-2.00004-2.

[4]   S. K. Joshi, *Thermal Behaviour of Amorphous Materials*. LAP LAMBERT Academic Publishing, 2012. Accessed: Jul. 02, 2021. [Online].   Available: https://www.morebooks.de/store/gb/book/thermal-behaviour-of-amorphous-materials/isbn/978-3-8465-8142-1

[5]   M. H. Harun, E. Saion, A. Kassim, N. Yahya, and E. Mahmud, "Conjugated Conducting Polymers: A Brief Overview," p. 7, 2007.

[6]   T.-H. Le, Y. Kim, and H. Yoon, "Electrical and Electrochemical Properties of Conducting Polymers," *Polymers*, vol. 9, no. 12, p. 150, Apr. 2017, doi: 10.3390/polym9040150.

[7]   X. Cao *et al.*, "A fluorescent conjugated polymer photocatalyst based on Knoevenagel polycondensation for hydrogen production," *New J. Chem.*, vol. 43, no. 18, pp. 7093–7098, May 2019, doi: 10.1039/C9NJ01686D.

[8]   C. K. Luscombe, U. Maitra, M. Walter, and S. K. Wiedmer, "Theoretical background on semiconducting polymers and their applications to OSCs and OLEDs," *Chem. Teach. Int.*, vol. 3, no. 2, pp. 169–183, Jun. 2021, doi: 10.1515/cti-2020-0020.

Modelling and characterization of electronic conductivity in 3D printed
PEGDA:PEDOT polymer composites - High frequency applications

169

[9]   B. Carsten, F. He, H. J. Son, T. Xu, and L. Yu, "Stille
        Polycondensation for Synthesis of Functional Materials," *Chem. Rev.*,
        vol. 111, no. 3, pp. 1493–1528, Mar. 2011, doi: 10.1021/cr100320w.

[10]   A. K. Mishra, "Conducting Polymers: Concepts and Applications," *J.
        At. Mol. Condens. Nano Phys.*, vol. 5, no. 2, pp. 159–193, Aug. 2018,
        doi: 10.26713/jamcnp.v5i2.842.

[11]   L. Akcelrud, "Electroluminescent polymers," *Prog Polym Sci*, p. 88,
        2003.

[12]   A. G. Macdiarmid and R. J. Mammone, "Polymer batteries and fuel
        cells having protic solvents and methods for their construction and
        use," EP0131829A1, Jan. 23, 1985 Accessed: Jul. 02, 2021. [Online].
        Available: https://patents.google.com/patent/EP0131829A1/en

[13]   S.-M. Kim *et al.*, "Influence of PEDOT:PSS crystallinity and
        composition on electrochemical transistor performance and long-term
        stability," *Nat. Commun.*, vol. 9, no. 1, p. 3858, Dec. 2018, doi:
        10.1038/s41467-018-06084-6.

[14]   M. Ates, T. Karazehira, and A. Sarac, "Conducting Polymers and their
        Applications," *Curr. Phys. Chem.*, vol. 2, pp. 224–240, May 2012,
        doi: 10.4028/www.scientific.net/MSF.42.207.

[15]   "Conducting Polymers and Classification of Conducting Polymers
        Notes," *semesters.in*, Sep. 19, 2014. https://semesters.in/conducting-
        polymers-and-classification-of-conducting-polymers-notes-pdf-ppt/
        (accessed Jul. 02, 2021).

[16]   C. D. Río and J. L. Acosta, "Extrinsic conducting and superconducting
        polymer systems. III. Electrical properties of PVDF/PS blends
        containing copper, carbon black, and YBaCuO fillers," *J. Appl.
        Polym. Sci.*, vol. 60, no. 1, pp. 133–138, 1996, doi:
        10.1002/(SICI)1097-4628(19960404)60:1<133::AID-
        APP15>3.0.CO;2-9.

[17]   R. Holze and Y. P. Wu, "Intrinsically conducting polymers in
        electrochemical energy technology: Trends and progress,"

Electrochimica Acta, vol. 122, pp. 93–107, Mar. 2014, doi: 10.1016/j.electacta.2013.08.100.

[18]   Y. Li and X. Wang, "Intrinsically Conducting Polymers and Their Composites for Anticorrosion and Antistatic Applications," in *Semiconducting Polymer Composites*, John Wiley & Sons, Ltd, pp. 269–298. doi: 10.1002/9783527648689.ch10.

[19]   A. D. Jenkins, "Photoinitiators for free radical cationic and anionic photopolymerisation, 2nd edition J V Crivello and K Dietliker Edited by G Bradley John Wiley & Sons, Chichester 1998. pp ix + 586, £ 90.00 ISBN 0-471-97892-2," *Polym. Int.*, vol. 49, no. 12, pp. 1729–1729, 2000, doi: 10.1002/1097-0126(200012)49:12<1729::AID-PI580>3.0.CO;2-D.

[20]   J. P. Fouassier, X. Allonas, and D. Burget, "Photopolymerization reactions under visible lights: principle, mechanisms and examples of applications," *Prog. Org. Coat.*, vol. 47, no. 1, pp. 16–36, Jul. 2003, doi: 10.1016/S0300-9440(03)00011-0.

[21]   L. Matějka, S. Pokorný, and K. Dušek, "Network formation involving epoxide and carboxyl groups," *Polym. Bull.*, vol. 7, no. 2, pp. 123–128, Apr. 1982, doi: 10.1007/BF00265462.

[22]   E. Andrzejewska, "Photopolymerization kinetics of multifunctional monomers," *Prog. Polym. Sci.*, vol. 26, no. 4, pp. 605–665, May 2001, doi: 10.1016/S0079-6700(01)00004-1.

[23]   F. Jiang and D. Drummer, "Curing Kinetic Analysis of Acrylate Photopolymer for Additive Manufacturing by Photo-DSC," *Polymers*, vol. 12, no. 5, p. 1080, May 2020, doi: 10.3390/polym12051080.

[24]   E.-G. Kim and J.-L. Brédas, "Electronic Evolution of Poly(3,4-ethylenedioxythiophene) (PEDOT): From the Isolated Chain to the Pristine and Heavily Doped Crystals," *J. Am. Chem. Soc.*, vol. 130, no. 50, pp. 16880–16889, Dec. 2008, doi: 10.1021/ja806389b.

[25]   A. M. Nardes *et al.*, "Microscopic Understanding of the Anisotropic Conductivity of PEDOT:PSS Thin Films," *Adv. Mater.*, vol. 19, no. 9, pp. 1196–1200, 2007, doi: 10.1002/adma.200602575.

[26]   G. Greczynski, T. Kugler, M. Keil, W. Osikowicz, M. Fahlman, and W. R. Salaneck, "Photoelectron spectroscopy of thin films of PEDOT–PSS conjugated polymer blend: a mini-review and some new results," *J. Electron Spectrosc. Relat. Phenom.*, vol. 121, no. 1, pp. 1–17, Dec. 2001, doi: 10.1016/S0368-2048(01)00323-1.

[27]   M. Dietrich, J. Heinze, G. Heywang, and F. Jonas, "Electrochemical and spectroscopic characterization of polyalkylenedioxythiophenes," *J. Electroanal. Chem.*, vol. 369, no. 1, pp. 87–92, May 1994, doi: 10.1016/0022-0728(94)87085-3.

[28]   L. Groenendaal, F. Jonas, D. Freitag, H. Pielartzik, and J. R. Reynolds, "Poly(3,4-ethylenedioxythiophene) and Its Derivatives: Past, Present, and Future," *Adv. Mater.*, vol. 12, no. 7, pp. 481–494, 2000, doi: 10.1002/(SICI)1521-4095(200004)12:7<481::AID-ADMA481>3.0.CO;2-C.

[29]   K. Kim and K. D. Jordan, "Comparison of Density Functional and MP2 Calculations on the Water Monomer and Dimer," *J. Phys. Chem.*, vol. 98, no. 40, pp. 10089–10094, Oct. 1994, doi: 10.1021/j100091a024.

[30]   P. J. Stephens, F. J. Devlin, C. F. Chabalowski, and M. J. Frisch, "Ab Initio Calculation of Vibrational Absorption and Circular Dichroism Spectra Using Density Functional Force Fields," *J. Phys. Chem.*, vol. 98, no. 45, pp. 11623–11627, Nov. 1994, doi: 10.1021/j100096a001.

[31]   "Essentials of Computational Chemistry: Theories and Models, 2nd Edition | Wiley," *Wiley.com*. https://www.wiley.com/en-us/Essentials+of+Computational+Chemistry%3A+Theories+and+Models%2C+2nd+Edition-p-9780470091821 (accessed Jul. 11, 2021).

[32]   A. D. Becke, "Density-functional thermochemistry. III. The role of exact exchange," *J. Chem. Phys.*, vol. 98, no. 7, pp. 5648–5652, Apr. 1993, doi: 10.1063/1.464913.

[33]   C. Alemán, E. Armelin, J. I. Iribarren, F. Liesa, M. Laso, and J. Casanovas, "Structural and electronic properties of 3,4-ethylenedioxythiophene, 3,4-ethylenedisulfanylfurane and thiophene oligomers: A theoretical investigation," *Synth. Met.*, vol. 149, no. 2, pp. 151–156, Mar. 2005, doi: 10.1016/j.synthmet.2004.12.012.

[34]   A. D. Becke, "Density-functional exchange-energy approximation with correct asymptotic behavior," *Phys. Rev. A*, vol. 38, no. 6, pp. 3098–3100, Sep. 1988, doi: 10.1103/PhysRevA.38.3098.

[35]   K. E. Aasmundtveit, E. J. Samuelsen, L. A. A. Pettersson, O. Inganäs, T. Johansson, and R. Feidenhans'l, "Structure of thin films of poly(3,4-ethylenedioxythiophene)," *Synth. Met.*, vol. 101, no. 1, pp. 561–564, May 1999, doi: 10.1016/S0379-6779(98)00315-4.

[36]   A. Lenz, H. Kariis, A. Pohl, P. Persson, and L. Ojamäe, "The electronic structure and reflectivity of PEDOT:PSS from density functional theory," *Chem. Phys.*, vol. 384, no. 1–3, pp. 44–51, Jun. 2011, doi: 10.1016/j.chemphys.2011.05.003.

[37]   Z. Hu, J. Zhang, Z. Hao, and Y. Zhao, "Influence of doped PEDOT:PSS on the performance of polymer solar cells," *Sol. Energy Mater. Sol. Cells*, vol. 95, no. 10, pp. 2763–2767, Oct. 2011, doi: 10.1016/j.solmat.2011.04.040.

[38]   J. Huang, P. F. Miller, J. C. de Mello, A. J. de Mello, and D. D. C. Bradley, "Influence of thermal treatment on the conductivity and morphology of PEDOT/PSS films," *Synth. Met.*, vol. 139, no. 3, pp. 569–572, Oct. 2003, doi: 10.1016/S0379-6779(03)00280-7.

[39]   Y.-J. Lin, F.-M. Yang, C.-Y. Huang, W.-Y. Chou, J. Chang, and Y.-C. Lien, "Increasing the work function of poly(3,4-ethylenedioxythiophene) doped with poly(4-styrenesulfonate) by ultraviolet irradiation," *Appl. Phys. Lett.*, vol. 91, no. 9, p. 092127, Aug. 2007, doi: 10.1063/1.2777147.

[40]   A. Moujoud, S. H. Oh, H. S. Shin, and H. J. Kim, "On the mechanism of conductivity enhancement and work function control in PEDOT:PSS film through UV-light treatment," *Phys. Status Solidi A*,

vol. 207, no. 7, pp. 1704–1707, May 2010, doi:
10.1002/pssa.200983711.

[41]   J. Ouyang, "'Secondary doping' methods to significantly enhance the
conductivity of PEDOT:PSS for its application as transparent
electrode of optoelectronic devices," *Displays*, vol. 34, no. 5, pp. 423–
436, Dec. 2013, doi: 10.1016/j.displa.2013.08.007.

[42]   X. Crispin *et al.*, "Conductivity, morphology, interfacial chemistry,
and stability of poly(3,4-ethylene dioxythiophene)–poly(styrene
sulfonate): A photoelectron spectroscopy study," *J. Polym. Sci. Part
B Polym. Phys.*, vol. 41, no. 21, pp. 2561–2583, 2003, doi:
10.1002/polb.10659.

[43]   J. Ouyang, Q. Xu, C.-W. Chu, Y. Yang, G. Li, and J. Shinar, "On the
mechanism of conductivity enhancement in poly(3,4-
ethylenedioxythiophene):poly(styrene sulfonate) film through solvent
treatment," *Polymer*, vol. 45, no. 25, pp. 8443–8450, Nov. 2004, doi:
10.1016/j.polymer.2004.10.001.

[44]   J. Y. Kim, J. H. Jung, D. E. Lee, and J. Joo, "Enhancement of electrical
conductivity of poly(3,4-ethylenedioxythiophene)/poly(4-
styrenesulfonate) by a change of solvents," *Synth. Met.*, vol. 126, no.
2, pp. 311–316, Feb. 2002, doi: 10.1016/S0379-6779(01)00576-8.

[45]   S. K. M. Jönsson *et al.*, "The effects of solvents on the morphology
and sheet resistance in poly(3,4-ethylenedioxythiophene)–
polystyrenesulfonic acid (PEDOT–PSS) films," *Synth. Met.*, vol. 139,
no. 1, pp. 1–10, Aug. 2003, doi: 10.1016/S0379-6779(02)01259-6.

[46]   H. Shi, C. Liu, Q. Jiang, and J. Xu, "Effective Approaches to Improve
the Electrical Conductivity of PEDOT:PSS: A Review," *Adv.
Electron. Mater.*, vol. 1, no. 4, p. 1500017, Apr. 2015, doi:
10.1002/aelm.201500017.

[47]   Y. Xia and J. Ouyang, "Significant Conductivity Enhancement of
Conductive   Poly(3,4-ethylenedioxythiophene):
Poly(styrenesulfonate) Films through a Treatment with Organic

Carboxylic Acids and Inorganic Acids," *ACS Appl. Mater. Interfaces*,
vol. 2, no. 2, pp. 474–483, Feb. 2010, doi: 10.1021/am900708x.

[48]   N. Kim *et al.*, "Highly Conductive PEDOT:PSS Nanofibrils Induced
by Solution-Processed Crystallization," *Adv. Mater.*, vol. 26, no. 14,
pp. 2268–2272, Apr. 2014, doi: 10.1002/adma.201304611.

[49]   A. M. Nardes, R. A. J. Janssen, and M. Kemerink, "A Morphological
Model for the Solvent-Enhanced Conductivity of PEDOT:PSS Thin
Films," *Adv. Funct. Mater.*, vol. 18, no. 6, pp. 865–871, 2008, doi:
10.1002/adfm.200700796.

[50]   K. Sun *et al.*, "Review on application of PEDOTs and PEDOT:PSS in
energy conversion and storage devices," *J. Mater. Sci. Mater.
Electron.*, vol. 26, no. 7, pp. 4438–4462, Jul. 2015, doi:
10.1007/s10854-015-2895-5.

[51]   D. Mantione, I. Del Agua, A. Sanchez-Sanchez, and D. Mecerreyes,
"Poly(3,4-ethylenedioxythiophene) (PEDOT) Derivatives: Innovative
Conductive Polymers for Bioelectronics," *Polymers*, vol. 9, no. 8, Art.
no. 8, Aug. 2017, doi: 10.3390/polym9080354.

[52]   "Introduction to 3D printing - additive processes | Make."
https://make.3dexperience.3ds.com/processes/introduction-to-
additive-processes (accessed Jul. 26, 2021).

[53]   G. Suresh and G. Suresh, "Advancements in Manufacturing
Technology With Additive Manufacturing and Its Context With
Industry   4.0,"   *https://services.igi-
global.com/resolvedoi/resolve.aspx?doi=10.4018/978-1-7998-4939-
1.ch001*,   Jan.   01,   1AD.   https://www.igi-
global.com/gateway/chapter/261179 (accessed Jul. 26, 2021).

[54]   J. Lee, H.-C. Kim, J.-W. Choi, and I. H. Lee, "A review on 3D printed
smart devices for 4D printing," *Int. J. Precis. Eng. Manuf.-Green
Technol.*, vol. 4, pp. 373–383, Jul. 2017, doi: 10.1007/s40684-017-
0042-x.

[55]   C. Y. Foo, H. N. Lim, M. A. Mahdi, M. H. Wahid, and N. M. Huang, "Three-Dimensional Printed Electrode and Its Novel Applications in Electronic Devices," *Sci. Rep.*, vol. 8, no. 1, p. 7399, May 2018, doi: 10.1038/s41598-018-25861-3.

[56]   N. Saengchairat, T. Tran, and C.-K. Chua, "A review: additive manufacturing for active electronic components," *Virtual Phys. Prototyp.*, vol. 12, no. 1, pp. 31–46, Jan. 2017, doi: 10.1080/17452759.2016.1253181.

[57]   F. Baldassarre and F. Ricciardi, "The Additive Manufacturing in the Industry 4.0 Era: The Case of an Italian FabLab," *J. Emerg. Trends Mark. Manag.*, vol. 1, no. 1, pp. 105–115, 2017.

[58]   J. Wade, J. R. Hollis, and S. Wood, *Printed Electronics*. IOP Publishing, 2018. doi: 10.1088/978-0-7503-1608-8.

[59]   "Printed Electronics: Materials, Technologies and Applications | Wiley," *Wiley.com*. https://www.wiley.com/en-us/Printed+Electronics%3A+Materials%2C+Technologies+and+Ap plications-p-9781118920923 (accessed Jul. 26, 2021).

[60]   I. Grunwald *et al.*, "Surface biofunctionalization and production of miniaturized sensor structures using aerosol printing technologies," *Biofabrication*, vol. 2, no. 1, p. 014106, Mar. 2010, doi: 10.1088/1758-5082/2/1/014106.

[61]   "Femtoliter-Scale Patterning by High-Speed, Highly Scaled Inverse Gravure Printing | Kitsomboonloha, Rungrot; Morris, S. J. S.; Rong, Xiaoying; Subramanian, Vivek | download." https://ur.booksc.eu/book/18624426/a87b7c (accessed Jul. 26, 2021).

[62]   "Room-temperature mixed-solvent-vapor annealing for high performance perovskite solar cells - Journal of Materials Chemistry A (RSC Publishing)." https://pubs.rsc.org/en/content/articlelanding/2016/ta/c5ta08565a#!di vAbstract (accessed Jul. 26, 2021).

[63]   C.-M. Chan, T.-M. Ko, and H. Hiraoka, "Polymer surface modification by plasmas and photons," *Surf. Sci. Rep.*, vol. 24, no. 1, pp. 1–54, May 1996, doi: 10.1016/0167-5729(96)80003-3.

[64]   C. E. Hendriks, P. J. Smith, J. Perelaer, A. M. J. van den Berg, and U. S. Schubert, "'Invisible' Silver Tracks Produced by Combining Hot-Embossing and Inkjet Printing," *Adv. Funct. Mater.*, vol. 18, no. 7, pp. 1031–1038, 2008, doi: 10.1002/adfm.200601062.

[65]   Y. S. Kim *et al.*, "Highly conductive and hydrated PEG-based hydrogels for the potential application of a tissue engineering scaffold," *React. Funct. Polym.*, vol. 109, pp. 15–22, Dec. 2016, doi: 10.1016/j.reactfunctpolym.2016.09.003.

[66]   R. K. Pal, E. E. Turner, B. H. Chalfant, and V. K. Yadavalli, "Mechanically robust, photopatternable conductive hydrogel composites," *React. Funct. Polym.*, vol. 120, pp. 66–73, Nov. 2017, doi: 10.1016/j.reactfunctpolym.2017.09.006.

[67]   A. Sabnis, M. Rahimi, C. Chapman, and K. T. Nguyen, "Cytocompatibility studies of an in situ photopolymerized thermoresponsive hydrogel nanoparticle system using human aortic smooth muscle cells," *J. Biomed. Mater. Res. A*, vol. 91, no. 1, pp. 52–59, Oct. 2009, doi: 10.1002/jbm.a.32194.

[68]   "Controllable properties and microstructure of hydrogels based on crosslinked poly(ethylene glycol) diacrylates with different molecular weights - Zhang - 2011 - Journal of Applied Polymer Science - Wiley Online Library." https://onlinelibrary.wiley.com/doi/abs/10.1002/app.33653 (accessed Jul. 26, 2021).

[69]   "Materials for Biomedical Applications," p. 36.

[70]   "Mechanical and cell viability properties of crosslinked low- and high-molecular weight poly(ethylene glycol) diacrylate blends - Mazzoccoli - 2010 - Journal of Biomedical Materials Research Part A - Wiley Online Library."

Modelling and characterization of electronic conductivity in 3D printed
PEGDA:PEDOT polymer composites - High frequency applications

177

https://onlinelibrary.wiley.com/doi/abs/10.1002/jbm.a.32563
(accessed Jul. 26, 2021).

[71]   P. J. Bártolo, "Stereolithographic Processes," in *Stereolithography: Materials, Processes and Applications*, P. J. Bártolo, Ed. Boston, MA: Springer US, 2011, pp. 1–36. doi: 10.1007/978-0-387-92904-0_1.

[72]   E. Andrzejewska and M. Andrzejewski, "Polymerization kinetics of photocurable acrylic resins," *J. Polym. Sci. Part Polym. Chem.*, vol. 36, no. 4, pp. 665–673, 1998, doi: 10.1002/(SICI)1099-0518(199803)36:4<665::AID-POLA15>3.0.CO;2-K.

[73]   T. N. Eren, N. Okte, F. Morlet-Savary, J. P. Fouassier, J. Lalevee, and D. Avci, "One-component thioxanthone-based polymeric photoinitiators," *J. Polym. Sci. Part Polym. Chem.*, vol. 54, no. 20, pp. 3370–3378, 2016, doi: 10.1002/pola.28227.

[74]   J. Manapat, Q. Chen, P. Ye, and R. Advincula, "3D Printing of Polymer Nanocomposites via Stereolithography," *Macromol. Mater. Eng.*, vol. 302, p. 1600553, May 2017, doi: 10.1002/mame.201600553.

[75]   A. Cavallo, M. Madaghiele, U. Masullo, M. G. Lionetto, and A. Sannino, "Photo-crosslinked poly(ethylene glycol) diacrylate (PEGDA) hydrogels from low molecular weight prepolymer: Swelling and permeation studies," *J. Appl. Polym. Sci.*, vol. 134, no. 2, 2017, doi: 10.1002/app.44380.

[76]   A. Urrios *et al.*, "3D-printing of transparent bio-microfluidic devices in PEG-DA," *Lab. Chip*, vol. 16, no. 12, pp. 2287–2294, Jun. 2016, doi: 10.1039/C6LC00153J.

[77]   F. Mochi *et al.*, "Advanced biocompatible photolithographic scaffolds for tissue engineering," p. 84 (4 .)-84 (4 .), Jan. 2016, doi: 10.1049/cp.2016.0944.

[78]   Y. Xia, K. Sun, and J. Ouyang, "Solution-Processed Metallic Conducting Polymer Films as Transparent Electrode of

Optoelectronic Devices," *Adv. Mater.*, vol. 24, no. 18, pp. 2436–2440, May 2012, doi: 10.1002/adma.201104795.

[79]   J. Parameswaranpillai, S. Thomas, and Y. Grohens, "Polymer Blends: State of the Art, New Challenges, and Opportunities," in *Characterization of Polymer Blends*, John Wiley & Sons, Ltd, 2014, pp. 1–6. doi: 10.1002/9783527645602.ch01.

[80]   I. Cruz-Cruz, M. Reyes-Reyes, M. A. Aguilar-Frutis, A. G. Rodriguez, and R. López-Sandoval, "Study of the effect of DMSO concentration on the thickness of the PSS insulating barrier in PEDOT:PSS thin films," *Synth. Met.*, vol. 160, no. 13, pp. 1501–1506, Jul. 2010, doi: 10.1016/j.synthmet.2010.05.010.

[81]   Z. Fan, D. Du, Z. Yu, P. Li, Y. Xia, and J. Ouyang, "Significant Enhancement in the Thermoelectric Properties of PEDOT:PSS Films through a Treatment with Organic Solutions of Inorganic Salts," *ACS Appl. Mater. Interfaces*, vol. 8, no. 35, pp. 23204–23211, Sep. 2016, doi: 10.1021/acsami.6b07234.

[82]   J.-B. Lee, K. Rana, B. H. Seo, J. Y. Oh, U. Jeong, and J.-H. Ahn, "Influence of nonionic surfactant-modified PEDOT:PSS on graphene," *Carbon*, vol. 85, pp. 261–268, Apr. 2015, doi: 10.1016/j.carbon.2014.12.101.

[83]   D. A. Mengistie, C.-H. Chen, K. M. Boopathi, F. W. Pranoto, L.-J. Li, and C.-W. Chu, "Enhanced Thermoelectric Performance of PEDOT:PSS Flexible Bulky Papers by Treatment with Secondary Dopants," *ACS Appl. Mater. Interfaces*, vol. 7, no. 1, pp. 94–100, Jan. 2015, doi: 10.1021/am507032e.

[84]   P. T. Hoang, H. Phung, C. T. Nguyen, T. Dat Nguyen, and H. R. Choi, "A highly flexible, stretchable and ultra-thin piezoresistive tactile sensor array using PAM/PEDOT:PSS hydrogel," in *2017 14th International Conference on Ubiquitous Robots and Ambient Intelligence (URAI)*, Jun. 2017, pp. 950–955. doi: 10.1109/URAI.2017.7992873.

[85]   U. Lange and V. M. Mirsky, "Chemiresistors based on conducting
        polymers: A review on measurement techniques," *Anal. Chim. Acta*,
        vol. 687, no. 2, pp. 105–113, Feb. 2011, doi:
        10.1016/j.aca.2010.11.030.

[86]   V. Bertana *et al.*, "3D Printed Active Objects based on the Promising
        PEDOT: PSS Resin: Investigation of their Integration inside an
        Electronic Circuit," *Int. J. Eng. Res. Technol.*, vol. 13, p. 462, Mar.
        2020, doi: 10.37624/IJERT/13.3.2020.462-469.

[87]   A. Elschner, S. Kirchmeyer, W. Lovenich, U. Merker, and K. Reuter,
        *PEDOT: Principles and Applications of an Intrinsically Conductive
        Polymer*, 0 ed. CRC Press, 2010. doi: 10.1201/b10318.

[88]   P. W. Anderson, "Absence of Diffusion in Certain Random Lattices,"
        Phys. Rev., vol. 109, no. 5, pp. 1492–1505, Mar. 1958, doi:
        10.1103/PhysRev.109.1492.

[89]   H. C. F. Martens, J. A. Reedijk, H. B. Brom, D. M. de Leeuw, and R.
        Menon, "Metallic state in disordered quasi-one-dimensional
        conductors," *Phys. Rev. B*, vol. 63, no. 7, p. 073203, Jan. 2001, doi:
        10.1103/PhysRevB.63.073203.

[90]   R. Noriega *et al.*, "A general relationship between disorder,
        aggregation and charge transport in conjugated polymers," *Nat.
        Mater.*, vol. 12, no. 11, pp. 1038–1044, Nov. 2013, doi:
        10.1038/nmat3722.

[91]   V. Coropceanu, J. Cornil, D. A. da Silva Filho, Y. Olivier, R. Silbey,
        and J.-L. Brédas, "Charge Transport in Organic Semiconductors,"
        Chem. Rev., vol. 107, no. 4, pp. 926–952, Apr. 2007, doi:
        10.1021/cr050140x.

[92]   "Soliton excitations in polyacetylene W. P. Su, J. R. Schrieffer, and
        A. J. Heeger Phys. Rev. B 22, 2099 - Cerca con Google."
        https://www.google.com/search?q=Soliton+excitations+in+polyacet
        ylene+W.+P.+Su%2C+J.+R.+Schrieffer%2C+and+A.+J.+Heeger+P
        hys.+Rev.+B+22%2C+2099&rlz=1C1CHBD_itIT969IT969&oq=So
        liton+excitations+in+polyacetylene+W.+P.+Su%2C+J.+R.+Schrieff

er%2C+and+A.+J.+Heeger+Phys.+Rev.+B+22%2C+2099&aqs=chr
ome..69i57.764j0j7&sourceid=chrome&ie=UTF-8 (accessed Sep. 07,
2021).

[93]   A. N. Aleshin, "Charge carrier transport in conducting polymers on
the metal side of the metal-insulator transition: A review," *Phys. Solid
State*, vol. 52, no. 11, pp. 2307–2332, Nov. 2010, doi:
10.1134/S106378341011017X.

[94]   W. Böhm, T. Fritz, and K. Leo, "Charge Transport in Thin Organic
Semiconducting Films: Seebeck and Field Effect Studies," *Phys.
Status Solidi A*, vol. 160, no. 1, pp. 81–87, 1997, doi: 10.1002/1521-
396X(199703)160:1<81::AID-PSSA81>3.0.CO;2-S.

[95]   R. E. Peierls, *Quantum Theory of Solids*. Oxford, New York: Oxford
University Press, 2001.

[96]   D. Jérome and H. J. Schulz, "Organic conductors and
superconductors," *Adv. Phys.*, vol. 51, no. 1, pp. 293–479, Jan. 2002,
doi: 10.1080/00018730110116362.

[97]   J. L. Bredas and G. B. Street, "Polarons, bipolarons, and solitons in
conducting polymers," *Acc. Chem. Res.*, vol. 18, no. 10, pp. 309–315,
Oct. 1985, doi: 10.1021/ar00118a005.

[98]   Y. Ling, H. Diliën, D. Vanderzande, and S. Van Doorslaer,
"Electronic Structure of the Positive Radical of 13C-Labeled Poly(3-
Octylthienylene Vinylene) Polymer," *Appl. Magn. Reson.*, vol. 45, p.
827, 2014, doi: 10.1007/s00723-014-0561-3.

[99]   J. Devreese and S. Alexandrov, "Froehlich Polaron and Bipolaron:
Recent Developments," *Rep. Prog. Phys.*, vol. 72, no. 6, p. 066501,
Jun. 2009, doi: 10.1088/0034-4885/72/6/066501.

[100]   J. Bonca, S. A. Trugman, and I. Batistic, "The Holstein Polaron,"
Phys. Rev. B, vol. 60, no. 3, pp. 1633–1642, Jul. 1999, doi:
10.1103/PhysRevB.60.1633.

[101]   G. Wellein, H. Röder, and H. Fehske, "Polarons and bipolarons in strongly interacting electron-phonon systems," *Phys. Rev. B*, vol. 53, no. 15, pp. 9666–9675, Apr. 1996, doi: 10.1103/PhysRevB.53.9666.

[102]   V. Cataudella, G. De Filippis, and C. A. Perroni, "Single Polaron Properties in Different Electron Phonon Models," in *Polarons in Advanced Materials*, A. S. Alexandrov, Ed. Dordrecht: Springer Netherlands, 2007, pp. 149–189. doi: 10.1007/978-1-4020-6348-0_4.

[103]   D. Emin, Ed., "Molecular polarons," in *Polarons*, Cambridge: Cambridge University Press, 2012, pp. 49–53. doi: 10.1017/CBO9781139023436.008.

[104]   A. Alexandrov and J. Devreese, "Lattice Polaron," Aug. 2010, doi: 10.1007/978-3-642-01896-1_3.

[105]   S. Butscher and A. Knorr, "Occurrence of Intersubband Polaronic Repellons in a Two-Dimensional Electron Gas," *Phys. Rev. Lett.*, vol. 97, no. 19, p. 197401, Nov. 2006, doi: 10.1103/PhysRevLett.97.197401.

[106]   R. Oulton *et al.*, "Subsecond spin relaxation times in quantum dots at zero applied magnetic field due to a strong electron-nuclear interaction," *Phys. Rev. Lett.*, vol. 98, no. 10, p. 107401, Mar. 2007, doi: 10.1103/PhysRevLett.98.107401.

[107]   K. Lee, S. Cho, S. Heum Park, A. J. Heeger, C.-W. Lee, and S.-H. Lee, "Metallic transport in polyaniline," *Nature*, vol. 441, no. 7089, pp. 65–68, May 2006, doi: 10.1038/nature04705.

[108]   A. J. Heeger, "Charge Storage in Conducting Polymers: Solitons, Polarons, and Bipolarons," *Polym. J.*, vol. 17, no. 1, pp. 201–208, Jan. 1985, doi: 10.1295/polymj.17.201.

[109]   R. Tautz *et al.*, "Structural correlations in the generation of polaron pairs in low-bandgap polymers for photovoltaics," *Nat. Commun.*, vol. 3, no. 1, p. 970, Jul. 2012, doi: 10.1038/ncomms1967.

[110]   N. Tessler, Y. Preezant, N. Rappaport, and Y. Roichman, "Charge Transport in Disordered Organic Materials and Its Relevance to Thin-

Film Devices: A Tutorial Review," *Adv. Mater.*, vol. 21, no. 27, pp. 2741–2761, 2009, doi: 10.1002/adma.200803541.

[111]   N. F. Mott, "Conduction in non-crystalline materials," *Philos. Mag. J. Theor. Exp. Appl. Phys.*, vol. 19, no. 160, pp. 835–852, Apr. 1969, doi: 10.1080/14786436908216338.

[112]   D. Farka *et al.*, "Anderson-Localization and the Mott–Ioffe–Regel Limit in Glassy-Metallic PEDOT," *Adv. Electron. Mater.*, vol. 3, no. 7, p. 1700050, 2017, doi: 10.1002/aelm.201700050.

[113]   C. Badre, L. Marquant, A. M. Alsayed, and L. A. Hough, "Highly Conductive   Poly(3,4-ethylenedioxythiophene):Poly (styrenesulfonate)   Films   Using   1-Ethyl-3-methylimidazolium Tetracyanoborate Ionic Liquid," *Adv. Funct. Mater.*, vol. 22, no. 13, pp. 2723–2727, 2012, doi: 10.1002/adfm.201200225.

[114]   C. S. S. Sangeeth, M. Jaiswal, and R. Menon, "Correlation of morphology   and   charge   transport   in   poly(3,4-ethylenedioxythiophene)–polystyrenesulfonic acid (PEDOT–PSS) films," *J. Phys. Condens. Matter*, vol. 21, no. 7, p. 072101, Jan. 2009, doi: 10.1088/0953-8984/21/7/072101.

[115]   O. Bubnova *et al.*, "Semi-metallic polymers," *Nat. Mater.*, vol. 13, no. 2, pp. 190–194, Feb. 2014, doi: 10.1038/nmat3824.

[116]   N. Massonnet, A. Carella, A. de Geyer, J. Faure-Vincent, and J.-P. Simonato, "Metallic behaviour of acid doped highly conductive polymers," *Chem. Sci.*, vol. 6, no. 1, pp. 412–417, Dec. 2014, doi: 10.1039/C4SC02463J.

[117]   Q. Wei, M. Mukaida, K. Kirihara, Y. Naitoh, and T. Ishida, "Recent Progress on PEDOT-Based Thermoelectric Materials," *Materials*, vol. 8, no. 2, Art. no. 2, Feb. 2015, doi: 10.3390/ma8020732.

[118]   A. M. Nardes, M. Kemerink, M. M. de Kok, E. Vinken, K. Maturova, and R. A. J. Janssen, "Conductivity, work function, and environmental stability of PEDOT:PSS thin films treated with sorbitol," *Org.*

Electron., vol. 9, no. 5, pp. 727–734, Oct. 2008, doi: 10.1016/j.orgel.2008.05.006.

[119]   S.-K. Hong, "Energy transfer by resonant dipole–dipole interaction from a conjugated polymer to a quantum-dot," *Phys. E-Low-Dimens. Syst. Nanostructures - Phys. E*, vol. 28, pp. 66–75, Jun. 2005, doi: 10.1016/j.physe.2005.01.017.

[120]   G. A. Jones and D. S. Bradshaw, "Resonance Energy Transfer: From Fundamental Theory to Recent Applications," *Front. Phys.*, vol. 7, p. 100, 2019, doi: 10.3389/fphy.2019.00100.

[121]   F. C. Grozema, P. Th. van Duijnen, Y. A. Berlin, M. A. Ratner, and L. D. A. Siebbeles, "Intramolecular Charge Transport along Isolated Chains of Conjugated Polymers: Effect of Torsional Disorder and Polymerization Defects," *J. Phys. Chem. B*, vol. 106, no. 32, pp. 7791–7795, Aug. 2002, doi: 10.1021/jp021114v.

[122]   A. Hariharan, S. K. Kumar, and T. P. Russell, "A lattice model for the surface segregation of polymer chains due to molecular weight effects," *Macromolecules*, vol. 23, no. 15, pp. 3584–3592, Jul. 1990, doi: 10.1021/ma00217a009.

[123]   B. Sherborne, "The Landauer model for electrical resistance: its extension from quantum to classical transport," 1989, doi: 10.1088/0953-8984/1/29/009.

[124]   G. Pace, I. Bargigia, Y.-Y. Noh, C. Silva, and M. Caironi, "Intrinsically distinct hole and electron transport in conjugated polymers controlled by intra and intermolecular interactions," *Nat. Commun.*, vol. 10, no. 1, p. 5226, Nov. 2019, doi: 10.1038/s41467-019-13155-9.

[125]   F. Lux, "Models proposed to explain the electrical conductivity of mixtures made of conductive and insulating materials," *J. Mater. Sci.*, vol. 28, no. 2, pp. 285–301, Jan. 1993, doi: 10.1007/BF00357799.

[126]   J. C. Maxwell, *A Treatise on Electricity and Magnetism: Volume 1*. Oxford, New York: Oxford University Press, 1998.

[127]   Y. Wang, "Conductive Thermoplastic Composite Blends for Flow
         Field Plates for Use in Polymer Electrolyte Membrane Fuel Cells
         (PEMFC)," Jan. 2006.

[128]   S. Kirkpatrick, "Percolation and Conduction," *Rev. Mod. Phys.*, vol.
         45, no. 4, pp. 574–588, Oct. 1973, doi: 10.1103/RevModPhys.45.574.

[129]   I. Balberg and N. Binenbaum, "Invariant properties of the percolation
         thresholds in the soft-core--hard-core transition," *Phys. Rev. A*, vol.
         35,   no.   12,   pp.   5174–5177,   Jun.   1987,   doi:
         10.1103/PhysRevA.35.5174.

[130]   R. Taherian, "Development of an Equation to Model Electrical
         Conductivity of Polymer-Based Carbon Nanocomposites," *ECS J.
         Solid State Sci. Technol.*, vol. 3, pp. M26–M38, May 2014, doi:
         10.1149/2.023406jss.

[131]   S. Wen and D. D. L. Chung, "Double percolation in the electrical
         conduction in carbon fiber reinforced cement-based materials,"
         Carbon,   vol.   2,   no.   45,   pp.   263–267,   2007,   doi:
         10.1016/j.carbon.2006.09.031.

[132]   C. Feng and L. Jiang, "Micromechanics modeling of the electrical
         conductivity of carbon nanotube (CNT)–polymer nanocomposites,"
         Compos. Part Appl. Sci. Manuf., vol. 47, pp. 143–149, Apr. 2013, doi:
         10.1016/j.compositesa.2012.12.008.

[133]   S. Kirkpatrick, "Classical Transport in Disordered Media: Scaling and
         Effective-Medium Theories," *Phys. Rev. Lett.*, vol. 27, no. 25, pp.
         1722–1725, Dec. 1971, doi: 10.1103/PhysRevLett.27.1722.

[134]   K. W. Wagner, "Erklärung der dielektrischen Nachwirkungsvorgänge
         auf Grund Maxwellscher Vorstellungen," *Arch. Für Elektrotechnik*,
         vol. 2, no. 9, pp. 371–387, Sep. 1914, doi: 10.1007/BF01657322.

[135]   "Electrical   Resistivity   of   Composites | Semantic   Scholar."
         https://www.semanticscholar.org/paper/Electrical-Resistivity-of-
         Composites-McLachlan-

Blaszkiewicz/5127f4b05636d676b5a8968040a632280b06d34d
(accessed Sep. 09, 2021).

[136]   S. Jiang and J. B. Wagner, "A theoretical model for composite
        electrolytes—I. Space charge layer as a cause for charge-carrier
        enhancement," *J. Phys. Chem. Solids*, vol. 56, no. 8, pp. 1101–1111,
        Aug. 1995, doi: 10.1016/0022-3697(95)00025-9.

[137]   J. Wu and D. S. McLachlan, "Percolation exponents and thresholds
        obtained from the nearly ideal continuum percolation system graphite-
        boron nitride," *Phys. Rev. B*, vol. 56, no. 3, pp. 1236–1248, Jul. 1997,
        doi: 10.1103/PhysRevB.56.1236.

[138]   J. Vilčáková, P. Sáha, and O. Quadrat, "Electrical conductivity of
        carbon fibres/polyester resin composites in the percolation threshold
        region," *Eur. Polym. J.*, vol. 12, no. 38, pp. 2343–2347, 2002.

[139]   A. Celzard, E. McRae, J. F. Marêché, G. Furdin, and B. Sundqvist,
        "Conduction mechanisms in some graphite–polymer composites:
        Effects of temperature and hydrostatic pressure," *J. Appl. Phys.*, vol.
        83, no. 3, pp. 1410–1419, Feb. 1998, doi: 10.1063/1.366904.

[140]   J. Bigalke, "Investigation of the conductivity of random networks,"
        Phys. Stat. Mech. Its Appl., vol. 272, no. 3, pp. 281–293, 1999.

[141]   C. Pennetta, L. Reggiani, E. Alfinito, and G. Trefan, "Stationary
        Regime of Random Resistor Networks Under Biased Percolation," *J.
        Phys. Condens. Matter*, vol. 14, no. 9, pp. 2371–2378, Mar. 2002, doi:
        10.1088/0953-8984/14/9/326.

[142]   Y. Li, M. L. Swartz, R. W. Phillips, B. K. Moore, and T. A. Roberts,
        "Effect of filler content and size on properties of composites," *J. Dent.
        Res.*, vol. 64, no. 12, pp. 1396–1401, Dec. 1985, doi:
        10.1177/00220345850640121501.

[143]   Ye. P. Mamunya, D. Valeriy, P. Pissis, and E. V. Lebedev, "Electrical
        and thermal conductivity of polymers filled with metal powders," *Eur.
        Polym. J.*, vol. 38, pp. 1887–1897, Sep. 2002, doi: 10.1016/S0014-
        3057(02)00064-2.

[144]   E. P. Mamunya, V. V. Davidenko, and E. V. Lebedev, "Effect of
        polymer-filler interface interactions on percolation conductivity of
        thermoplastics filled with carbon black," *Compos. Interfaces*, vol. 4,
        no. 4, pp. 169–176, Jan. 1996, doi: 10.1163/156855497X00145.

[145]   M. L. Clingerman, J. A. King, K. H. Schulz, and J. D. Meyers,
        "Evaluation of electrical conductivity models for conductive polymer
        composites," *J. Appl. Polym. Sci.*, vol. 83, no. 6, pp. 1341–1356, Feb.
        2002, doi: 10.1002/app.10014.

[146]   O. Ijaodola *et al.*, "Evaluating the Effect of Metal Bipolar Plate
        Coating on the Performance of Proton Exchange Membrane Fuel
        Cells," *Energies*, vol. 11, no. 11, p. 3203, Nov. 2018, doi:
        10.3390/en11113203.

[147]   M. L. Clingerman, E. H. Weber, J. A. King, and K. H. Schulz,
        "Development of an additive equation for predicting the electrical
        conductivity of carbon-filled composites," *J. Appl. Polym. Sci.*, vol.
        88, no. 9, pp. 2280–2299, 2003, doi: 10.1002/app.11938.

[148]   V. N. Prigodin and K. B. Efetov, "Metal-insulator transition in an
        irregular structure of coupled metallic chains," *Synth. Met.*, vol. 65,
        no. 2, pp. 195–201, Aug. 1994, doi: 10.1016/0379-6779(94)90181-3.

[149]   A. N. Aleshin, S. R. Williams, and A. J. Heeger, "Transport properties
        of poly(3,4-ethylenedioxythiophene)/poly(styrenesulfonate)," *Synth.
        Met.*, vol. 94, no. 2, pp. 173–177, Apr. 1998, doi: 10.1016/S0379-
        6779(97)04167-2.

[150]   S. Fratini, M. Nikolka, A. Salleo, G. Schweicher, and H. Sirringhaus,
        "Charge transport in high-mobility conjugated polymers and
        molecular semiconductors," *Nat. Mater.*, vol. 19, no. 5, pp. 491–502,
        May 2020, doi: 10.1038/s41563-020-0647-2.

[151]   W. Warta and N. Karl, "Hot holes in naphthalene: High, electric-field-
        dependent mobilities," *Phys. Rev. B*, vol. 32, no. 2, pp. 1172–1182,
        Jul. 1985, doi: 10.1103/PhysRevB.32.1172.

Modelling and characterization of electronic conductivity in 3D printed
PEGDA:PEDOT polymer composites - High frequency applications
187

[152] "Crossover from hopping to band-like transport in crystalline organic semiconductors: The effect of shallow traps: The Journal of Chemical Physics: Vol 150, No 4." https://aip-scitation-org.ezproxy.biblio.polito.it/doi/10.1063/1.5066563 (accessed Sep. 09, 2021).

[153] N. Karl, "Charge Carrier Transport in Organic Semiconductors," *Synth. Met.*, vol. 133–134, pp. 649–657, Mar. 2003, doi: 10.1016/S0379-6779(02)00398-3.

[154] Y. Li and J. B. Lagowski, "Charge carrier mobility in conjugated organic polymers: simulation of an electron mobility in a carbazole-benzothiadiazole-based polymer," vol. 8007, p. 80071Z, Aug. 2011, doi: 10.1117/12.905452.

[155] A. Kokil, K. Yang, and J. Kumar, "Techniques for characterization of charge carrier mobility in organic semiconductors," *J. Polym. Sci. Part B Polym. Phys.*, vol. 50, no. 15, pp. 1130–1144, 2012, doi: 10.1002/polb.23103.

[156] B. I. Shklovskii and A. L. Efros, *Electronic Properties of Doped Semiconductors*. Berlin Heidelberg: Springer-Verlag, 1984. doi: 10.1007/978-3-662-02403-4.

[157] N. F. Mott and E. A. Davis, *Electronic Processes in Non-Crystalline Materials*. Oxford, New York: Oxford University Press, 2012.

[158] I. G. Austin and N. F. Mott, "Polarons in crystalline and non-crystalline materials," *Adv. Phys.*, vol. 18, no. 71, pp. 41–102, Jan. 1969, doi: 10.1080/00018736900101267.

[159] D. M. Pai, J. F. Yanus, and M. Stolka, "Trap-controlled hopping transport," *ACS Publications*, May 01, 2002. https://pubs.acs.org/doi/pdf/10.1021/j150664a054 (accessed Sep. 10, 2021).

[160] W. D. Gill, "Charge Transport in TNF: PVK and TNF:Polyester Films and in Liquid, Amorphous and Crystalline TNF," in *Energy and Charge Transfer in Organic Semiconductors*, K. Masuda and M.

Silver, Eds. Boston, MA: Springer US, 1974, pp. 137–141. doi: 10.1007/978-1-4684-2109-5_18.

[161] N. Vukmirović and L.-W. Wang, "Carrier hopping in disordered semiconducting polymers: How accurate is the Miller–Abrahams model?," *Appl. Phys. Lett.*, vol. 97, no. 4, p. 043305, Jul. 2010, doi: 10.1063/1.3474618.

[162] M. Sahimi, *Applications Of Percolation Theory*. CRC Press, 1994.

[163] N. S. Sariciftci, "Primary Photoexcitations In Conjugated Polymers: Molecular Exciton Versus Semiconductor Band Model," 1997. doi: 10.1142/3299.

[164] V. I. Arkhipov, E. V. Emelianova, P. Heremans, and H. Bässler, "Analytic model of carrier mobility in doped disordered organic semiconductors," *Phys. Rev. B*, vol. 72, no. 23, p. 235202, Dec. 2005, doi: 10.1103/PhysRevB.72.235202.

[165] L. Wang, A. V.-Y. Thean, and G. Liang, "A statistical Seebeck coefficient model based on percolation theory in two-dimensional disordered systems," *J. Appl. Phys.*, vol. 125, no. 22, p. 224302, Jun. 2019, doi: 10.1063/1.5098862.

[166] S. Boutiche, "Variable Range Hopping Conductivity: Case of the non-constant density of states," 2001. Accessed: Sep. 10, 2021. [Online]. Available: https://hal.archives-ouvertes.fr/hal-00004661

[167] W. F. Pasveer and M. A. J. Michels, "Understanding Mott's law from scaling of variable-range-hopping currents and intrinsic current fluctuations," *Phys. Rev. B*, vol. 74, no. 19, p. 195129, Nov. 2006, doi: 10.1103/PhysRevB.74.195129.

[168] A. K. Sen and S. Bhattacharya, "Variable Range Hopping Conduction in Complex Systems and a Percolation Model with Tunneling," *ArXivcond-Mat0506089*, Jun. 2005, Accessed: Sep. 10, 2021. [Online]. Available: http://arxiv.org/abs/cond-mat/0506089

[169]   Y. Koval, I. Lazareva, and P. Müller, "Coulomb gap variable range hopping in graphitized polymer surfaces," *Lancet*, vol. 161, pp. 528–534, Mar. 2011, doi: 10.1016/j.synthmet.2011.01.007.

[170]   M. Abdel Rehim, "Morphology of Conducting Polymers: Focus on Polyaniline," in *Polymer Morphology*, 2012, pp. 163–181.

[171]   R. P. Feynman, "Slow Electrons in a Polar Crystal," *Phys. Rev.*, vol. 97, no. 3, pp. 660–665, Feb. 1955, doi: 10.1103/PhysRev.97.660.

[172]   R. P. Feynman, R. W. Hellwarth, C. K. Iddings, and P. M. Platzman, "Mobility of Slow Electrons in a Polar Crystal," *Phys. Rev.*, vol. 127, no. 4, pp. 1004–1017, Aug. 1962, doi: 10.1103/PhysRev.127.1004.

[173]   J. T. Devreese, "Fr\"ohlich Polarons. Lecture course including detailed theoretical derivations - 8th edition," *ArXiv161106122 Cond-Mat*, Nov. 2016, Accessed: Aug. 18, 2019. [Online]. Available: http://arxiv.org/abs/1611.06122

[174]   N. V. Smith, "Classical generalization of the Drude formula for the optical conductivity," *Phys. Rev. B*, vol. 64, no. 15, p. 155106, Sep. 2001, doi: 10.1103/PhysRevB.64.155106.

[175]   T. L. Cocker *et al.*, "Microscopic origin of the Drude-Smith model," *Phys. Rev. B*, vol. 96, no. 20, p. 205439, Nov. 2017, doi: 10.1103/PhysRevB.96.205439.

[176]   R. Lovrinčić and A. Pucci, "Infrared optical properties of chromium nanoscale films with a phase transition," *Phys. Rev. B*, vol. 80, no. 20, p. 205404, Nov. 2009, doi: 10.1103/PhysRevB.80.205404.

[177]   "Semiconductive Polymer Blends: Correlating Structure with Transport Properties at the Nanoscale - Ionescu-Zanetti - 2004 - Advanced Materials - Wiley Online Library." https://onlinelibrary.wiley.com/doi/10.1002/adma.200305747 (accessed Sep. 10, 2021).

[178]   "Carrier transport of conducting polymer PEDOT:PSS investigated by temperature dependence of THz and IR spectra," *Infrared Millim.*

Terahertz Waves IRMMW-THz 2014 39th Int. Conf. On, vol. 2014, no. 9, pp. 1–2, 2014.

[179]   Y. Du, X. Cui, L. Li, H. Tian, W.-X. Yu, and Z.-X. Zhou, "Dielectric Properties of DMSO-Doped-PEDOT:PSS at THz Frequencies," *Phys. Status Solidi B*, vol. 255, no. 4, p. 1700547, Apr. 2018, doi: 10.1002/pssb.201700547.

[180]   M. Geoghegan and G. Hadziioannou, *Polymer electronics*, First edition. Oxford: Oxford University Press, 2013.

[181]   L. Pauling, "Electronic Processes in Ionic Crystals. By N. F. Mott and R. W. Gurney.," *ACS Publications*, May 01, 2002. https://pubs.acs.org/doi/pdf/10.1021/j150412a015 (accessed Sep. 10, 2021).

[182]   X. Zhang and S. Pantelides, "Theory of Space Charge Limited Currents," *Phys. Rev. Lett. - PHYS REV LETT*, vol. 108, Jun. 2012, doi: 10.1103/PhysRevLett.108.266602.

[183]   J. M. Montero, J. Bisquert, G. Garcia-Belmonte, E. M. Barea, and H. J. Bolink, "Trap-limited mobility in space-charge limited current in organic layers," *Org. Electron.*, vol. 10, no. 2, pp. 305–312, Apr. 2009, doi: 10.1016/j.orgel.2008.11.017.

[184]   R. Schmechel and H. von Seggern, "Electronic traps in organic transport layers," *Phys. Status Solidi A*, vol. 201, no. 6, pp. 1215–1235, 2004, doi: 10.1002/pssa.200404343.

[185]   "Electrical Characterization of Organic Electronic Materials and Devices | Wiley," *Wiley.com*. https://www.wiley.com/en-ao/Electrical+Characterization+of+Organic+Electronic+Materials+and+Devices+-p-9780470750094 (accessed Sep. 10, 2021).

[186]   L. V. Keldysh, "Dynamic Tunneling," *Her. Russ. Acad. Sci.*, vol. 86, no. 6, pp. 413–425, Nov. 2016, doi: 10.1134/S1019331616060113.

[187]   A. Kiveris, Š. Kudžmauskas, and P. Pipinys, "Release of electrons from traps by an electric field with phonon participation," *Phys. Status*

Solidi A, vol. 37, no. 1, pp. 321–327, 1976, doi: 10.1002/pssa.2210370140.

[188] "Anomalous off-current mechanisms in n-channel poly-Si thin film transistors."
https://scholar.google.it/citations?view_op=view_citation&hl=en&user=XLVz-HYAAAAJ&cstart=20&pagesize=80&sortby=pubdate&citation_for_view=XLVz-HYAAAAJ:IjCSPb-OGe4C (accessed Sep. 10, 2021).

[189] "On the physics of metal-semiconductor interfaces - IOPscience."
https://iopscience-iop-org.ezproxy.biblio.polito.it/article/10.1088/0034-4885/53/3/001 (accessed Sep. 10, 2021).

[190] O. Engström and A. Alm, "Energy concepts of insulator–semiconductor interface traps," *J. Appl. Phys.*, vol. 54, no. 9, pp. 5240–5244, Sep. 1983, doi: 10.1063/1.332751.

[191] G.-M. Lin *et al.*, "Effect of the Chemical Potentials of Electrodes on Charge Transport across Molecular Junctions," *J. Phys. Chem. C*, vol. 123, no. 36, pp. 22009–22017, Sep. 2019, doi: 10.1021/acs.jpcc.9b05927.

[192] J. Li, H. Wang, Z. Yu, Y. Gao, Q. Chen, and K. Zhang, "Emission Mechanism of High Current Density Thermionic Cathodes," in *2007 IEEE International Vacuum Electronics Conference*, May 2007, pp. 1–2. doi: 10.1109/IVELEC.2007.4283257.

[193] S. Y. Sayed, J. A. Fereiro, H. Yan, R. L. McCreery, and A. J. Bergren, "Charge transport in molecular electronic junctions: Compression of the molecular tunnel barrier in the strong coupling regime," *Proc. Natl. Acad. Sci.*, vol. 109, no. 29, pp. 11498–11503, Jul. 2012, doi: 10.1073/pnas.1201557109.

[194] J. Frenkel, "On Pre-Breakdown Phenomena in Insulators and Electronic Semi-Conductors," *Phys. Rev.*, vol. 54, no. 8, pp. 647–648, Oct. 1938, doi: 10.1103/PhysRev.54.647.

[195] P. N. Murgatroyd, "Theory of space-charge-limited current enhanced by Frenkel effect," *J. Phys. Appl. Phys.*, vol. 3, no. 2, pp. 151–156, Feb. 1970, doi: 10.1088/0022-3727/3/2/308.

[196] D. Barbe, "RESEARCH NOTE: Space-charge-limited current enhanced by Frenkel effect," 1971, doi: 10.1088/0022-3727/4/11/427.

[197] G. G. Malliaras, J. R. Salem, P. J. Brock, and C. Scott, "Electrical characteristics and efficiency of single-layer organic light-emitting diodes," *Phys. Rev. B*, vol. 58, no. 20, pp. R13411–R13414, Nov. 1998, doi: 10.1103/PhysRevB.58.R13411.

[198] J. L. Hartke, "The Three-Dimensional Poole-Frenkel Effect," *J. Appl. Phys.*, vol. 39, no. 10, pp. 4871–4873, Sep. 1968, doi: 10.1063/1.1655871.

[199] E. Fantino *et al.*, "3D Printing of Conductive Complex Structures with In Situ Generation of Silver Nanoparticles," *Adv. Mater.*, vol. 28, no. 19, pp. 3712–3717, 2016, doi: 10.1002/adma.201505109.

[200] C. Sciancalepore, F. Moroni, M. Messori, and F. Bondioli, "Acrylate-based silver nanocomposite by simultaneous polymerization–reduction approach via 3D stereolithography," *Compos. Commun.*, vol. 6, pp. 11–16, Dec. 2017, doi: 10.1016/j.coco.2017.07.006.

[201] L. L. Lebel, B. Aissa, M. A. E. Khakani, and D. Therriault, "Ultraviolet-Assisted Direct-Write Fabrication of Carbon Nanotube/Polymer Nanocomposite Microcoils," *Adv. Mater.*, vol. 22, no. 5, pp. 592–596, 2010, doi: 10.1002/adma.200902192.

[202] Q. Mu *et al.*, "Digital light processing 3D printing of conductive complex structures," *Addit. Manuf.*, vol. 18, pp. 74–83, Dec. 2017, doi: 10.1016/j.addma.2017.08.011.

[203] G. Gonzalez *et al.*, "Development of 3D printable formulations containing CNT with enhanced electrical properties," *Polymer*, vol. 109, pp. 246–253, Jan. 2017, doi: 10.1016/j.polymer.2016.12.051.

[204] K. Kurselis, R. Kiyan, V. N. Bagratashvili, V. K. Popov, and B. N. Chichkov, "3D fabrication of all-polymer conductive microstructures

by two photon polymerization," *Opt. Express*, vol. 21, no. 25, p. 31029, Dec. 2013, doi: 10.1364/OE.21.031029.

[205]   G. Scordo *et al.*, "A novel highly electrically conductive composite resin for stereolithography," *Mater. Today Commun.*, vol. 19, pp. 12–17, Jun. 2019, doi: 10.1016/j.mtcomm.2018.12.017.

[206]   T.-G. Chen, B.-Y. Huang, E.-C. Chen, P. Yu, and H.-F. Meng, "Micro-textured conductive polymer/silicon heterojunction photovoltaic devices with high efficiency," *Appl. Phys. Lett.*, vol. 101, no. 3, p. 033301, Jul. 2012, doi: 10.1063/1.4734240.

[207]   G. Scordo *et al.*, "Effect of Volatile Organic Compounds Adsorption on 3D-Printed PEGDA:PEDOT for Long-Term Monitoring Devices," *Nanomaterials*, vol. 11, no. 1, Art. no. 1, Jan. 2021, doi: 10.3390/nano11010094.

[208]   R. Colucci, G. C. Faria, L. F. Santos, and G. Gozzi, "On the charge transport mechanism of cross-linked PEDOT:PSS films," *J. Mater. Sci. Mater. Electron.*, vol. 30, no. 18, pp. 16864–16872, Sep. 2019, doi: 10.1007/s10854-019-01474-y.

[209]   S. Garreau, G. Louarn, J. P. Buisson, G. Froyer, and S. Lefrant, "In Situ Spectroelectrochemical Raman Studies of Poly(3,4-ethylenedioxythiophene) (PEDT)," *Macromolecules*, vol. 32, no. 20, pp. 6807–6812, Oct. 1999, doi: 10.1021/ma9905674.

[210]   A. Zykwinska, W. Domagala, A. Czardybon, B. Pilawa, and M. Lapkowski, "In situ EPR spectroelectrochemical studies of paramagnetic centres in poly(3,4-ethylenedioxythiophene) (PEDOT) and poly(3,4-butylenedioxythiophene) (PBuDOT) films," *Chem. Phys.*, vol. 292, pp. 31–45, Jul. 2003, doi: 10.1016/S0301-0104(03)00253-2.

[211]   "PRIME PubMed | Polaron pair versus bipolaron on oligothiophene chains: a theoretical study of the singlet and triplet states." https://www.unboundmedicine.com/medline/citation/12785266/Pola ron_pair_versus_bipolaron_on_oligothiophene_chains:_a_theoretica l_study_of_the_singlet_and_triplet_states_ (accessed Oct. 25, 2021).

[212]   I. Zozoulenko, A. Singh, S. K. Singh, V. Gueskine, X. Crispin, and M. Berggren, "Polarons, Bipolarons, And Absorption Spectroscopy of PEDOT," *ACS Appl. Polym. Mater.*, vol. 1, no. 1, pp. 83–94, Jan. 2019, doi: 10.1021/acsapm.8b00061.

[213]   S. S. Kalagi and P. S. Patil, "Secondary electrochemical doping level effects on polaron and bipolaron bands evolution and interband transition energy from absorbance spectra of PEDOT: PSS thin films," *Synth. Met.*, vol. 220, pp. 661–666, Oct. 2016, doi: 10.1016/j.synthmet.2016.08.009.

[214]   S. S. Li, "Metal–Semiconductor Contacts," in *Semiconductor Physical Electronics*, S. S. Li, Ed. New York, NY: Springer, 2006, pp. 284–333. doi: 10.1007/0-387-37766-2_10.

[215]   "Work Functions for Photoelectric Effect." http://hyperphysics.phy-astr.gsu.edu/hbase/Tables/photoelec.html#c1 (accessed Oct. 25, 2021).

[216]   J. R. Macdonald *et al.*, *Impedance Spectroscopy: Theory, Experiment, and Applications, Third Edition*. 2018.

[217]   "Permittività elettrica," *Wikipedia*. Mar. 11, 2021. Accessed: Oct. 27, 2021. [Online]. Available: https://it.wikipedia.org/w/index.php?title=Permittivit%C3%A0_elett rica&oldid=119203848

[218]   "Electrical Impedance: Principles, Measurement, and Applications - Luca Callegaro - Taylor & Francis Ltd - Series in Sensors| IBS." https://www.ibs.it/electrical-impedance-principles-measurement-applications-libro-inglese-luca-callegaro/e/9781138199439 (accessed Oct. 27, 2021).

[219]   I. Miccoli, F. Edler, H. Pfnür, and C. Tegenkamp, "The 100th anniversary of the four-point probe technique: the role of probe geometries in isotropic and anisotropic systems," *J. Phys.: Condens. Matter*, vol. 27, no. 22, p. 223201, May 2015, doi: 10.1088/0953-8984/27/22/223201.

[220]   Y. Singh, "ELECTRICAL RESISTIVITY MEASUREMENTS: A REVIEW," *Int. J. Mod. Phys. Conf. Ser.*, vol. 22, pp. 745–756, Jan. 2013, doi: 10.1142/S2010194513010970.

[221]   R. S. Waremra and P. Betaubun, "Analysis of Electrical Properties Using the four point Probe Method," *E3S Web Conf.*, vol. 73, p. 13019, 2018, doi: 10.1051/e3sconf/20187313019.

[222]   "Haldor Topsoe 'Geometric Factors in Four Point Resistivity Measurement.'" http://four-point-probes.com/haldor-topsoe-geometric-factors-in-four-point-resistivity-measurement/ (accessed Oct. 28, 2021).

[223]   Keysight, "4192A LF Impedance Analyzer, 5 Hz to 13 MHz [Discontinued]," *Keysight*. https://www.keysight.com/it/en/product/4192A/lf-impedance-analyzer-5-hz-to-13-mhz.html (accessed Nov. 05, 2021).

[224]   B. A. Boukamp, "A Linear Kronig-Kramers Transform Test for Immittance Data Validation," *J. Electrochem. Soc.*, vol. 142, no. 6, p. 1885, Jun. 1995, doi: 10.1149/1.2044210.

[225]   M. Schönleber, D. Klotz, and E. Ivers-Tiffée, "A Method for Improving the Robustness of linear Kramers-Kronig Validity Tests," *Electrochimica Acta*, vol. 131, pp. 20–27, Jun. 2014, doi: 10.1016/j.electacta.2014.01.034.

[226]   M. Schönleber and E. Ivers-Tiffée, "Approximability of impedance spectra by RC elements and implications for impedance analysis," *Electrochem. Commun.*, vol. 58, Jun. 2015, doi: 10.1016/j.elecom.2015.05.018.

[227]   Farnell, an Avnet Company, "LCR-8110G - Misuratore LCR, da banco, 10 MHz, 100 kH, 1 F, 0.1 Gohm, LCR-8000G Series." https://it.farnell.com/gw-instek/lcr-8110g/misuratore-precisione-lcr-10mhz/dp/2748540 (accessed Nov. 05, 2021).

[228]   L. H. Omari, R. Moubah, A. Boutahar, L. Hajji, and R. El Ouatib, "Analysis of electrical properties using complex impedance

spectroscopy in solid solutions (PbTiO3)0.97-(LaFeO3)0.03 prepared by sol-gel technique," *J. Electroceramics*, vol. 44, no. 1–2, pp. 23–31, Apr. 2020, doi: 10.1007/s10832-020-00199-3.

[229] F. Tian and Y. Ohki, "Electric modulus powerful tool for analyzing dielectric behavior," *IEEE Trans. Dielectr. Electr. Insul.*, vol. 21, no. 3, pp. 929–931, Jun. 2014, doi: 10.1109/TDEI.2014.6832233.

[230] C. Chen, A. Kine, R. D. Nelson, and J. C. LaRue, "Impedance spectroscopy study of conducting polymer blends of PEDOT:PSS and PVA," *Synth. Met.*, vol. 206, pp. 106–114, Aug. 2015, doi: 10.1016/j.synthmet.2015.05.003.

[231] M. Siekierski and W. Wieczorek, "Application of the 'universal power law' to the studies of ac conductivity of polymeric electrolytes," *Solid State Ion.*, vol. 60, no. 1–3, pp. 67–71, Mar. 1993, doi: 10.1016/0167-2738(93)90276-9.

[232] J. Macdonald, "Comparison of the universal dynamic response power-law fitting model for conducting systems with superior alternative models," *Solid State Ion.*, vol. 133, no. 1–2, pp. 79–97, Aug. 2000, doi: 10.1016/S0167-2738(00)00737-2.

[233] D. P. Almond and B. Vainas, "The dielectric properties of random R - C networks as an explanation of the `universal' power law dielectric response of solids," *J. Phys. Condens. Matter*, vol. 11, no. 46, pp. 9081–9093, Nov. 1999, doi: 10.1088/0953-8984/11/46/310.

[234] E. M., A. B.C., O. O.I., and S. M. C, "Extended Complex Plane and Riemann Sphere," *Sci. Res. J.*, vol. 08, no. 04, pp. 44–51, Apr. 2020, doi: 10.31364/SCIRJ/v8.i4.2020.P0420762.

[235] A. N. Papathanassiou, I. Sakellis, and J. Grammatikakis, "Universal frequency-dependent ac conductivity of conducting polymer networks," *Appl. Phys. Lett.*, vol. 91, no. 12, p. 122911, Sep. 2007, doi: 10.1063/1.2779255.

[236]   W. H. Press and S. A. Teukolsky, "Savitzky-Golay Smoothing Filters," *Comput. Phys.*, vol. 4, no. 6, p. 669, 1990, doi: 10.1063/1.4822961.

[237]   A. N. Papathanassiou, I. Sakellis, J. Grammatikakis, E. Vitoratos, and S. Sakkopoulos, "Exploring electrical conductivity within mesoscopic phases of semiconducting poly(3,4-ethylenedioxythiophene):poly(4-styrene-sulfonate) films by broadband dielectric spectroscopy," *Appl. Phys. Lett.*, vol. 103, no. 12, p. 123304, Sep. 2013, doi: 10.1063/1.4821101.

[238]   W. G. Wang and X. Y. Li, "Impedance and dielectric relaxation spectroscopy studies on the calcium modified Na0.5Bi0.44Ca0.06TiO2.97 ceramics," *AIP Adv.*, vol. 7, no. 12, p. 125318, Dec. 2017, doi: 10.1063/1.5012108.

[239]   C. S. Pathak, J. P. Singh, and R. Singh, "Effect of dimethyl sulfoxide on the electrical properties of PEDOT:PSS/n-Si heterojunction diodes," *Curr. Appl. Phys.*, vol. 15, no. 4, pp. 528–534, Apr. 2015, doi: 10.1016/j.cap.2015.01.020.

[240]   "Strategies to Reduce Oxygen Inhibition in Photoinduced Polymerization | Chemical Reviews." https://pubs.acs.org/doi/full/10.1021/cr3005197?src=recsys (accessed Oct. 31, 2021).

[241]   A. Verma *et al.*, "6 GHz microstrip patch antennas with PEDOT and polypyrrole conducting polymers," in *2010 International Conference on Electromagnetics in Advanced Applications*, Sydney, Australia, Sep. 2010, pp. 329–332. doi: 10.1109/ICEAA.2010.5651030.

[242]   S. J. Chen, C. Fumeaux, B. Chivers, and R. Shepherd, "A 5.8-GHz flexible microstrip-fed slot antenna realized in PEDOT:PSS conductive polymer," in *2016 IEEE International Symposium on Antennas and Propagation (APSURSI)*, Fajardo, PR, USA, Jun. 2016, pp. 1317–1318. doi: 10.1109/APS.2016.7696366.

[243]   H.-J. Lee, N. Jeong, and H. H. Choi, "Microwave Properties of Coplanar Waveguide-Based PEDOT:PSS Conducting Polymer Line

in Ethanol Gas Atmosphere," *Materials*, vol. 13, no. 7, p. 1759, Apr. 2020, doi: 10.3390/ma13071759.

[244]   T. Kim *et al.*, "Megahertz-wave-transmitting conducting polymer electrode for device-to-device integration," *Nat. Commun.*, vol. 10, no. 1, p. 653, Dec. 2019, doi: 10.1038/s41467-019-08552-z.

[245]   N. K. Nikolova, Ed., "Scattering Parameters in Microwave Imaging," in *Introduction to Microwave Imaging*, Cambridge: Cambridge University Press, 2017, pp. 154–181. doi: 10.1017/9781316084267.004.

[246]   P. Sabouroux, "EpsiMu, A TOOLKIT FOR PERMITTIVITY AND PERMEABILITY MEASUREMENT IN," p. 6.

[247]   J. Baker-Jarvis, E. J. Vanzura, and W. A. Kissick, "Improved technique for determining complex permittivity with the transmission/reflection method," *IEEE Trans. Microw. Theory Tech.*, vol. 38, no. 8, pp. 1096–1103, Aug. 1990, doi: 10.1109/22.57336.

[248]   A. M. Nicolson and G. F. Ross, "Measurement of the Intrinsic Properties of Materials by Time-Domain Techniques," *IEEE Trans. Instrum. Meas.*, vol. 19, no. 4, pp. 377–382, Nov. 1970, doi: 10.1109/TIM.1970.4313932.

[249]   "Introduction to Electromagnetic Compatibility, 2nd Edition | Wiley," *Wiley.com*.   https://www.wiley.com/en-us/Introduction+to+Electromagnetic+Compatibility%2C+2nd+Editi on-p-9780471755005 (accessed Nov. 02, 2021).

[250]   M. Dresselhaus, G. Dresselhaus, S. B. Cronin, and A. Gomes Souza Filho, "Review of Fundamental Relations for Optical Phenomena," in *Solid State Properties: From Bulk to Nano*, M. Dresselhaus, G. Dresselhaus, S. Cronin, and A. Gomes Souza Filho, Eds. Berlin, Heidelberg: Springer, 2018, pp. 317–327. doi: 10.1007/978-3-662-55922-2_15.

[251]   "Appendix F: Overview of S Parameters," in *Grounds for Grounding*,
        John Wiley & Sons, Ltd, 2009, pp. 1045–1055. doi:
        10.1002/9780470529324.app6.

[252]   M. M. Ovhal, N. Kumar, and J.-W. Kang, "3D direct ink writing
        fabrication of high-performance all-solid-state micro-
        supercapacitors," *Mol. Cryst. Liq. Cryst.*, vol. 705, no. 1, pp. 105–111,
        Jul. 2020, doi: 10.1080/15421406.2020.1743426.

[253]   H. Wang *et al.*, "Energy storing bricks for stationary PEDOT
        supercapacitors," *Nat. Commun.*, vol. 11, no. 1, p. 3882, Aug. 2020,
        doi: 10.1038/s41467-020-17708-1.